Magnetic Force Microscopy Imaging of Current Paths in Integrated Circuits with Overlayers

By

Anle Pu

A Thesis
Submitted to the Faculty of Graduate Studies
In Partial Fulfillment of the Requirements
For the Degree of

Doctor of Philosophy

Department of Electrical and Computer Engineering
University of Manitoba
Winnipeg, Manitoba
Canada

ABSTRACT

Mapping current paths in integrated circuits (IC) is expected to be important for design debug and failure analysis. Due to the rapid development of IC technology with higher transistor densities and smaller feature sizes, accurate location of the current paths buried under several layers of conducting interconnect is expected to have several important applications. Magnetic force microscope (MFM) holds great promise to meet this challenge and this work focuses on MFM based techniques for mapping current in conductors with over layers.

This thesis presents a systematic study of MFM based mapping of current in model circuits by using force and force gradient techniques. In comparing these two techniques with respect to signal to noise ratio as a function of the tip height above the surface of conducting lines, force was found to have a much higher SNR (from ~150 to ~580 times) than force gradient. As a result, force based techniques will have better sensitivity and are able to detect much smaller minimum currents. For model circuits that mimic ICs, we have achieved a measurement sensitivity of approximately 1.02 $\mu A/\sqrt{Hz}$ for force and 0.29 $mA/\sqrt{Hz}$ for force gradient in air without magnet to maintain the orientation of the magnetic moments of the probe during the measurement (~0.64 $\mu A/\sqrt{Hz}$ in air and ~0.095 $\mu A/\sqrt{Hz}$ in vacuum for force with a magnet), this was achieved with a probe to circuit separation of one micron. We can conclude that the force measurement technique is superior for the application of MFM current imaging of buried conductors in ICs. However, this comes at the price of reduced spatial resolution.

Extensive numerical modeling of the magnetic fields and the MFM images has shown that the simple point probe approximation is insufficient to model MFM mapping of current flow in ICs for the conductors used in this work. An extended model, which

considers realistic MFM probe geometries and the forces acting on the whole probe including along the cantilever of the probe, has been shown to be necessary. Qualitative and quantitative comparison of the experimental results and simulation results with this model are in agreement to within experimental uncertainty. Analysis of the comparison suggested that the thickness of Cobalt coating is not uniform on different regions of the probe, which was verified by scanning electron microscope (SEM) cross section images of the probes cut by a focused ion beam (FIB). The thickness of the CoCr coating varies from 60 nm to 130 nm on the surface of the cantilever and from 30 nm to 110 nm on the surface of the tip. Correcting for film thickness variation in the model produced images for current flowing in buried conductors in very close agreement with the experimental results.

Based on the simulation and experimental results, we have devised a method to locate accurately the internal current path from MFM images with submicrometer uncertainty for simple model circuits. The method was tested for different patterns of model conducting lines. It was shown to be a useful technique for fault location in IC failure analysis when current flows through the devices buried under several layers and no topographic features are on the surface to provide clues about the positions of the devices.

ACKNOWLEDGEMENTS

The work presented in this thesis would not have been possible without the help of many others. I would like to thank my supervisor, Dr. Doug Thomson, for giving me the opportunity to study in nanotechnology, and for his support, guidance, and valuable advice throughout this research project and carefully reading my thesis. I have greatly benefited in many ways by working with him.

I would also like to thank Dr. Greg Bridges and Dr. Cyrus Shafai for their spending time and assistance.

I am grateful to everyone who contributed to this thesis. I would like to thank all members of SPM group, the department's technical staff at University of Manitoba. Special thanks to Dwayne Chrusch for his help to fabricate the sample circuits. Thanks to Allan McKay and Allan Symmons for their valuable help and technical support. Thanks are also due to the Ecole Polytechnique of Montreal for facilitating Focused Ion Beam and Mechanical Engineering at the University of Manitoba for Scanning Electron Microscope

Finally, I would like to thank my family for their unconditional love and support. To my wife, Yulan Yang, my son, Sirui Pu, and my daughter, Sarah Siyu Pu, for all their understanding, encouragement and continuous support over the years. To Yulan, thanks for the endless love you give to me, and all the happiness you created in our life. To Sirui, your academic work and excellent basketball ability gives me pride. To my lovely Sarah, your smile offers me comfort and inspiration.

TABLE OF CONTENTS

Page

LIST OF FIGURES

LIST OF TABLES

LIST OF ABBREVIATIONS

Ac, dc	Alternating Current, Direct Current
AFM	Atomic Force Microscopy
a.u.	Arbitrary Unit
EFM	Electrostatic Force Microscopy
FWHM	Full Width at Half Maximum
IC	Integrated Circuit
IDDQ	VDD current Quiescent, or Quiescent power-supply current
MFM	Magnetic Force Microscopy
RMS	Root Mean Square
SEM	Scanning Electron Microscopy
SFM	Scanning Force Microscopy
SNR	Signal to Noise Ratio
SPM	Scanning Probe Microscopy
SQUID	Superconducting Quantum Interference Device
SSM	Scanning SQUID Microscopy
STM	Scanning Tunneling Microscopy
VLSI	Very Large Scale Integrated

Chapter 1
INTRODUCTION

1.1 Introduction

The rapid development of very large-scale integrated (VLSI) circuit technology has resulted in the production of progressively smaller microelectronic devices with higher transistor densities and smaller feature sizes. This progressive shrinkage, as predicted by Moore's Law (quadrupling the number of transistors in a single chip every three years) [1], has rapidly evolved the current technology into the realm of nanoelectronics [1,2]. The nanometer size of state of the art electronic devices poses an enormous diagnostic and verification challenge [3]. Microscopes based on the scanning tunneling and atomic force microscopes (STM and AFM) hold great promise for some of these challenges because they can sense a variety of physical and chemical properties with nanometer-scale resolution [4-7]. During the past two decades, the SPM has become a powerful general-purpose method for analyzing nanometer scale devices. It has revolutionized the field of microscopy by leading to an entire family of microscopes - generally referred to

as scanning probe microscopes (SPM), among which scanning force microscopy (SFM) is the most prominent.

Imaging of the current of internal circuits is of growing interest [8-10] in the integrated circuits (IC) industry. It not only provides information about magnitude and distribution of current but also allows us to extract details of the internal structure and locations of current paths which are often buried under several interconnect layers. One approach for current measurements is the mapping of the magnetic fields produced by currents flowing through the devices. Magnetic force microscopy, one kind of SFM, using a magnetic probe is capable of imaging these magnetic fields with submicron resolution. This thesis will presents a comprehensive study of the use of MFM for the mapping of currents in ICs with overlayers.

1.2 Motivation for Current Imaging

As process technologies for ICs become more complex, techniques for performance verification, design, fabrication, debug, and failure analysis have become increasing more difficult [3]. It is often not sufficient or impossible to make only circuit voltage measurements. There are significant advantages to have techniques for mapping current paths in IC's [10-12]. The mapping of current in IC could provide an important tool for several stages of IC; design debug, process development, and failure analysis.

Current imaging is a very useful technique for identifying buried metallic interconnect structures which can support the flow of the current and providing information about current crowding phenomena which drive formation mechanism of defects [13-14]. In addition, in order to study the electrical transport in fine structures like molecular wire networks and in situ study superconducting current transport, current mapping without having to physically modify the circuit is preferable [15-16].

Electromigration is the phenomenon of the macroscopic transport of mass due to the passage of current. It is generally considered to be the result of momentum transfer from

the electrons, which are moved by the applied electric field, to the ions which make up the lattice of the metallic interconnect material. It increasingly affects the reliability of the devices as the dimensions of the device become ever smaller with each new technology. It has great interest for both fundamental research and technological applications [17-20]. Obviously, the study of electromigration is important to image the current which is used to deduce the correlation of current densities with the evolution of defects in the device.

Quiescent current testing (IDDQ) refers to the IC testing method based upon measurement of steady state power-supply current and has been recognized to be an important testing method for IC industry [8-9,21-25] since it was first publicly proposed in 1981 [26]. In today's semiconductor industries, the majority of ICs are made by complementary metal-oxide-semiconductor (CMOS) technology. Once all nodes settle to a stable state (quiescent state) following a switching transient, CMOS circuits have low quiescent current (on the order of few nanoamperes) [9,21,27]. This is because at steady state there is no direct path from the supply rail (V_{DD}) to the ground rail (V_{SS}). However, in the case of physical defects such as gate-oxide short or short between source and drain, a conduction path from power-supply (V_{DD}) to ground (V_{SS}) is formed and subsequently quiescent current will be elevated a few orders of magnitude higher than the fault-free leakage current [9,21,27]. Therefore, quiescent current information can be used to distinguish between faulty and fault-free circuits. Figure 1.2.1 illustrates the quiescent current conduction paths formed due to several physical defects in ICs.

In the conventional quiescent current test, by monitoring the power-supply current, faulty and fault-free circuits may be distinguished. Once a defect is detected by electrical testing, the location of the fault must be isolated. But, since each power supply line connects to too many transistors, it is very difficulty to determine which of the millions of circuits between V_{DD} and ground V_{SS} is causing the excess current. It is possible to identify the error locations if we know the current path. Therefore, the ability to map current flow nondestructively in ICs is highly desirable for failure analysis.

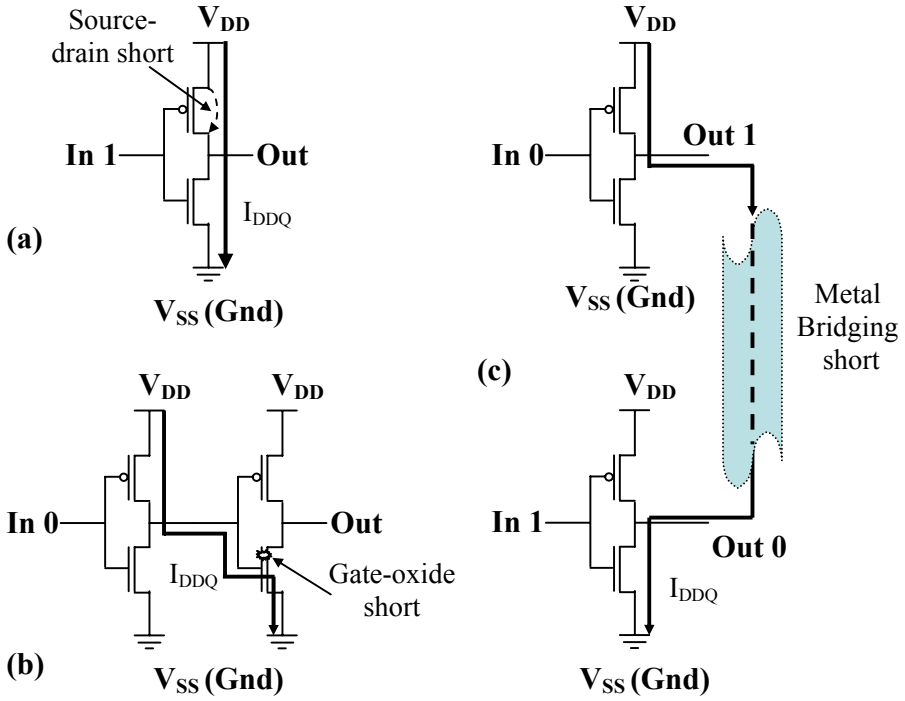

Figure 1.2.1. Formation of current path in presence of source-drain short **(a)**, gate-oxide short **(b)**, and outputs short (metal bridging) **(c)** in CMOS circuit. Thick lines indicate the current conduction paths formed due to the defects.

Several methods for current mapping have been developed during the last decade, which mainly involves optical, thermal and magnetic field imaging techniques.

1.3 Existing Current Mapping Techniques

1.3.1 Optical Techniques

The current optical technique for detecting light-emitting defects is photon emission microscopy, or light emission microscopy. It is primarily based on carrier recombination radiation [28-32] resulting from holes and electrons recombining. Normally, the emitted light is quite faint; emission microscopy uses image intensification technology to amplify the light emitted by photo-emitting defect sites. Defect location on the circuit is pinpointed by overlaying an image of the circuit taken in ordinary light or mask layouts

and an image taken in the dark with the circuit powered up, in which defects appear as bright spots. Photon emission occurs in ICs devices under various operating conditions. Some anomalies or defect sites emitting extraordinary light during device operation would otherwise be absent in a fault-free device, which can identify an excess current path [31-32]. For example: Normally, no emission is detected if there is no gate current since current flow in the channel itself is not sufficient to generate emission, unless there is an anomaly. As leakage current increases in the reverse direction, the light emission sources typically become smaller and brighter. Light emission analysis is simple, quick, non-invasive, and requires little sample preparation. It is often used as a powerful early-stage failure analysis tool to identify defective sites. In both silicon and GaAs devices, the emitted photons are in the visible and the near-infrared range (390-1500nm wavelength). This results in light emission which can be detected from the back side of the chip without decapsulation since silicon and GaAs are virtually transparent to near-infrared light. The major drawback to the optical technique is its spatial resolution limited by the wavelength of the light. The maximum resolution is usually 0.5 to two times the emitting wavelength, typically no better than 1 μm for near-infrared radiation and 0.2 μm for visible radiation [28]. This is especially a limitation for submicron IC technologies. On the other hand, for multilayer metallizations, many emission sources are covered by subsequent metallization layers. Not all abnormal light emissions emanate from the actual defect site itself and many defects do not create an abnormal light emission such as a metal-metal short. Therefore, light emission results should be complemented by results from other failure analysis techniques.

1.3.2 Thermal Imaging Techniques

Thermal imaging techniques are based on temperature changes due to current flow through a conducting line inducing a local temperature increase due to increased power dissipation. These techniques are nondestructive, economical, and relatively convenient to perform, which commonly include Liquid crystal analysis [28,33-34], infrared thermography [28, 35], and Fluorescent microthermographic imaging [28, 36-38].

A typical liquid crystal test setup is illustrated in Figure 1.2.2.

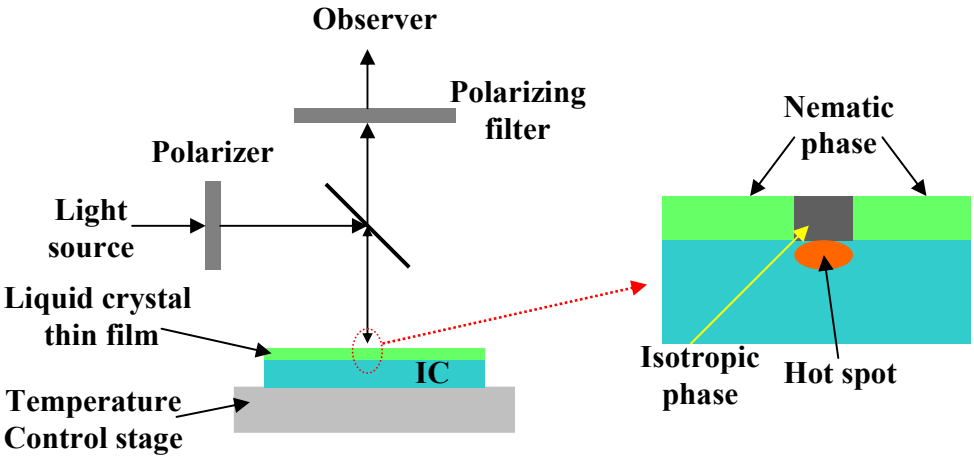

Figure 1.2.2. A typical liquid crystal test setup.

The IC device ambient temperature is controlled with a heated or cooled stage. A thin film of liquid crystal material with a phase transition temperature just above the IC device ambient temperature is applied on the IC surface so that minute amounts of heat from the defect can change the phase of the liquid crystal. An image is viewed with a polarized light system. Heated location will show a black image (see Figure 1.2.2). Liquid crystal analysis can easily detect a point source of 1 mW. Nevertheless, its spatial resolution is only several micrometers and temperature resolution is about 0.5^{o}C, which limits its applications.

Infrared thermography provides a temperature map of the IC surface with an infrared photoconductor detector and computer aided emissivity correction. It is actually a non-contact optical microscopy technique that collects infrared photons emitted by the device. The spatial distribution of temperature can be obtained because the photons emitted by the device are a function of its local temperature. This technique has relatively poor spatial resolution typically about 5 μm and quite good temperature resolution about 0.025 to 0.1^{o}C.

Fluorescent microthermographic imaging (FMI) is a thermal detection technique similar to liquid crystal but is implemented in a similar fashion to emission microscopy. It uses the temperature-dependent fluorescence of a rare earth chelate film on the IC surface to provide a direct, quantitative conversion of surface temperature into detectable photons which are able to be detected by the optical system. Under ultraviolet excitation, the fluorescent film emits light at 612 nm with the quantum efficiency decreasing with temperature, which provides a spatial resolution as small as 0.3μm. Furthermore, unlike liquid crystal, FMI has the ability to acquire an absolute temperature map of an operation device and offers better than 0.01^{o}C temperature resolution capability.

Though optical and thermal techniques have shown great success in failure analysis, they are becoming less effective as microelectronics technology has rapidly evolved to smaller feature sizes, more metal layers, and a flip-chip configuration. For example, defect sizes tend to decrease as feature sizes continue to decrease. The imaging of smaller defects and structures requires higher spatial resolution. If the defect is far beneath the surface thermal techniques will become ineffective due to heat diffusion. Optical techniques have similarly affects due to the reflection and refraction of the light through the multiple metal layers. Magnetic field imaging techniques are a rapidly growing field that is attempting to overcome some of these difficulties [26]. Scanning SQUID (superconducting quantum interference device) microscopy (SSM) [12, 39-40] and MFM are most commonly used [4-7].

1.3.3 Magnetic Field Imaging Techniques for Current Mapping

SSM and MFM are based on measuring the magnetic field or magnetic field gradients around the conducting lines generated by current flow through the lines. They provide an entirely new capability for imaging current. Unlike thermal and optical techniques, magnetic fields are not affected by the multiple metal layers and non-ferrous materials in IC devices, notwithstanding the field strength decreases with increase in distance. Thus, imaging can be performed over the multiple metal layers, inter metal dielectrics, or

encapsulation materials. In addition, the source currents can be calculated from the image, which provides the ability to map a distribution of the current in the IC devices.

SSM is a technique that uses other types of the probes. It uses a SQUID sensor [39] to obtain images of the magnetic field above a sample surface. Normally, two Josephson tunnel junctions are connected together in a superconducting loop to form a SQUID. A SQUID is the most sensitive magnetic sensor known. It can be designed to measure fields as small as 1 fT (10^{-15} T) [38], this sensitivity is high enough to image currents as small as 600 nA at a 100 μm working distance. In order to operate, a SQUID requires low temperatures that is less than 90 K (liquid nitrogen temperatures) for a high temperature SQUID and less than 9 K (liquid helium temperatures) for a low temperature SQUID. In addition, SSM has relatively poor spatial resolution of about a few microns since the SQUID pick-up loop can only be made with a minimum of a few microns range. These limit SSM's applications. However, the extreme sensitivity of SQUID sensors renders them effective to measure the weak magnetic fields generated by currents on ICs. It is becoming an important tool to help overcome some of the hurdles involved in failure analysis present in the next generations of IC technology.

The MFM technique with its inherent superior spatial resolution capabilities has been used to image magnetic fields and domains in magnetic materials. Further expanding, MFM current contrast imaging has been developed to analyze IC current direction and magnitude with a sensitivity of about 1 mA dc and about 1 μA ac [41-42]. It seems to be a good basis for advanced measurement techniques for current mapping. SFM is also commonly available in IC development and failure analysis facilities. In this thesis a state-of-the-art of current measurement via MFM and a numerical modeling calculation for MFM imaging of current faults and experimental results demonstrating the ability to isolate the IC faults are presented.

1.4 Research Outline

The impetus of the work presented in this thesis was to devise a method to locate accurately the position of current paths in ICs by using MFM to meet the requirements of ICs failure analysis. In order to carry it out, two MFM current contrast imaging techniques, force and force gradient detection, were considered and compared. During this work, it was discovered that the simple point-probe model for the magnetic coating on the probe, usually used to model MFM images, was not adequate to simulate MFM images of current flow in ICs. A numerical modeling calculations based on the realistic MFM probe geometry (tip + cantilever) was developed for simulating MFM images in order to give a systematic explanation of the experiments. Experimental models for current flow in devices were fabricated on test sample circuits. Experimental measurements were performed using both force and force gradient under different conditions including different sample-probe separations. Numerical simulations were compared with experimental results both qualitatively and quantitatively. From comparison of the experimental and simulation results and data analysis, a method to locate current paths and fault devices was devised. In addition, this thesis also presented a detailed study and comparison of the force and force gradient with regards to measurement sensitivity, signal-to-noise ratio, and spatial resolution.

1.5 Research Significance

A modest number of studies of MFM current mapping in ICs have been presented over the last decade [10,13-17,41-64] including needle sensor consisting of a quartz resonator and a probe tip [65-68]. Nearly all MFM investigations are based on the force-gradient technique. MFM was initially used to image magnetic materials, in which the tip scans over the surface of the sample within 100 nm so that a high resolution and high signal can be achieved by force gradient rather than force. Perhaps in later MFM extensions to magnetic field imaging in current carrying devices, force gradient continued to be used due to its past success. Bonnell *et al*. [68] proposed a technique which used force rather than force gradient in MFM to distinguish electrostatic and magnetic interactions and

collect simultaneously surface-potential and magnetic-force images. A contribution of this thesis is a systematic study of MFM current mapping of model circuits by using force and force gradient techniques at relevant probe to sample separations. Comparing these two techniques using signal to noise (SNR) showed that force has much higher SNR (~by several hundreds times), which results in higher sensitivity, and enables the detection of much smaller currents than that of the force gradient, especially at larger probe to sample distances (1.0~2.0μm). Therefore, force gradient is not a good choice for current mapping, when the conductor is covered with several passivation layers. Typical currents in IC with one micrometer lift will not produce signals large enough to form images by force gradient. This thesis demonstrated the force measurement technique has the ability to measure currents as small as a few microamperes (~0.64 $\mu A/\sqrt{Hz}$ in air and ~ 0.095 $\mu A/\sqrt{Hz}$ in vacuum), which could have significant practical applications.

The point probe approximation is a simple model that has proven to be quite successful in simulation of MFM force gradient images [57-69]. However, in this work, it was discovered that the simple point-probe model is insufficient to be used to model MFM images based on force measurement. An extended model, which considers realistic MFM probe geometry including tip and cantilever, was developed for simulating MFM force images. The results show an excellent agreement with the experimental results. This will help in the understanding of image formation in MFM and give an accurate means to model MFM images of current carrying conductors on ICs.

From comparison of the experimental and simulation results and data analysis, a method to accurately locate current paths and faulty devices from MFM images with submicrometer uncertainty was devised. Detail studies of the method showed it is a useful technique for fault location in IC failure analysis when current flows through devices buried several layers below the surface.

Application of the MFM current imaging is still in its infancy. The work we have done here will be a great aid in making MFM a useful failure analysis tool.

1.6 Thesis Outline

This thesis will continue in Chapter 2, which introduces the basic SPM techniques and their corresponding basic principles and theoretical background. Chapter 3 provides a detailed introduction to magnetic force microscopy, which includes its operating principles, detection technique, sensitivity, and comparison of force and force gradient detection. Chapter 4 describes a numerical model that was developed for simulating MFM images. This model takes full account of both the cantilever and the tip.

The experimental portion of the thesis begins in Chapter 5, which presents the test circuit design, measurement instrumentation, experimental details, as well as measurement results of force and force gradient, sensitivity, signal to noise ratio, and comparison of these two detections. Chapter 6 discusses a normalized and quantitative comparison of the simulation and the experiment. Modified simulations are presented to correct for deviations from the models. Based on the simulation and experimental results, a method was devised to accurately locate the internal current path from MFM images which will be presented in Chapter 7. Finally, chapter 8 summarizes the main findings and presents possibilities for future development.

Chapter 2
INTRODUCTION TO SCANNING PROBE MICROSCOPY (SPM)

This chapter focuses on the technique used in this work, scanning probe microscopy (SPM). In 1986, Gerd Binnig and Heinrich Rohrer were awarded the Nobel Prize in physics for inventing the scanning tunneling microscope (STM) in 1981 [70]. A STM works similar to a profilometer in that the signal image is obtained by scanning a fine probe tip over the surface of a sample with nanometer resolution using piezoelectric scanners. The success of the STM has stimulated the development of a whole new set of related scanning probe microscopes, which are based on the same scanning and feedback principles used in STM. The differences between SPM techniques originate from the type of interactions between tip and sample, which are used to investigate a wide range of material properties including electrical, optical and thermal aspects. This chapter will focus on the working principles of the technique used in this work, magnetic force microscopy (MFM).

2.1 Scanning Force Microscopy (SFM)

The scanning force microscope, invented by Binnig *et al.* in 1986 [71], is one of the most

successful scanning probe microscopes. As its name suggests, the SFM senses the force or force gradient between a scanning probe and a surface. The basic principle of a SFM is illustrated in Figure 2.1.1; a sharp tip is mounted at the end of a micro-machined cantilever and scans over the sample to be investigated. Forces from the sample acting on the probe tip cause the cantilever to deflect from its original height. A displacement sensor then measures the deflection which is proportional to the force or force gradient. To form an image, the strength of the sample-tip interaction is mapped as a function of position on the sample.

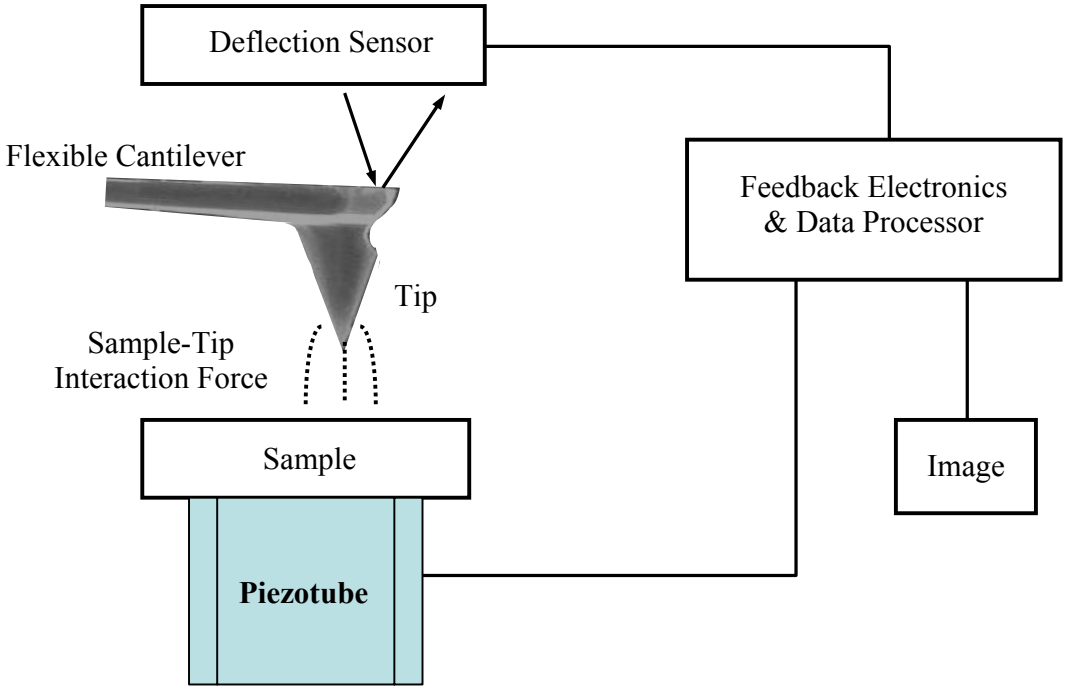

Figure 2.1.1. Schematic of scanning force microscopy operating principle.

SFM techniques are strongly dependent on the development of the displacement sensor. Binnig *et al.* [71] proposed the first displacement sensor that was based on electron tunneling [72]. Later, different sensors were introduced that included optical interferometry [73-77], beam-bounce deflection [78-80] and capacitance measurements [81-83]. In this work, we use a laser beam-bounce deflection system.

In the original work by Binnig *et al*.[71], their motivation was to observe atomic forces between the tip and the sample. When the tip is placed in contact with the surface of the sample, i.e. in contact mode, the atomic scale surface topography can be imaged. The interaction force is typically the repulsive interatomic forces. When the tip is held above the surface of the sample at a small distance, usually on the micro- or nanometer scale, the interactions between the tip and sample are dominated by long-range forces, including magnetic, electrostatic and van der Waals forces. In this thesis contact mode is used for topographic imaging of surfaces, and non-contact magnetic force imaging is used to image magnetic fields produced by current carrying conductors.

2.1.1 Contact Mode

In contact-mode, also known as repulsive mode, a SFM operates by scanning a tip across the sample surface, making a soft "physical contact" with the sample. As the scanner gently traces the tip in a raster pattern across the sample, surface topographic information (also called contours of constant force) are obtained from the feedback signal, which monitors the cantilever deflection to accommodate changing forces due to surface height variations. In this case, the interaction force deflects the cantilever quasistatically according the Hooke's Law, and this deflection is directly measured [77,84]. The force curve in Figure 2.1.2 shows this concept [85-87].

Figure 2.1.2 shows that when the sample is far from the tip, the force between them is nearly zero. However, as the tip is gradually brought near the sample's surface, they first weakly attract each other and the cantilever bends toward the sample. The attractive force increases until the electron clouds surrounding the tip and surface atoms begin to experience electrostatic repulsion. As the interatomic separation decreases further, the electrostatic repulsion increases and weakens the attractive force. When the total force becomes positive (repulsive), the tip and the specimen surface are in contact, and the sample pushes the cantilever away rather than forcing it to come closer.

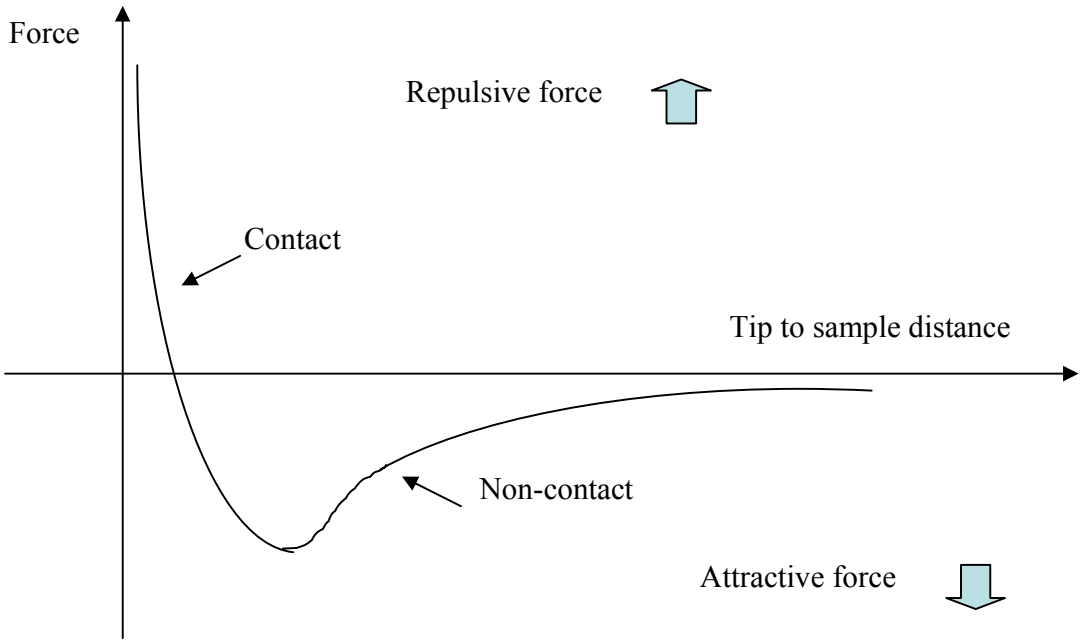

Figure 2.1.2. Probe to surface force vs. distance graph.

The slope of the force curve is very steep in the repulsive or contact regime (Figure 2.1.2). As a result, the repulsive force can balance almost any force that attempts to push the tip and sample closer together. As the tip contacts the surface, feedback circuits keep the deflection constant between the cantilever and the sample by vertically moving the scanner up and down at each (x,y) data point to maintain a reference deflection. This is constant-force mode of operation. In this case, the topographic image is generated from the scanner's motion with the cantilever deflection holding constant or the total force applied to the sample keeping constant.

While operating in contact mode, the typical achievable spatial resolution is approximately 1~10 nm in the x-y surface plane, and less than 1 nm in the vertical z direction [71]. Such high resolutions are achieved by applying very small loading forces to the tips, which have very small radii of curvature. Consequently, the contact area between the tip and the sample is very small.

In contact mode, the sample experiences compressive forces, which are produced from the tip-sample contact, and shear forces, which come from the lateral scanning motion. Both forces can induce sample deformations, which degrade the resolution. The stick-slip motion of the tip caused by the lateral shear force also changes the tip radius. Therefore, it is important to minimize the contact and lateral forces between the tip and sample in some situations. Contact SFM has been successfully used to measure the surface topography of a wide range of samples.

2.1.2 Non-Contact Mode

In contact SFM, the short-range interatomic forces dominate over the other forces acting on the tip. When the tip-surface separation increases, long-range interaction forces such as van der Waals, electrostatic, and magnetic forces become dominant. These forces are significant over greater separations as indicated in Figure 2.1.3 [88].

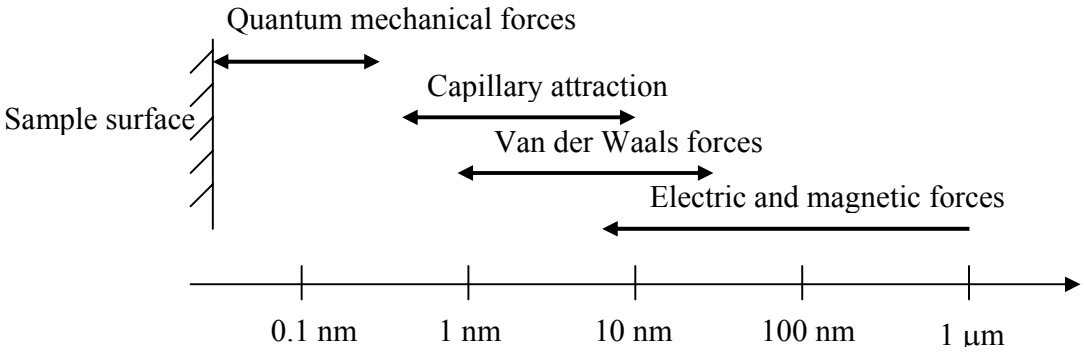

Figure 2.1.3. Different forces acting on a tip and the approximate distance region where they dominate [88].

This difference provides a means to distinguish the different types of interactions. For example, the magnetic and electric forces most strongly influence the tip when the separation exceeds 10 nm. Since the long-range forces are often considerably smaller than short-range forces, which can be several orders of magnitude greater, the method of the force detection in the non-contact SFM operation is quite different from the contact

SFM. The non-contact type of microscope has its tip held farther from the sample surface, instead of measuring quasistatic cantilever deflection, the cantilever can be made to vibrate at or near its resonant frequency in order to increase the sensitivity to the interactions (measurement techniques will be discussed later).

2.2 Beams and Cantilevers

An important part of SFM is the microcantilever that interacts with a force at the surface of a sample. The tip is mounted on a flexible cantilever whose mechanical properties play an important role in determining the sensitivity and stability of the instrument. The role of the cantilever is to translate the force acting on the tip into a deflection that subsequently can be detected by various deflection sensors. The cantilever acts as a spring, its spring constant and fundamental resonant frequency are the most important properties.

2.2.1 Spring Constant

The spring constant of a cantilever, k that is the amount of force needed to deflect a cantilever, depends on its shape, its dimensions, and the material from which it is fabricated, and is given by [89]:

$$\mathbf{k} = \frac{3\mathbf{EI}}{\ell^3} \qquad (2.2.1)$$

Where ℓ is the length of a cantilever, E is the modulus of the elasticity, and I is the moment of inertia. The modulus of the elasticity E is dependent on the material composition of the cantilever. The moment of inertia I is a function of the geometries of the cantilever. For the cantilever with a rectangular cross section, I is given by:

$$\mathbf{I} = \frac{\mathbf{wt}^3}{12} \qquad (2.2.2)$$

where *w* is the width and *t* is the thickness of the cantilever. In this case, the spring constant is:

$$\mathbf{k} = \frac{\mathbf{E}\mathbf{w}\mathbf{t}^3}{4\ell^3} \tag{2.2.3}$$

Therefore the spring constant of the cantilever can be controlled through its width, length and thickness.

If we consider the mechanical resonance properties with [90]

$$\mathbf{f}_0 = 0.162\sqrt{\frac{\mathbf{E}}{\rho}} \times \frac{\mathbf{t}}{\ell^2}, \tag{2.2.4}$$

we obtain

$$\mathbf{k} = \frac{\rho\ell\mathbf{w}\mathbf{t}\mathbf{f}_r^2}{0.105} \tag{2.2.5}$$

where f_r is the resonant frequency and ρ is the density of the cantilever material.

2.2.2 Resonant Properties

The mechanical resonance properties of a cantilever dictate how fast the microscope can track the surface and play an important role in determining the force resolution [91]. The fundamental resonant frequency of a vibrating cantilever with a rectangular cross section, ω_r, is given by [89]

$$\boldsymbol{\omega}_r \approx \sqrt{\frac{\mathbf{k}}{0.24\rho\mathbf{w}\mathbf{t}\ell + \mathbf{m}_{tip}}} \tag{2.2.6}$$

where *k* is the spring constant, ρ is the mass density of the cantilever, and m_{tip} is the

lumped mass of the tip.

Using the simple harmonic oscillator model to describe the fundamental mode, when the cantilever vibrates under an external force (F_z) with unit amplitude in a damped medium, the response of the cantilever (i.e. the cantilever deflection $\Delta z(\omega)$) in the frequency domain can be written as:

$$\Delta z(\omega) = F_z(\omega)|G(\omega)| \quad , \tag{2.2.7}$$

where $G(\omega)$ is the transfer function given by:

$$|G(\omega)| = \frac{(Q/k)(\omega_r/\omega)}{\sqrt{1+Q^2(\frac{\omega_r}{\omega}-\frac{\omega}{\omega_r})^2}}, \qquad \omega > 0 \tag{2.2.8}$$

$$|G(\omega)| = \frac{1}{k}, \qquad \text{at } \omega = 0 \tag{2.2.9}$$

Q is the quality factor, which represents how fast energy is dissipated by the system. It is defined as [91]

$$Q = 2\pi\frac{U}{\Delta U}, \tag{2.2.10}$$

where *U* is the energy, *U/ΔU* is the ratio of the stored energy in the cantilever to the energy lost during a full oscillation cycle. When the cantilever is driven at a particular amplitude and then abruptly stopped, the Q can be determined from the exponential ring down time according to $Q = \pi f_r \tau$, where τ is the time to reach the 1/e-point amplitude of the cantilever during the ring down [91]. The Q-factor can also be approximated by [92]

$$Q = \frac{\omega_r}{\Delta\omega}, \tag{2.2.11}$$

where $\Delta\omega$ is the 3-dB bandwidth from the resonance, which is at 0.707 of the maximum amplitude, i.e.

$$\frac{|\mathbf{G}(\omega)|}{|\mathbf{G}(\omega_r)|} = 0.707, \tag{2.2.12}$$

From equation (2.2.7) and (2.2.8), we obtain

$$\Delta\mathbf{z}(\omega) = \mathbf{F}_z(\omega)|\mathbf{G}(\omega)| = \mathbf{F}_z(\omega)\frac{(\mathbf{Q}/\mathbf{k})(\omega_r/\omega)}{\sqrt{1+\mathbf{Q}^2(\frac{\omega_r}{\omega}-\frac{\omega}{\omega_r})^2}}, \quad \omega > 0; \tag{2.2.13}$$

When $\omega << \omega_r$, equation (2.4.13) simplifies to

$$\Delta\mathbf{z}(\omega)\big|_{\omega\approx 0} = \frac{\mathbf{F}_z(\omega=0)}{\mathbf{k}}, \tag{2.2.14}$$

which is the static response of the system, i.e. Hook's Law.

If the driving frequency is equal to the resonance frequency ($\omega = \omega_r$), the cantilever deflection is enhanced by a factor of Q from that of $\omega = 0$ (static response) with the same magnitude of external force. Therefore, the maximum response of the system is given by

$$\Delta\mathbf{z}(\omega)\big|_{\omega=\omega_r} = \mathbf{Q}\frac{\mathbf{F}_z(\omega_r)}{\mathbf{k}}. \tag{2.2.15}$$

A SFM probe is usually driven at or near its resonant frequency to maximize the amplitude of the cantilever deflection. On the other hand, the Q-factor depends on the mechanical characteristics of the cantilever and the ambient damping properties [91].

$$Q = \frac{k}{\omega_r \gamma}, \qquad (2.2.16)$$

where γ is the viscous damping coefficient. It is a dissipative term coupling stored mechanical energy in the cantilever to the environment, which includes air damping, internal friction, inelastic phonon damping, etc [91]. In order to maximize the cantilever Q it is important to minimize sources of the cantilever damping. When the cantilever is placed in a vacuum less than 10^{-4} Torr, it is well known that both viscous air damping and molecular damping are practically negligible [91]. For this reason some of the measurements were performed in a vacuum below 10^{-4} Torr in order to increase the Q of the cantilever and hence facilitate measurement of smaller MFM signals.

2.2.3 Micro-machined Cantilever

Cantilevers and their tips are critical components of a SFM system because they determine the force applied to the sample and the ultimate spatial resolution of the system.

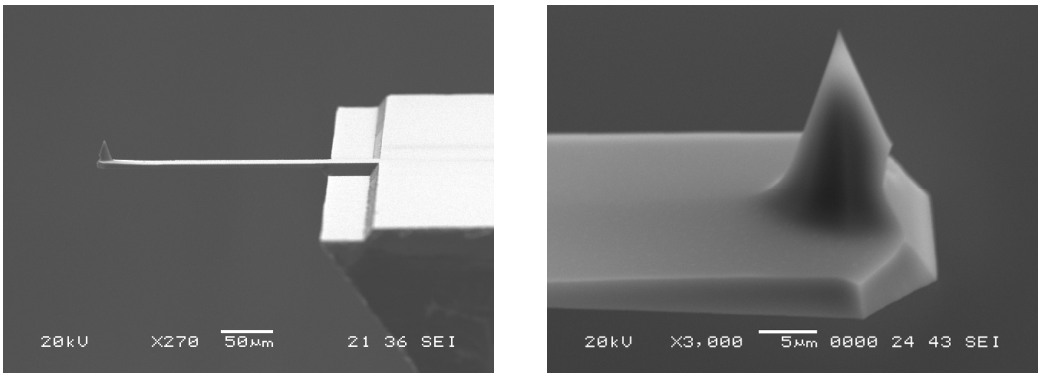

Figure 2.2.1. SEM images of a typical rectangular shaped cantilever and tip used in this work.

An ideal probe should have a high resonance frequency and quality factor, low in mass and spring constant, with a very small mechanical structure. The high resonant frequency requirement minimizes the sensitivity to low frequency noise sources such as mechanical vibrations and acoustic noise. A small tip will improve the spatial resolution and

minimize parasitic loading of the instrument. Equation (2.2.6) suggests that the resonant frequency of a probe could be increased by raising the spring constant, k, or lowering the mass of the probe. However, cantilevers with high spring constants are not often a good choice since the same force would induce smaller deflections, which is more difficult to detect. Therefore, using a low spring constant is essential in elevating the measurement sensitivity [93-94].

Low mass and low spring constant probes can be achieved by using microfabrication technologies [95-97]. The probes employed in this research were commercially available micro-machined probes produced by Silicon-MDT in cooperation with the MikroMasch Company [98]. A SEM image of a typical rectangular shaped cantilever probe is shown in Figure 2.2.1. Cantilever probes are built using silicon and coated with CoCr thin film to form MFM tips.

2.2.4 Thermo-mechanical Noise

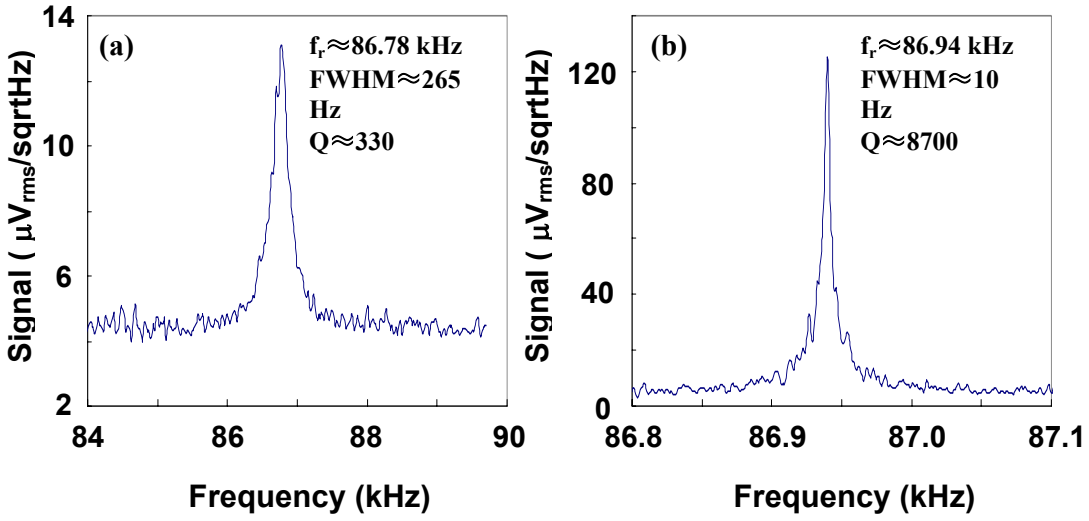

Figure 2.2.2. Mechanical response of the MFM cantilever as a function of frequency. (a) in air and (b) in vacuum environment (~5×10^{-6} Torr).

The equipartition theorem tells us that the cantilever will be excited at all frequencies by

a force equivalent to [93-94]

$$\mathbf{F} = \left(\frac{4\mathbf{k}\mathbf{k}_B \mathbf{T}\Delta\mathbf{f}}{\mathbf{Q}\omega_r} \right)^{1/2}, \qquad (2.2.17)$$

where k_BT is the thermal energy and Δf is the bandwidth.

The frequency response of the cantilever can be easily obtained by either observing the thermo-mechanical noise spectrum using a spectrum analyzer or recording the resulting vibration of the probe by a deflection sensor. Since the deflection sensor output corresponds to the cantilever vibration amplitude, the recorded data represents the frequency response of the cantilever.

Fig. 2.2.2 is an example of the thermo-mechanical noise spectrum of a typical MFM cantilever used in this research. Its resonant frequency is around 87 kHz. The quality factor Q is about 330 in air (Figure 2.2.2 (a)) and 8700 in vacuum (Figure 2.2.2(b)). As mentioned, the quality factor increases significantly in a vacuum environment.

2.3 Beam Bounce Deflection Measurement

SFM techniques are strongly dependent on the development of deflection sensors, which must be sensitive enough to measure sub-angstrom scale deflections. To date, a number of alternative detection methods have been developed. Optical techniques such as diode laser feedback detection [99-100], interferometry [73-77], and optical beam deflection [78-80] are the most commonly used. The deflection sensors used in this research are a laser beam-bounce detection system, which will be discussed next.

Meyer and Amer introduced the beam bounce detection technique in 1988 [78]. It is a very reliable, simple, and the most common detection method, which is widely used in many scanning force applications and commercially available SFMs [101-102]. A schematic diagram of the method is shown in Figure 2.3.1. A laser beam is focused onto the end of the cantilever. The deflected beam from the cantilever is then collected by a

split photodetector.

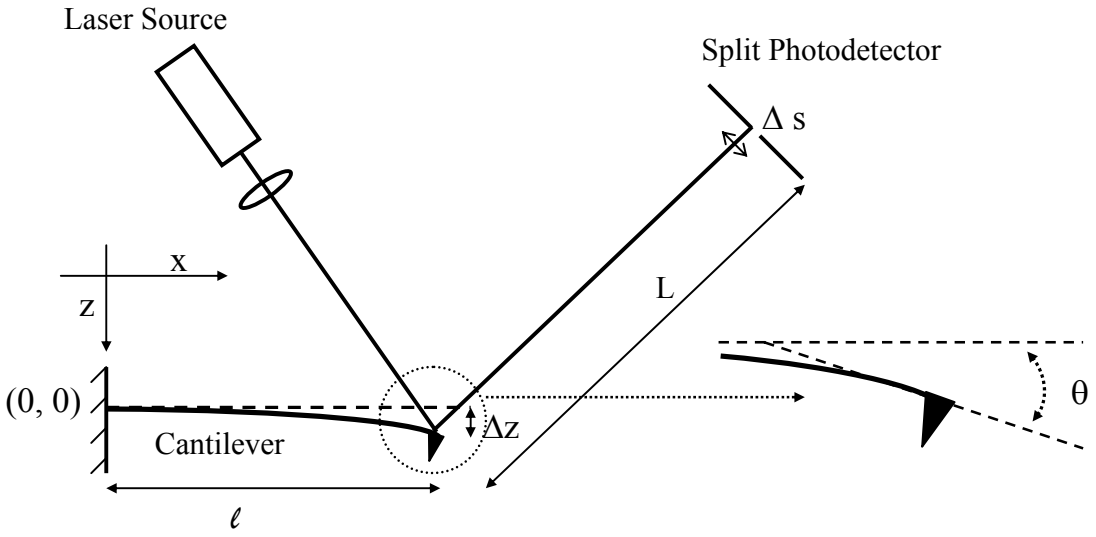

Figure 2.3.1. Beam Bounce Detection

When a force *F* is applied perpendicular to the end of the cantilever, the deflection of the cantilever is given by:

$$\Delta z(x) = \frac{F}{6EI}(3\ell x^2 - x^3), \tag{2.3.1}$$

where ℓ is the length of the cantilever, *E* is the modulus of elasticity, and *I* is the moment of inertia of the cantilever. For small deflections, the deflection angle θ of the cantilever can be expressed approximately by:

$$\Delta\theta \approx \left.\frac{dz(x)}{dx}\right|_{x=\ell} = \frac{F\ell^2}{2EI}, \tag{2.3.2}$$

Using Eq. (2.3.1) and F=kΔz, we obtain:

$$\Delta\theta \approx \frac{3\Delta z}{2\ell}, \tag{2.3.3}$$

In Figure 2.3.1, Δs is the displacement of the reflected laser beam at the split photodetector when the cantilever vertically deflects by Δz. Using similar triangles, it can be shown that the deflection of the optical beam is equal to

$$\Delta s \approx \frac{3L\Delta z}{2\ell}, \tag{2.3.4}$$

where L is the distance from the end of cantilever to the center of the split photodetector. The beam deflection causes a displacement Δs at the photodetector, and it results in more optical power falling on one side of the split detector than the other in Figure 2.3.2.

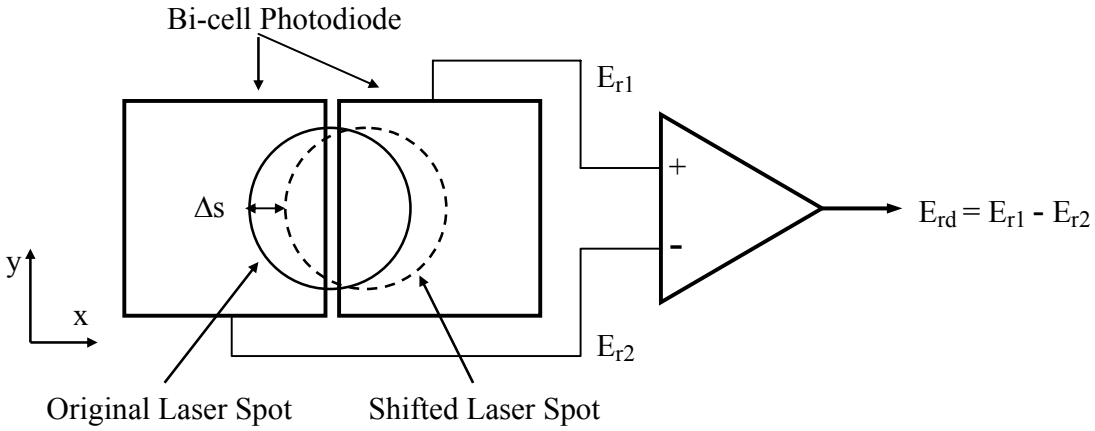

Figure 2.3.2. The shift in the optical spot is measured from the difference of the signals from the two photodiode detectors.

Therefore the output signal variation represents a cantilever deflection. Upon further analysis, it was found that the difference in photocurrent of the split photodetector is linearly proportional to the cantilever deflection as follows [84]:

$$\mathbf{I_d} = 2\mathbf{Nq}\left(\frac{\mathbf{\Delta s}}{\boldsymbol{\sigma}\sqrt{2}}\right)\frac{2}{\sqrt{\boldsymbol{\pi}}}, \qquad (2.3.5)$$

where N is the photon density rate (photons/ms), q is the charge of an electron, and σ is the spread of the beam.

Using parameters typical for SPM, beam bounce deflection sensors minimum detectable deflections of $0.001\text{nm}/\sqrt{\mathbf{Hz}}$ are easily achievable [76,103].

Chapter 3
MAGNETIC FORCE MICROSCOPY

3.1 Introduction

Magnetic force microscopy (MFM), an offshoot of atomic force microscopy [71], is based on the magnetic interaction between a sharp magnetic tip and the magnetic fields emanating from a sample under test. Over the past 20 years, magnetic force microscopy [75, 104-106] has been a useful tool for studying microscopic magnetic systems due to its ability to directly image the magnetic field distribution above the surfaces of a magnetic sample on a nanometer scale without extensive sample preparation [107-108]. Since the original MFM work by Martin and Wickramasinghe [75], a number of experimental and theoretical works have been reported, including high resolution imaging of various domain wall structures [109-110] and magnetic writing recording media [88, 111-112], quantifying MFM images [61-63], MFM-image simulations [113], and micromagnetic modeling of MFM tips [114]. In addition, numerical simulations have compared favorably with experimental MFM investigations, yielding highly precise quantitative analyses [115-116]. Recently, the MFM technique has been further improved by

controlling the preferred orientation of the tip magnetization, which allows the directional sensitivity to be defined [117]. However, only a modest number of works have dealt with the application of MFM to integrated circuits (IC) [10,13-17,41-68]. Nearly all of the works are based on the force gradient technique. A pioneering work by Bonnell *et al.* [68] used the force rather than force gradient in MFM to distinguish electrostatic and magnetic interactions. The force technique is sensitive to the current-induced magnetic field. In this work the use of magnetic force rather than force gradient is investigated. The reasons for this approach are improvements in SNR (signal to noise ratio) at tip to sample separations suitable for imaging currents in IC's with multiple conductors and inter-metal dielectrics.

3.2 Basic Principles of MFM

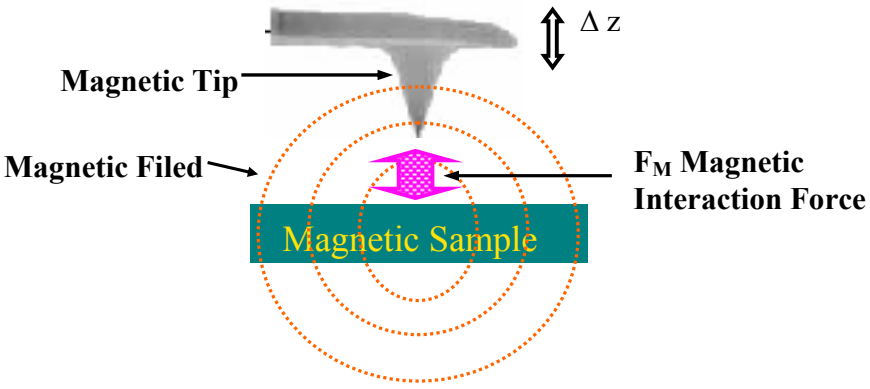

Figure 3.2.1. The operation principle of a MFM

In Figure 3.2.1, a magnetic tip is mounted at the end of a micro-machined flexible cantilever that is raster scanned over the surface of a magnetic sample at small distances. The near field magnetic interaction for a typical probe-sample configuration tends to be quite strong. As a result, MFM has become a technique which is quite easy to perform and applicable under various environmental conditions without special sample preparation [88]. The magnetic interaction between the tip and the magnetic field emanating from the sample causes a deflection of the cantilever. A high-sensitivity deflection sensor is used to detect cantilever deflection and hence the force or force

gradient. The strength of the magnetic interaction, when mapped as a function of the sample position, forms an MFM image.

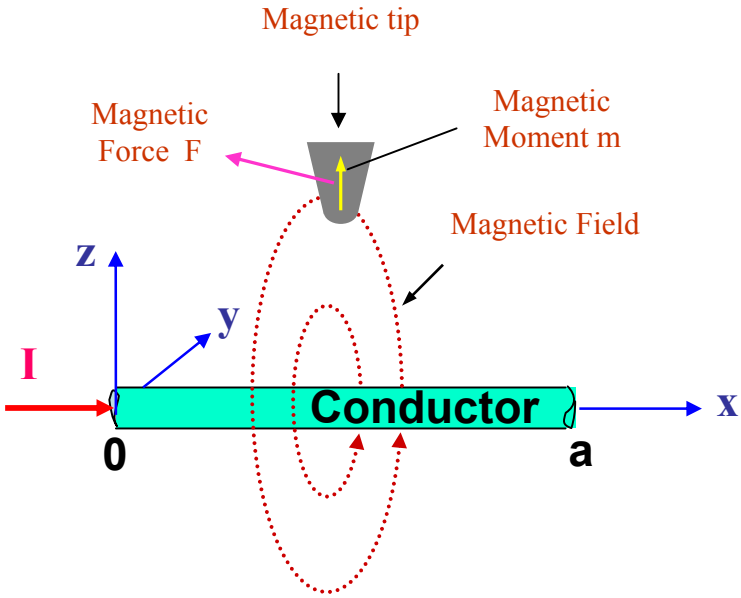

Figure 3.2.2. Magnetic interaction between the tip and the current-carrying conductor.

In our case, the sample is a current-carrying metallic conductor within an IC. According to Ampere's Law, a current flow in a conductor will induce a magnetic field ($\vec{\mathbf{B}}$) around the conductor (see Figure 3.2.2). If the MFM tip is composed of a distribution of magnetic moments, the force exerted on these magnetic moments is calculated using [105]

$$\vec{\mathbf{F}} = \sum_{tip} \nabla \vec{\mathbf{m}}(\vec{\mathbf{r}}_i) \bullet \vec{\mathbf{B}}(\vec{\mathbf{r}}_i) \qquad (3.2.1)$$

where $\vec{\mathbf{B}}$ is the magnetic field generated by the current-carrying conductor and $\vec{m}(\vec{r}_i)$ is a magnetic moment on the MFM tip at location $\vec{r}_i$. The magnetic force will cause the cantilever to deflect given by F_n/k, where k represents the spring constant of the cantilever and F_n is the component of the force **F** normal to the cantilever.

3.3 Magnetic Force Microscopy Cantilevers & Tips

The MFM tips employed in this research were commercially available thin film coated MFM tips produced by Silicon-MDT in cooperation with the MikroMasch Company. The tips have a magnetic cobalt coating, specified by the manufacturer to be 60nm thickness on the tip side and backside of the probe cantilever, and protected from oxidation by a 20 nm chrome coating [118]. Cross sectional images of the probes in chapter 6 will show that this coating thickness varies considerably from tip to tip and on various parts of the tip. The cobalt coating is a polycrystalline film, which is assumed to be uniformly magnetized along a direction that depends on the magnetization field and will be discussed in detail later. The tip has a conical octagonal shape, with a 30-50-degree full cone angle, 15-20 μm tip height, and a tip curvature radius of approximately 80 nm as shown in Figure 2.2.1. Since each tip has a slightly different size and also will change with wear after being used, we used scanning electron microscope (SEM) images of the tip to calibrate its size for the numerical simulations.

3.4 Magnetic Interaction

In this section, we will take a more detailed look at the magnetic interactions in the MFM. This will provide a basis for interpreting the images obtained with the instrument.

When a voltage (V) from a power supply is applied to the sample circuit, a current ($\mathbf{I}$) will flow through that circuit. For simplicity, we only consider a straight conducting section of the sample circuit. The field at an observation point $\vec{\mathbf{r}}_i$ ($i \in x, y, z$) produced by the current in the wire line segment, whose path is defined by L, can be determined through the vector potential $\vec{\mathbf{A}}$ (see Figure 3.4.1) [119],

$$\vec{\mathbf{A}}(\vec{\mathbf{r}}_i) = \frac{\mu_0 \mathbf{I}}{4\pi} \int_L \frac{d\vec{\mathbf{L}}}{|\vec{\mathbf{r}}_i - \vec{\mathbf{r}}'|} , \qquad (3.4.1)$$

where $\vec{\mathbf{r}}'$ is a point along L, $\mathbf{d}\vec{\mathbf{L}}$ is the current direction at that point and μ_0 is the permeability of free space that is equal to $4\pi \times 10^{-7}$ Wb/A•m.

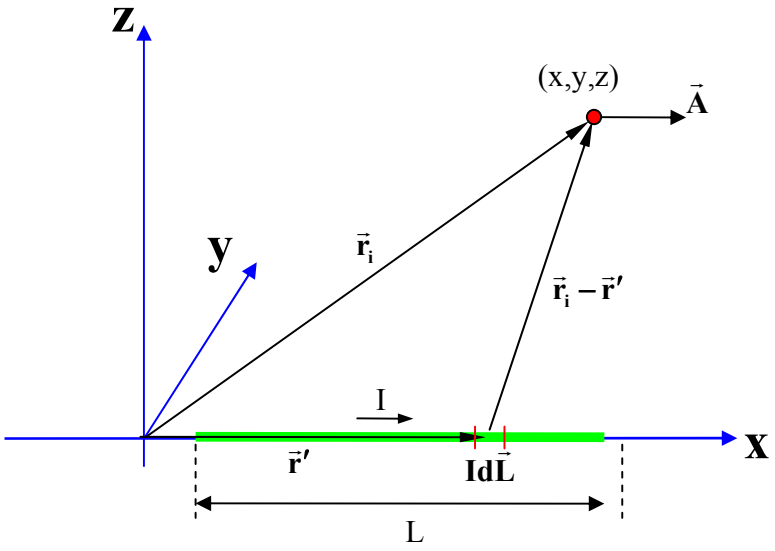

Figure 3.4.1. A linear distribution of current.

The magnetic field is then given by

$$\vec{\mathbf{B}}(\vec{\mathbf{r}}_i) = \nabla \times \vec{\mathbf{A}}(\vec{\mathbf{r}}_i), \qquad (3.4.2)$$

where the space derivatives are taken with respect to the (x, y, z) coordinates at the observation point.

When the magnetic tip is brought closer to the sample surface, a mutual magnetic interaction occurs between the MFM tip magnetization and a magnetic field from the sample. To calculate the force acting on the tip mathematically, we assume: 1) the tip is magnetized uniformly in a given direction that it is usually along the tip's axis or along an axis determined by an external field. The magnetic field from the sample is not strong enough to alter the tip's magnetization. 2) the sample's current distribution or, in other

words, the magnetic field from the sample is unaffected by the interaction with the magnetic field produced by the tip [86, 120-121]. These are good approximations in our case as the generated magnetic fields are small (< 0.006 T). They will be discussed further in modeling calculations in the next chapter. If these assumptions are not fulfilled, MFM images will reflect mutual deformations of the probe magnetization and sample current configurations. This type of destructive MFM imaging has been experimentally observed when studying soft magnetic materials [122-125].

Once the magnetic field from the sample is known, the force acting on the tip can be obtained from the gradient of the energy using equation (3.2.1)

$$\vec{\mathbf{F}} = \sum_{\text{tip}} \nabla \vec{\mathbf{m}}(\vec{\mathbf{r}}_{\mathbf{i}}^{''}) \bullet \vec{\mathbf{B}}(\vec{\mathbf{r}_{\mathbf{i}}} + \vec{\mathbf{r}}_{\mathbf{i}}^{''}) \tag{3.4.3}$$

where $\vec{\mathbf{m}}(\vec{\mathbf{r}}_{\mathbf{i}}^{''})$ is a magnetic moment on the MFM tip at the location $\vec{\mathbf{r}}_{\mathbf{i}}^{''}$. $\vec{\mathbf{B}}(\vec{\mathbf{r}}_{\mathbf{i}} + \vec{\mathbf{r}}_{\mathbf{i}}^{''})$ is the stray field from the sample at the location $\vec{\mathbf{r}}_{\mathbf{i}}^{''}$ and is given by equation (3.4.2). The tip apex coordinate $\vec{\mathbf{r}}_{\mathbf{i}}$ defines the tip position (see Figure 3.4.2). Coordinate $\vec{\mathbf{r}}_{\mathbf{i}}^{''}$ is the internal position of the volume element in the tip.

In the above expressions we assume the MFM tip is composed of a distribution of magnetic moments. The sum $\sum_{\text{tip}}$ encompasses all these magnetic moments. Expanding Eq. (3.4.3) results in

$$\begin{aligned}\vec{\mathbf{F}} = \sum_{\text{tip}} \Bigg\{ & \left(\mathbf{m}_{\mathbf{x}}(\vec{\mathbf{r}}_{\mathbf{i}}^{''}) \frac{\partial \mathbf{B}_{\mathbf{x}}(\vec{\mathbf{r}}_{\mathbf{i}} + \vec{\mathbf{r}}_{\mathbf{i}}^{''})}{\partial \mathbf{x}} + \mathbf{m}_{\mathbf{y}}(\vec{\mathbf{r}}_{\mathbf{i}}^{''}) \frac{\partial \mathbf{B}_{\mathbf{y}}(\vec{\mathbf{r}}_{\mathbf{i}} + \vec{\mathbf{r}}_{\mathbf{i}}^{''})}{\partial \mathbf{x}} + \mathbf{m}_{\mathbf{z}}(\vec{\mathbf{r}}_{\mathbf{i}}^{''}) \frac{\partial \mathbf{B}_{\mathbf{z}}(\vec{\mathbf{r}}_{\mathbf{i}} + \vec{\mathbf{r}}_{\mathbf{i}}^{''})}{\partial \mathbf{x}} \right) \vec{\mathbf{x}} \\ & + \left(\mathbf{m}_{\mathbf{x}}(\vec{\mathbf{r}}_{\mathbf{i}}^{''}) \frac{\partial \mathbf{B}_{\mathbf{x}}(\vec{\mathbf{r}}_{\mathbf{i}} + \vec{\mathbf{r}}_{\mathbf{i}}^{''})}{\partial \mathbf{y}} + \mathbf{m}_{\mathbf{y}}(\vec{\mathbf{r}}_{\mathbf{i}}^{''}) \frac{\partial \mathbf{B}_{\mathbf{y}}(\vec{\mathbf{r}}_{\mathbf{i}} + \vec{\mathbf{r}}_{\mathbf{i}}^{''})}{\partial \mathbf{y}} + \mathbf{m}_{\mathbf{z}}(\vec{\mathbf{r}}_{\mathbf{i}}^{''}) \frac{\partial \mathbf{B}_{\mathbf{z}}(\vec{\mathbf{r}}_{\mathbf{i}} + \vec{\mathbf{r}}_{\mathbf{i}}^{''})}{\partial \mathbf{y}} \right) \vec{\mathbf{y}} \\ & + \left(\mathbf{m}_{\mathbf{x}}(\vec{\mathbf{r}}_{\mathbf{i}}^{''}) \frac{\partial \mathbf{B}_{\mathbf{x}}(\vec{\mathbf{r}}_{\mathbf{i}} + \vec{\mathbf{r}}_{\mathbf{i}}^{''})}{\partial \mathbf{z}} + \mathbf{m}_{\mathbf{y}}(\vec{\mathbf{r}}_{\mathbf{i}}^{''}) \frac{\partial \mathbf{B}_{\mathbf{y}}(\vec{\mathbf{r}}_{\mathbf{i}} + \vec{\mathbf{r}}_{\mathbf{i}}^{''})}{\partial \mathbf{z}} + \mathbf{m}_{\mathbf{z}}(\vec{\mathbf{r}}_{\mathbf{i}}^{''}) \frac{\partial \mathbf{B}_{\mathbf{z}}(\vec{\mathbf{r}}_{\mathbf{i}} + \vec{\mathbf{r}}_{\mathbf{i}}^{''})}{\partial \mathbf{z}} \right) \vec{\mathbf{z}} \Bigg\}\end{aligned} \tag{3.4.4}$$

where m_j ($j \in x, y, z$) is a component of the magnetic moment on the tip at location $\vec{r}_i''$. The $\vec{x}$, $\vec{y}$, $\vec{z}$ are the unit vectors of the coordinate system, their coefficients are the force Cartesian components which is along x, y, z axis, respectively. That is

$$\vec{F} = \sum_{tip} \left(F_x \vec{x} + F_y \vec{y} + F_z \vec{z} \right) \tag{3.4.5}$$

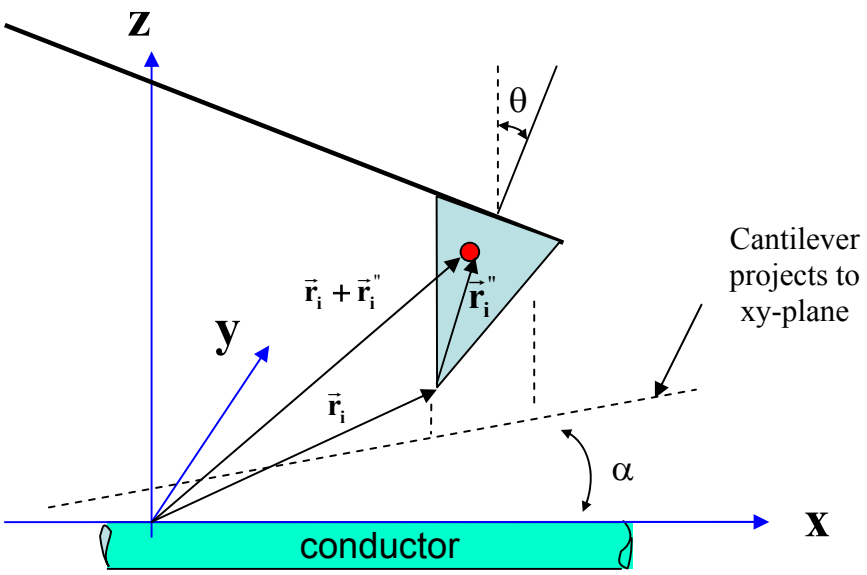

Figure 3.4.2. Geometry used for calculating the force acting on the tip

Referring to Figure 3.4.2, the measured force $\mathbf{F}_n$ in the MFM experiment is the force component in the direction normal to the cantilever surface. This direction is given by the unit vector $\vec{n} = (\cos\alpha \sin\theta, \sin\alpha \sin\theta, \cos\theta)$, where θ is the canting angle between the normal of the cantilever surface (the long tip axis) and the normal of the sample surface (the z-axis of the coordinate system) (Fig. 3.4.2), and α is the angle between x-axis and the projection of the long tip axis or cantilever to the xy-plane. Therefore

$$\mathbf{F_n} = \sum_{\text{tip}} \left(\mathbf{F_x} \cos\alpha \sin\theta + \mathbf{F_y} \sin\alpha \sin\theta + \mathbf{F_z} \cos\theta \right) \qquad (3.4.6)$$

This is a general expression of the magnetic force acting on the cantilever. By considering special cases, Eq.(3.4.6) can be considerably simplified. If we consider the case where the cantilever is parallel to the sample surface, that is $\vec{n} = \vec{z}$ or $\theta = 0$, then Eq. (3.4.6) reduces to

$$\mathbf{F_n} = \sum_{\text{tip}} \mathbf{F_z} = \sum_{\text{tip}} \left(\mathbf{m_x}(\vec{\mathbf{r}_i}) \frac{\partial \mathbf{B_x}(\vec{\mathbf{r}_i})}{\partial \mathbf{z}} + \mathbf{m_y}(\vec{\mathbf{r}_i}) \frac{\partial \mathbf{B_y}(\vec{\mathbf{r}_i})}{\partial \mathbf{z}} + \mathbf{m_z}(\vec{\mathbf{r}_i}) \frac{\partial \mathbf{B_z}(\vec{\mathbf{r}_i})}{\partial \mathbf{z}} \right) \qquad (3.4.7)$$

In the ideal case, the cantilever is assumed to be parallel with the sample circuit, so Eq. (3.4.7) can be used to evaluate the interaction force. This approximation is often used in MFM analysis. However, in most cases the measurements are made with the cantilever tilted at approximately 15 degrees relative to the sample plane in order to scan conveniently. The effects of tilting on MFM images of current in ICs are discussed more extensively in chapter 4.

3.5 Current Sensitivity

An important quantity of interest in MFM detection of current in ICs is the current sensitivity. Current sensitivity refers to the minimum RMS (root-mean-square) current on the circuit that can be detected by the MFM system. It is of course important to establish the smallest current that can be measured in a conductor.

To estimate the current sensitivity, it is necessary to determine the probe deflection caused by noise sources, and then calculate the magnetic field acting on the probe from a current carrying conductor that will induce an equivalent probe deflection.

The noise is any signal detected by the deflection sensor that is not induced by the magnetic interaction between the probe and sample. The noise sources in an MFM system include:

1) Environmental mechanical and acoustic noise that couple into the deflection measurement system,
2) Shot noise arising from the random charges at the detector surface and laser intensity noise for the optical detection scheme,
3) Electrical noise in the detection electronics that are coupled to the probe from the external sources,
4) 1/f noise resulting the low frequency fluctuations in the output power of the laser source and detection electronics, and
5) Mechanical noise vibration of the cantilever due to its finite temperature.

Since our MFM probe structure is designed with high rigidity and operates on a vibration-isolation table, noise due to the environmental mechanical vibration is negligible. In addition, external electrical noise sources have been eliminated by shielding the probe signal path and using a common referenced ground.

With good design, the laser and electrical noise can also be made negligibly small. The optical beam bounce system can resolve cantilever displacements on the order of 10^{-4} nm/$\sqrt{\mathbf{Hz}}$, depending on the setup and optical power used [76,103]. When a lock-in amplifier is used to narrow the measurement bandwidth, thermo-mechanical vibration noise of cantilever is at least an order of magnitude larger than the above optical system resolution (10^{-4} nm/$\sqrt{\mathbf{Hz}}$). Therefore, in non-contact SFM measurements, thermal vibration of the cantilever is normally the dominant noise source [126]. Current sensitivity is therefore fundamentally limited by the thermal energy and the energy dissipation within the cantilever.

A plot of the theoretical deflection power density along with the experimental spectrum using a spectrum analyzer is shown in Figure 3.5.1.

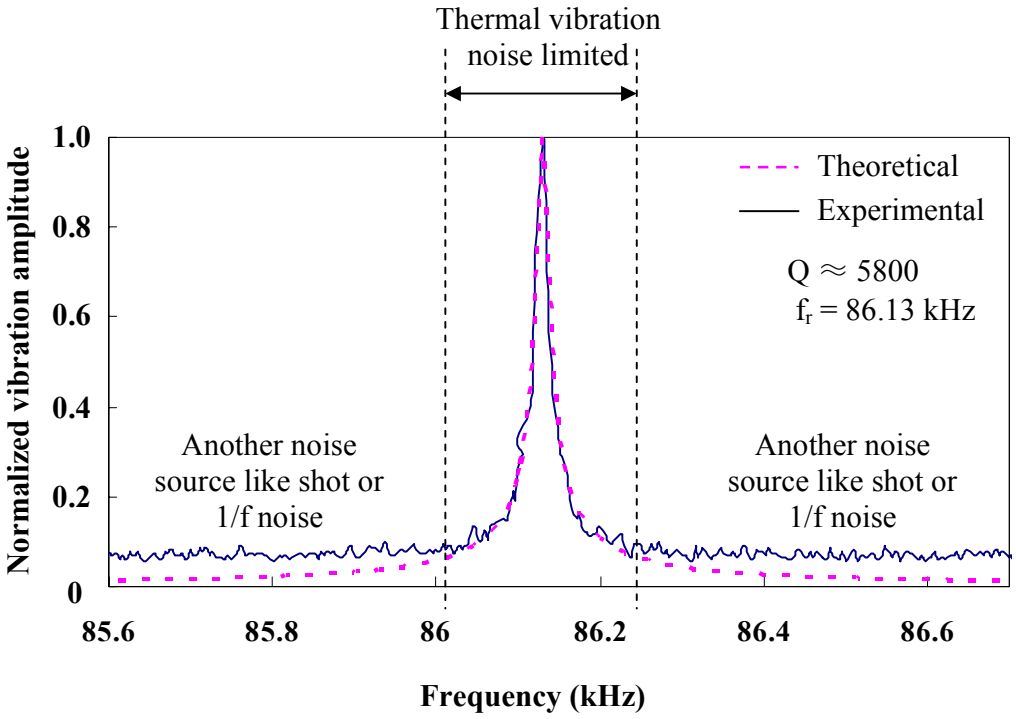

Figure 3.5.1. Theoretical and experimental deflection noise density.

The thermal noise is a random Brownian motion around the equilibrium position of the cantilever. The equipartition theorem states that each internal degree of freedom of a system has a RMS thermal energy given by $0.5k_BT$, where k_B is Boltzman's constant (1.38×10^{-16} erg K^{-1}) and T is the absolute temperature. The simple harmonic oscillator can be used to model the probe as being a mechanical spring capable of one-dimensional motion. In this case, the total integrated RMS vibration noise amplitude x_n at the free end of the cantilever is considered to result from a noise force, which is characterized by a flat power spectrum [91,127],

$$\mathbf{x_n^2} = \frac{1}{2\pi}\int_0^\infty \mathbf{S_n^2}\left|\mathbf{G}(\omega)\right|^2 \mathbf{d}\omega \ , \tag{3.5.1}$$

where

$$\left|\mathbf{G}(\omega)\right| = \frac{(\mathbf{Q}/\mathbf{k})(\omega_r/\omega)}{\sqrt{1+\mathbf{Q}^2(\frac{\omega_r}{\omega}-\frac{\omega}{\omega_r})^2}} \tag{3.5.2}$$

is the transfer function of the probe. $\mathbf{S_n^2}$ is the power density of the force noise and has units of N^2/Hz. Using complex analysis, for Q>>1,

$$\mathbf{S_n} = \left(\frac{4}{\mathbf{Q}\omega_r}\right)^{1/2} \mathbf{k}\mathbf{x_n}. \tag{3.5.3}$$

If the probe is in thermal equilibrium with the outside environment, the equipartition theorem predicts that

$$\frac{1}{2}\mathbf{k}\mathbf{x_n^2} = \frac{1}{2}\mathbf{k_B}\mathbf{T}. \tag{3.5.4}$$

Therefore

$$\mathbf{S_n} = \left(\frac{4\mathbf{k}\mathbf{k_B}\mathbf{T}}{\mathbf{Q}\omega_\mathbf{r}} \right)^{1/2} \tag{3.5.5}$$

If a lock-in amplifier is used to narrow the bandwidth, the minimum detectable force is [91],

$$\mathbf{F}_{\min} = \left(\frac{4\mathbf{k}\mathbf{k_B}\mathbf{T}\Delta\mathbf{f}}{\mathbf{Q}\omega_\mathbf{r}} \right)^{1/2}, \tag{3.5.6}$$

where Δf is the measurement bandwidth.

This force will cause the cantilever deflection. If the measurement is centered at the resonant frequency, we obtain,

$$\Delta\mathbf{z_n} = \Delta\mathbf{z_n}(\omega)\big|_{\omega=\omega_\mathbf{r}} = \mathbf{Q}\frac{\mathbf{F}_{\min}}{\mathbf{k}} = \left(\frac{4\mathbf{Q}\mathbf{k_B}\mathbf{T}\Delta\mathbf{f}}{\mathbf{k}\omega_\mathbf{r}} \right)^{1/2}, \tag{3.5.7}$$

where Δz_n is the RMS deflection of the cantilever due to thermal noise.

The current sensitivity can be calculated by using

$$\Delta\mathbf{z_n} = \Delta\mathbf{z_{mfm}}, \tag{3.5.8}$$

where Δz_{mfm} is the RMS deflection of the cantilever from the magnetic field produced by the conductor current acting on the probe. Since the measurement is commonly made at the resonant frequency, this deflection can be derived from equation (2.2.13), (3.4.3) and (3.4.6). We obtain,

$$\Delta \mathbf{z}_{\mathbf{mfm}} = \frac{\mathbf{Q}}{\mathbf{k}}\mathbf{F}_{\mathbf{n}} = \frac{\mathbf{Q}}{\mathbf{k}}\sum_{\mathbf{tip}}\left(\mathbf{F}_{\mathbf{x}}\cos\alpha\sin\theta + \mathbf{F}_{\mathbf{y}}\sin\alpha\sin\theta + \mathbf{F}_{\mathbf{z}}\cos\theta\right), \qquad (3.5.9)$$

where F_n is force acting normal to the cantilever. Comparing this formula with eqn.(3.5.7), where

$$\mathbf{F}_{\min} = \mathbf{F}_{\mathbf{n}}, \qquad (3.5.10)$$

this expression can be used to estimate the current sensitivity from the force resolution.

The magnetic field cannot typically be analytically calculated, and numerical techniques are usually required, these will be presented in Chapter 4, where numerical methods are used to simulate the magnetic fields produced from the current-carrying conductor and the magnetic forces acting on MFM probes. In Chapter 6 we will present experimental results of the current sensitivity, comparing it with the theory later. A simple example that can be analytically calculated will be presented in the next section.

3.5.1 A Simple Example of the Current Sensitivity

In this thesis we will be using force imaging the magnetic fields generated by the currents. To help understand why force was chosen we will look at a simple example of the current sensitivity for which analytical expressions can be relatively easily derived.

Let us consider a small circular loop carrying a current **I.** At the center of the loop, the magnetic field has only the vertical component, and its value at height z above the loop plane is given by

$$\mathbf{B}_{\mathbf{z}} = \frac{\mu_0 \mathbf{R}^2 \mathbf{I}}{2(\mathbf{R}^2 + \mathbf{z}^2)^{3/2}} \qquad (3.5.11)$$

where R is the radius of the loop. Therefore,

$$\frac{\partial B_z}{\partial z} = -\frac{3}{2}\mu_0 R^2 \frac{z}{(R^2 + z^2)^{5/2}} I . \qquad (3.5.12)$$

In this simple example let us assume the tip can be modeled as a single magnetic moment m_z. It is located within the real tip at a distance d measured from the tip apex as shown in Fig. 3.5.2. Thus, we obtain

$$F_n = m_z \frac{\partial B_z}{\partial z} = -\frac{3}{2}\mu_0 m_z R^2 \frac{z+d}{[R^2 + (z+d)^2]^{5/2}} I , \qquad (3.5.13)$$

Figure 3.5.2 gives the schematic representation of the experimental arrangement within the point probe approximation [63].

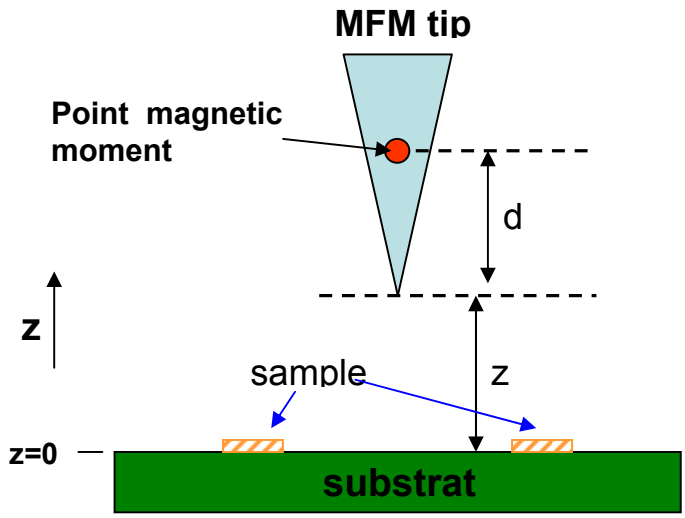

Figure 3.5.2. Illustrating the experimental arrangement of the MFM tip showing the location of the point magnetic moment of the tip. An additional replacement d along the z-axis with respect to the actual lift height of z. z is the experimentally controllable tip lift height.

Lohau *et al.* [63] have estimated the effective magnetic moments of commercially available MFM thin film tips. Using the results given by J.Lohau,

$m_z = 6.009 \times 10^{-15}\ Am^2$, $R = 6.030 \times 10^{-7}$ m, $d = 5.20 \times 10^{-7}$ m.

Typical mechanical and electrical parameters are

T = 300 K, $\Delta f \approx 30$ Hz, $f_r = 100.45$ kHz, k = 1.35 N/m, Q =3047 in vacuum, and 271 in air, $z = 1.0 \times 10^{-6}$ m.

We obtain,

in vacuum:

$$F_{min} = \left(\frac{4\mathbf{k}k_B\mathbf{T}\Delta\mathbf{f}}{\mathbf{Q}\omega_r}\right)^{1/2} = \left(\frac{4\times1.35\times1.38\times10^{-23}\times300\times30}{3047\times2\times3.14\times100.45\times10^{3}}\right)^{1/2}$$

$$= 1.87 \times 10^{-14}\ N = 3.41 \times 10^{-15}\ \frac{\mathbf{N}}{\sqrt{\mathbf{Hz}}}\ ,$$

$$\Delta z_n = 7.70 \times 10^{-12}\ \frac{\mathbf{m}}{\sqrt{\mathbf{Hz}}} = 7.70 \times 10^{-2}\ \text{Å}/\sqrt{\mathbf{Hz}}\ ,$$

$$\mathbf{I}_{min} \approx 6.43 \times 10^{-6}\ A\ /\sqrt{\mathbf{Hz}} = 6.43\ \mu A/\sqrt{\mathbf{Hz}}\ .$$

in air:

$$F_{min} = 6.30 \times 10^{-14}\ N = 1.15 \times 10^{-14}\ \frac{\mathbf{N}}{\sqrt{\mathbf{Hz}}},$$

$$\Delta z_n = 2.27 \times 10^{-12} \frac{\mathbf{m}}{\sqrt{\mathbf{Hz}}} = 2.27 \times 10^{-2} \text{ Å}/\sqrt{\mathbf{Hz}} ,$$

$$\mathbf{I}_{min} \approx 21.66 \ \mu\text{A}/\sqrt{\mathbf{Hz}} .$$

These results show that the deflection, Δz_n, due to thermal noise is much larger than the resolution of the optical beam bounce system (10^{-4} nm/$\sqrt{\mathbf{Hz}}$). In other words, thermal noise is the dominant noise source in the system. The current sensitivity is around the order of microampere for the force detection, which will be discussed in next chapter.

3.6 Comparison of Force and Force-Gradient Detection

In this work, force was chosen to image currents rather than force gradient as force has much greater sensitivity. Justification for this choice can be glanced by comparing the minimum detectable current for the simple case outlined in the previous section.

Forces are detected as the deflection of the cantilever, which is proportional to QF_n/k for driving frequencies at the cantilever's resonance. Force gradients are commonly detected by using one of three methods: amplitude slope detection [84,128], phase detection [129], or frequency modulation detection (FM) [84, 127]. In these methods, the cantilever is driven at a constant frequency near its resonance by employing an external vibration oscillator to modulate the tip-sample distance, and force gradients are detected as variations in the amplitude or phase of the probe vibration caused by the frequency shift of the resonance point.

In the previous section, we have shown the minimum detectable force, thus, the signal-to-noise ratio (SNR), which characterizes the accuracy of the system with which one can measure F_n is given by

$$SNR_F = \frac{\Delta z_F}{\Delta z_n} = \frac{F_n}{F_{min}} = F_n\left(\frac{Q\omega_r}{4kk_B T\Delta f}\right)^{1/2}, \qquad (3.6.1)$$

where F_n is the magnetic force generated by a current.

Similarly, an estimate for the minimum detectable force gradient for slope detection is given by [127]

$$F'_{min} = \frac{\partial F}{\partial z} = \left(\frac{2kk_B T\Delta f}{Q\omega_d < z_{osc}^2 >}\right)^{1/2}, \qquad (3.6.2)$$

where $< z_{osc}^2 >$ is the mean-square amplitude of the driven cantilever vibration typically a few nanometers (< 10nm) [86] and ω_d is the driven frequency of the cantilever. In the case of FM detection, a careful analysis shows that F'_{min} is given Eqn. (3.6.2) multiplied by $\sqrt{2}$. Thus, slope detection and FM detection have similar sensitivity [130].

With the approximation $\omega_d \approx \omega_r$, the SNR for the force gradient is

$$SNR_{FG} = \frac{\Delta z_{FG}}{\Delta z_{ng}} = \frac{F'_n}{F'_{min}} = F'_n\sqrt{< z_{osc}^2 >}\left(\frac{Q\omega_r}{2kk_B T\Delta f}\right)^{1/2}, \qquad (3.6.3)$$

Comparing force detection with force-gradient detection and ignoring a factor of constant, then,

$$\frac{SNR_F}{SNR_{FG}} \propto \frac{F_n}{F'_n\sqrt{< z_{osc}^2 >}}, \qquad (3.6.4)$$

In many situations, the magnetic field generated by a current carrying wire has the form

$$B(z) \propto \frac{1}{z}, \tag{3.6.5}$$

where z is a tip-sample separation. This yields a force of

$$F_S \propto \frac{1}{z^2}, \tag{3.6.6}$$

and a force gradient of

$$F_s' \propto \frac{1}{z^3}. \tag{3.6.7}$$

In this situation, Eqn.(3.6.4) becomes

$$\frac{SNR_F}{SNR_{FG}} \propto \frac{z}{\sqrt{< z_{osc}^2 >}}. \tag{3.6.8}$$

From Eq. (3.6.8), we see that the force based current detection will be better than force-gradient detection by a ratio equal to the ratio of the tip to sample spacing divided by cantilever oscillation amplitude multiplied by a constant factor.

For a small circular loop carrying a current we can calculate this ratio more specifically. At the center of the loop, we have

$$F_n' = m_z \frac{\partial^2 B_z}{\partial z^2} = -\frac{3}{2}\mu_0 m_z R^2 \left(\frac{R^2 - 4(z+d)^2}{[R^2 + (z+d)^2]^{7/2}} \right) I, \tag{3.6.9}$$

and substituting (3.5.13) and (3.6.9) into (3.6.4) yields

$$\frac{SNR_F}{SNR_{FG}} = \frac{(z+d)[R^2+(z+d)^2]}{[R^2-4(z+d)^2]\sqrt{<z_{osc}^2>}} \tag{3.6.10}$$

Using the same values for R and d as before, and $\sqrt{<z_{osc}^2>}$ = 10 nm, the ratio of force SNR and force-gradient SNR as a function of separation z is shown in Figure 3.6.1.

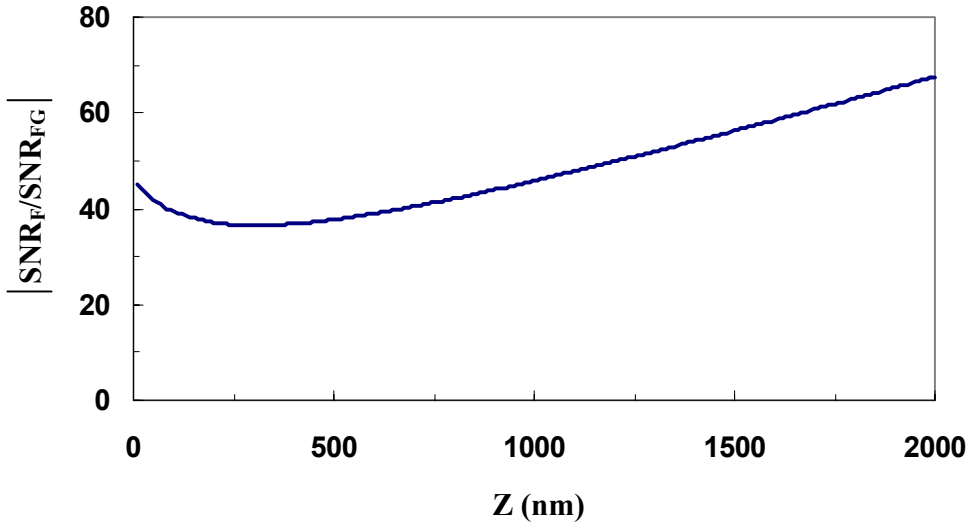

Figure 3.6.1. The ratio of force SNR and force-gradient SNR at the center of a small circular loop carries a current.

In Figure 3.6.1, the graph has the minimum 38, which means the SNR of the force detection is at least 38 times greater than the SNR of the force-gradient detection at the center of the circular loop. At more typical spacings for ICs such as z = 2 μm (2000nm), the advantage of force over force gradient is greater than a factor of 60-80. Generally, the SNR of the force is much higher than that of the force-gradient. Thus, force detection will result in better sensitivity and enable the detection of much smaller minimum currents than that of the force-gradient method. However, this comes at the price of reduced resolution. In a later chapter simulations and experiments will examine the ratio of the detection limit in geometries that are more representative of Integrated Circuits.

In addition, since the force has an inverse relationship with respect to the tip-sample distance and the force gradient has a higher order inverse of it, the advantage of detecting the force gradient instead of the force is obvious. Hubert *et al.* [131] used the reciprocity idea [132], which considers the tip-sample interaction as occurring between the magnetization in the sample and the magnetic field from the MFM tip. For different tip geometries, the tip potential and its derivatives were analyzed by comparing the full width at half maximum (FWHM) of the different potential derivatives. The first and second order derivatives corresponded to force mode and force-gradient mode microscopy respectively. The results show the advantage of detecting the force gradient instead of the force. Although the point tip geometry still displays an advantage in the first order derivative except for very small distances, in the second order derivative their difference becomes insignificant. The force gradient minimizes the contribution from the tip sidewall and the cantilever and is not sensitive to the tip's geometry. As a result, the force-gradient detection approach has been developed to improve the spatial resolution of the MFM system.

To date, nearly all MFM current imaging work has been based on the force-gradient technique. Theoretical work on the tip to sample interaction [133], MFM image simulation [113] and micromagnetic modeling of MFM tips [114,131,134] using simple point probe models have successfully described MFM image formation.

However, unlike force-gradient detection, for the force detection method simple point magnetic moment models cannot adequately explain the MFM images. In this thesis, I will present MFM results based on the force detection method. To quantitatively model MFM image formation, a numerical technique has been developed. The model takes full account of the MFM tip and cantilever.

The next chapter is dedicated to describing a numerical method that was developed to simulate the magnetic fields and forces in realistic MFM tip geometries in order to enable quantitative comparisons with the experimental results provided in the subsequent chapters.

3.7 Effect of Multi-Metallic Layers

In this thesis force using an applied sinusoidal current was investigated for imaging current with over layers. The possible effects of the multi-layers on the magnetic fields will be discussed in this section.

In the case of non-ferrous dielectric material layers, the signal dependence of the MFM signal on the thickness of the layer is shown to be in quantitative agreement with the structure without the layer [14]. However, with metallic over layers, induced eddy currents [143-146] within conducting materials due to the time-varying magnetic field will affect magnetic fields penetrating through this over layers. However, the effects on the low frequency magnetic fields are generally ignored in the current imaging [12,39]. Here we will give a quantitative analysis.

The penetration depth of the plane electromagnetic excitation wave is limited by the skin depth [143]

$$\delta_0 = \frac{1}{\sqrt{\pi\mu\sigma f}}, \tag{3.7.1}$$

where σ is the conductivity and μ is the permeability. δ_0 denotes that the amplitude of the fields in the conductor decay to 1/e and the phase is rotated by π. Table 3.1 gives the skin depth of aluminum, copper, gold, and silver at frequency of 1 MHz and 10 GHz.

Table 3.1. Skin depth in the good conductors.

	Aluminum	Copper	Gold	Silver
1 MHz	81.4 μm	66.0 μm	78.6 μm	64.0 μm
10 GHz	0.814 μm	0.66 μm	0.786 μm	0.64 μm

These results show that low frequency (less than 1 MHz) plane electromagnetic wave is not affected by the multiple metal layers.

Furthermore let us consider a current carrying conductor is buried under two copper layers as shown in Fig.3.7.1.

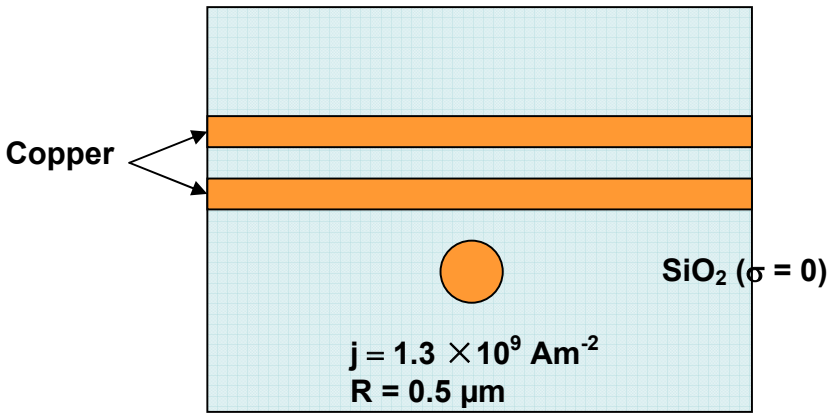

Figure 3.7.1. A current carrying conductor is buried under two copper layers. The conductor has a radius of 0.5 μm and each copper has a thickness of 0.5 μm.

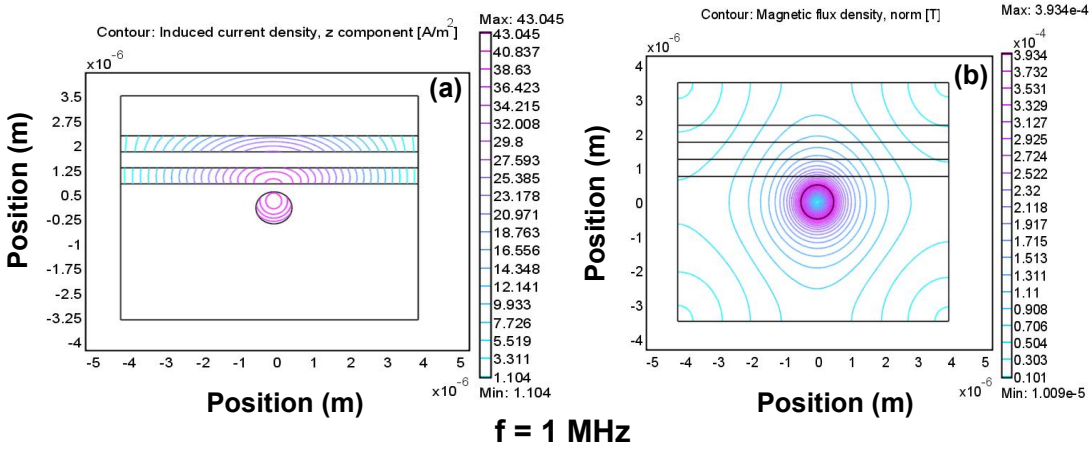

Figure 3.7.2. Femlab simulation results of induced current density (a) and magnetic flux density (b) at frequency of 1 MHz.

When current density j = 1.3 × 10^9 Am^{-2} and frequency f = 1 MHz, Femlab simulation results about induced current density (edd current) and magnetic flux density are shown in Fig.3.7.2. The induced current density is significantly less than the source current density; therefore it has almost no contribution to the magnetic flux density, which is

shown by the symmetric magnetic flux density above and below the current carrying conductor in Fig.3.7.2 (b). For comparison, Fig.3.7.3 shows Femlab simulation results of the frequency f = 10 GHz. Obviously, the induced current has almost same value as the source current which interferes magnetic fields go through the two copper layers as shown in Fig.3.7.3 (b).

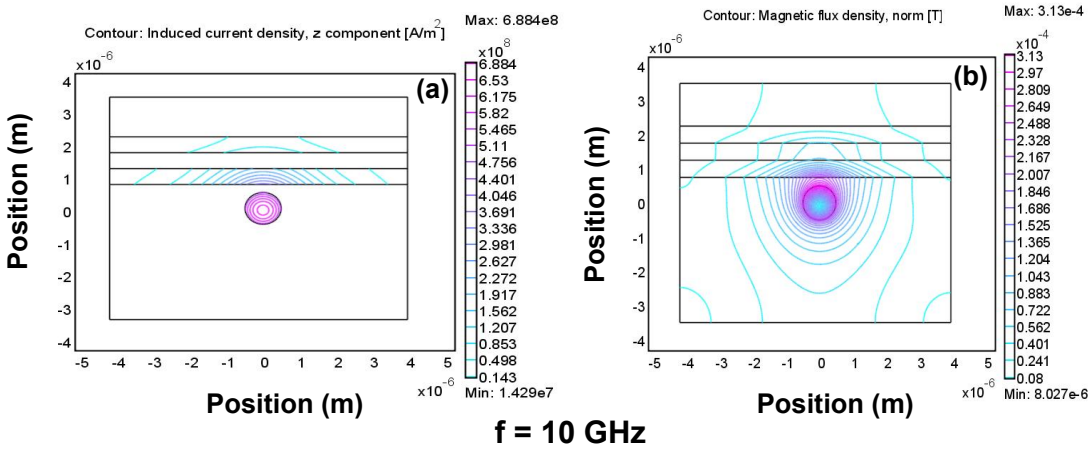

Figure 3.7.3. Femlab simulation results of induced current density (a) and magnetic flux density (b) at frequency of 10 GHz.

The above results show that at low frequencies (less than 1 MHz) magnetic fields are not affected by the multiple metal layers and non-ferrous materials in an IC. Therefore, the results without material layers in this thesis will be suitable to the conductors buried under several layers in real ICs as long as the tip to sample is at the same distance.

Chapter 4
NUMERICAL SIMULATION OF THE MFM IMAGES

4.1 Introduction

We have discussed the fundamental components of the MFM. Since the detailed magnetic properties of MFM-tips, such as the micromagnetization of the tip and the distribution of magnetic material on the tip used in the imaging process, are generally not well known, a true quantitative interpretation of MFM images is difficult [59]. This chapter will focus on numerical techniques that were used to model the experimental measurements. The theory of MFM tells us that we may calculate the probe-sample interaction using the magnetic field emanating from the sample and the magnetic moments that make up the probe. Therefore, we will first consider the magnetic field from the current carrying conducting line on the sample circuits. Then, we will model the magnetization of the MFM tip and cantilever based on the realistic MFM probe geometries. Finally, simulation of the magnetic interaction between the probe and sample will be presented in order to compare and explain the MFM image formation.

4.2 Modeling Magnetic Fields from Conductors

In order to provide well defined magnetic fields, a thin (~ 100-400 nm) gold single-turn-rectangular microscopic conducting line has been fabricated on a silicon substrate by patterning a thin metal film using photolithography. The rectangular shape is used to mimic the steady state current flow in ICs which is produced through a device. The details of the fabrication process and the motivation of the test circuit design will be given in the next chapter. Figure 4.2.1 (a) is a schematic view of a rectangle conducting line.

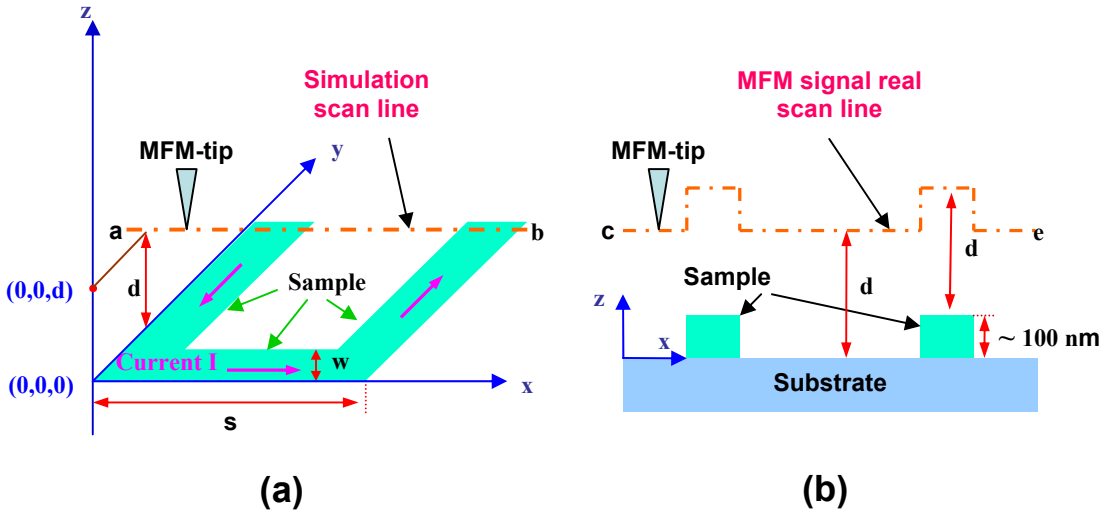

Figure 4.2.1. (a) Schematic representation of position of a rectangle conducting line in the theoretical modeling. The conducting line lies on the x-y plane. The dashed line $\overline{\mathbf{ab}}$ indicates a single scan line at the lift height of d above the surface of the sample in the modeling calculation. We ignored the thickness of the conducting line in the modeling. **(b)** Schematic cross section view of the experimental arrangement. The dashed line $\overline{\mathbf{ce}}$ indicated a MFM signal real single scan line in the experiment.

The coordinate system is defined in the figure. The conducting line has a width w from 1.0 μm to 5.0 μm and a thickness less than 400 nm. s is the dimension of the conducting line along the x-direction. The length of the conducting line along the y-direction is

around 200 μm in the experimental model. The scanning area in our experiments is less than 110 μm × 110 μm. Therefore, we chose 120 μm as the length of the conducting line in the model calculations. This will be adequate since the length over 120 μm has an insignificant influence in the scanned area. This was verified in our calculations.

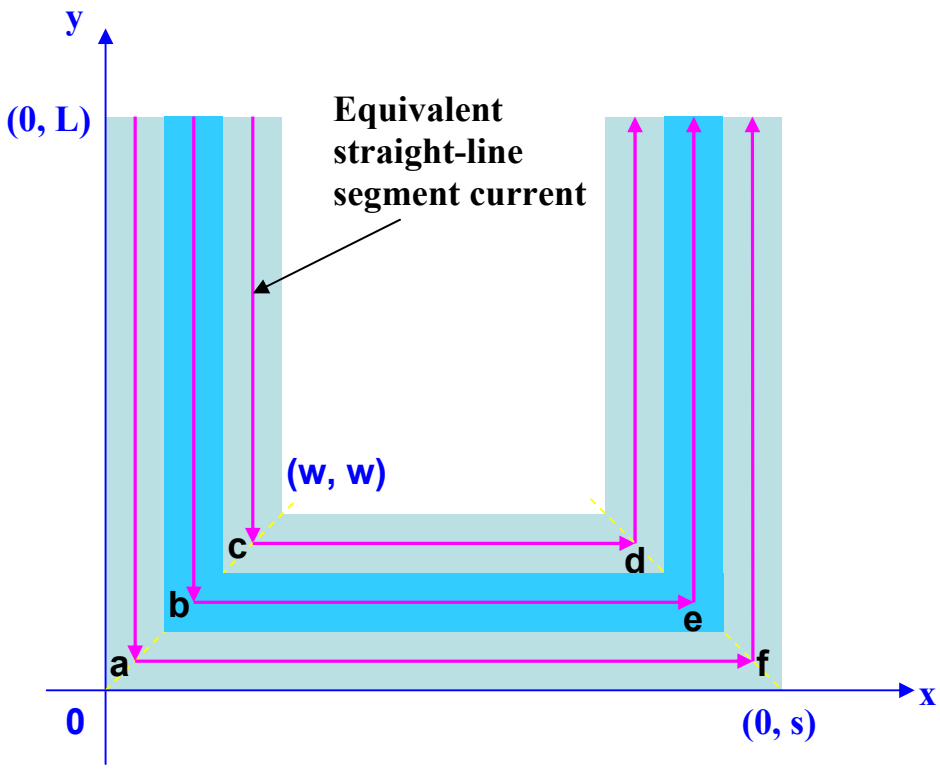

Figure 4.2.2. A model of current in the straight line segments equivalent to current in the conducting line. Each straight line segment current is equivalent to each shaded current area of the conducting line.

The thickness of the circuits is less than 400 nm and the MFM signal scan is obtained with the probe held a constant distance above the sample (Fig.4.2.1.(b)). The effects of the thickness on the magnetic field are ignored and a uniform planar distribution of current flowing through the conducting line was assumed. As we know, a planar current may be decomposed into any number of current line segments. How many current line segments are chosen to be equivalent to the planar current depends on the accuracy required. The more current line segments used, the better the accuracy.

To simplify the following discussion, 'n-current model' indicates that current in the conducting line has been broken up into n current line segments that are taken to be equivalent to the current flowing through the conducting line circuit. Figure 4.2.2 is an example for 3-current model.

Since the width w is usually less than 5 μm, the current is often approximated with a 3-current model. There are nine straight line segments in the 3-current model for this sample as shown in Figure 4.2.2. If the total current is **I**, the current in each line segment will be $\frac{1}{3}\mathbf{I}$. Considered the uniform distribution of current, the three current lines in each straight conducting line will be located in $\frac{1}{6}\mathbf{w}, \frac{1}{2}\mathbf{w}, \frac{5}{6}\mathbf{w}$, respectively. In Figure 4.2.2, the coordinates of a, b, and c are $(\frac{1}{6}\mathbf{w}, \frac{1}{6}\mathbf{w})$, $(\frac{1}{2}\mathbf{w}, \frac{1}{2}\mathbf{w})$, and $(\frac{5}{6}\mathbf{w}, \frac{5}{6}\mathbf{w})$, respectively. Furthermore, according to superposition theorem the total magnetic field B can be obtained by superposition of the magnetic fields generated by each line segment. For each line segment, calculation of the magnetic field is quite simple.

Consider the segment $\overline{\mathbf{af}}$ carrying a current of $\frac{1}{3}\mathbf{I}$ shown in Fig.4.2.2, with the current flowing from left to right which is along the x-direction, the vector potential $\vec{\mathbf{A}}$ using equation (3.4.1) at any observation point P(x,y,z) above the surface of the sample is given by [119]

$$\vec{\mathbf{A}}(\mathbf{x},\mathbf{y},\mathbf{z}) = \mathbf{A}_{\mathbf{x}}(\mathbf{x},\mathbf{y},\mathbf{z})\vec{\mathbf{x}}, \tag{4.2.1}$$

and

$$\mathbf{A}_{\mathbf{x}}(\mathbf{x},\mathbf{y},\mathbf{z}) = \frac{\mu_0 \frac{1}{3}\mathbf{I}}{4\pi} \ln \frac{(\mathbf{x}-\mathbf{x}_{\mathbf{f}}) + \sqrt{(\mathbf{x}-\mathbf{x}_{\mathbf{f}})^2 + (\mathbf{y}-\mathbf{y}_{\mathbf{f}})^2 + \mathbf{z}^2}}{(\mathbf{x}-\mathbf{x}_{\mathbf{a}}) + \sqrt{(\mathbf{x}-\mathbf{x}_{\mathbf{a}})^2 + (\mathbf{y}-\mathbf{y}_{\mathbf{a}})^2 + \mathbf{z}^2}}, \tag{4.2.2}$$

where $\vec{\mathbf{x}}$ is the unit vector of x-axis, (x_a, y_a) and (x_f, y_f) are the coordinates of point **a** and point **f**, respectively.

The magnetic field is given by Eqn.(3.4.2), $\vec{\mathbf{B}} = \nabla \times \vec{\mathbf{A}}$, where the spatial derivatives are taken with respect to the coordinates of the observation point P(x,y,z). Once the $\vec{\mathbf{B}}$ is known, the gradient of the components of the magnetic field, $\frac{\partial \mathbf{B_i}}{\partial \mathbf{j}}$ (i, j ∈ x, y, z), can be calculated. From the derivatives of the magnetic field, Eqn. (3.4.4) can be used to calculate the forces acting on the tip.

By analogy with calculation of the segment $\overline{\mathbf{af}}$, we can get the gradient of the components of the magnetic field from nine line segments. Simple addition gives the total $\frac{\partial \mathbf{B_i}}{\partial \mathbf{j}}$, and from that the force acting on the probe using Eqn. (3.4.4). Complete analytical expressions for B_j and $\frac{\partial \mathbf{B_i}}{\partial \mathbf{j}}$ are given in Appendix 1 of this thesis. In the next step, we employ a probe model to obtain magnetic moments $\vec{\mathbf{m}}$ of the probe which is included in Eqn. (3.4.4).

4.3 Modeling MFM Tip and Cantilever

Modeling of the tip is challenging as the magnetic field from the surface extends out a considerable distance. Simply modeling the probe as a lumped magnetic moment, which is the so-called point-probe approximation [69] that idealizes a more or less complicated tip magnetization distribution by either an effective magnetic single moment or a magnetic monopole moment, does not provide an adequate model to explain MFM images produced by current carrying conductors, especially when force detection is employed.

The probe is modeled in this work by considering the magnetic material coating the surface of the probe to be segmented into a series of smaller regions. Applying a point moment approximation to each region, its assigned moment strength is

$$\left|\vec{\mathbf{m}}\right| = \mathbf{M}_s \mathbf{V}, \qquad (4.3.1)$$

where V is the volume of the region and M_s is the magnetization of the tip's magnetic coating material. The dipole moment is located at the center of each region and the direction depends on the properties of the thin film magnetic material, which will be discussed later. In our model calculation it is assumed that each region is not affected by the magnetic field from the sample and that there is no exchange interaction between them [86,120-121].

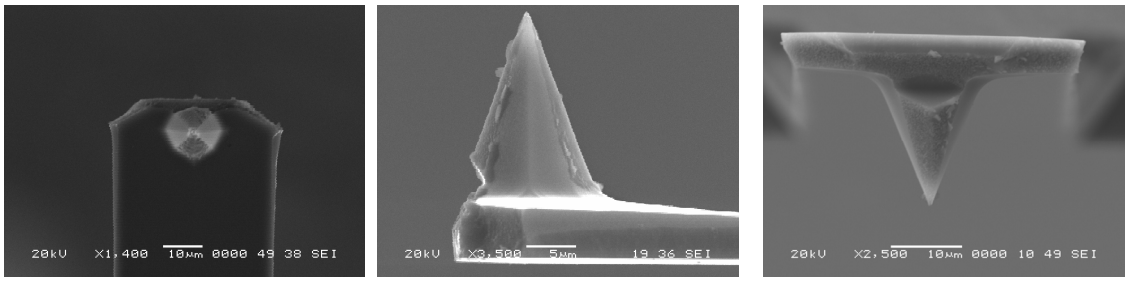

Figure 4.3.1. SEM images of MFM tip.(a) Top view. (b) Side view. (c) Front view.

Figure 4.3.1 shows a scanning electron micrograph of a MFM probe with three side views. Since the tip has a conical octagonal shape and the cantilever has a rectangle shape, the tip and cantilever will be treated separately. Note: Magnetic material, Cobalt, coating is formed a thin film on the whole surface of the probe which includes the backside of the cantilever. The thickness of the Cobalt coating is about 30~100 nm.

The tip is divided into several layers that are perpendicular to the long axis of the tip as shown in Figure 4.3.2 (a). The thickness of each layer is chosen to be less than 0.5 μm.

Several simulations were carried out for layer thicknesses less than 0.5 μm. Deviations of less than 5% were observed. Therefore, 0.5 μm thickness layers were chosen for all simulations. Each layer was divided into eight equal regions whose centers were located at eight symmetrical directions as shown in Figure 4.3.2 (b). For the sake of simplified calculation a circle was used instead of the octagonal shape of the tip (Figure 4.3.2(b)).

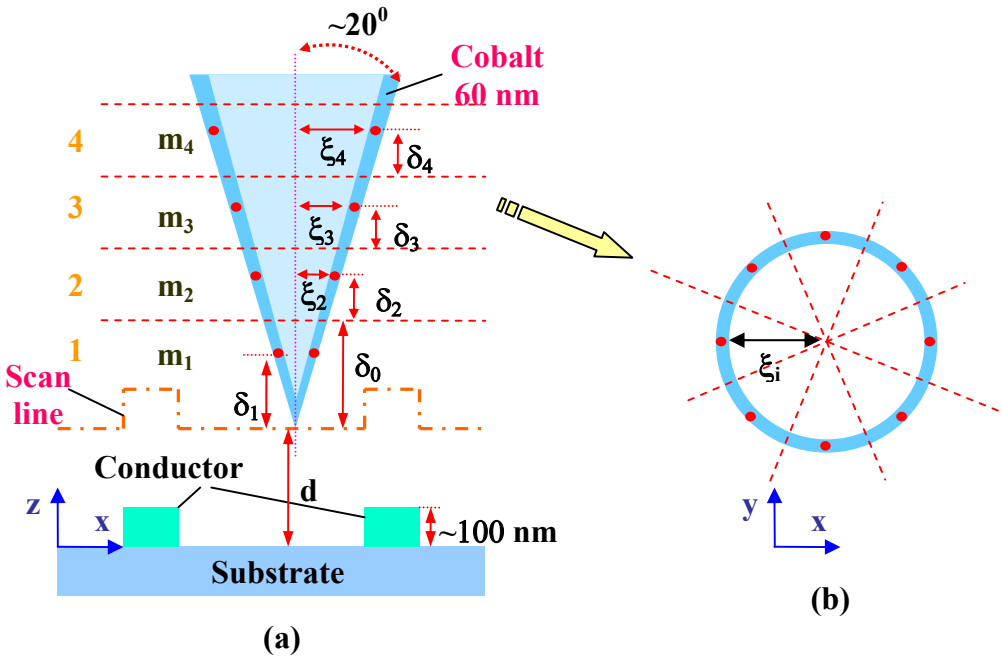

Figure 4.3.2. Schematic diagram of the MFM tip model is in the case of the cantilever parallel to the sample surface. **(a)** Cross section view along the long axis of the tip. We divide tip into several layers, each layer is divided into eight equal regions and used the point probe approximation in each region. There are only 4 layers shown in the figure. **(b)** Top view of one layer. Circle is approximated instead of octagonal shape.

According to the data sheet and SEM measurements, the tips have a radius of curvature of less than 90 nm. After several or many SFM scans, SEM images of the tip show that the tip was worn with a tip apex of more than 200 nm. This is due to the tip dragging across the sample's surface during the topography scan. In this situation, it is reasonable to assume that the tip apex has no coating on it. We found that the tip apex tended to

stabilize after several scans on the same sample surface. Thus, after the tip was used, an SEM was used to obtain the size of the tip apex used for the calculation.

Some parameters are shown schematically in Figure 4.3.2 (a). Here, d is the experimentally controllable lift height which is the distance from the tip apex to the substrate surface. The parameters δ_i and ξ_i (i = 1, 2, 3, etc.) indicate the positions of the point magnetic moments in each region. In Table 4.1 we give the values of these parameters at first five layers in the case of the long tip axis perpendicular to the sample's surface or, in other word, the cantilever parallel to the sample, with a 48-degree full tip cone angle and a tip curvature radius of approximate 220 nm.

Table 4.1. Values of some parameters in MFM tip model. Magnetization of Cobalt is 0.870×10^6 Am^{-1}.

Layer (i)	m_i (Am^2)	δ_i (μm)	ξ_i (μm)
1	7.42×10^{-15}	0.47	0.331
2	1.74×10^{-14}	0.25	0.776
3	2.74×10^{-14}	0.25	1.222
4	3.74×10^{-14}	0.25	1.667
5	4.74×10^{-14}	0.25	2.112

Although the higher layer coupling is less due to the increased distance from the conducting line, the higher layer has larger magnitude moments due to the increased volume of the magnetic coating region.

As to the cantilever, since it has a rectangle shape, it was simply divided into small rectangular regions. Each region was modeled using point dipole moment approximation, with the moment located at the center of the region. The number of regions chosen for the simulation was determined by shrinking the region size until there was a deviation less than 10 % from a larger to smaller region size. Each region is less than 2 μm × 2 μm and only the cantilever within 130 μm from the free end is considered in the model. The rest of the cantilever is far enough away from the scanning areas to be ignored. The tip area of

the tip side cantilever has to be taken out from the calculation, as well as the cut off corner of the cantilever refers to Figure 4.3.3. The backside and lateral side of the cantilever was considered similarly. Since each probe has a different dimension, we have to consider it individually in modeling calculations according to the SEM images.

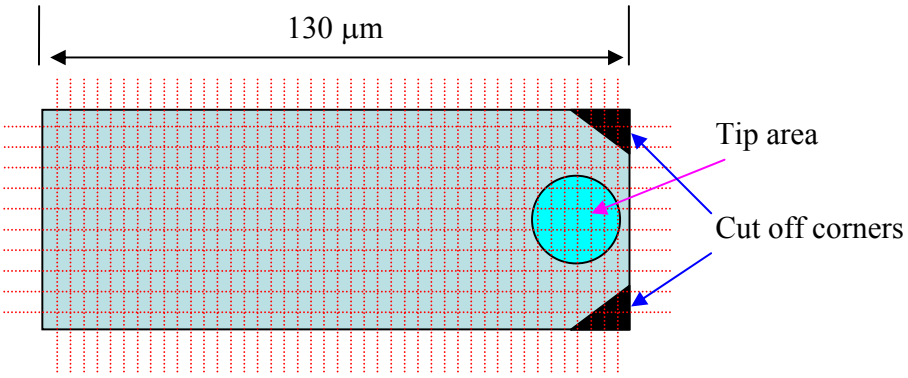

Figure 4.3.3. Schematic diagram of the cantilever model from the tip side view. We divide surface of the cantilever into a number of the small rectangular regions.

In most cases the measurements are made with the cantilever tilted at some angle (typically about 15^0) from the sample in order to make imaging convenient. Under the coordinate system defined in Figure 4.2.1, we will use angle θ and α to characterize the orientation of the tip and cantilever refer to Figure 3.4.1.

With a numeral model of the probe and sample magnetic field, Eqn. (3.4.4) and (3.4.6) can be used to calculate the magnetic force acting on the cantilever probe.

When summing the forces calculated using Eqn. (3.4.4), we also need to consider that forces acting at different locations of the cantilever produce different deflections of the cantilever. Figure 4.3.4 shows a cantilever anchored rigidly on its left side and a force F acting on the cantilever at point b causing a bending moment and a deflection of the cantilever. With the small bending approximation, the deflection of the cantilever can be written as [135-137] (also see Egn.(2.3.1))

$$z(x) = \frac{Fx^2}{6EI}[3(L-b)-x], \tag{4.3.2}$$

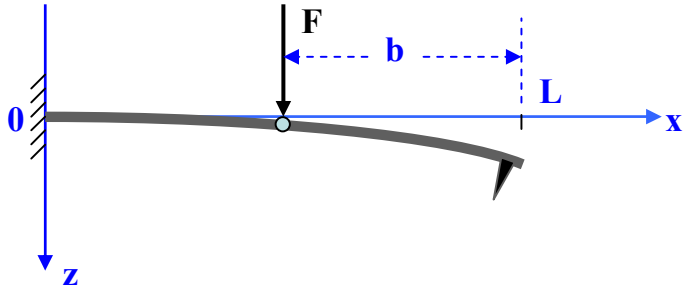

Figure 4.3.4. A force F acting on a cantilever at point **b** causing a bending moment and a deflection of the cantilever.

Therefore, when F acts at the free end of the cantilever with b=0, we obtain

$$z(L)\big|_{F\to L} = \frac{FL^2}{6EI}(3L-L) = \frac{FL^3}{3EI}, \tag{4.3.3}$$

which compares with F acting at point b,

$$z(L)\big|_{F\to b} = \frac{FL^2}{6EI}(2L-3b), \tag{4.3.4}$$

we get

$$\frac{z(L)\big|_{F\to b}}{z(L)\big|_{F\to L}} = \frac{(2L-3b)}{2L} = 1-\frac{3b}{2L}, \tag{4.3.5}$$

From this expression, we see that the deflection of the cantilever will vary depending on the location at which the force is acting. The deflection of the cantilever will be at maximum when the force is exerted at the free end. Most often, the force acting on the probe is assumed to be concentrated at the free end of the cantilever and the effect on the rest of the cantilever is ignored. However, in this case, since the cantilever has a significant effect, the location of the force using Eqn (4.3.5) must be taken into account.

4.4 Simulation Results

In this section we will focus on the simulation. Matlab was selected as the CAD tool to calculate the magnetic field and magnetic field gradient from the sample, as well as the distribution of the forces acting on the probe.

4.4.1 Magnetic Field and Magnetic Field Gradient

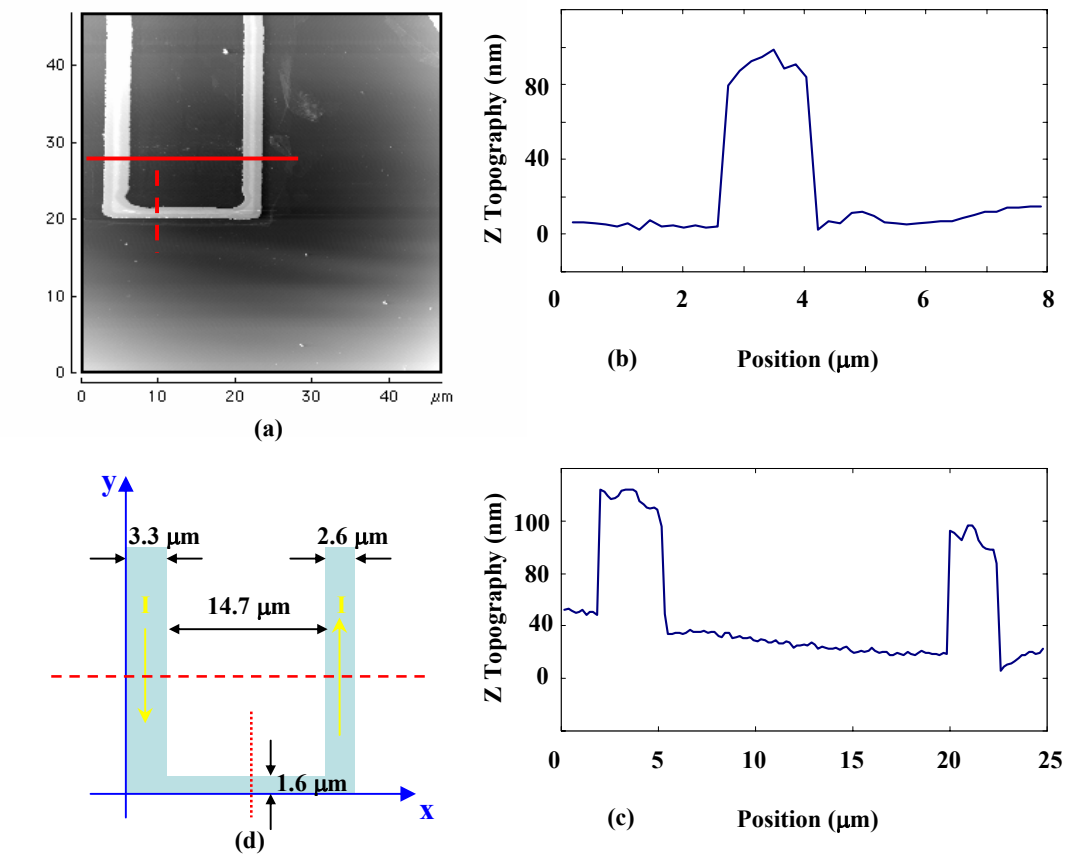

Figure 4.4.1.(a) 50 μm × 50 μm topographic (AFM) image of the sample circuit by SFM contact mode. **(b)** The topography data recorded along the dashed line was shown in (a). **(c)** The topography data recorded along the solid line in (a). **(d)** Schematic drawing of the sample circuit with the corresponding geometrical dimensions and the coordinate system.

The sample geometry used in these simulations was measured using AFM. Figure 4.4.1(a) is an AFM (topographic) image of the single-turn-rectangle structure. Its geometrical dimensions are determined and measured by using the cross section topography plot shown in Figure 4.4.1 (b) and (c). The conducting lines have the thickness of approximately 80 nm. The geometrical dimensions are shown in Figure 4.4.1 (d).

Figure 4.4.2 displays the z-component of the magnetic field in the 3- and 6-current model simulation with a current of I = 1 mA in a direction as indicated in Figure 4.4.1 (d) at the 100nm (z = 100nm) above the sample surface (z = 0). In Figure 4.4.2 (c) labeled points 1~6 describe different regions. The regions between point 1 to 2 and 5 to 6 are outside the enclosed conducting lines, and have a decaying magnetic field that falls to less than 7.0 $\times 10^{-6}$T at points 1 and 6.

The regions between point 2 to 3 and 4 to 5 are above the conducting line and show a rapid change in the magnetic field (negative to positive or vice versa) due to the current direction. 3 to 4 region is inside the enclosed conducting line and shows a weak magnetic field. The same analysis can be made in Figure 4.4.2 (d).

Comparing the 3- and 6-current models, we found the only difference occurred exactly above the transmission line in the regions between point 2 to 3 and 4 to 5. In these regions, several peaks in the line scan [Figure 4.4.2(c) and (d)] indicate the disadvantages of the finite number of line segment currents used to model the conducting line. Obviously, each current in the straight line segment has narrower and higher peak of the magnetic field than its equivalent current in the area of the conducting line does. However, the peaks will disappear when we use enough line segment currents to model the conducting line. The force produced by the line segments are also averaged out through the coupling to multiple moments on the probe. This can be used as a criterion to determine how many line segment currents we have to use to model the conducting line.

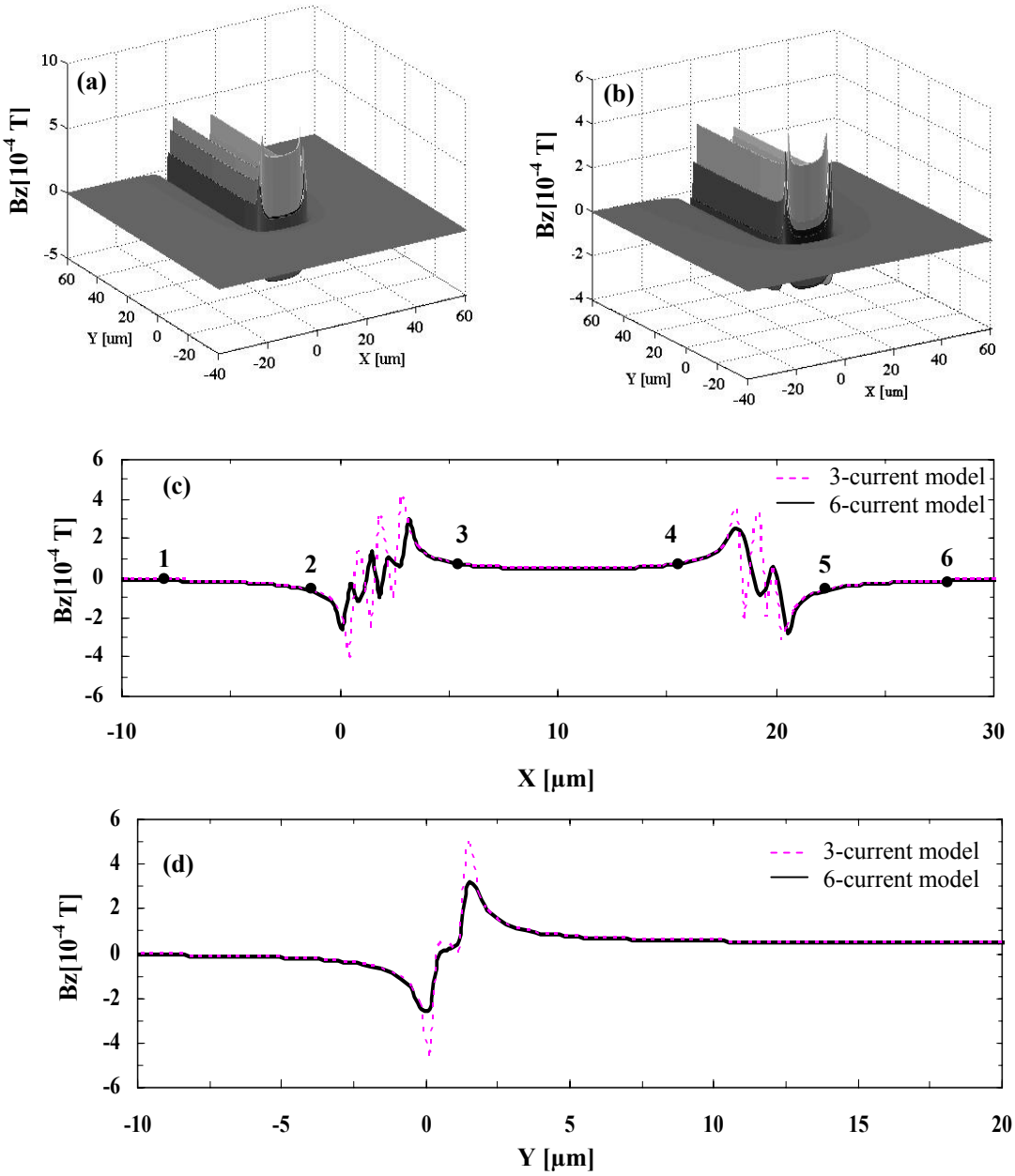

Figure 4.4.2. z-component of the magnetic field at z =100nm above the sample surface (z =0 plane) with a current of I = 1 mA in a direction as indicated in Figure 4.4.1(d). **(a)** 3-current model. **(b)** 6-current model. Line-scan taken along the dashed and dotted lines in Figure 4.4.1(d) is shown in **(c)** and **(d)**, respectively.

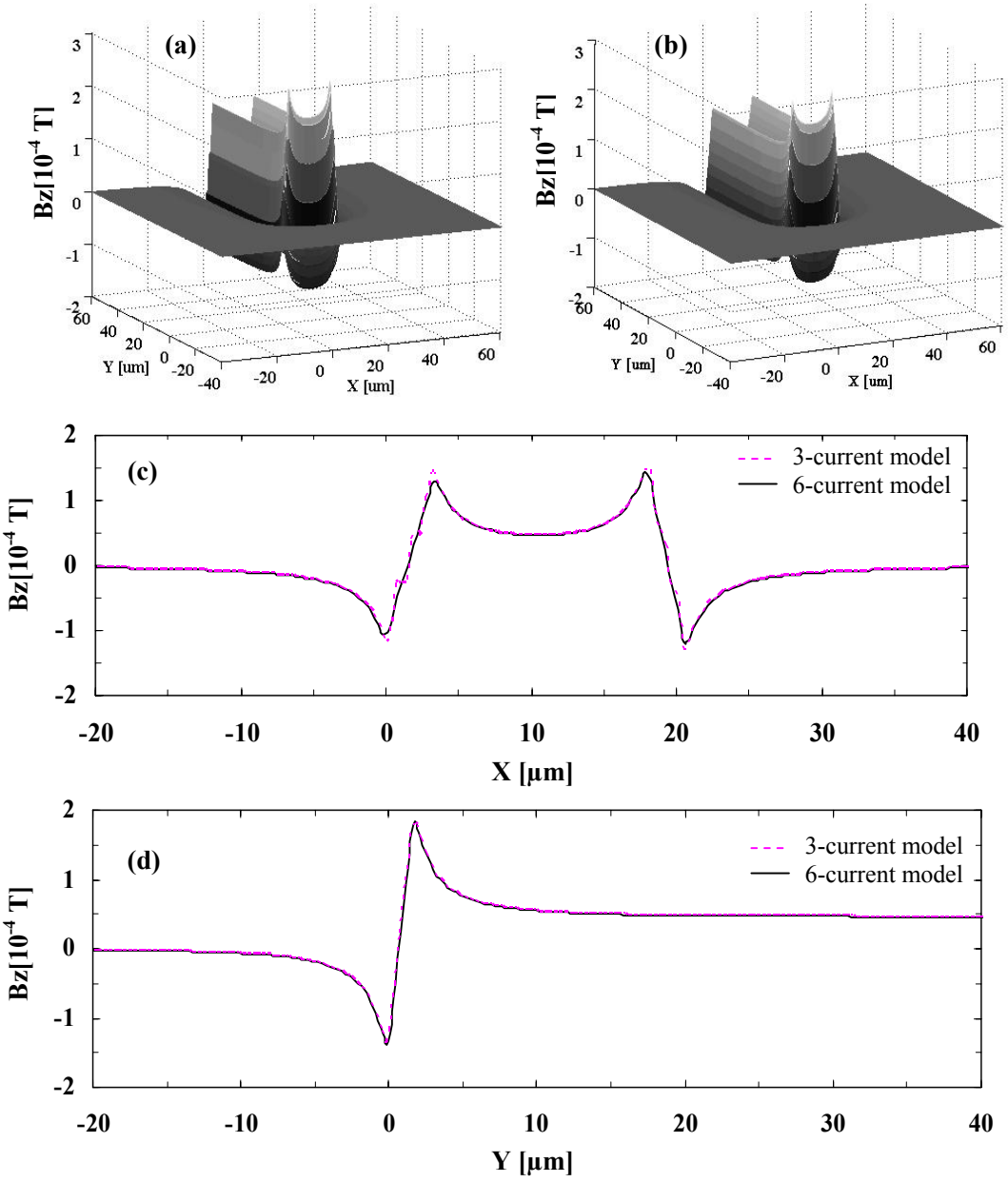
(a)
(b)
Bz[10^-4 T]
Y [um]
X [um]
(c)
3-current model
6-current model
X [µm]
(d)
Y [µm]

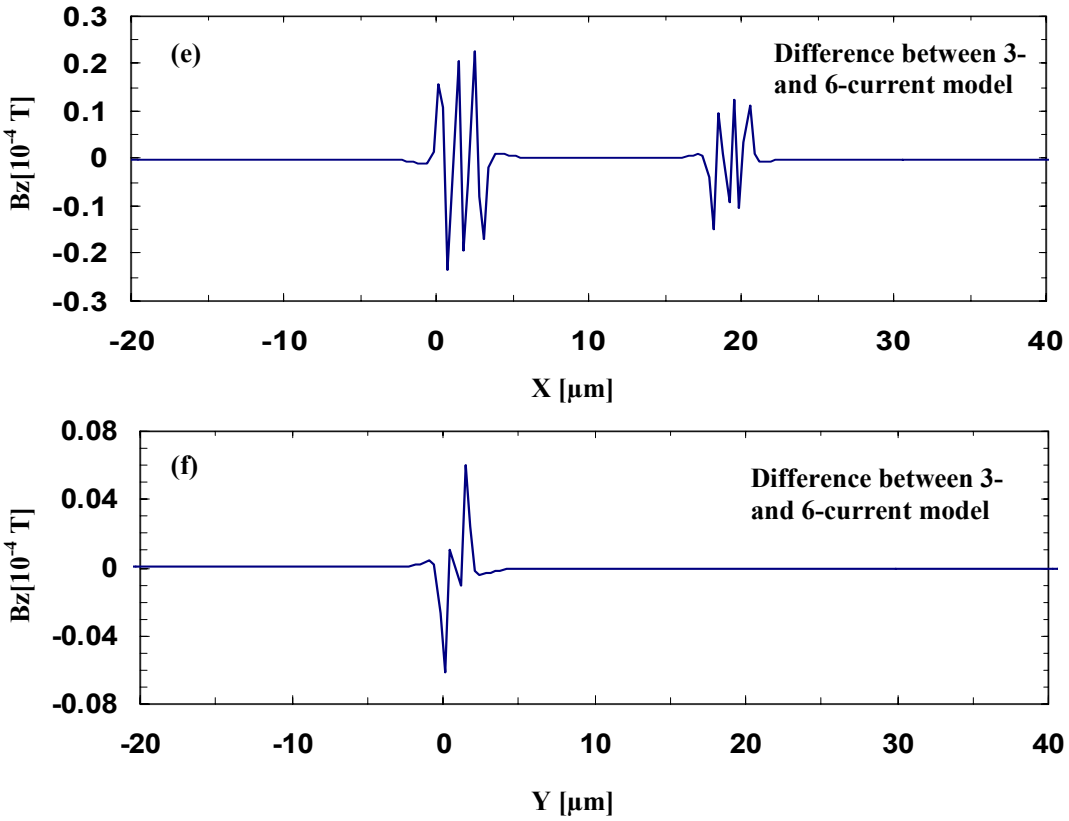

Figure 4.4.3. z-component of the magnetic field at z =500nm above the sample surface (z =0 plane) with a current of I = 1 mA in a direction as indicated in Figure 4.4.1(d). **(a)** 3 linear current model. **(b)** 6 linear current model. Line-scan taken along the dashed and dotted lines in Figure 4.4.1(d) is shown in **(c)** and **(d)**, respectively. Line-scan difference between 3-current and 6-current model in (c) and (d) is shown in **(e)** and **(f)**, respectively.

To establish this criterion, either we could use more line segment currents to decrease the equivalent width of the planar current by each linear current, or increase the magnetic field's FWHM of each line segment current by only considering the magnetic field at the larger distance above the sample (larger z). For this typical sample, the 3-current model works very well at minimum 500nm above the sample plane. The simulation results show that the difference between 3- and 6-current model is less than 10% of peak to peak values shown in Figure 4.4.3 (e) and (f). The 6-current model was only needed at ~300nm over the sample surface.

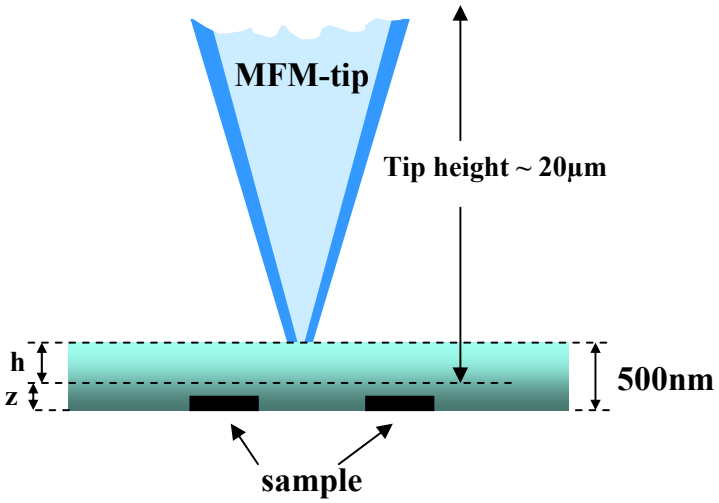

Figure 4.4.4.Schematic drawing of the MFM tip which is affected by 3-current model calculation of the magnetic field. z is the lift-height as measured between the tip-apex and the substrate. h is the affected part of the tip by the inaccuracy calculation of the magnetic field from the 3-current model. h at most can be 500nm in the contact mode (topography scan).

From Fig. 4.4.3 (e) and (f), we found the two models (3- and 6-current) have a difference of less than 10%, and also no obvious peaks shown in the line scan (c) and (d), although their difference shows some peaks that are too small to be ignored. Thus, the 3-current model is good enough to model the sample in this situation. Even though this is only accurate at more than 500nm from the sample surface, in reality, the MFM tip has a tip height of 20μm, almost all of the magnetic moment on the tip is in the magnetic field produced by the sample over 500nm at any scan condition as shown as in Figure 4.4.4. Therefore, in most cases we will use a 3-current model to simulate MFM images over this thesis. In some conditions, such as sample width over 5 μm, we will use a 6-current model.

Similar behaviors are also found in the x and y components of the magnetic field. Here, we give the 3d-plot shown in Figure 4.4.5.

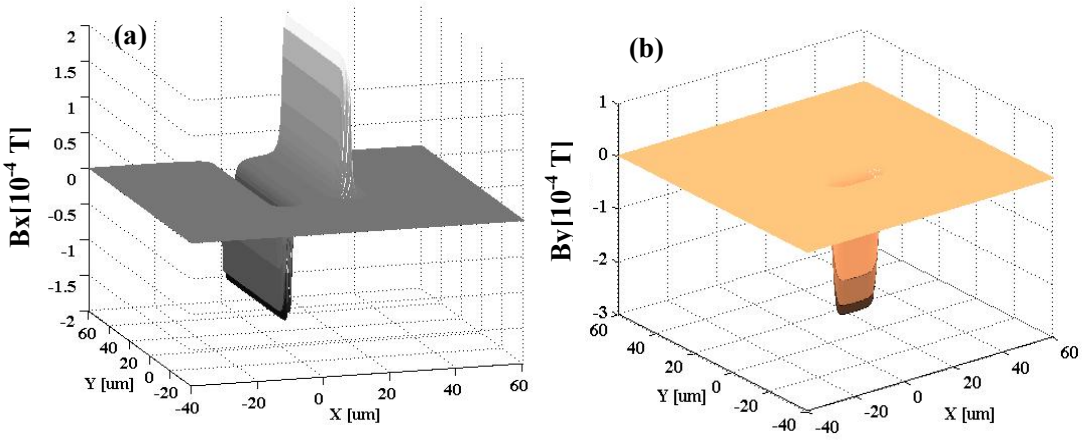

Figure 4.4.5. (a) x-component of the magnetic field at z =500nm above the sample surface (z =0 plane) with a current of I = 1 mA in a direction as indicated in Figure 4.4.1(d). y-component shown in **(b)**.

According to the simulation, the maximum magnetic field value produced by the sample at the apex of the tip is about 6 Gauss ($1T=10^4$ Gauss) when the tip lift is 100nm with an applied current of 1mA. Since the magnetic field is linearly proportional to the current, a 20mA current (maximum current used in the measurements) will produce a 120 Gauss magnetic field at the tip apex location. This is much smaller than the coercivity of the (magnetic etched silicon probe) MESP-type MFM tip, 400 Gauss, which is the typical number as quoted for Cobalt coating tips [60]. Thus, the field due to the current will not have a significant effect on the magnetic moments of the tip. From this analysis we can conclude that the interaction between the tip and the magnetic field due to the current is not so strong as to affect the magnetic moments of the tip with a tip scan height of greater than 100nm and an applied current of 20mA. In our experiment, the scan height of the tip is always greater than 100nm and the applied current less than 20mA. Nevertheless, during the topography scan the tip contacts the sample. Whether this changes the magnetic moments of the tip or not remains unknown. Even if the magnetic moments at the very end of the tip does change, we still don't have to consider it as this affects only a very small amount of magnetic moments of the tip (refer to Figure 4.4.4).

On the other hand, let us consider the current distribution in the sample affected by the magnetic field emanating from the MFM tip. For simplicity, we treat the MFM tip as a dipole moment approximation (same as consideration in section 3.5) with the moment of $m_z = 6.009 \times 10^{-15}$ Am^2 given by J.Lohau [63]. Then the field due to the magnetic moment of the tip at the location of the sample is

$$\left|\vec{\mathbf{B}}\right| = \frac{\mu_0}{4\pi}\frac{\left|\vec{\mathbf{m}}\right|}{\mathbf{r}^3} \qquad (4.4.1)$$

where μ_0 is the permeability in the vacuum and r is the distance from the tip dipole to the location of the sample. For a rough estimation, we ignore the direction of the **m** and **r** and assume them as being in the same direction (in maximum case). When the separation between the tip dipole and the sample is 100nm (note: $d = 5.20 \times 10^{-7}$ m in Fig.3.5.2), from (4.4.1), the magnetic field produced by the tip dipole at the location of the sample surface is about 26 Guass. This weak field's effect on the current distribution in the sample is negligible.

The above analysis suggests both the MFM tip moment and the current distribution in the sample are not affected by the tip-current mutual interaction. This justifies the two assumptions we made in section 3.4 as for the theoretical calculation.

For the magnetic field gradient generated by the current flowing in the sample circuits, a higher spatial resolution is required for the simulations, and hence more line segments or simulations will only be valid at larger separations. Similar analysis, simulations at 1.0 μm of the 3-current model and at 500nm for the 6-current model have deviations of less than 10% of peak to peak values for the sample above, which will be shown in Appendix 2.

The z-component (B_z) of magnetic field derivatives generated by the current in the sample with respect to the x, y, z-coordinate at 1.0μm above the sample surface with 1 mA current in the 3-current model are shown in Figure 4.4.6. Other components of the magnetic field derivatives in the same conditions will show in Appendix 2.

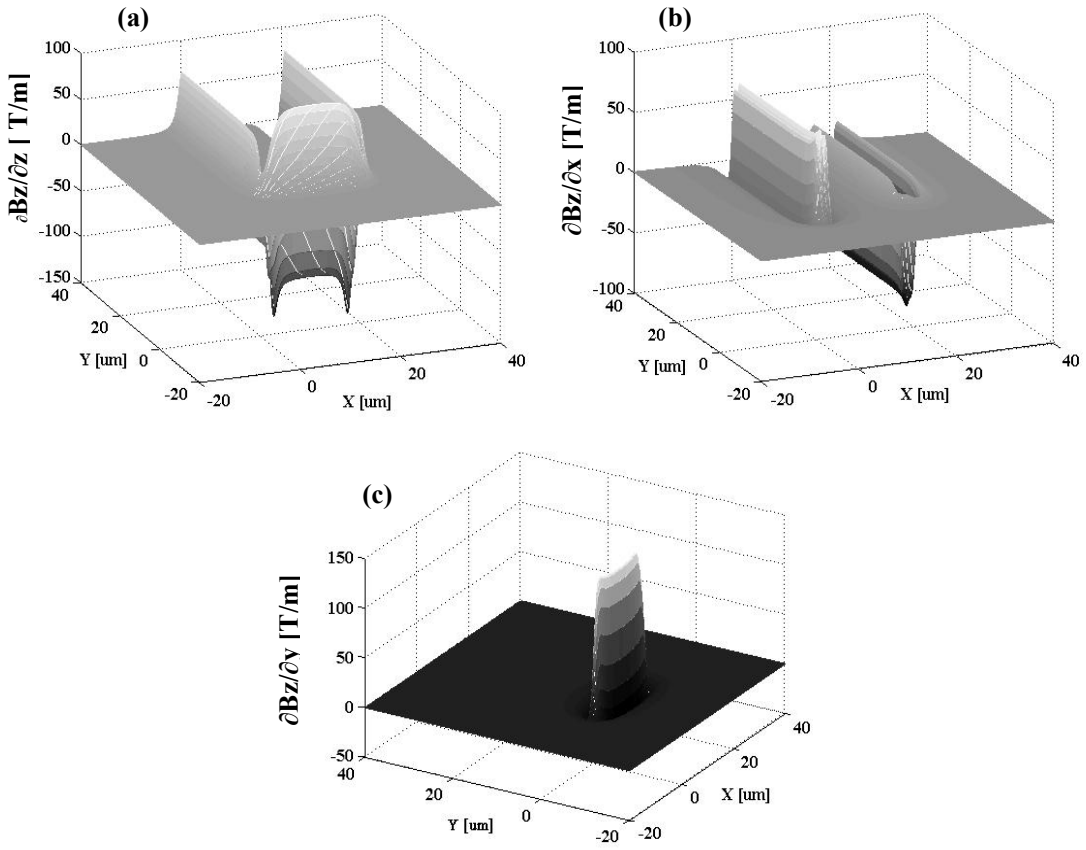

Figure 4.4.6. z-component of the magnetic field derivatives generated by the current in the sample with respect to the x, y, z- coordinate at z =1.0 μm above the sample surface (z =0 plane) with a current of I = 1 mA in a direction as indicated in Figure 4.4.1(d).

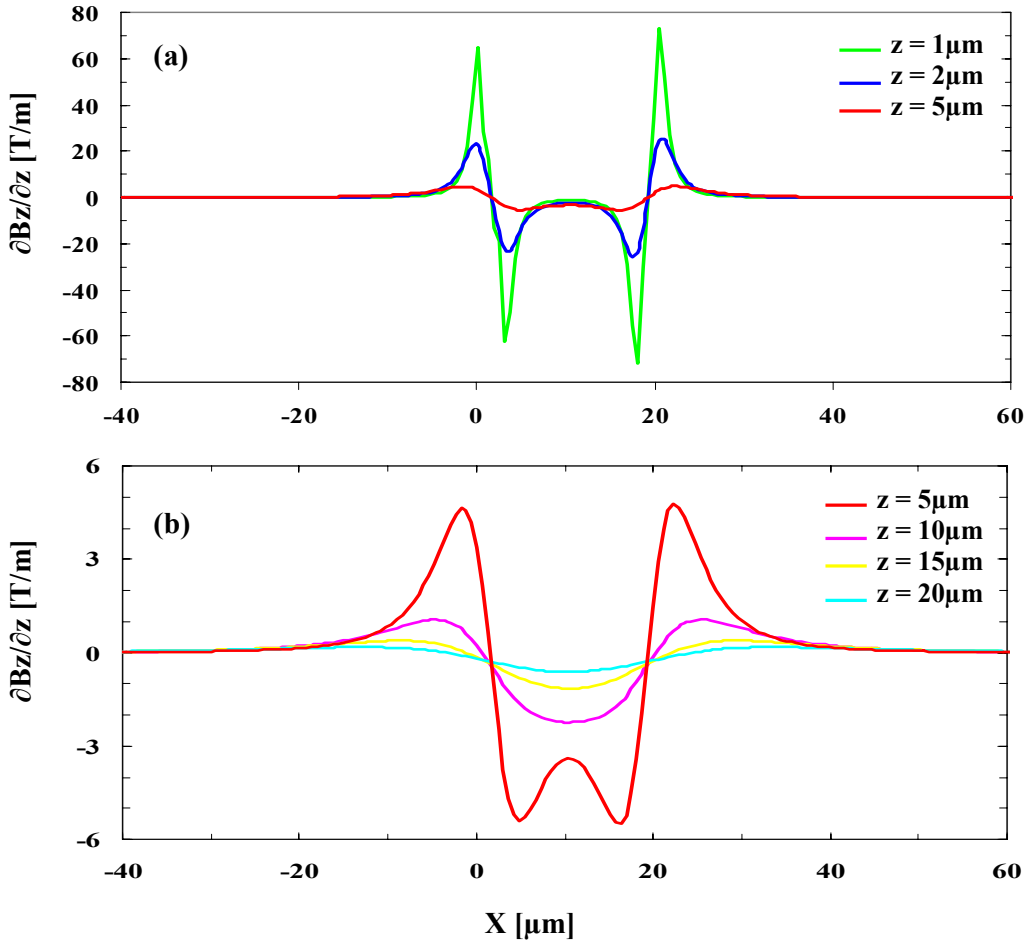

Figure 4.4.7. Line-scan of the z-component of the magnetic field derivatives with respect to the z-coordinate at z =1, 2, 5, 10, 15, and 20 µm above the sample surface (z =0 plane) with a current of I = 1 mA along the dashed line as indicated in Figure 4.4.1(d).

As a comparison, Figure 4.4.7 shows a cross section plot of the z-component of the magnetic field derivative with respect to the z-coordinate at various heights above the sample surface with a current of 1 mA. Since the magnetic field gradient has an inverse relationship with respect to the square of the height, it is much weaker at the cantilever position (z > 20 µm) than that at the tip-apex. Due to the larger amount of magnetic material on the cantilever surface than on the tip surface, the force on the cantilever can be comparable in magnitude. In the following sections we will calculate the forces and simulate MFM images.

4.4.2 Magnetic Interaction Force and MFM image

To simulate the magnetic interaction force, we have to model the shape of the probe. We use SEM images to obtain the dimensions of the probe used in our experiments. A schematic for a model tip is shown in Figure 4.4.8 (refer to SEM image in Figure 4.3.1).

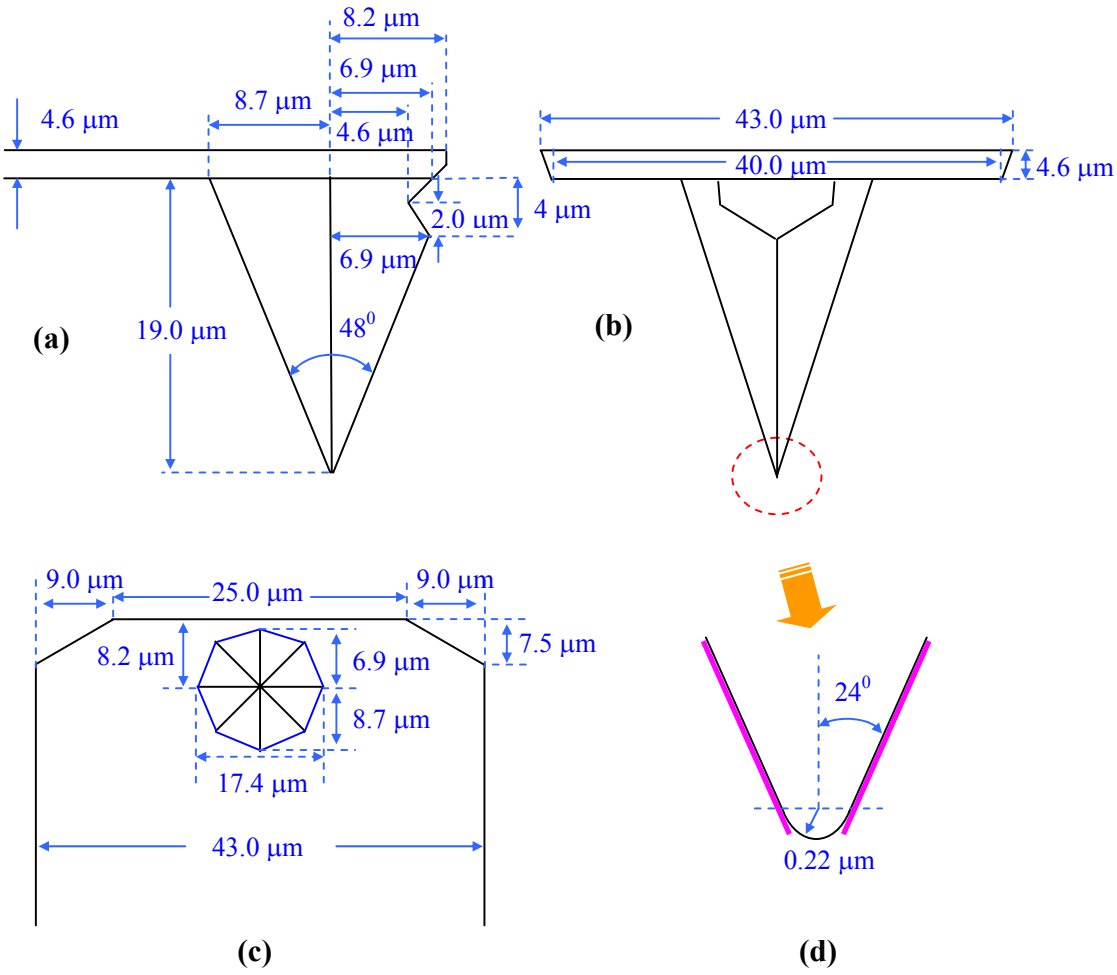

Figure 4.4.8. Schematic drawing of the probe with the corresponding geometrical dimensions. **(a)** Side view. **(b)** Front view. **(c)** Bottom view. **(d)** Enlarged view of the tip apex. Cobalt coating is indicated by the thick pink (dark) lines and taken out from the tip apex by the topography scan.

From figure 4.4.8, we see that the tip apex has a radius of 0.22 μm due to the damage to the tip during image scans, as discussed before. Due to the depth of the damage we assume there is no cobalt on the end of the tip. Cobalt starts on the side of the tip as shown in Figure 4.4.8 (d).

By using measured MFM probe geometries and the model discussed above, we can calculate the magnetic force acting on the probe and simulate the MFM images by using Eqs.(3.4.4), (3.4.6), and (4.3.5). Note: The coordinate system is defined as shown in Figure 4.2.1. The orientation of the cantilever related to the sample will be determined by using α, θ (defined in Figure 3.4.2), and tip lift height. To calculate the force, since F_n and m_i (i = x, y, and z) are linearly related through Eqs. (3.4.4) and (3.4.6), we first obtain the forces, F_{nx}, F_{ny}, and F_{nz}, which are due to the tip-magnetization along the x, y, and z-axes, respectively. F_{nx} is the force when all magnetic moments of the tip are along the x-axis, F_{ny} is the force when all magnetic moments of the tip are along the y-axis, and F_{nz} is the force when all magnetic moments of the tip are along the z-axis.

Then the force F_n can be calculated by

$$F_n = \zeta_x F_{nx} + \zeta_y F_{ny} + \zeta_z F_{nz} \tag{4.4.2}$$

where ζ_i (i = x,y,z) are the coefficients of the tip-magnetization projected on the x, y, and z-axes, respectively. That is

$$\vec{\mathbf{m}} = \mathbf{m}_x \vec{\mathbf{x}} + \mathbf{m}_y \vec{\mathbf{y}} + \mathbf{m}_z \vec{\mathbf{z}} = \left|\vec{\mathbf{m}}\right|(\zeta_x \vec{\mathbf{x}} + \zeta_y \vec{\mathbf{y}} + \zeta_z \vec{\mathbf{z}}) \tag{4.4.3}$$

where $\vec{\mathbf{m}}$ is the magnetic moment of the probe, m_j ($j \in$ x, y, z) is a component of the magnetic moment. The $\vec{x}$, $\vec{y}$, $\vec{z}$ are the unit vectors of the coordinate system.

4.4.2.2 Simulation Results for Several Typical Conditions

With the sample as shown in Fig.4.4.1 and tip in Fig.4.4.8, some typical conditions have been calculated and discussed by using Eqn. (4.4.2) as follows:

Case (1). The most symmetrical case is for $\alpha = 90$, $\theta = 15$. We chose I = 1.0mA, and scan height of 1.0 μm. In the calculation, we use $M_s = 0.870 \times 10^6$ Am^{-1} given by A. Carl *et al.* [60] as the saturation magnetization of the CoCr coating. In this orientation of the sample and cantilever, MFM images with different tip-magnetization are considered as follows:

a: All magnetic moments on the probe are saturated along the x-axis

In this case, Eqn. (4.4.2) becomes $F_n = F_{nx}$. The MFM images are shown in Figure 4.4.9.

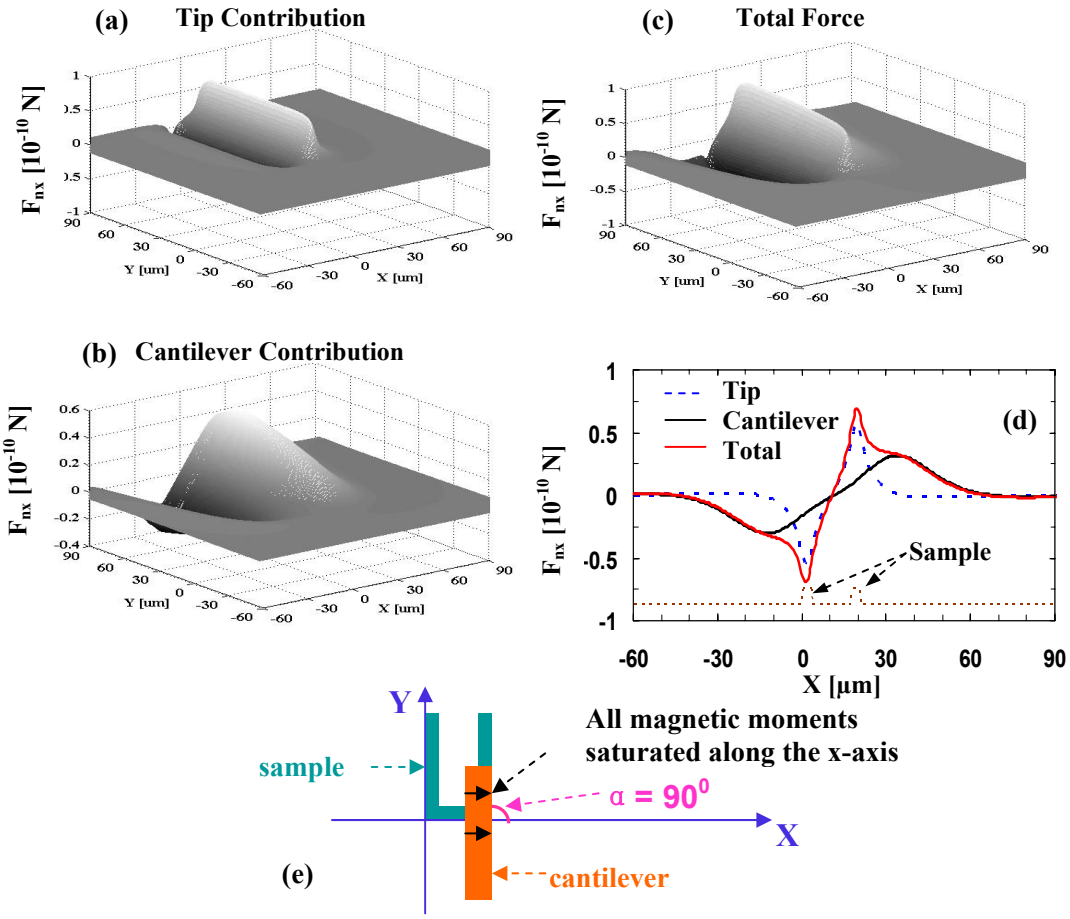

Figure 4.4.9. Simulation of the magnetic force F_{nx} with a current of 1.0 mA, the scan height of d = 1.0 μm, magnetization along the x-axis, and $\alpha = 90^0$, $\theta = 75^0$ for the cantilever. **(a)** Only consider the tip. **(b)** Only consider the cantilever. **(c)** The sum of (a) and (b). Line-scan taken along the dashed line in Figure 4.4.1(d) is shown in **(d)**, respectively. **(e)** Schematic drawing of orientation of the sample, cantilever, and magnetic moment for this simulation.

b: All magnetic moments are saturated along the y-axis

In this case, Eqn. (4.4.2) becomes $F_n = F_{ny}$. The MFM images are shown in Figure 4.4.10.

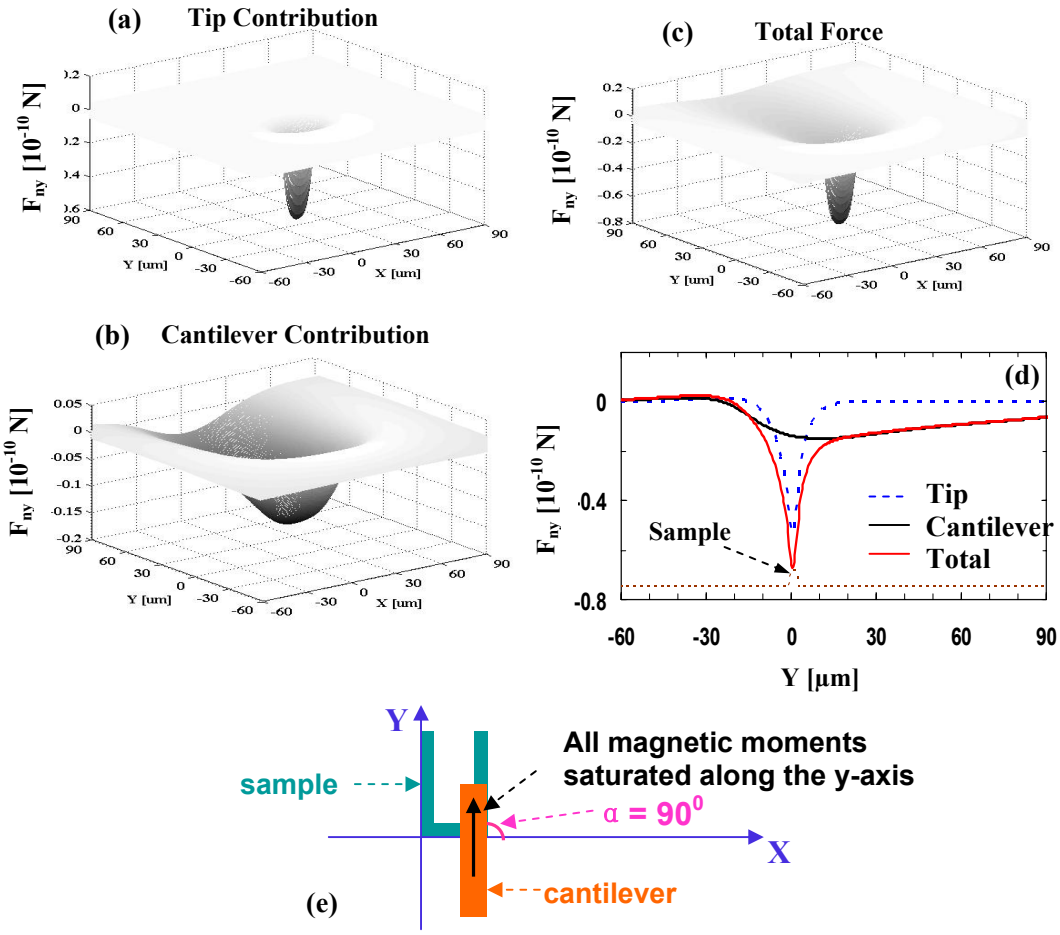

Figure 4.4.10. Simulation of the magnetic force F_{ny} with a current of 1.0 mA, the scan height of d = 1.0 µm, magnetization along the y-axis, and $\alpha = 90^0$, $\theta = 75^0$ for the cantilever. **(a)** Only consider the tip. **(b)** Only consider the cantilever. **(c)** The sum of (a) and (b). Line-scan taken along the dotted line in Figure 4.4.1(d) is shown in **(d)**, respectively. **(e)** Schematic drawing of orientation of the sample, cantilever, and magnetic moment.

c: All magnetic moments are saturated along the z-axis

In this case, Eqn. (4.4.2) becomes $F_n = F_{nz}$. The MFM images are shown in Figure 4.4.11.

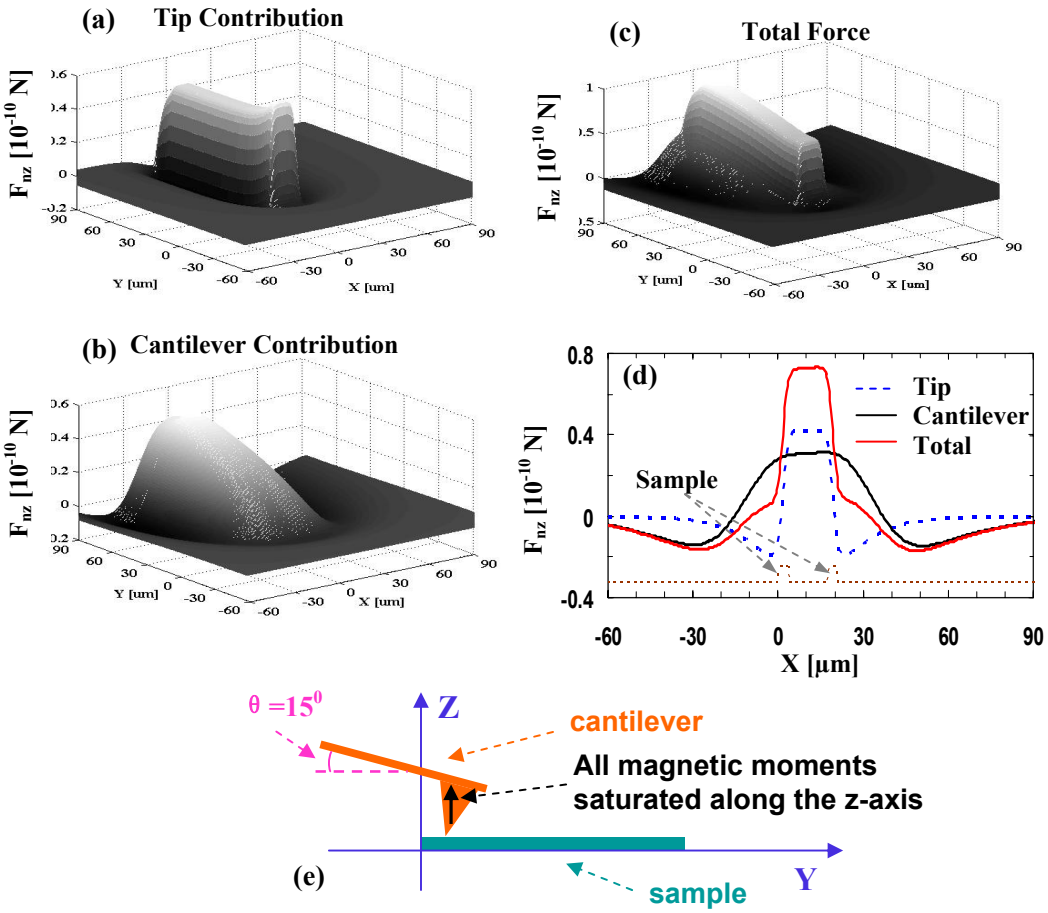

Figure 4.4.11. Simulation of the magnetic force F_{nz} with a current of 1.0 mA, the scan height of d = 1.0 μm, magnetization along the z-axis, and $\alpha = 90^0$, $\theta = 75^0$ for the cantilever. **(a)** Only consider the tip. **(b)** Only consider the cantilever. **(c)** The sum of (a) and (b). Line-scan taken along the dashed line in Figure 4.4.1(d) is shown in **(d)**, respectively. (e) Schematic drawing of orientation of the sample, cantilever, and magnetic moment.

In these three cases, we plot the cantilever and tip contributions to the force for comparison. Although the cantilever is further from the sample circuits than the tip is, it has almost the same magnitude of contribution as the tip has since it has much more magnetic material on it, and can not be neglected in most cases. However, since the cobalt coating is formed as a thin film about 30~130-nm in thickness on the tip and the cantilever surface, its magnetization behavior is much different between the parallel and

perpendicular to the film plane, which makes the quantitative interpretation of the MFM-images difficult. Under most circumstances the contribution of the tip and the cantilever can not be simply added since there are different magnetizations on each surface of the probe. Later on, in this chapter we will address this issue in detail.

d: All magnetic moments are saturated along the long tip axis

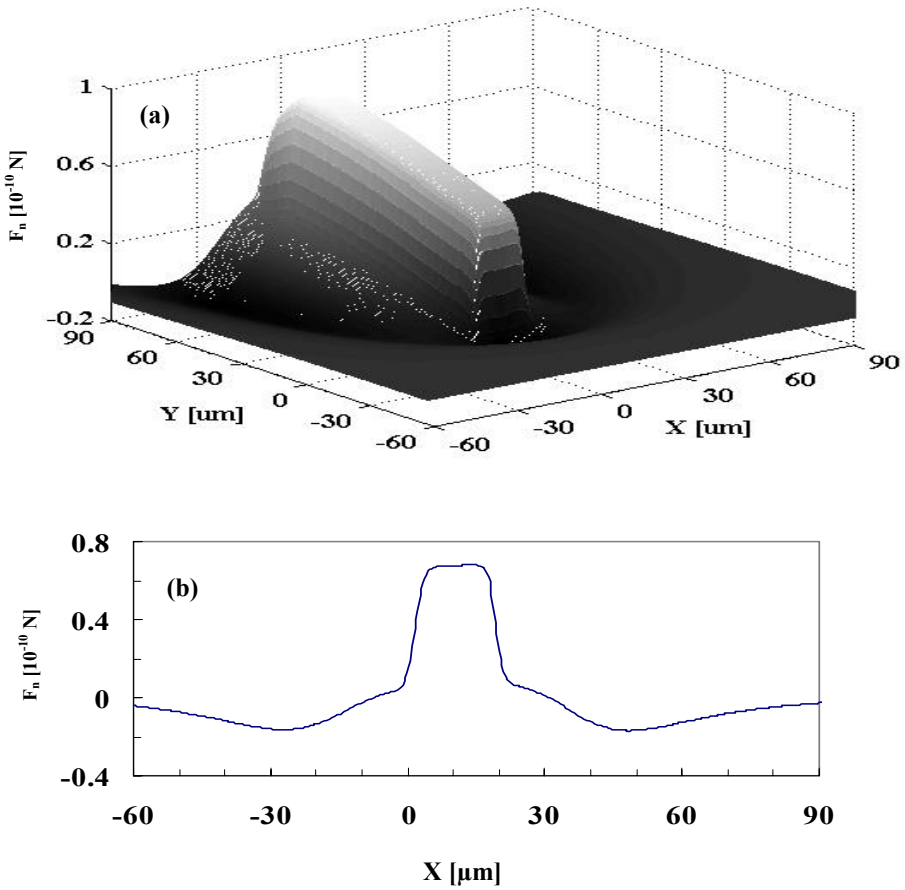

Figure 4.4.12. Simulation of the magnetic force F_n with a current of 1.0 mA, the scan height of d = 1.0 μm, magnetization saturated along the long tip axis, and $\alpha = 90^0$, $\theta = 15^0$ for the cantilever. **(a)** 3-d image. **(b)** Cross section plot along the dashed line in Figure 4.4.1 (d).

According to simple geometry, Eqn. (4.4.2) can be written

$$\mathbf{F_n} = \sin\theta\cos\alpha\mathbf{F_{nx}} + \sin\theta\sin\alpha\mathbf{F_{ny}} + \cos\theta\mathbf{F_{nz}} \quad (4.4.4)$$

where $\alpha = 90$, $\theta = 15$. Therefore,

$$\mathbf{F_n} = 0.2588\mathbf{F_{ny}} + 0.9659\mathbf{F_{nz}} \quad (4.4.5)$$

F_{nx}, F_{ny}, and F_{nz} are all magnetic moments along the x, y, and z-axes, respectively, and shown in above. A MFM-image is shown in Figure 4.4.12.

In the above discussions we assumed that all of the magnetic moments on the probe surface are aligned along one direction, ignoring the geometric effect on the film magnetization and the complicated properties of the tip-magnetization. To assure that the tip-magnetizations are aligned, an external magnetic field that is large enough to align all the magnetic moments along one direction is needed. In our experiments, we apply a uniform external magnetic field in the z direction, which is perpendicular to the sample plane, in order to assure the orientation of the magnetic moments in the tip and cantilever. With the magnetic moments all in alignment then we can compare the experimental results with the MFM image shown in Fig.4.4.11 (c).

Case (2). In order to specify the cantilever contribution, $\alpha = 135$, $\theta = 15$ is chosen. When I = 1.0 mA, and scan height of 1.0 μm, all magnetic moments saturated along the x-axis F_{nx}, y-axis F_{ny}, and z-axis F_{nz} are shown in Figure 4.4.13(a), (b), and (c), respectively.

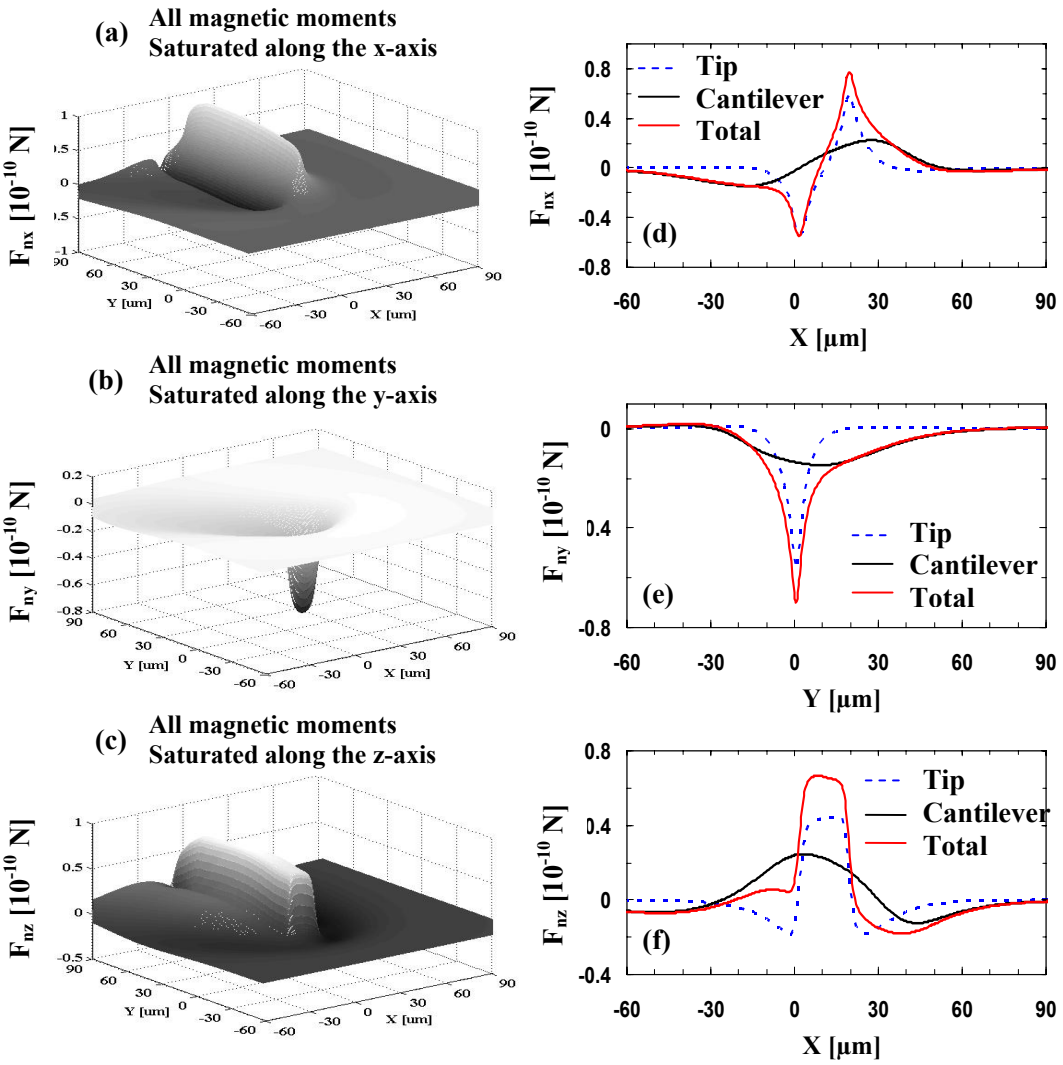

Figure 4.4.13. Magnetic force generated by a current of 1.0 mA, the scan height of d = 1.0 μm, $\alpha = 135^0$, $\theta = 75^0$ for the cantilever. Magnetization along the x-axis **(a)**, y-axis **(b)**, and z-axis **(c)**. Line-scan is shown in **(d)**, **(e)**, and **(f)**, respectively. **(d)** and **(f)** are along the dashed line in Fig.4.4.1(d), **(e)** is along the dotted line in Fig.4.4.1 (d).

From Figure 4.4.13, we can see that the main difference with α = 90 is the contribution from the cantilever since the tip changes only slightly but the cantilever contribution is significant (refer to Figure 4.4.14). For example, let's consider scan point **A** in Figure 4.4.14. In two cases the tip is slightly different with respect to the sample due to the tilt angle θ (not show in the plot), but the cantilever shows a big difference relative to the

sample, most part of the red (dark) one is much closer to the sample than most part of the green (light) one.

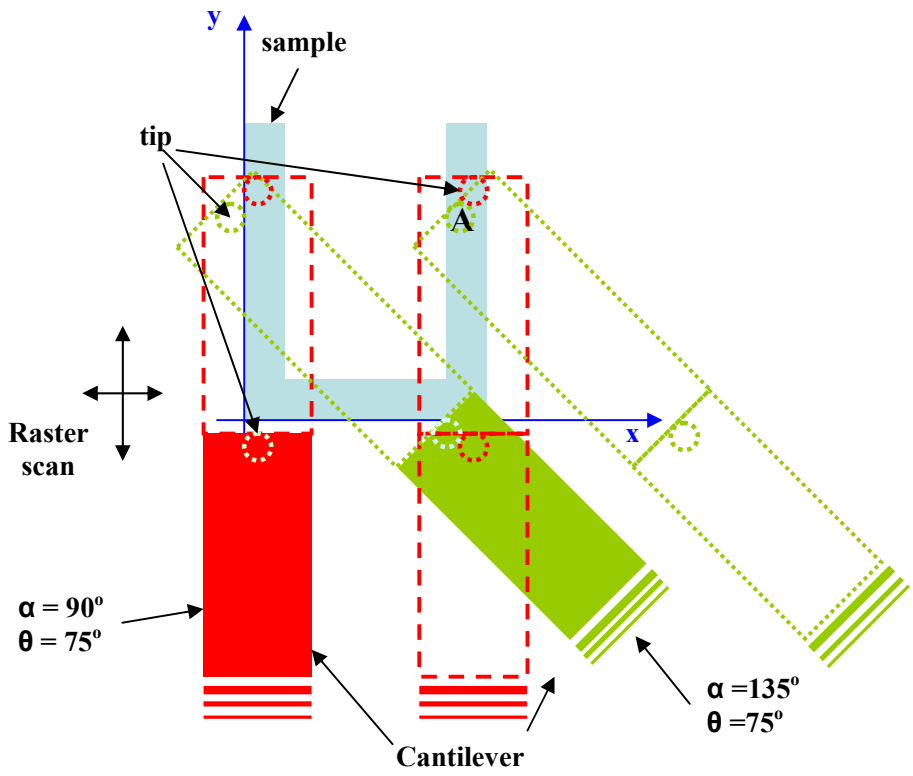

Figure 4.4.14. Schematic representation of the cantilever with respect to the sample position during the raster scanning. Dashed line in the shape of the cantilever indicates the several scan positions of the cantilever. Red and green colors represent two different orientations of the cantilever, respectively.

4.4.2.2 Effect of Variation in Tip and Cantilever Magnetic Moments

Since its invention in 1987[75], the MFM has become an increasingly important tool used to investigate magnetic micro- or nano-structures. However, to date, a true quantitative interpretation of MFM-images is still difficult except in a few special cases. Though theoretical work based on, the rather simple point probe model [69], the tip to sample interaction [133], MFM-image simulation [113], micromagnetic modeling of the MFM tips [114, 131, 134] and numerical magnetization techniques [115, 138] with certain more

general provisos has proven to be quite successful in the understanding of the image formation in MFM. The difficulties mainly rest on the fact that the detailed magnetic properties of MFM tips, such as the effects of tip hysteresis and coercivity, as well as the resulting magnetization distribution in the tip, are generally not well known [59], in particular, when the contribution of the cantilever has to be considered.

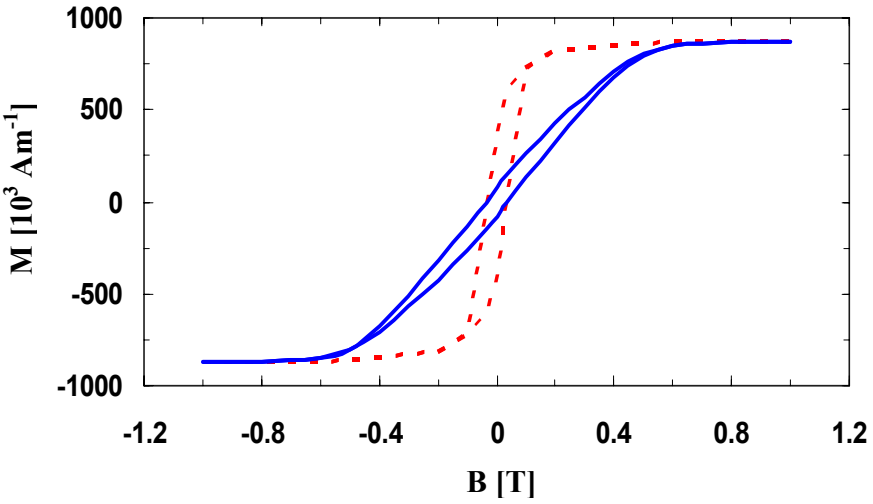

Figure 4.4.15. Magnetization of the CoCr coating of a commercially available thin-film tip as a function of external magnetic field oriented parallel (red dashed line) and perpendicular (blue solid line) to the plane of the silicon substrate, measured with a superconducting quantum interference device (SQUID) magnetometer [60].

Figure 4.4.15 shows two hysteresis loops measured with a superconducting quantum interference device (SQUID) magnetometer on a commercially available thin-film tip investigated by Carl *et al*. [60]. The magnetization **M** versus external magnetic field shows a quite difference when an external magnetic field is oriented parallel or perpendicular to the substrate plane, though the same value for the saturation magnetization and the coercivity is found in both measurements. The nanoscale current-carrying rings were also used by Carl *el at*. [60] to measure the hystersis loop and the coercivity of the same tips with MFM. Carl's results show a lack of reproducibility of the magnetic properties of MFM tips taken from different batches. This is an unsettling result

and leads to the conclusion that quantitative interpretation of images will require individual characteristics of magnetic probes. This study concludes that the easy direction of the magnetization of the CoCr film is predominantly oriented in the substrate plane. We will use their average value of the magnetizations as the basis for our simulation [60].

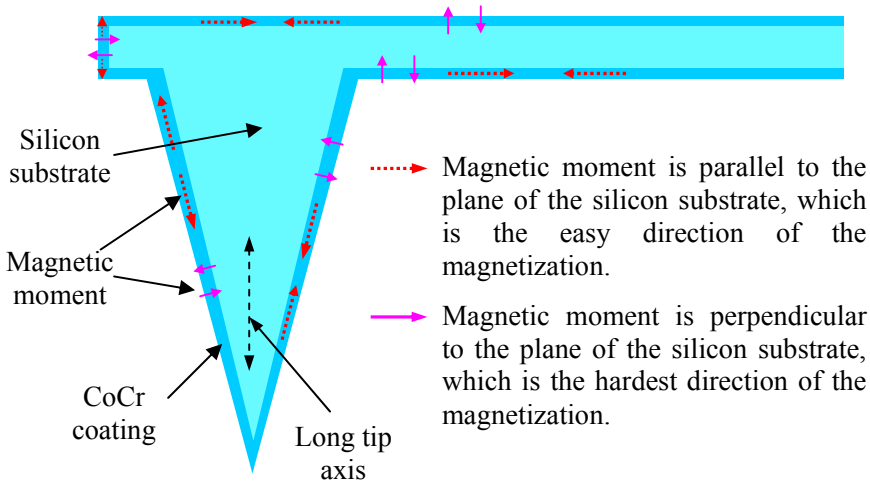

Figure 4.4.16. Schematic representation of a silicon tip covered with a CoCr coating. Arrows indicate the directions of the magnetic moments, which are parallel and perpendicular to the plane of the silicon substrate.

Figure 4.4.16 schematically shows the probe covered with a Cobalt film used in our experiments. The easy direction of the magnetization is predominantly oriented within the plane of the Cobalt coating (see Figure 4.4.15), which is parallel to the substrate plane. Notably, once the tip itself has been magnetized along the long tip axis, the resultant remanent magnetization of the tip should predominantly point into the positive or negative this direction, but this is not so for the cantilever. In this direction the dominant magnetization of the cantilever is perpendicular to the substrate plane. Therefore, except through application of an external magnetic field sufficient to saturate the magnetization, we have to individually consider the magnetization of each region of the probe.

Case (3). If the tip is magnetically saturated into the long tip axis prior to measurements and we assume its magnetization as shown in Fig. 4.4.15, each region of the probe should have the remanent magnetization. The remanent magnetization of the tip and side of the cantilever along the long tip axis is approximately $M_r = 0.384 \times 10^6$ Am^{-1} according to the hystersis loop parallel to the plane of the film in Figure 4.4.15. However for the remanent magnetization of the cantilever in the bottom and top we should use $M_r = 0.086 \times 10^6$ Am^{-1} from the hystersis loop perpendicular to the plane of the film in Figure 4.4.15. The result shows in Figure 4.4.17.

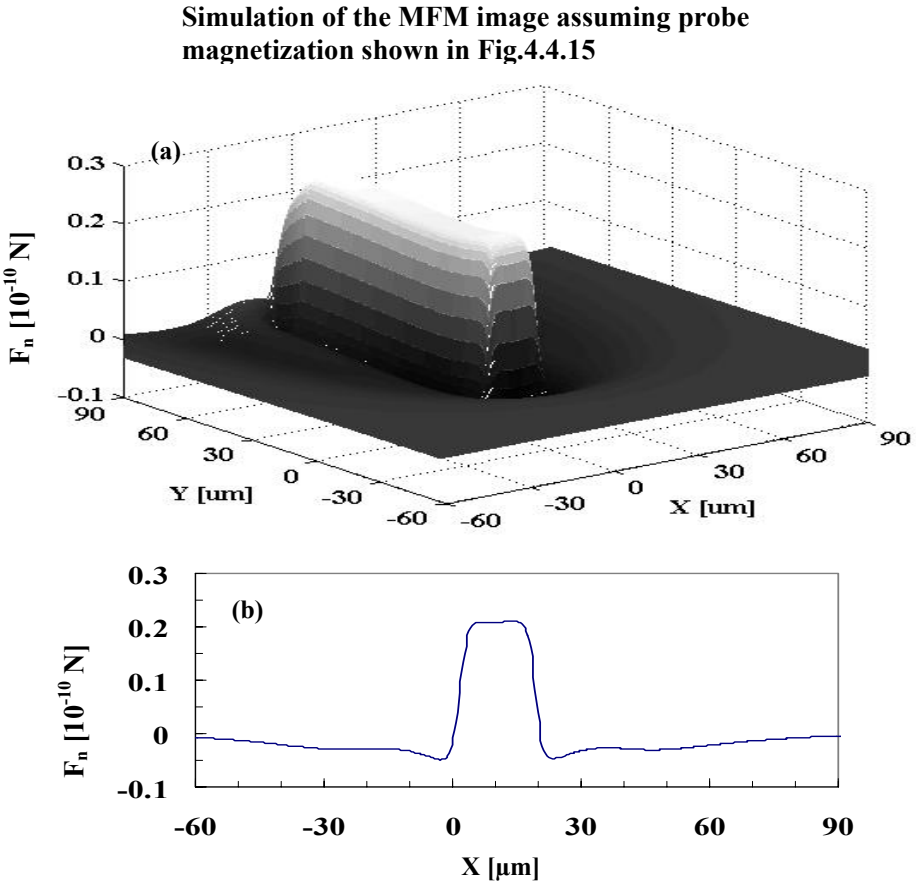

Figure 4.4.17. Magnetic force F_n with a current of 1 mA, the scan height of d = 1.0 μm, and $\alpha = 90^0$, $\theta = 75^0$ for the cantilever. Before use, tip is magnetized along the long tip axis. Consider the different remanent magnetization in each side of the probe. **(a)** 3-d image. **(b)** Cross section plot along the dashed line in Figure 4.4.1 (d).

Chapter 5
MFM FORCE AND FORCE GRADIENT IMAGING OF MODEL CIRCUITS

The theoretical aspects of this work have been discussed in previous chapters. In this chapter MFM experimental measurements on the model circuits are presented. We start with the test circuit design, measurement instrumentation, experimental details, results, and discussions.

5.1 Model IC Short Circuit Defect

In today's semiconductor industry, failure analysis on defective devices has become key to improving product qualify and process development. An important tool in failure analysis is the measurement of current. Excessive current flowing into devices after the initial transient is often used to indicate the presence of faulty devices. Location of these faulty devices can be problematic as the devices are often buried under several

interconnect layers. VDD current quiescent (IDDQ) testing can limit the number of possible fault locations, but can not extract the precise fault location [9, 21] (also refer to section 1.2).

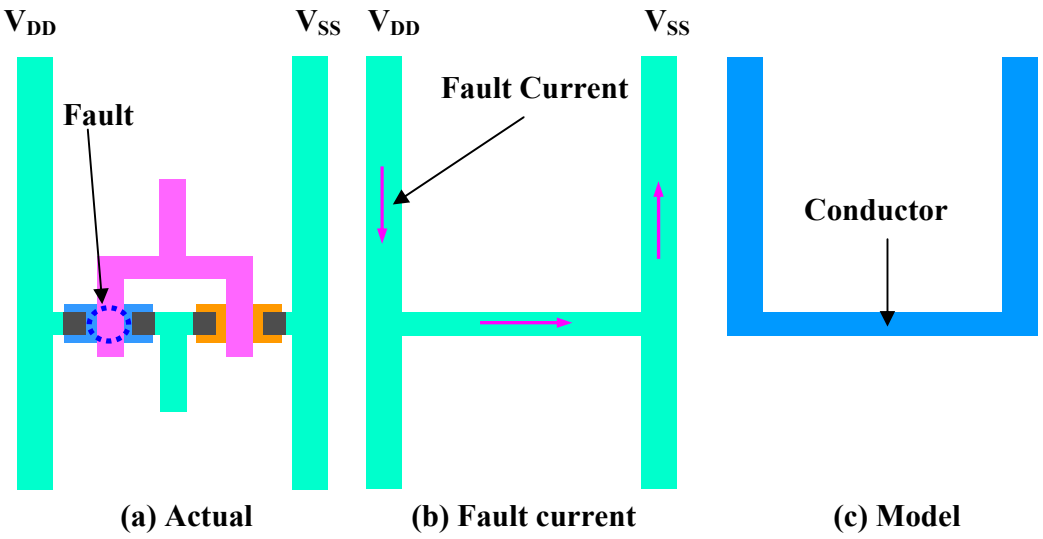

Figure 5.1.1. An experimental model for IC fault. (a) A CMOS inverter has a fault that produces the fault current in **(b)**. **(c)** An experimental model used for sample design.

There are many types of faults which can cause an integrated circuit to fail. The technique we are proposing in this research would be applicable to faults which result in steady state current flow, such as transistor with high leakage current or bridging effect of interconnection lines. In a typical IC this will result in abnormal current flow between the power supply (V_{DD}) and ground (V_{SS}). Consider the example of a CMOS inverter which has a fault as shown as in Figure 5.1.1 (a). In this situation the fault produces a steady current flowing from V_{DD} to V_{SS} via the faulty device, and forms the equivalent rectangle-shaped current path in Figure 5.1.1 (b). We have developed an experimental model for this type of fault using an interconnect shaped as a single-turn-rectangle (as shown in Figure 5.1.1(c)) fabricated by patterning a thin metal film onto a SiO_2 substrate.

In our fabrication, a 10/50 up to 10/400-nm-thick Titanium/Gold (Ti/Au) layer was first sputtered onto a SiO_2 substrate. Photoresist was then spun onto the top of the Ti/Au layer, and soft baked. Patterns of the circuit structure (using a mask) were exposed in the resist using a UV light source. The exposed photoresist was removed during the development, leaving resist on the top of the circuit structure to define the etch process. Then KI etches the Gold and buffered hydrofluoric acid (HF) etches the Titanium. Finally, the photoresist was dissolved in acetone, leaving the metal circuit structures on the SiO_2 substrate.

5.1.1 Test Circuit Structure

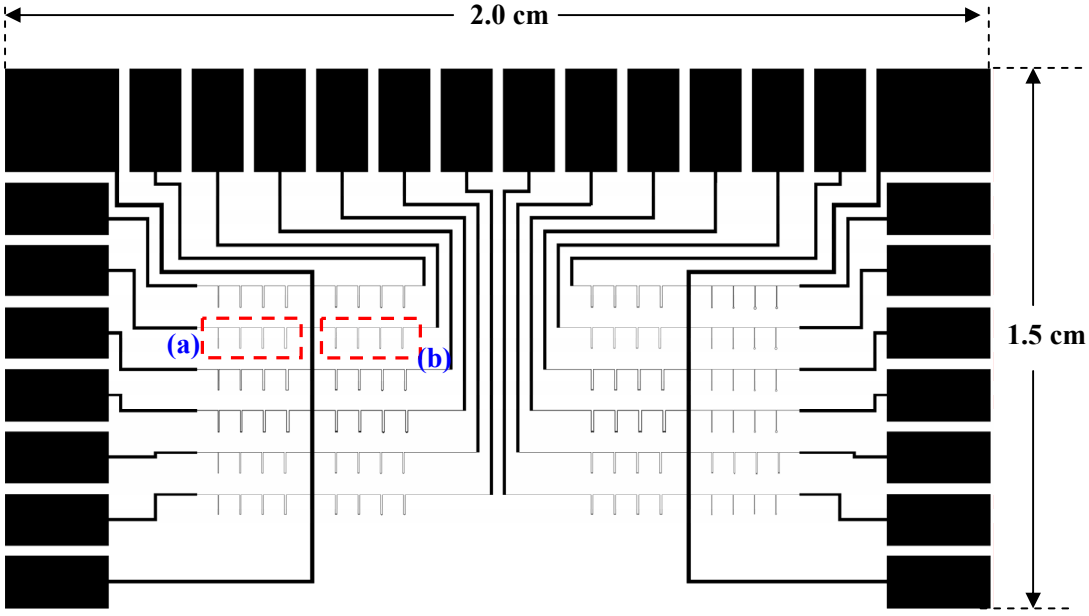

Figure 5.1.2. A layout of the sample circuit, which is designed using Cadence MUMPs technology. Dash line area (a) and (b) is enlarged shown in Figure 5.1.3 **(a)** and **(b)**, respectively.

Considering different shapes and sizes of abnormal current flow between the power supply (V_{DD}) and ground (V_{SS}), we designed a 1.5cm × 2.0cm test circuit structure mask for this experiment using Cadence MUMPs layout tools. A layout of the mask is shown

in Figure 5.1.2. The resolution to fabricate a mask only allows 2.0μm as the minimum width and spacing of the conducting lines.

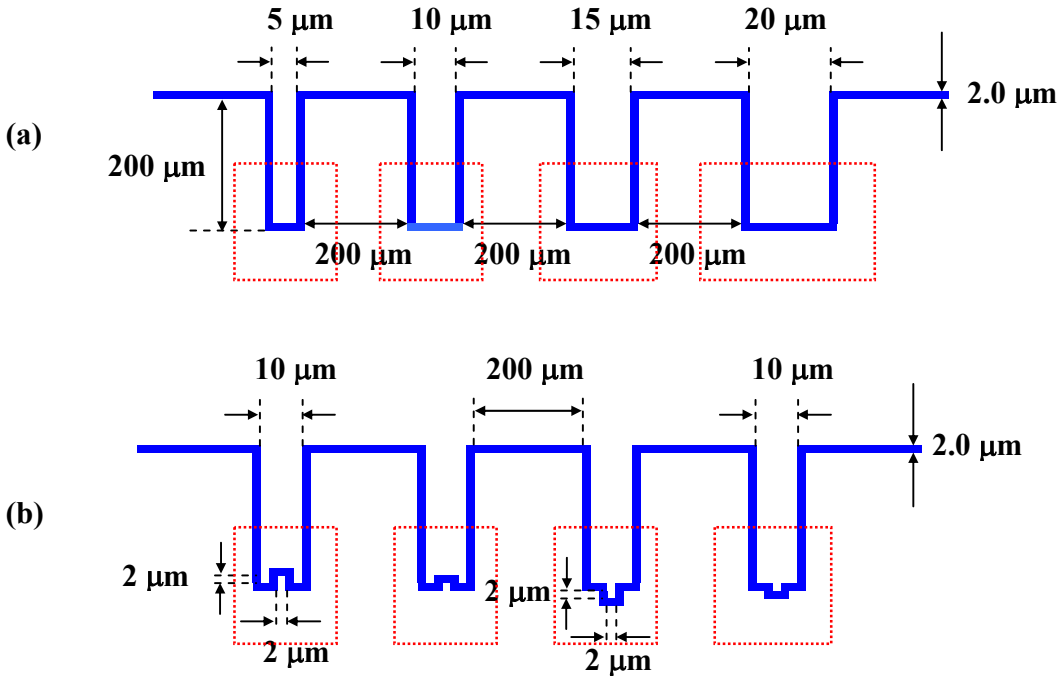

Figure **5.1.3.**(a) A schematic enlarged view of the dash line area (a) in Figure 5.1.2. **(b)** A schematic enlarged view of the dash line area (b) in Figure 5.1.2. Plot scale is not proportional to the actual dimensions. The dotted line areas indicate the MFM image taken areas

The test circuit structure contains the different rectangular turns. They have the different line widths and spacing specification with the minimum being 2.0μm and maximum being 5.0 μm, and the 5μm minimum and 20 μm maximum, respectively. Figure 5.1.3 (a) and (b) enlarged show the selected dash line areas (a) and (b) in Figure 5.1.2, respectively. A 200 μm separation between each fault model structure is selected in order to minimize the mutual influence on the MFM images. The dimensions of the model structures are based on the typical distances between VDD and VSS of a CMOS transistor.

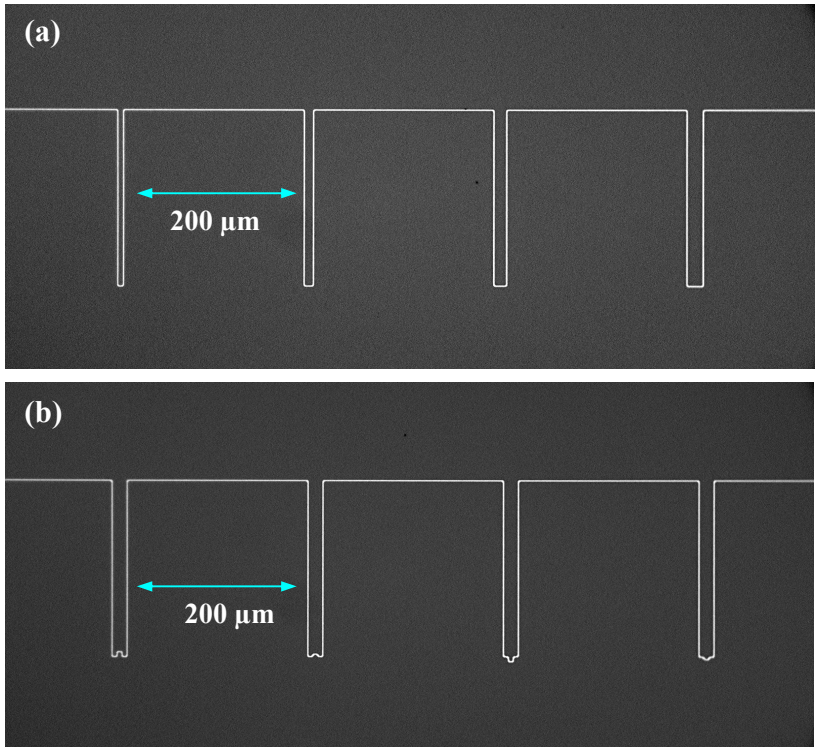

Figure 5.1.4. Optical micrographs of two typical samples are schematic drawing in Fig.5.1.3 (a) and (b), respectively.

Figure 5.1.4 (a) and (b) show optical micrographs of two typical samples which are schematic drawing in Fig. 5.1.3. All MFM measurements presented in this thesis are for these conducting structures.

The actual sample has slightly different dimensions than the mask, due to the fabrication process. Therefore, we use AFM topographic images to determine the final dimensions of the rectangular turns as a base of our modeling and analysis.

5.2 Experimental Apparatus

All MFM experimental measurements were taken using a Digital Instrument EnviroScope™ (E-Scope) by Veeco operated in contact/lift™ mode. A photograph of the E-Scope is shown in Figure 5.2.1.

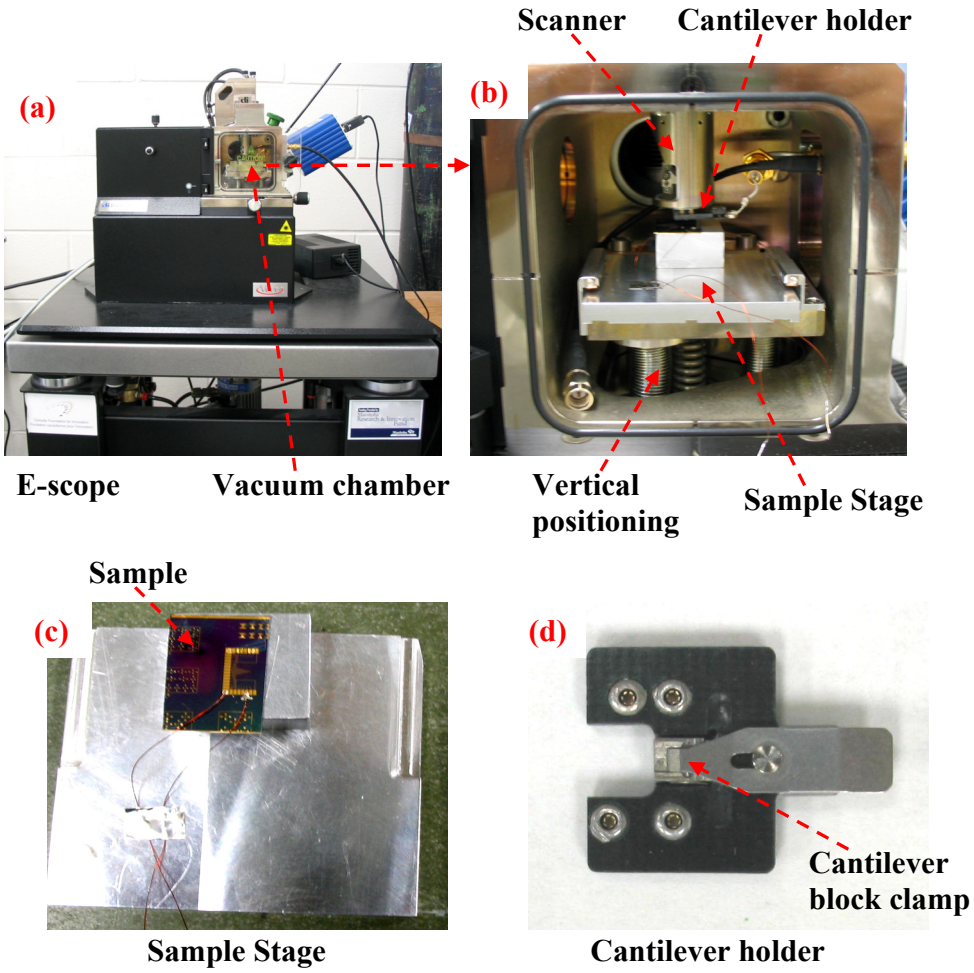

Figure 5.2.1. Photograph of the E-scope.

In the E-scope, an optical beam bounce system was used to detect the deflection of the probe cantilever and the tip rather than the sample stage was scanned. The sample under test was manually positioned beneath the probe and was held up by the stage, which was mounted on the top of the vertical positioning. The vertical positioning can move the sample stage coarsely up and down using a stepper motor by the controller, and then piezoelectric scanner was used for finer movement and raster scanning the sample. The cantilever was connected to the scanner with the cantilever holder shown in Fig. 5.2.1 (d). A piezoelectric stack may be used to vibrate the cantilever for force gradient detection. E-

scope can measure in a vacuum up to ~10^{-6} Torr. More details including the controller and software can be found in the SPM manuals supplied by Veeco [139].

5.3 Magnetic Force

5.3.1 Experimental Details for MFM Force Detection

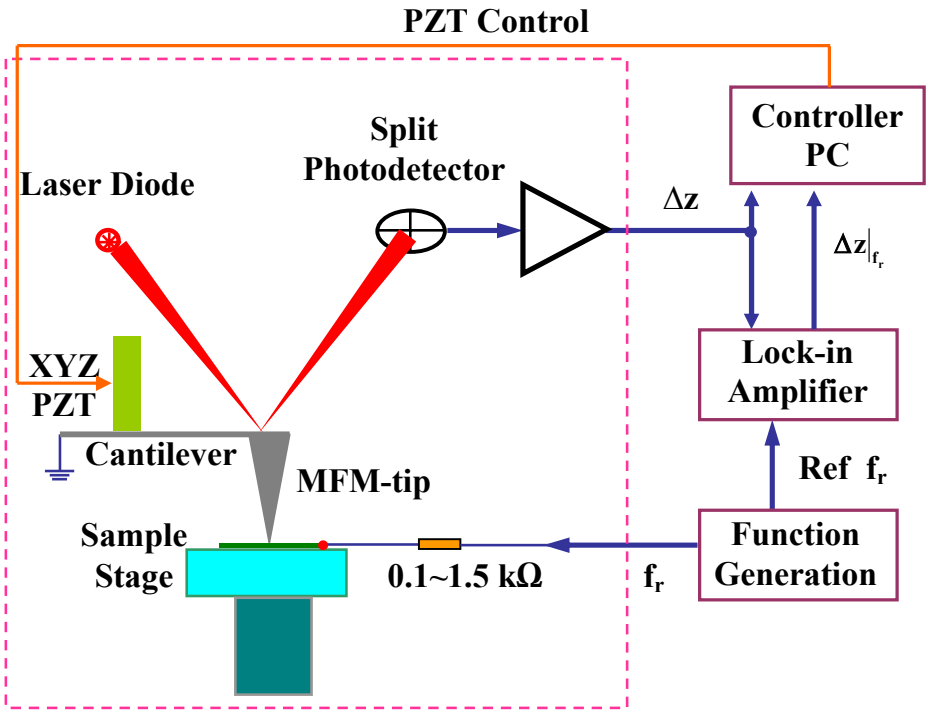

Figure 5.3.1. Schematic diagram of the MFM experimental setup showing beam-bounce detection system used to detect topographic data (contact mode) and the MFM force image (lift mode). Dash line area is in the vacuum environment.

A schematic diagram of our measurement apparatus setup for force detection illustrated in Figure 5.3.1 is based on an established MFM technique that is discussed in Chapter 3.

An AC current up to 10.0 mA peak-to-peak at the cantilever resonance frequency (f_r from 70 to 105 kHz) was supplied by a function generator and passed through the sample

circuit. A series resistor of 0.1~1.5 kΩ was used to limit current flow, since the resistance of the sample circuit sometimes is less than 5 Ω. The cantilever was grounded in order to minimize interference from electrostatic effects. In E-Scope the tip rather than the sample stage is scanned.

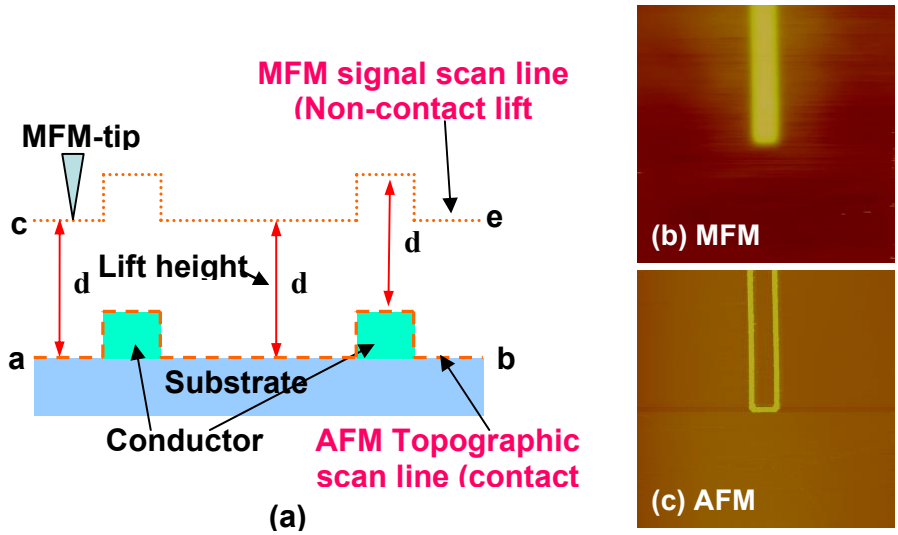

Figure 5.3.2. (a) Schematic representation of contact/lift mode scan line. The dotted line ce indicates a single MFM signal scan line at the lift height of d above the surface of the sample. The dashed line ab indicated the corresponding AFM topographic scan line in the experiment. **(b)** MFM. **(c)** AFM.

The atomic force (AFM) image and magnetic force (MFM) image of the sample circuit were taken simultaneously using the E-Scope in UM SPM lab operated in contact/lift mode. During operation, each line of the raster is traced and retraced twice (normally we record the retraced line), first in contact AFM mode to obtain a surface topographic image and secondly in non-contact mode to obtain a MFM image as shown as Figure 5.3.2. In contact mode, the probe is held against the sample surface, the deflection of the cantilever is sensed, and a feedback loop keeps the deflection, and hence the force, constant. The topographic trace of the sample's surface is recorded by vertically moving the piezoelectric tube (PZT) scanner at each (x,y) data point. In non-contact mode, the PZT is retraced along the scan line with the probe held at a set distance above the surface

and hence only the longer range magnetic forces influence the probe. During this scan, the force exerted on the probe (MFM signal) is extracted by using an external lock-in amplifier (SRS Model 830 or 844). The lock-in amplifier is used to measure the amplitude and phase of MFM signals at a particular frequency. The sample is driven by a signal set near to the resonant frequency of the cantilever to enhance the cantilever deflection. The magnitude or phase of the MFM signal output from the lock-in amplifier was acquired by the E-scope controller where it was synchronously sampled with the raster scan.

MFM measurements were made with maximum currents in the individual lines of about I = 6.0 or 20.0mA (20.0mA dc for force gradient measurement). With the minimum quantities w = 1.4 or 2.0μm, the width of the transmission line, and t = 45 or 200 nm of the thickness, the maximum current density j = I/wt is on the order of 9.5×10^{10} or 5.0×10^{10} Am^{-2}. This value is lower than 3×10^{11} Am^{-2}, the highest current density that can be driven in the gold sample without destroying it [59]. The current can lead to an increase of the temperature of the sample, which could affect an increase of the resistance of the transmission line. Kebe *et al.* have studied this issue experimentally in recent work [59]. The results showed: When the current density is less than 1.04×10^{11} Am^{-2} (in our case of I = 6.55 or 41.6 mA current driven in our circuits), the current *versus* voltage curve is linear which reflects no significant resistance change of the sample. Considering $\gamma = 3.9 \times 10^{-3}$ K^{-1} which is the temperature coefficient of the electrical resistance of gold, at the current density of 1.56×10^{11} Am^{-2} (in our case of I = 9.83 or 62.4mA current driven in our circuits), the increase of temperature of the sample is at $\Delta T = 9$ ^{o}C. Notably, we did not use the current in excess of I = ± 6.0 or 20.0 mA, it is therefore very unlikely that the MFM-tip and the resistance of the circuits will be subjected to any temperature increase during the measurement. Experimental results will be shown later.

As we discussed in chapter 4, a strong uniform external magnetic field will orient the magnetization of the MFM probe and does not affect the magnetic field due to the current. In our measurements, a permanent magnet was put underneath the sample to produce external magnetic fields of up to 0.5 T (measured by a Gauss meter) in the ± z direction

at the sample's location. However, if the permanent magnet is placed at the side of the sample in the perpendicular z direction, it only produces a field of up to 0.06 T at the sample's location. Since this field magnitude is not sufficient to assure saturation, we did not obtain the tip-magnetization in the perpendicular z direction.

The E-Scope has been designed such that MFM measurements can be made in a vacuum, which increases the quality factor Q up to approximately 10^4. Auto Tune in the E-scope can calculate Q up to ~ 10^3 [139]. In the case of higher value of Q, a spectrum analyzer is used to monitor the thermal vibration of the cantilever, and to determine Q by measuring the cantilever resonance frequency f_r and the 3-dB bandwidth, Δf_r, which is at 0.707 of the maximum amplitude, $Q = f_r/\Delta f_r$.

The tip's spring constant k follows Eqn. (2.2.5), $k = (\rho l w t f_r^2)/0.105$ as given by Wolter *et al.* [90]. The dimensions of the cantilevers are determined from SEM images. k-values are calculated by using $\rho = 2.33$ [gcm^{-3}] which is the density of the cantilever material, Si.

5.3.2 Magnetic Force Measurements

This section presents the MFM measurement results. Measurement sensitivity and magnetic force distribution images from several typical conditions are presented and discussed.

5.3.2.1 Measurement Sensitivity

In section 3.5 we have theoretically discussed the current sensitivity which is an important quantity for MFM current imaging applications. In this section results are presented for current sensing sensitivity for the model circuits.

a: Measurement in air.

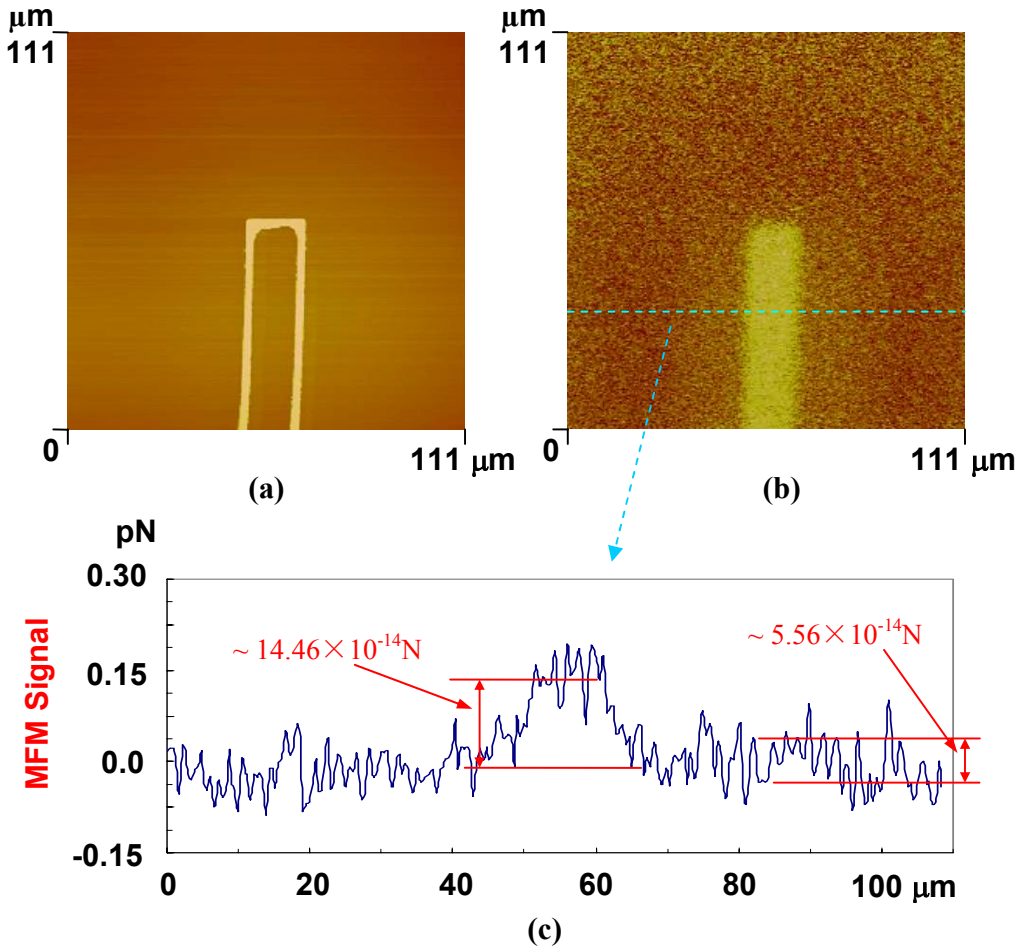

Figure 5.3.3. Corresponding AFM (a) and MFM (b) images of a metal line with the current I_{rms} = 6.7 µA and the scan height of 1.0 µm with the bandwidth 16 Hz. (c) MFM signal along the dashed line in (b). Noise $N \approx 5.56 \times 10^{-14}$N and signal $F_S \approx 14.46 \times 10^{-14}$N are shown in (c).

The measurement apparatus setup is shown in Figure 5.3.1. A permanent magnet (~ 0.5 T measured by a Gauss meter) was put underneath the sample, to hold the magnetic moments of the probe along the z-axis, so that the quantitative comparisons can be made with the theoretical calculations. The orientation of the cantilever was set at $\alpha = 90^0$ and $\theta = 15^0$.

Figure 5.3.3 (a) and (b) show corresponding AFM (topographic) and MFM images of the single-turn rectangle structure of Figure 5.1.3(a) for a current $I_{rms} \approx 6.7\mu A$, a lock-in

measurement bandwidth of 16 Hz, and a probe scan height of 1.0 μm above the surface of the sample. Note, that in Figure 5.3.3 (b) and in all MFM force detection images discussed throughout this thesis, as indicated in section 3.6, we have measured the deflection Δz (not phase shift ΔΦ) of the tip vibration, which is due to the force in the direction of the normal to the cantilever surface as resulting from the magnetic field of the current acting upon the tip. The deflection signal result from magnetic forces was detected using a lock-in amplifier and hence the polarity of the signal reverses as the forces change from in to out of phase with the driving signal. The signal and the noise are clearly observable in the MFM image of Figure 5.3.3 (b), and allow us to obtain an estimate for the signal to noise ratio.

Noise or the minimum detectable force: $\mathbf{F}_{\min} \approx 5.56\times10^{-14}\,\mathbf{N}$, or $1.39\times10^{-14}\mathrm{N}/\sqrt{\mathbf{Hz}}$.

MFM force for a current $I_{rms} \approx 6.7\mu A$: $\mathbf{F}_s \approx 14.46\times10^{-14}\,\mathbf{N}$,

The signal-to-noise ratio: $\mathrm{SNR}_F = \dfrac{\mathbf{F}_s}{\mathbf{F}_{\min}} = 2.6$.

In these calculations, we use a cantilever of rectangular geometry with the spring constant k = 4.0 N/m calculated by using Eqn. (2.2.5), $\mathbf{k} = \rho\ell\mathbf{wtf}_0^2 / 0.105$, the quantities l = 222 μm, w = 38 μm, and t = 4.0 μm are the length, width, and thickness of the cantilever, respectively, determined from a SEM image of the MFM probe. The deflection sensitivity of E-Scope in this measurement is 70 nm/V calibrated by Force Calibration mode, and other parameters are T = 300 K, $\Delta f \approx$ 16 Hz, f_r = 73.14 kHz, and Q =378 (calculated by Auto Tune in the E-scope) [139].

From the above results, we deduce the MFM rms signal to noise ratio decreases to one when the current is reduced to 2.58 μA or $\dfrac{2.58}{\sqrt{16}}$ =0.64 $\mu A/\sqrt{\mathbf{Hz}}$, and force signal F_{min} = $1.39 \times 10^{-14}\mathrm{N}/\sqrt{\mathbf{Hz}}$.

In E-Scope under the conditions used in this experiment, the thermal vibration of the cantilever is the dominant source of noise. In this situation as discussed in section 3.5, the minimum detectible force is theoretically calculated as $F_{min} \approx 7.8 \times 10^{-14}$ N or 1.95×10^{-14} N/$\sqrt{\mathbf{Hz}}$ from Eq. (3.5.6), $\mathbf{F_{min} = \left(\frac{4kk_B T \Delta f}{2\pi Q f_r} \right)^{1/2}}$. This result is consistent with the experimental result from above.

b: Measurement in vacuum.

In a vacuum environment, the quality factor Q will be increased up to approximately 10^4 or, approximately 20 ~ 30 times than that in the air. According to the theory in section 3.5 and keeping all other conditions the same, measuring in a vacuum will increase the sensitivity to approximately $\sqrt{\frac{Q_{vacuum}}{Q_{air}}}$ times. From the thermal vibration spectrum of the cantilever and using $Q = f_r/\Delta f_r$, we obtain

$$Q_{vacuum} \approx 8000,$$

and

$$\sqrt{\frac{Q_{vacuum}}{Q_{air}}} \approx 4.6.$$

Therefore, we expect

$$\frac{2.58}{4.6} = 0.56\mu A \text{ or } 0.14\ \mu A/\sqrt{\mathbf{Hz}}$$

RMS current driving in the circuit when the SNR is close to one in the vacuum environment, which is the measurement sensitivity.

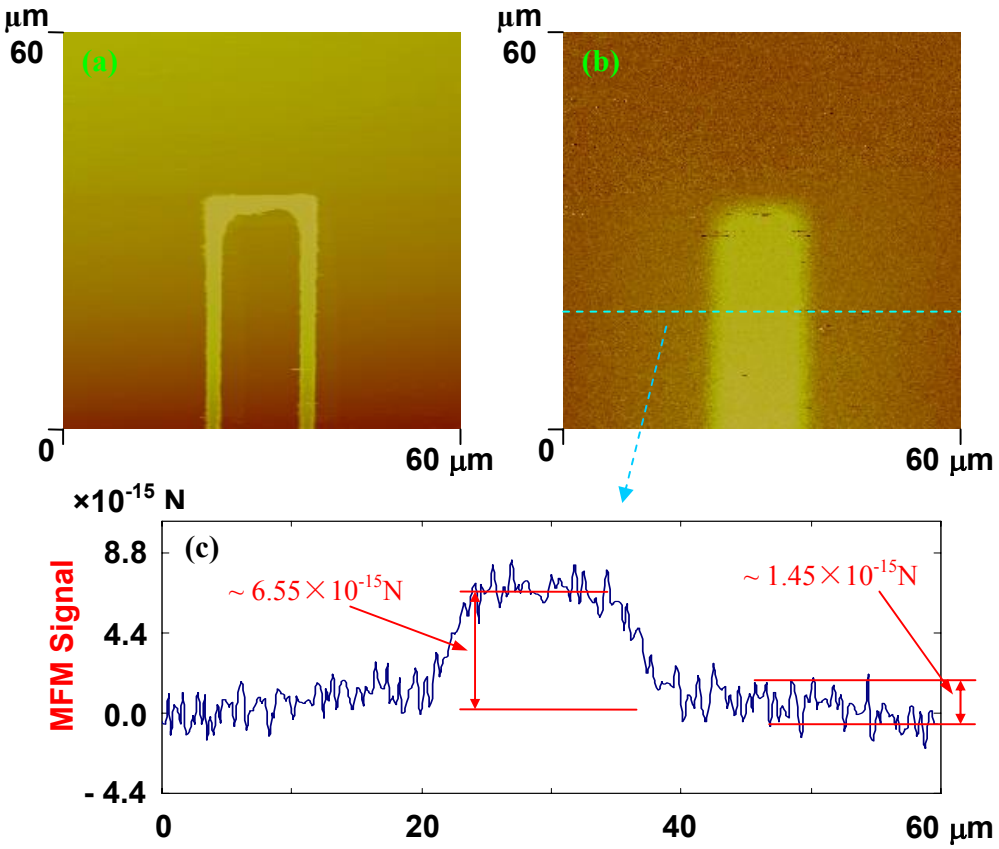

Figure 5.3.4. Corresponding AFM **(a)** and MFM **(b)** images of a metal line in vacuum system with the current I_{rms} = 1.69 µA and the scan height of 1.0 µm with the bandwidth 16 Hz. **(c)** MFM signal along the dashed line in **(b)**. Noise $N \approx 1.45 \times 10^{-15}$N, signal $F_S \approx 6.55 \times 10^{-15}$N, and SNR ≈ 4.5 are shown in **(c)**.

Figure 5.3.4 (a) and (b) show corresponding AFM (topographic) and MFM images of the same sample as above in a vacuum system for a current I_{rms} ≈ 1.69 µA, a lock-in measurement bandwidth of 16 Hz, and a probe scan lift height of 1.0 µm. From the results we obtained the measurement sensitivity of about 0.38 µA or 0.095 µA/$\sqrt{\mathbf{Hz}}$. In Table 5.1 we summarize the corresponding results for measurement sensitivity in the air and vacuum environments.

Table 5.1. Summary of the measurement sensitivity in the air and vacuum environments.

	Air		Vacuum	
	Experimental	Theoretical	Experimental	Theoretical
Minimum Detectable Force	1.4×10^{-14} N/$\sqrt{\mathbf{Hz}}$	1.9×10^{-14} N/$\sqrt{\mathbf{Hz}}$	0.36×10^{-15} N/$\sqrt{\mathbf{Hz}}$	4.2×10^{-15} N/$\sqrt{\mathbf{Hz}}$
Sensitivity	0.64 μA/$\sqrt{\mathbf{Hz}}$	0.43 μA/$\sqrt{\mathbf{Hz}}$	0.095 μA/$\sqrt{\mathbf{Hz}}$	0.093 μA/$\sqrt{\mathbf{Hz}}$

In Table 5.1, the theoretical minimum detectible force is calculated from Eq. (3.5.6**),** $\mathbf{F}_{\min} = \left(\frac{4\mathbf{k}\mathbf{k}_B\mathbf{T}\Delta\mathbf{f}}{2\pi\mathbf{Q}\mathbf{f}_r} \right)^{1/2}$, and the theoretical sensitivity is from our modeling calculation that is 1.7 μA current will produce a force of 7.8×10^{-14}N acting on the cantilever. In the model calculation, we assume the magnetic moments of the cantilever are saturated along the z-axis as shown in Fig.5.3.6, using $M_s = 0.87 \times 10^6$ Am^{-1} as the magnetization, and 60 nm thickness of Cobalt on the cantilever surface. The results show a good agreement between theory and experiment in the air, but there is a large discrepancy of the thermal noise in the vacuum, where the minimum detectable force is not followed by Eq. (3.5.6) in the vacuum. We found the SNR in the vacuum does not exhibit a square root of Q_{vacuum}/Q_{air} dependence as expected from theory. We suspect this is due to the change in the deflection sensitivity or a slight change of the resonance frequency. However, the minimum detectable current is in excellent agreement with theoretical estimates.

5.3.2.2 MFM Force Images for Different Conditions

This section, measurements obtained with the model circuits with different experimental configurations, specifically images taken at different probe to sample distances.

Measurement apparatus setup is the same as the last section and shown in Figure 5.3.1. A schematic representation of the experimental arrangement of the permanent magnet, the sample circuit, and the MFM tip is shown in Figure 5.3.5. This is the most symmetrical case for cantilever tilting off surface of $\alpha = 90^0$ and $\theta = 15^0$. A quite large permanent magnet with dimension of 2.5cm×2.5cm×1.0cm was used for applying a uniform magnetic field around 0.5T in the scan area to hold the magnetization of the MFM probe along the z-axis with respect to the sample plane during the MFM scanning. This is the easiest situation for implementation and comparison with the simulation calculation as discussed in section 4.4.2.

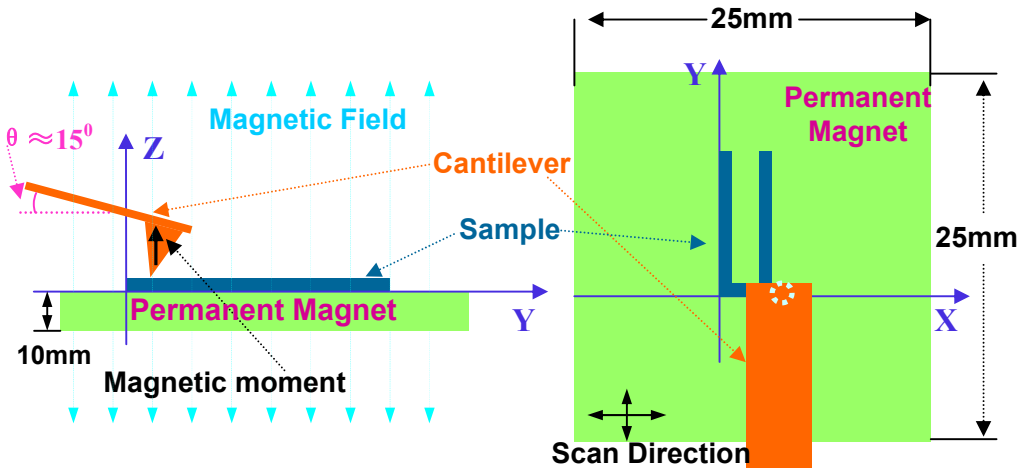

Figure 5.3.5. Schematic representation of the experimental arrangement of the sample circuit, permanent magnet, and the MFM probe showing the magnetic moment of the probe along the z-axis with respect to the sample plane.

Figure 5.3.6 illustrates the images with varying current and a scan height of d = 1.0 μm in the air environment. Figure 5.3.6 (a) shows an AFM image of the circuit with the horizontal dashed line indicating the position of a single scan line across the circuit. This line has been scanned repeatedly in time while subsequently increasing the AC current flowing through the circuit from 0 to 0.8 mA (rms) stepwise after about 43 scan lines each. The respective AFM image given in Figure 5.3.6 (b) is for the consecutive line scans with the time evolving from the top to the bottom of the image. Two straight lines

in this image without any notable slip and shift indicate that it has been indeed always scanned the same single line and the experimental setup was quite stable during the whole image taken (~ 2.0 hours). Figure 5.3.6 (c) shows the corresponding MFM signal image taken simultaneously for the same scan line at a lift height of d = 1.0 μm. Single line MFM signal along the horizontal dashed line in Figure 5.3.6 (c) for each current is shown in Figure 5.3.6 (d). As it can be seen from Figure 5.3.6 (d) changing the current leads to a nearly linear variation of the MFM signal for each signal point.

The signal point along the vertical dotted line, which is the center between the parallel conductor lines in Figure 5.3.6 (c) as a function of the current, is shown in Figure 5.3.6 (f) with a linear relationship. The linear relation will extend to 10 mA current from our experimental results, which is consistent with the theoretical calculation in section 3.4. This suggests that the two assumptions for the theoretical calculation we made in section 3.4, in which the MFM tip magnetization stays constant when the magnetic field from the circuit current increases and the current distribution in the circuit does not change during the scanning, are acceptable. MFM signal along the vertical dotted line in Figure 5.3.6 (c) is shown in Figure 5.3.6 (e). It can be seen that the rather sharp and flat stairs' signal also indicates that the experimental setup was quite stable during MFM signal acquisition.

The same set of measurements was made in a vacuum environment, and the results were identical to those from air except in magnitude. From the excellent match between these two results we can conclude that even in a vacuum with high currents the cantilever response is still linear, which indicates that the experimental setup was quite stable for data acquisition and that the assumptions for the theoretical calculation we made in section 3.4 hold for both air and vacuum environments. Similar to Figure 5.3.6, Figure 5.3.7 shows the current change in vacuum environment.

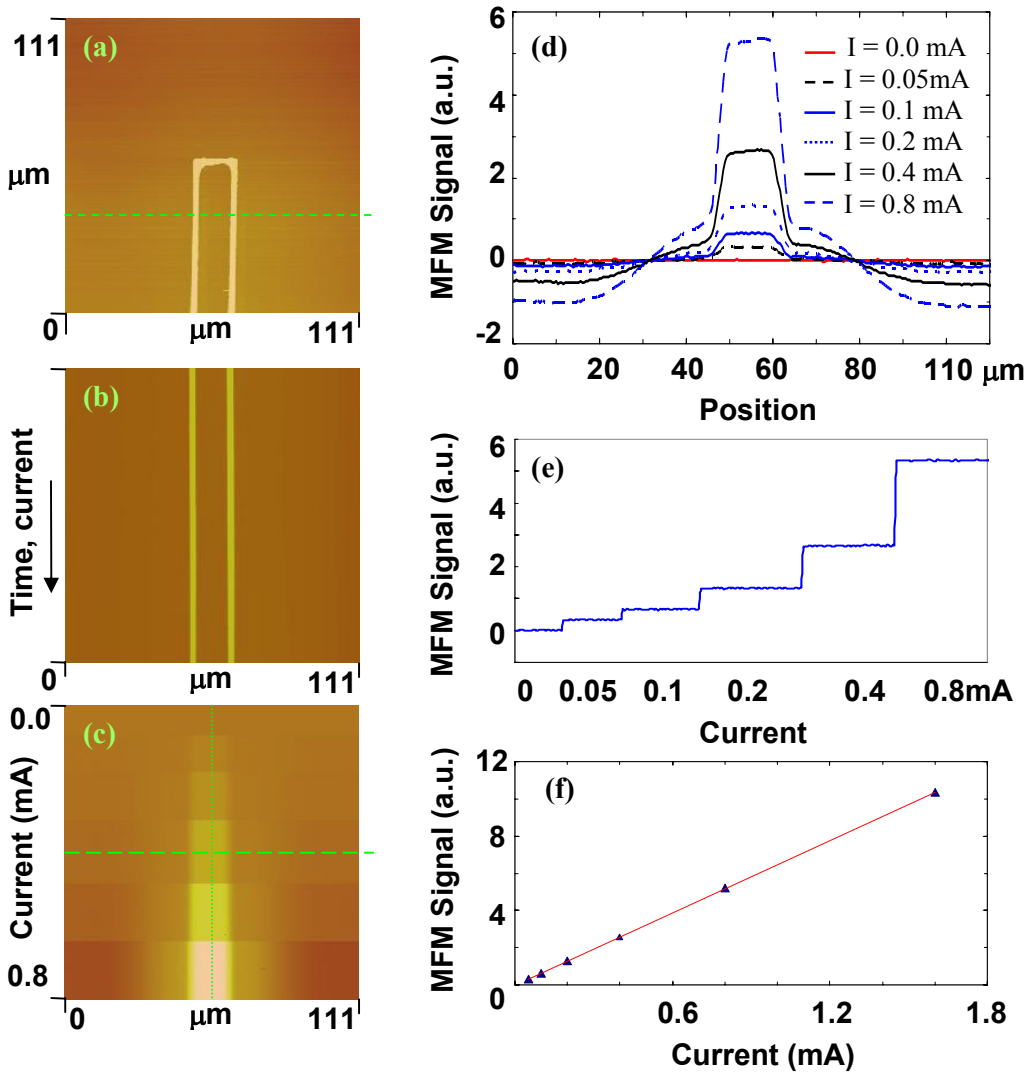

Figure 5.3.6. Image with varying current and a scan height of d = 1.0µm in the air. **(a)** AFM image of the circuit. The horizontal dashed line indicates a single scan line that has been scanned repeatedly in time with subsequently increasing AC current flowing through the circuit from 0 to 0.8 mA (rms) stepwise after about 43 scans each. **(b)** AFM image of the line scans according to (a) where the time is evolving from the top to the bottom of the picture. **(c)** Corresponding MFM image taken simultaneously for the same scan line at a tip-lift height of d = 1.0µm. **(d)** MFM signal along the horizontal dashed line in (c) for each current. **(e)** MFM signal along the vertical dotted line in (c). **(f)** MFM signal along the vertical dotted line in (c) as a function of the circuit current from which the signal varies nearly linearly with the current (one more current 1.6 mA point adds in plot).

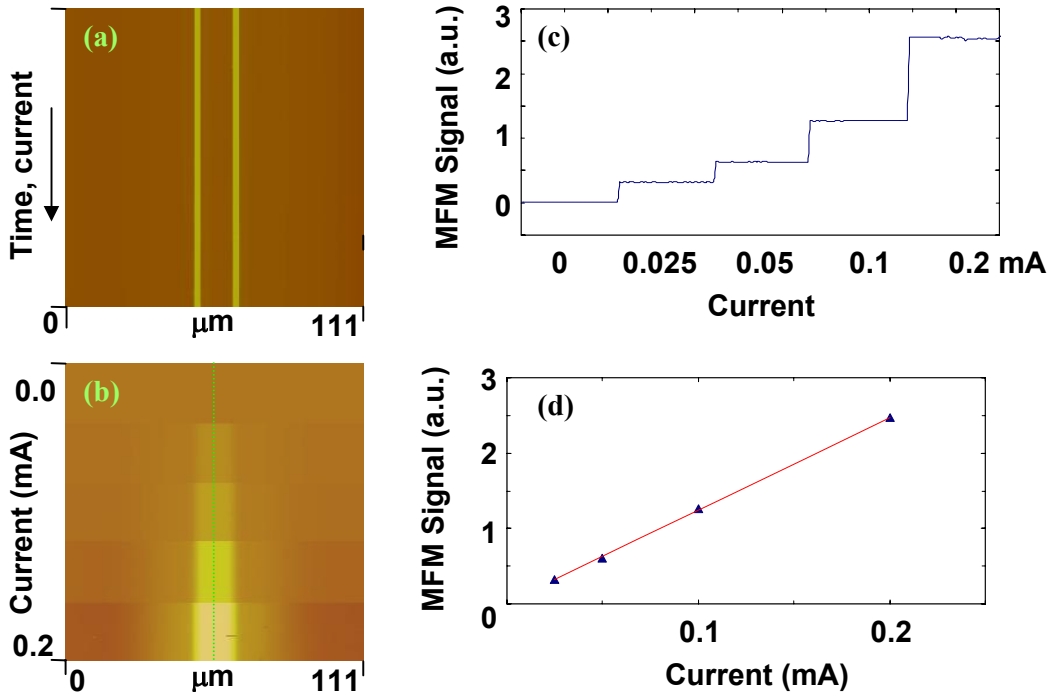

Figure 5.3.7. (a) AFM image of the line scans according to Figure 5.3.6 (a) where the time is evolving from the top to the bottom of the picture, and the current from 0 to 0.2 mA (rms). **(b)** Corresponding MFM image taken simultaneously for the same scan line at a lift height of d = 1.0μm. **(c)** MFM signal along the vertical dotted line in (b). **(d)** MFM signal along the vertical dotted line in (b) as a function of the circuit current from which the signal varies nearly linearly with the current.

As mentioned above, changing the current leads to a linear variation of the MFM signal for each signal point. In other words, the shape of the MFM signal stays the same with the changing current, as shown in Figure 5.3.8. Two MFM signals with different currents in Figure 5.3.6 (d) show a good match in the air, as well as in a vacuum environment shown in Figure 5.3.8 (a) and (b), respectively. The signals in the air and vacuum are slightly different in Figure 5.3.8 (c) due to different scanning lines and scanning areas, which are impossible to keep exactly the same in two environments. All of these results are consistent with our theoretical discussion in previous chapters. The vacuum system will only enhance a MFM signal $\sim Q_{vacuum}/Q_{air}$ times more than the atmosphere at the

resonant frequency. Because of this, in the following we will concentrate on image analysis in an air environment for the most cases except when considering sensitivity and resolution. Further more, we only need to choose one current value for our analysis if absolute values are not considered.

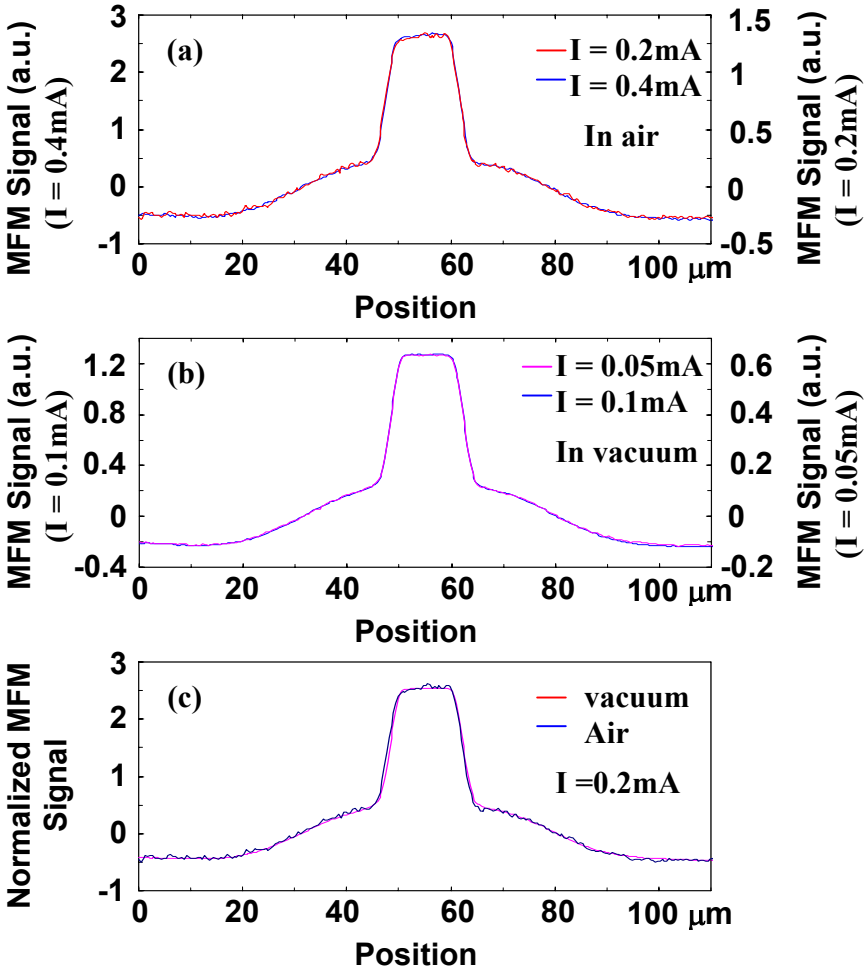

Figure 5.3.8. MFM signal comparison with different current for the same scan line. Different scales in MFM signal are for showing that the signal varies linearly with the current **(a)** in air. **(b)** in vacuum. **(c)** Comparison of results in air and vacuum.

In order to systematically understand imaging current-carrying faults on ICs, we have made the measurement and analysis for various values of the lift height d ranging from 0.2 to 2.5μm. These will be presented in the next chapter.

5.4 Magnetic Force Gradient

In section 3.6, we discussed force and force-gradient current detections. In the previous section, we presented a comprehensive study for the MFM force detection. In this section, we will focus on MFM force gradient detection.

5.4.1 Force Gradient Detection

In MFM, force gradient detection is the most commonly used technique. It is most often done in three ways: amplitude detection, phase detection, and frequency modulation. We will use the phase detection method in this research work [129].

The principle of MFM force gradient imaging can be understood through the mechanical response of the MFM probe. In the presence of a force gradient, the equation of the cantilever modeled as a simple harmonic oscillator with damping becomes [4,136]

$$\mathbf{m}\frac{\mathbf{d}^2\mathbf{z}}{\mathbf{dt}^2}+\gamma\frac{\mathbf{dz}}{\mathbf{dt}}+\mathbf{kz}=\mathbf{W}_T+\mathbf{F}_z(\mathbf{z},\mathbf{t})+\mathbf{F}_z'(\mathbf{z},\mathbf{t})\mathbf{z}\,, \tag{5.1}$$

where m is the mass of the probe, W_T is the contribution due to the weight of the cantilever at the tip plus the weight of the tip, γ is the damping factor, and k is the spring constant. The vibration is produced by the time varying force $F_z(z,t)$. The prime in the term $\mathbf{F}_z'(\mathbf{z},\mathbf{t})$ is the force gradient with respect to z. It has units of N/m which is the unit of a spring constant. For harmonic time dependence, the steady state solution of (5.1) can be obtained by using the Fourier transformation as

$$-\mathbf{m}\omega^2\mathbf{Z}(\omega)+\mathbf{j}\gamma\omega\mathbf{Z}(\omega)=\mathbf{F}_z(\omega)+\mathbf{F}_z'(\omega)\mathbf{Z}(\omega)\,, \tag{5.2}$$

where j is the complex $\sqrt{-1}$, and $\mathbf{F}_z'(\omega)$ is the Fourier transform of the force gradient. The cantilever frequency response can then be derived by [136]

$$\mathbf{G(\omega)} = \frac{\mathbf{Z(\omega)}}{\mathbf{F_z(\omega)}} = \frac{1}{[(\mathbf{k} - \mathbf{F_z'(\omega)}) - \mathbf{m\omega^2}] + \mathbf{j\omega\gamma}} = \mathbf{|G(\omega)|e^{j\theta}}, \tag{5.3}$$

where $\mathbf{|G(\omega)|}$ is the cantilever deflection amplitude normalized to the applied force amplitude and θ is the vibration phase relative to that of the force. Substituting for the damping factor $\gamma = k/Q\omega_r$ from equation (2.2.16) and $\omega_r \approx (k/m)^{1/2}$ (ω_r is the resonant frequency), we obtain

$$\mathbf{|G(\omega)|} = \frac{\mathbf{Q/k}}{\sqrt{\mathbf{Q^2}(1 - \frac{\mathbf{F_z'}}{\mathbf{k}} - \frac{\omega^2}{\omega_r^2})^2 + \frac{\omega^2}{\omega_r^2}}}, \tag{5.4}$$

and

$$\theta(\omega) = -\tan^{-1}\frac{\omega/\omega_r}{\mathbf{Q}(1 - \frac{\mathbf{F_z'}}{\mathbf{k}} - \frac{\omega^2}{\omega_r^2})}, \tag{5.5}$$

To examine the change in the relative phase due to the force gradient, differentiating θ(ω) with respect to $\mathbf{F_z'(\omega)}$ gives

$$\frac{\partial\theta}{\partial\mathbf{F_z'}} = -\frac{\mathbf{Q\omega/k\omega_r}}{\mathbf{Q^2}(1 - \frac{\mathbf{F_z'}}{\mathbf{k}} - \frac{\omega^2}{\omega_r^2}) + \frac{\omega^2}{\omega_r^2}}, \tag{5.6}$$

The maximum change in the relative phase of the cantilever response due to a force gradient can be determined by solving $\partial^2\theta(\omega)/\partial\omega\partial\mathbf{F_z'} = 0$ for ω. It gives $\omega_r' = \omega_r\sqrt{1 - \mathbf{F_z'/k}}$. At ω_r', equation (5.6) becomes

$$\frac{\partial\theta}{\partial\mathbf{F_z'}} = -\frac{\mathbf{Q}}{\mathbf{k}}\left(1 - \frac{\mathbf{F_z'}}{\mathbf{k}}\right)^{-\frac{1}{2}} \approx -\frac{\mathbf{Q}}{\mathbf{k}}\left(1 + \frac{\mathbf{F_z'}}{2\mathbf{k}}\right), \tag{5.7}$$

Therefore, for a small change in the magnitude of the force gradient, $\mathbf{F_z'(\omega)} << k$, the maximum change at ω_r' in the vibration relative phase of the cantilever is

$$\Delta\theta_{max} = \Delta\theta(\omega_r') \approx -\frac{Q}{k}\Delta F_z' \ . \tag{5.8}$$

It is clear from (5.8) that the phase shift in the tip vibration is directly proportional to the force gradient. The force gradient can be derived by differentiating the Eq. (3.4.4). In the special case where the cantilever is parallel to the sample surface, (5.8) becomes

$$\Delta\theta = -\frac{Q}{k}\sum_{tip}\left(m_x(\vec{r_i})\frac{\partial^2 B_x(\vec{r_i})}{\partial^2 z} + m_y(\vec{r_i})\frac{\partial^2 B_y(\vec{r_i})}{\partial^2 z} + m_z(\vec{r_i})\frac{\partial^2 B_z(\vec{r_i})}{\partial^2 z}\right), \tag{5.9}$$

If considering tip as a point dipole, then we find

$$\Delta\theta = -\frac{Q}{k}\left(m_x(\vec{r_i})\frac{\partial^2 B_x(\vec{r_i})}{\partial^2 z} + m_y(\vec{r_i})\frac{\partial^2 B_y(\vec{r_i})}{\partial^2 z} + m_z(\vec{r_i})\frac{\partial^2 B_z(\vec{r_i})}{\partial^2 z}\right), \tag{5.10}$$

This is the result used to interpret the results in most MFM research work [59,120,130].

5.4.2 Experimental Configuration for MFM Force Gradient Measurements

The schematic diagram of the setup for the MFM force gradient measurement is shown in Figure 5.4.1.

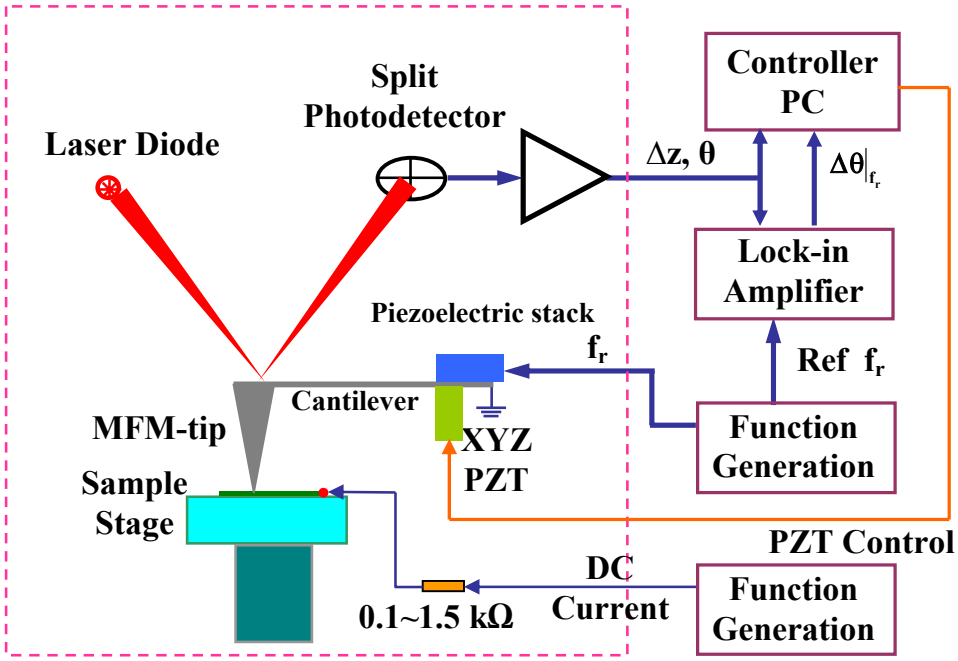

Figure 5.4.1. Schematic diagram of the setup for the MFM force gradient detection showing beam-bounce detection system used to detect topographic data (contact mode) and the MFM-image (lift mode). Dash line area may be in the vacuum environment.

The MFM measurements were taken using a Digital Instrument EnviroScope™ (E-Scope) by Veeco operated in contact/lift™ mode (not in tapping/lift™ mode), in which we used an external lock-in amplifier (SRS Model 830 or 844) to extract the MFM signal at the resonant frequency of the cantilever. A function generator stimulated the piezoelectric stack that vibrates the cantilever at resonance and is synchronized to the lock-in amplifier in order to obtain the phase shift of the cantilever response due to the MFM force gradient. DC stimulation of the IC sample was provided by the other function generator.

AFM and MFM images taken are quite similar to the force detection except the phase rather than magnitude of the MFM signal was used to form the images.

As indicated in the previous chapter, the most popular model in MFM research is to assume that the tip magnetization is predominantly oriented along the long tip axis due to the magnetization characteristics of the thin film CoCr coating. In force detection we used holding magnets to control the magnetic moments in the probe for comparison with our modeling. This proved that the model provides a good simulation of the MFM force. From the modeling, we also obtained an insight into the tip magnetization (detail discussions in next chapter). Since the cantilever holder includes the ferromagnetic materials, a strong external field will influence the piezoelectric vibrating the cantilever at resonance to carry out the force gradient measurements. For the force gradient measurements the magnetic moments of the tip were magnetically saturated along the long tip axis prior to each measurement but no magnet was used to maintain this orientation during the measurements. The orientation of the cantilever was chosen at $\alpha = 90^0$ and $\theta = 15^0$ for all force gradient measurements.

5.4.3 Force Gradient Measurements

Before presenting measurements, we would like to show a three-dimensional MFM force gradient representation in Figure 5.4.2 (b) in order to give an impression of its spatial distribution.

The MFM force gradient is considerably different than the force discussed in section 5.3. A brief comparison in Fig. 5.4.2 (c) and (d) with the dashed and dotted lines, respectively, demonstrates that the force gradient is a more localized interaction (narrower peak) and also has a much lower SNR compared to the force interaction. Also, the contribution from the cantilever is not obvious in the force gradient interaction. Thus, the force gradient detection method is expected to improve the spatial resolution of the MFM measurements, but has a far poorer measurement sensitivity.

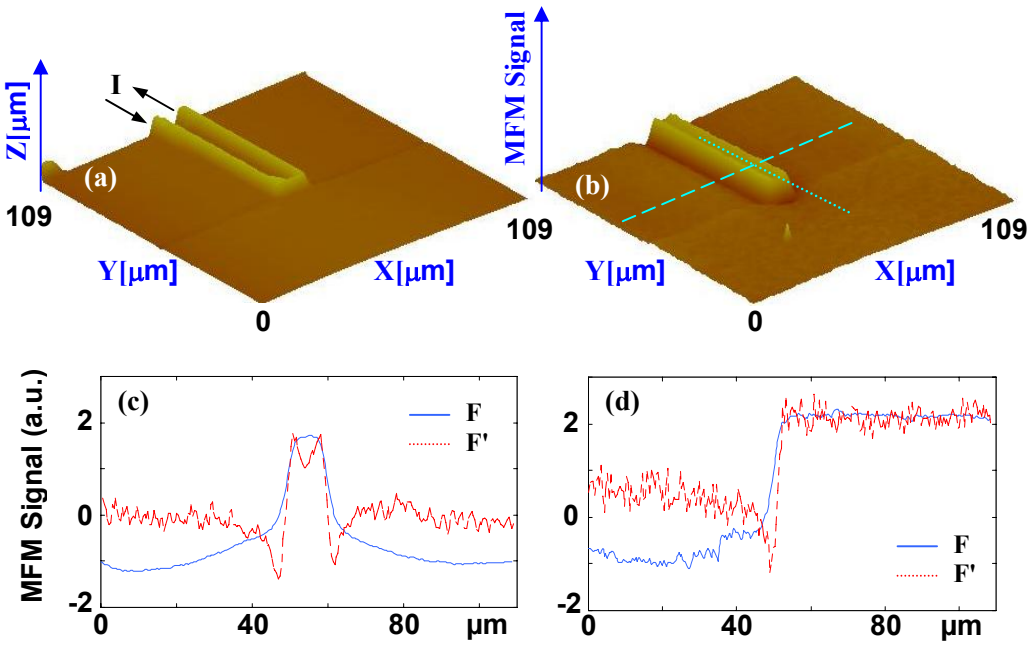

Figure 5.4.2. AFM **(a)** and MFM force gradient **(b)** images of a typical sample used in our investigation with the scan height of 1.0 µm and a dc-current of I = +20 mA in a direction as indicated in (a). MFM signals (force and Force gradient) along the dashed and dotted line as indicated in (b) are shown in **(c)** and **(d)**, respectively.

5.4.3.1 Measurement Sensitivity

Figure 5.4.3 (a) and (b) show corresponding AFM and MFM images of the sample circuit. During imaging the circuit was driven with a dc current of I ≈ 4.5 mA, the MFM image in (b) was measured at a tip lift-height of 1.0 µm, and a lock-in measurement bandwidth is about 16 Hz. As mentioned above, the tip is magnetically saturated along the long tip axis prior to each measurement using a permanent magnet such that the direction of the remanent tip magnetization is predominantly oriented into this direction. Moreover, we have measured the phase shift in the tip vibration relative to the excitation signal due to the force gradient resulting from the magnetic field of the sample current. The images are presented using dark and light regions that correspond to attractive or repulsive forces and negative or positive phase shifts, respectively.

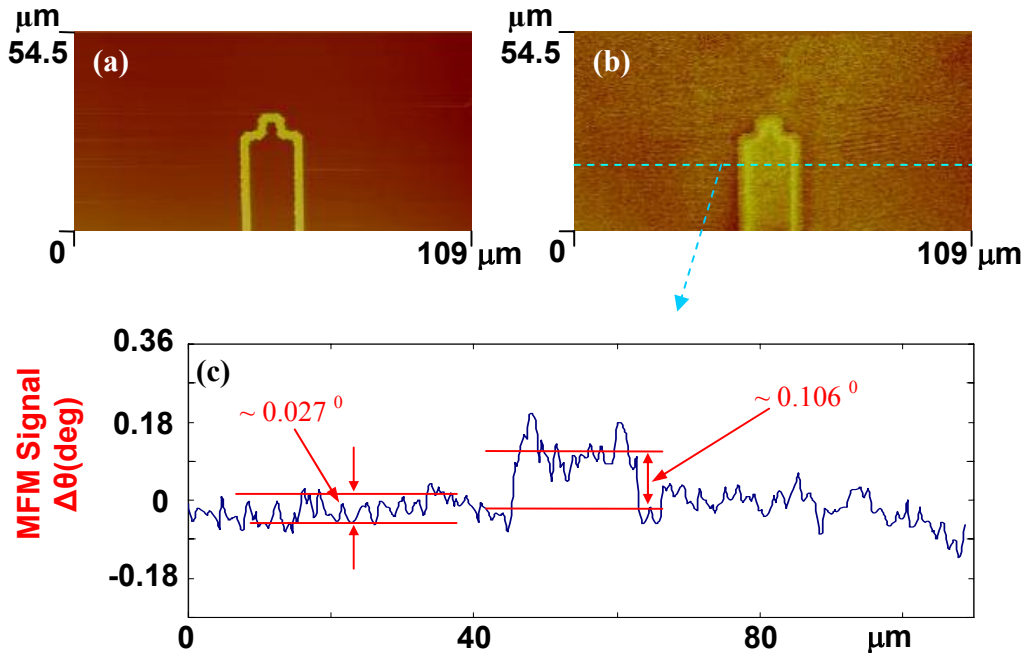

Figure 5.4.3. Corresponding AFM **(a)** and MFM force gradient **(b)** images of a metal line with a dc current I = 4.5 mA and the scan height of 1.0 µm with the bandwidth 16 Hz. **(c)** MFM signal along the dashed line in **(b)**. Noise $\Delta\theta_{rms} \approx 0.027^{0}$ and signal $\Delta\theta \approx 0.106^{0}$ are shown in **(c)**. SNR is around 3.93.

The signal and the noise are clearly observable in the MFM image of Figure 5.4.3 (c), and allow us to obtain experimentally

Noise and the minimum detectable force gradient:

$$\Delta\theta_{rms} \approx 0.027 \text{ (degree)},$$

$$\mathbf{F'_{z\,min}} = \frac{\pi}{180}\frac{\mathbf{k}}{\mathbf{Q}}\Delta\theta = \frac{3.14\times 4}{180\times 350}\times 0.027 = 5.38\times 10^{-6}\,(\text{N/m}) \qquad (5.11)$$

MFM force gradient for a current I ≈ 4.5 mA:

$$\mathbf{F_z'} = \frac{\pi}{180}\frac{\mathbf{k}}{\mathbf{Q}}\Delta\theta = \frac{3.14\times 4}{180\times 350}\times 0.106 = 21.1\times 10^{-6}\ \text{(N/m)} \qquad (5.12)$$

The signal-to-noise ratio:

$$SNR_{FG} = 3.93.$$

As in the force calculation in the previous chapter, we use the spring constant k=4.0 N/m and the quality factor Q=350 which are obtained experimentally. The additional factor of $\pi/180$ has been added on since the phase shift $\Delta\theta$ is in degrees (not radians) as measured in the experiment.

From these results, assuming a linear dependence, we deduce the MFM rms signal to noise ratio will decrease to approximately one when the current is reduced to 1.15 mA or $\frac{1.15}{\sqrt{16}}$ =0.29 mA/$\sqrt{\mathbf{Hz}}$.

Theoretically, the minimum detectable force gradient can be calculated by using Eq. (3.6.2)

$$\mathbf{F'}_{\min} = \frac{\partial \mathbf{F}}{\partial \mathbf{z}} = \left(\frac{4\mathbf{k}\mathbf{k}_\mathbf{B}\mathbf{T}\Delta\mathbf{f}}{\mathbf{Q}\omega_\mathbf{d} < \mathbf{z}_\mathbf{osc}^2 >}\right)^{1/2} = 3.82\times 10^{-6}\ \text{(N/m)}. \qquad (5.13)$$

In the calculation, we use the parameters: T = 300 K, $\Delta f \approx 16$ Hz, f_r = 74.08 kHz, k =4.0 N/m, and Q = 350. The amplitude of the driven cantilever vibration $\sqrt{< \mathbf{z}_\mathbf{osc}^2 >}$ is about 17 nm in this measurement, which was obtained by using E-Scope force mode calibration [139]. The experimental (5.11) and theoretical (5.13) results are in good agreement. In Table 5.2 we summarize the corresponding results for the force gradient measurements.

Table 5.2. Measurement sensitivity of the force gradient. Theoretical calculation of the sensitivity uses the saturate magnetization $M_s = 0.87 \times 10^6$ Am^{-1} and assumes the magnetic moments are all along the z-axis, so the experimental result are a little bit higher than the theoretical estimate.

	Experimental	Theoretical
Minimum Detectable Force Gradient	1.3×10^{-6} (N/m)/ $\sqrt{\mathbf{Hz}}$	0.96×10^{-6} (N/m)/ $\sqrt{\mathbf{Hz}}$
Sensitivity	0.29 mA/ $\sqrt{\mathbf{Hz}}$	0.21mA/ $\sqrt{\mathbf{Hz}}$

Here, we would like to point out that the measurement sensitivity is only for this special case. As mentioned in previous chapters, without the external magnetic field to saturate the tip magnetization and hold the tip's magnetic moments aligned during the measurement, the net remanent magnetization will be less than the saturated one. However, although the tip magnetization is predominantly oriented along the long tip axis, it will result in a reduced sensitivity to the current. Moreover, the sensitivity will be variable with each magnetization and each tip, but the minimum detectable force gradient will stay the same due to the thermal noise.

According to equation (5.13), the minimum detectable force gradient depends on the bandwidth ($\sqrt{\Delta \mathbf{f}}$) and the amplitude of the driven cantilever vibration ($\sqrt{< \mathbf{z}_{\mathbf{osc}}^2 >}$). It has been proven in experiments as shown in Figure 5.4.4. The MFM force gradient signal stays the same, but the RMS noise is variable with the different bandwidth ($\sim\sqrt{\Delta \mathbf{f}}$) and the amplitude of the driven cantilever vibration ($\sim\sqrt{< \mathbf{z}_{\mathbf{osc}}^2 >}$**).**

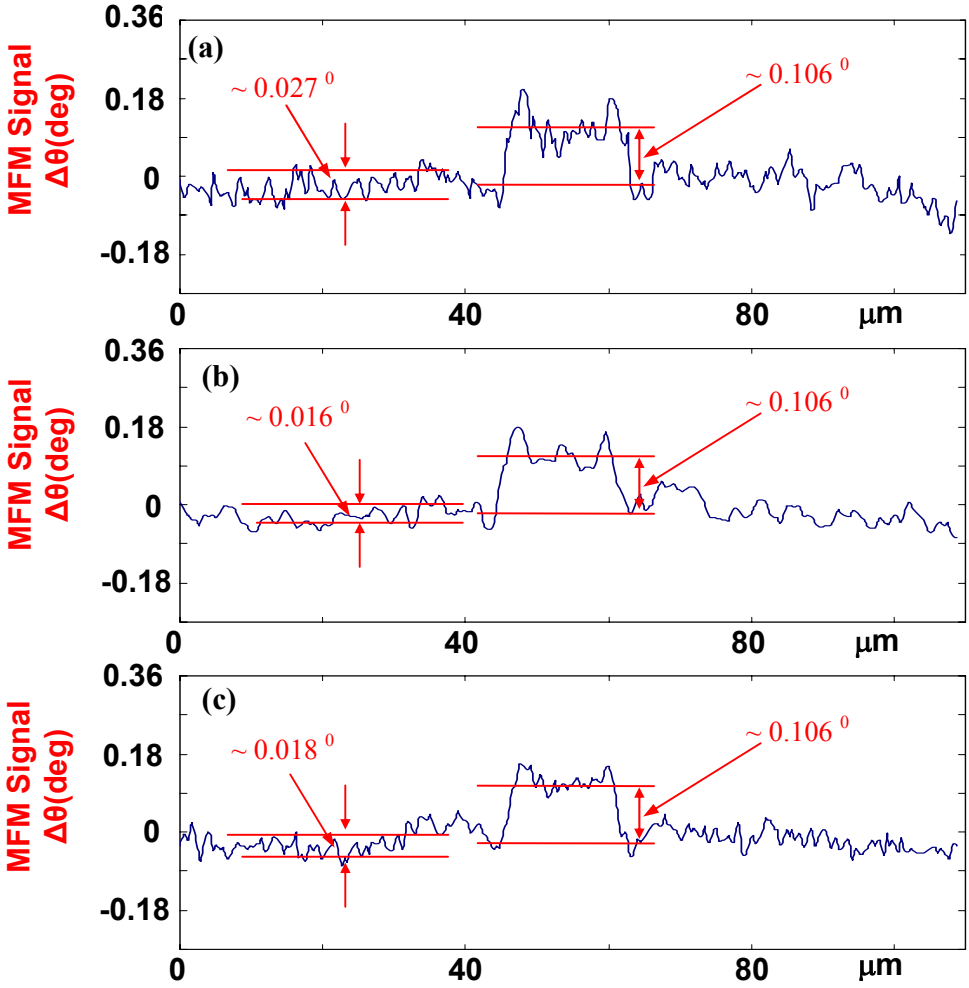

Figure 5.4.4. MFM force gradient signal along the dashed line in Figure 7.3.2 (b) with a dc current I = 4.5 mA and the scan height of 1.0 μm, **(a)** with the bandwidth ~16 Hz and the amplitude of the driven cantilever vibration ~17nm, **(b)** with the bandwidth ~5.3 Hz and the amplitude of the driven cantilever vibration ~17nm, and **(c)** with the bandwidth ~16 Hz and the amplitude of the driven cantilever vibration ~ 25 nm.

5.4.3.2 Magnetic Force Gradient Images of Model Circuits

This section presents measurements conducted by MFM force gradient detection.

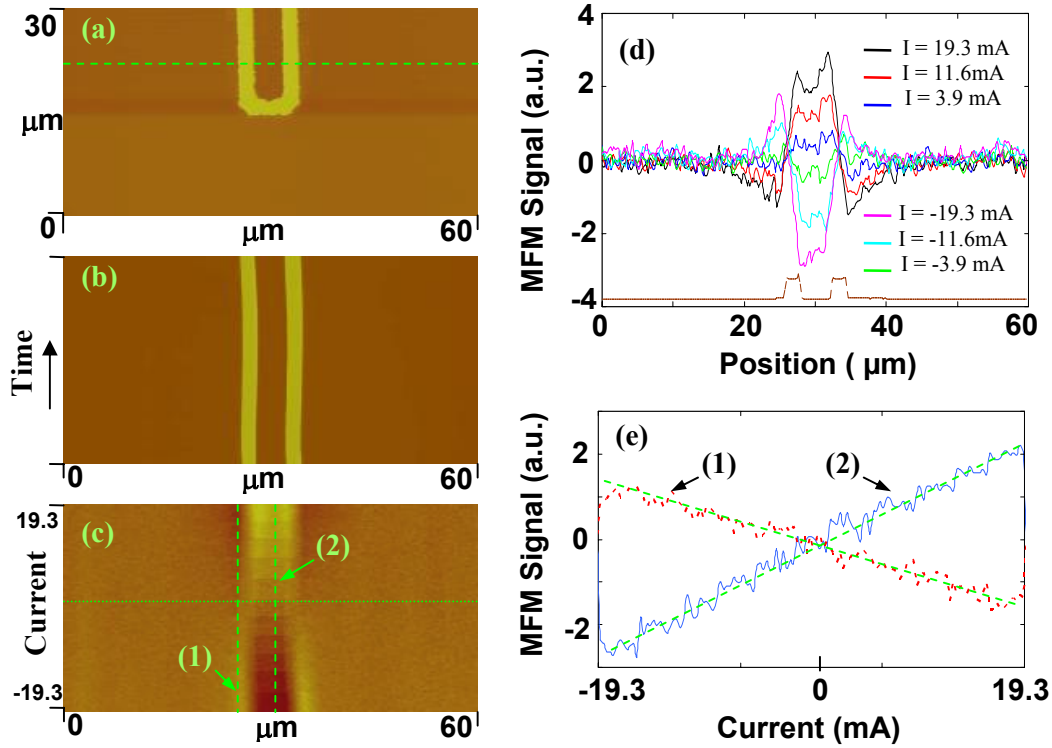

Figure 5.4.5. Image with varying current and a scan height of d = 1.0µm in the air. **(a)** AFM image of the circuit. The horizontal dashed line indicates a single scan line that has been repeatedly scanned in time with subsequently increasing the DC current flowing through the circuit from -19.3 mA to 19.3 mA stepwise after about 12 scans each. **(b)** AFM image of the line scans according to (a) where the time is evolving from the bottom to the top of the picture. **(c)** Corresponding MFM force gradient image taken simultaneously at a tip-lift height of d = 1.0µm for the same line scan. **(d)** MFM signal along the horizontal dotted line in (c) for six DC currents. Topographic cross section of the circuit is shown as a dotted line for positional reference. **(e)** MFM signal along the two vertical dashed lines in (c). Near linear signal suggests that the MFM tip magnetization stays constant.

Figure 5.4.5 shows the images with varying current and a scan height of d = 1.0 µm. Figure 5.4.5 (a) is an AFM image of the sample with the horizontal dashed line indicating the position of a single scan line, which has been repeatedly scanned in time. From bottom to top the DC current is flowing through the circuit from -19.3 mA to 19.3 mA stepwise during the same time interval. The AFM image in Figure 5.4.5 (b) is for the

consecutive line scans with the time evolving from the bottom to the top of the image shown as two straight lines with a slight slip or shift, which indicates a small degree of drift. As mentioned above, unlike force detection, the cantilever vibration is driven for force gradient detection. The cantilever drive is carried out by using an external function generator. This external stimulation may be a reason for the shift. However, this slight shift does not add significant measurement uncertainty and we will ignore it in the following discussions. Figure 5.4.5 (c) shows the corresponding MFM signal image at a lift height of 1.0 μm for the same scan line. As can be seen from Figure 5.4.5 (c) changing the current flowing from direction (negative) to the inverse direction (positive) leads to a reversal of the image contrast due to a reversal of the magnetic field direction produced by the current. Single line MFM signal along the horizontal dotted line in Figure 5.4.5 (c) for six dc currents is shown in Figure 5.4.5 (d). It is not obvious due to the low SNR. From Figure 5.4.5 (d) we can see there is an imbalance of the signal between left and right sides, similar to force detection, probably due to the tip remanent magnetization not being exactly perpendicular to the circuit's plane. The other imbalance of the signal between the positive and negative currents comes from the thickness of the sample circuits (~200nm) and electrostatic force gradient, since we found it still has the 'signal' when there is no current flowing in the circuit, which will not be analyzed further in this thesis. The signal along two vertical dashed lines in Figure 5.4.5 (c) is shown in Figure 5.4.5 (e). The near linear behavior of signal proves that it is proportional to the current and that the MFM tip magnetization stays constant in this range of currents.

Like force detection, Figure 5.4.6 (a) and (b) show two overlays of MFM signals with two positive and negative currents, respectively. The good match within the noise of the measurements suggests a linear relationship of the MFM signals for each signal point, and that the shape of the MFM signal will stay same with the varying current. Therefore, similarly to force detection, we only need choose one positive and one negative current values for our measurements. The signal with different currents can be made by a proportional factor. These will be presented in the next chapter.

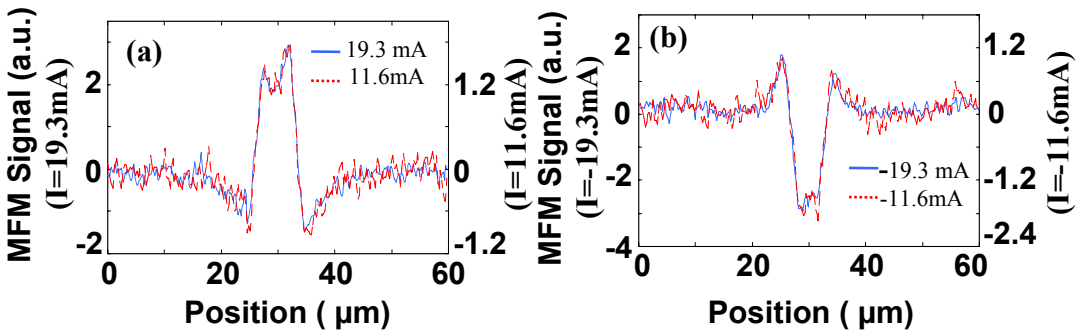

Figure 5.4.6. (a) MFM signal comparison of two different currents for the same scan line along the horizontal dotted line in Fig.5.4.5 (c), which is completely matched within the noise range. **(b)** Same as (a) with an inverse current. Different scales in MFM signal in (a) and (b) are for showing that the signal varies linearly with the current.

5.5 Signal to Noise Ratio (SNR)

In previous sections, the experimental results of the force and force gradient measurements were presented. In section 3.6, some theoretical analyses and comparisons of these two approaches have been given and discussed. In this section, the signal to noise ratio (SNR) of the force and force gradient will be discussed.

In section 3.6, we have theoretically analyzed and compared the force SNR with the force gradient SNR for one simple case. Within the point-probe approximation, we have calculated a ratio of force SNR and force-gradient SNR as a function of tip lift height z at the center of a small circular loop carrying a current, which was shown in Figure 3.6.1. The SNR for force detection is much greater than the SNR of the force gradient detection (minimum 38 times in that situation). We can conclude that force detection is able to image much smaller currents than force gradient detection. However, this comes at the price of reduced resolution. In the following, a comparison of force and force gradient sensitivity is presented for the model circuit.

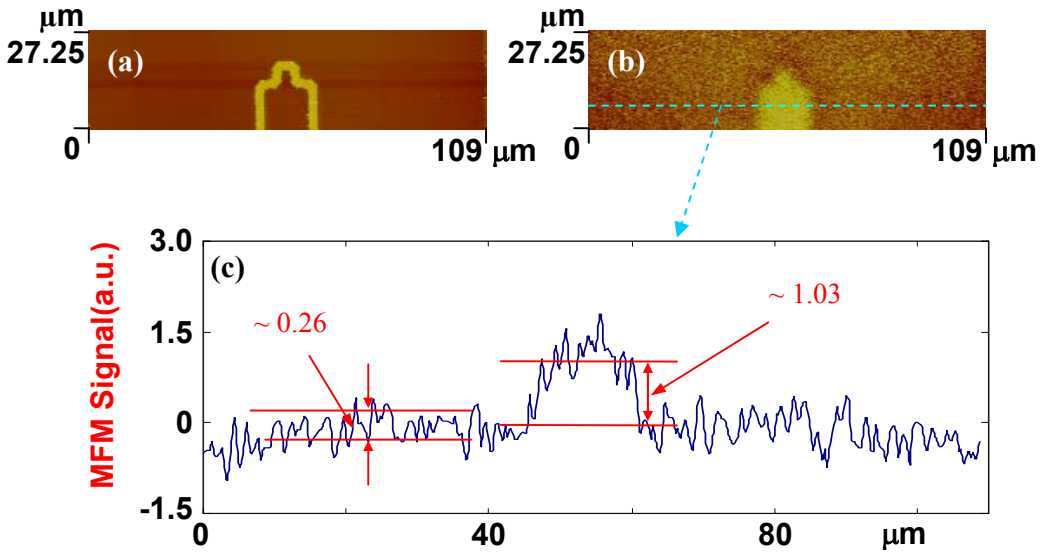

Figure 5.5.1. Corresponding AFM **(a)** and MFM force **(b)** images of a metal line with an ac current $I_{rms} \approx$ 16.2 µA and the scan height of 1.0 µm with the bandwidth 16 Hz. **(c)** MFM signal along the dashed line in **(b)**. Noise N ≈0.26 (a.u.) and signal F_s ≈1.03 (a.u.) are shown in **(c)**. SNR is around 3.96.

In previous section 5.4.3, a measurement sensitivity of the MFM force gradient about 1.15 mA or $\frac{1.15}{\sqrt{16}}$=0.29 mA/$\sqrt{\mathbf{Hz}}$ was measured for the model circuit, and was measured by magnetically saturating the tip into the long tip axis prior to the measurement. As stated before, the tip magnetization is variable with each magnetization process. In order to carry out this comparison, it is necessary to keep the same situation of the tip and experimental setting. The corresponding MFM force image shown in Figure 5.5.1 was measured at a tip lift height of 1.0 µm with an ac-current of $I_{rms} \approx$ 16.2 µA and a bandwidth of 16 Hz.

The signal and the noise are clearly observable in image of Figure 5.5.1 (b) and indicated in Figure 5.5.1 (c). Note, that since the SNR does not need absolute values of MFM signals; the calibration was not made in Figure 5.5.1 (c). The experimental result shows SNR is around 3.96 at a current of $I_{rms} \approx$ 16.2 µA. Therefore, according to the linear relationship between MFM signal and the current, we can easily deduce the MFM rms

SNR decreased to approximately one when the current was reduces to 4.09 μA or $\frac{4.09}{\sqrt{16}}$=1.02 μA/$\sqrt{\mathbf{Hz}}$, which is the measurement sensitivity of the MFM force detection for this particular case. In Table 5.3 we summarize the corresponding results for our force and force gradient measurements.

Table 5.3. Measurement sensitivity of the force and force gradient comparison.

	Force Detection	Force Gradient Detection	Force to Force Gradient Minimum Detectable Current Ratio
Sensitivity	1.02 μA/$\sqrt{\mathbf{Hz}}$	0.29 mA/$\sqrt{\mathbf{Hz}}$	284

The results indicate that force detection has dramatically smaller measurement sensitivity by a factor of as much as 284 times compared to force gradient detection. This results in the force method being more suitable for use on ICs where currents from conductors are under several layers of materials.

5.5.1 Force SNR to Force Gradient SNR Ratio

When comparing the SNR of the two detection techniques, the same RMS current should be used. From the above result, a high dc-current is needed for the force gradient measurements, typically over 10 mA for getting a good signal of over 2.0 μm tip lift height. However, these currents are too high for the force measurements because of the limited dynamic range of the instruments, therefore, different current values were used in the measurements and the results were scaled linearly since the thermal noise is not related with the current and the scan height, which results in SNR having a linear relation with the current.

Figure 5.5.2 (b) shows a schematic drawing of the sample circuit used in this investigation with the corresponding definition of lateral dimensions. We will use w_1, w_2, w_3, t, and s to define the dimensions of the sample in the following discussions. Although the dimensions of the samples were designed in the mask, the actual size will vary for

each conducting line due to the fabrication process. Within our data analysis we have always used the dimensions of the samples as measured from AFM images.

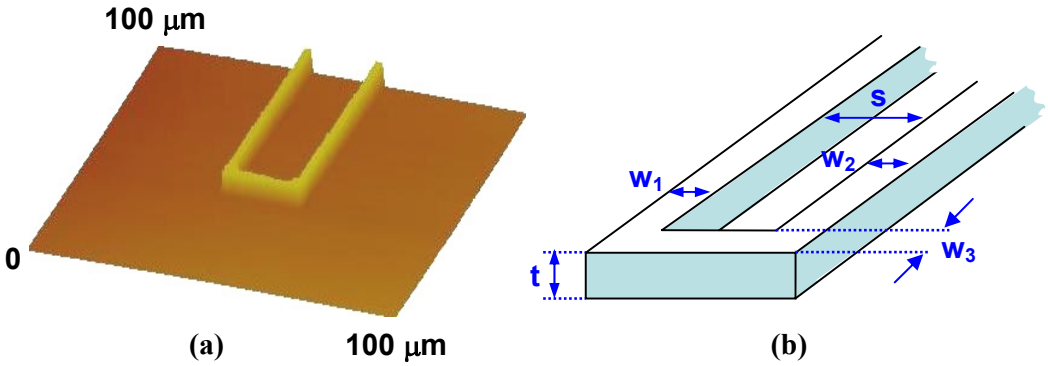

Figure 5.5.2. (a) AFM image of a typical sample used in our investigation. **(b)** Schematic drawing of the sample with the corresponding definition of lateral dimensions. Each sample has a different dimension of the width w_1, w_2, w_3, the thickness t, and separation s due to the "proximity-effect" of the fabrication process. .

Typical experimental results are shown in Figure 5.5.3 which displays the ratio of the SNR of force and SNR of force gradient as a function of the tip lift height with a current of $I_{rms} \approx 18.0$ mA driven through the circuits and ~25nm amplitude of the driven cantilever vibration for four samples with $w_1 \approx w_2 \approx w_3 \approx 2.0$ μm, t ≈ 215 nm, and four different separations of s ≈ 4.5, 8.5, 12.4, and 16.2μm, respectively (see definition of the symbols in Fig.5.5.2(b)). The signals were chosen for analysis at the middle of the two parallel wires (w_1 and w_2) and ~ 25 μm away from the end wire (w_3). As one can see, the force has a much higher SNR than the force gradient has for all samples. The larger the separation s, the larger the ratio of the SNR of force and SNR of force gradient. As a function of the tip lift height between 0.3 μm to 2.5 μm, the ratio of each sample shows moderate change, but for the sample with small separation of s = 4.5 the ratio has a slight increase with respect to the increase of the tip lift height. An inverse behavior is shown in the other separations.

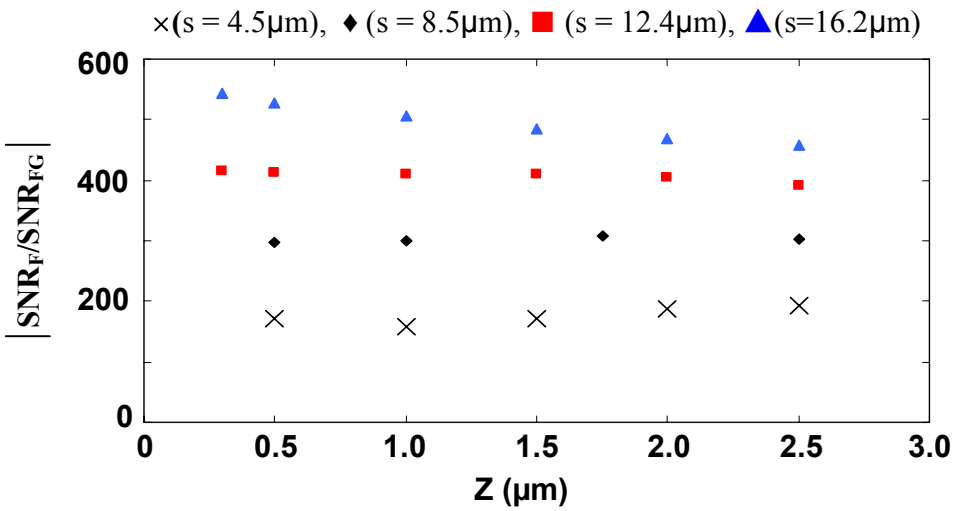

Figure 5.5.3. The experimental results of the ratio of the force SNR and force gradient SNR as a function of the tip lift height with a current of 18.0 mA rms flowing through the circuits and ~ 25 nm amplitude of the cantilever vibration for four sample size of $w_1 \approx w_2 \approx w_3 \approx$ 2.0 μm and different separations of s ≈ 4.5, 8.5, 12.4, and 16.2 μm. The compared signals were chosen at the middle of the two parallel wires (w_1 and w_2) and ~25 μm away from the end wire (w_3).

Modeling calculations are shown in Figure 5.5.4 with same dimensions of the samples. The results are in an excellent agreement with the experimental data above, both qualitatively and even quantitatively. Error is within the noise uncertainty. Therefore, this model not only provides an accurate means to simulation MFM force but also for the force gradient, which will allow one to obtain more information about MFM force and force gradient signals. In the modeling calculation, we only considered the z-component of the magnetic moments on the probe and used the spring constant k = 4.0 N/m, the quality factor Q = 327, resonance frequency f_r = 69.295 kHz, the amplitude of cantilever vibration $\sqrt{< z_{osc}^2 >}$ = 25 nm, thermal noise for force $N_f = 8.63 \times 10^{-14}$N, and thermal noise for force gradient $N_{fg} = 3.45 \times 10^{-6}$ N/m.

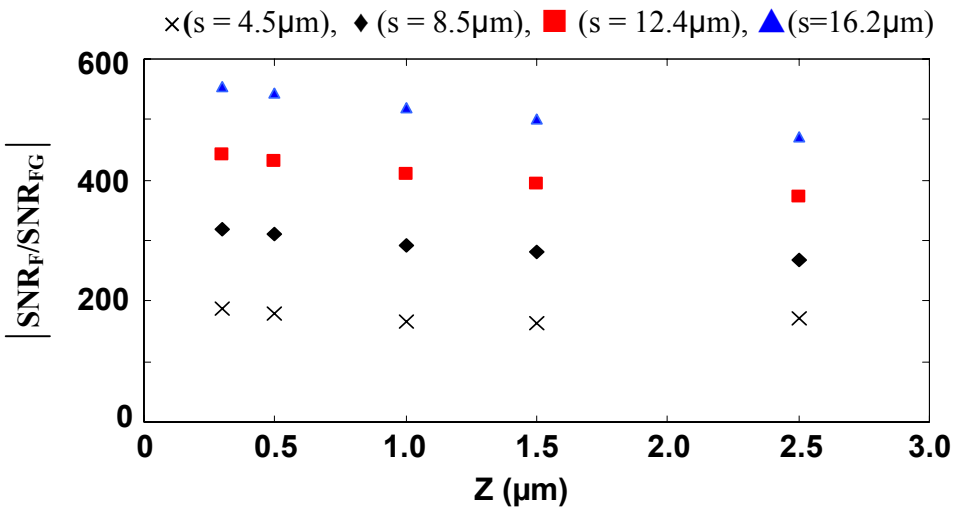

Figure 5.5.4. The modeling calculations of the ratio of the force SNR and force gradient SNR as a function of the tip lift height with a current of 18.0 mA rms flowing through the circuits and ~ 25 nm amplitude of the cantilever vibration for five sample sizes of $w_1 \approx w_2 \approx w_3 \approx 2.0$ μm and different separations of s ≈ 4.5, 8.5, 12.4, and 16.2 μm. The compared signals were chosen at the middle of the two parallel wires (w_1 and w_2) and ~25 μm away from the end wire (w_3).

Obviously, the results suggest the force method has a significant advantage over the force gradient method to use for mapping the current in ICs, where the probe is expected to be several microns away from the current carrying conductor.

Chapter 6
COMPARISON OF EXPERIMENTAL RESULTS WITH SIMULATIONS

In the previous chapter, the experimental results of the force and force gradient measurements were presented. In this chapter, a normalized and quantitative comparison of the simulation and the experiment will be presented. In addition, modified simulations are presented to correct deviations from previously presented models. In particular, the corrections are presented for varying magnetic film thickness. Cross section SEM images of FIB milled probes were taken to verify these assumptions.

6.1 Comparison of MFM Normalized Images

In the normalized comparison, only the shapes of the MFM signal are compared. In the previous chapter, the response to the current was found to be linear and hence only one current value needed to be compared. In order to systematically understand imaging current, we have made the measurements for various values of the lift height d ranging from 0.2 to 2.5μm with various dimensions of the sample circuit.

6.1.1 Magnetic Force

Table 6.1 gives geometrical dimensions of four samples used in this research (see definition of the symbols, w, t, and s, in Fig. 5.5.2) and measured from AFM images.

.

Table 6.1. Geometrical dimensions of four typical samples used in this investigation.

Sample	w_1 (μm)	w_2 (μm)	w_3 (μm)	t (μm)	s (μm)
1	2.5	2.7	2.5	~ 0.34	6.4
2	2.5	2.7	2.5	~ 0.34	11.3
3	2.6	2.8	2.4	~ 0.34	16.2
4	2.7	2.7	2.5	~ 0.34	21.3

The width of the conducting lines for these four samples is fairly constant. The separation **s** between the two parallel conducting lines is varied from 6.4 μm up to 21.3 μm. Several experimental conditions were explored.

6.1.1.1 All Magnetic Moments are Saturated along the z-axis

A permanent magnet (~0.5T) was used to apply a field to hold the magnetization of the MFM probe along the z-axis with respect to the sample plane during the MFM scanning. In this way the probe magnetization can be known. We will consider two orientations of the cantilever and the sample.

a) Cantilever tilting off surface with $\theta = 15^0$ and $\alpha = 90^0$

Measurement setup is shown in Fig.5.3.1 and the experimental arrangement of the permanent magnet, the sample, and the MFM tip is shown in Fig. 5.3.5. A three-dimensional corresponding AFM (a) and MFM force (b) images of a typical sample are shown in Figure 6.1.1.

From this MFM image, it can be seen that the rather strong magnetic fields above the rectangular sample area lead to a much stronger MFM signal (white areas), which is quite similar with our modeling calculation in Chapter 4.

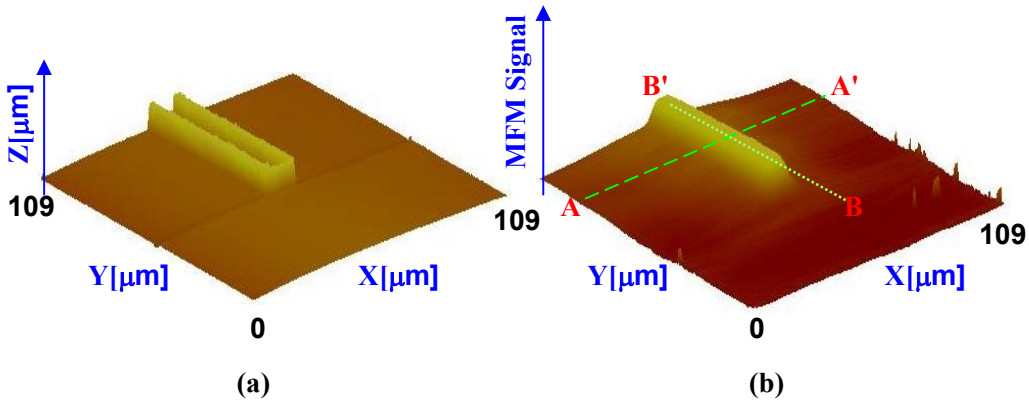

Figure 6.1.1. AFM **(a)** and MFM **(b)** images of a typical sample used in our investigation with the current I_{rms}=1.0 mA and the scan height of 1.0 μm.

Considering its geometrical symmetry, we will choose two line-scans (A-A' and B-B'), one is along the center of the rectangular sample circuits (the dotted line B-B' in Fig. 6.1.1 (b)), while the other goes across it (the dashed line A-A' in Fig. 6.1.1 (b)), for further data analysis and comparison with the modeling calculations. In order to limit influence on the MFM image contrast stemming from the w_3 segment, the A-A' cross section is measured up to approximately 50 μm away from the w_3 segment.

First of all, let us compare the results to a simple point-probe model. The results are dramatically different in shape as shown in Fig.6.1.2. The point probe model predicts a rapid change in signal near the circuit, which is not observed. The point probe model also predicts a rapid decent in the signal and approaches zero within 20 μm of the conductor, this is also not observed. This result clearly shows that the point probe model is inadequate to model the MFM signals in these experiments. Therefore, an extended model is required.

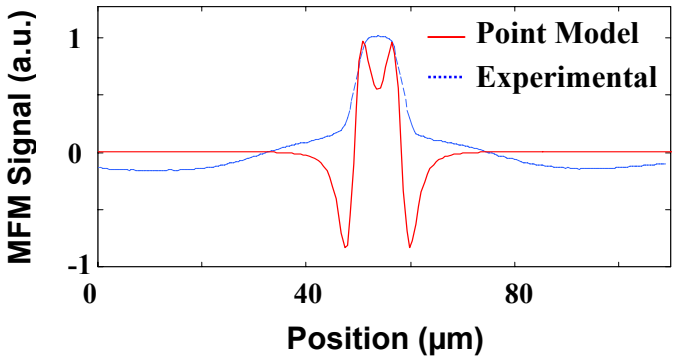

Figure 6.1.2 MFM line scan measurements and point-probe model calculations taken along the dashed line (A-A')

Figure 6.1.3 and 6.1.4 show MFM signals taken along these two lines at the different tip lift height from 0.5 μm to 2.5 μm and 0.5 μm to 1.5 μm, respectively. During imaging we chose a current of I_{rms} = 1.0 mA to drive through the sample.

In Figure 6.1.3 there is an slight imbalance between the left and right sides in the experimental results, in which the signal of the right side is slightly lower than that of the left side. This could be resulted from a slight inclination of the vertical tip magnetization with respect to the z direction, the external magnetic field slight off from the z-axis with respect to the sample plane, or the asymmetric probe. Note, that all characteristics of the normalized MFM signal, such as the shape, high and low position of the signals, and trend of the signal with different lift heights, etc. show good qualitative agreement between theory and experiment. One interesting observation seen in Figure 6.1.3 and 6.1.4 is that there are cross over points with different lift height located right above the conducting line. This will lead to a useful technique for fault location and will be discussed in next chapter.

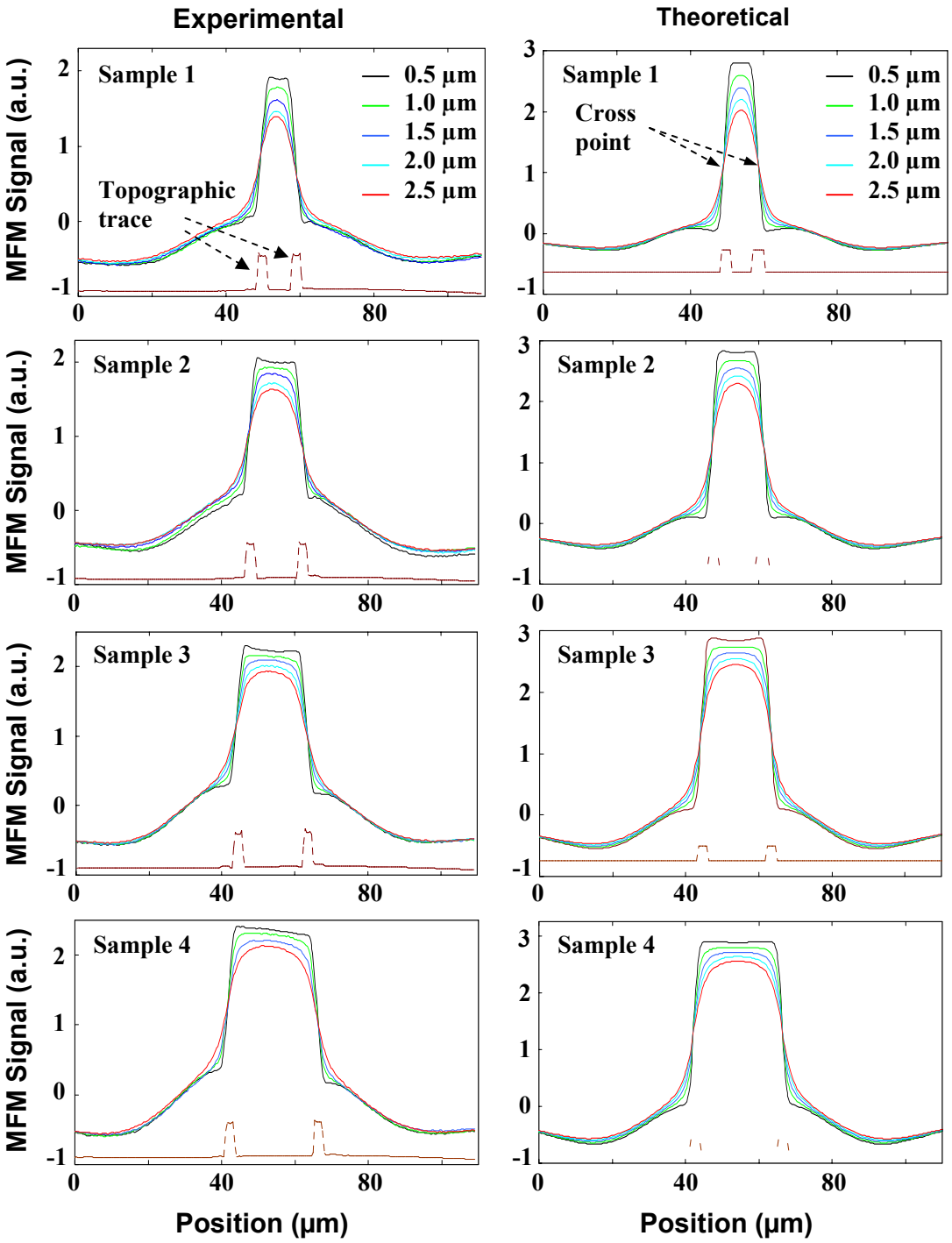

Figure 6.1.3. MFM line scan measurements and modeling calculations taken along the dashed line (A-A') in Figure 6.1.1 (b) for different sizes of the circuits with a current of I_{rms}=1.0 mA at a tip lift height from 0.5 µm to 2.5 µm. Topographic cross section of the sample is shown as a dotted line, for positional reference.

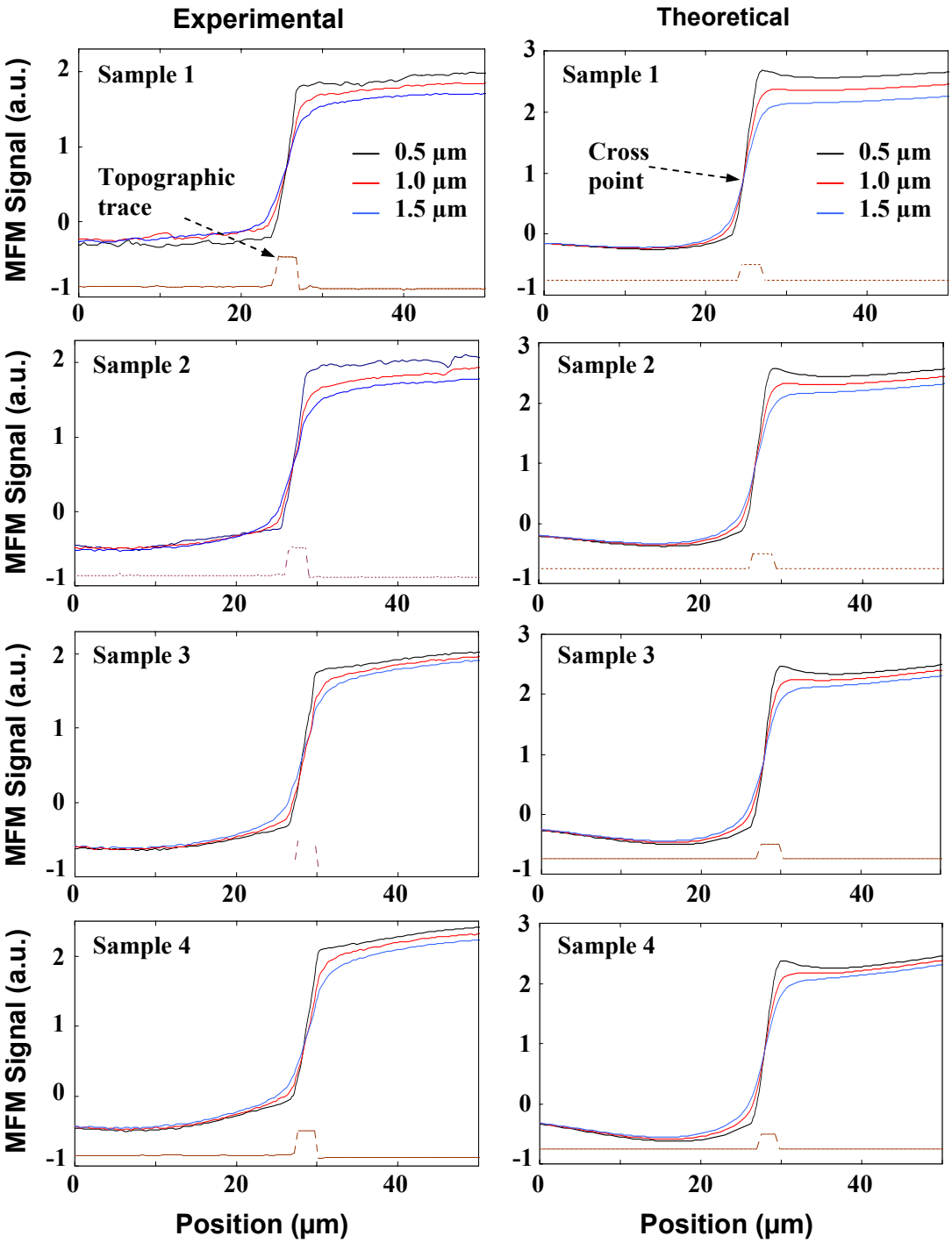

Figure 6.1.4. MFM line scan measurements and modeling calculations taken along the dotted line (B-B') in Figure 6.1.1 (b) for different sizes of the circuits with a current of I_{rms}=1.0 mA at a tip lift height from 0.5 µm to 1.5 µm. Topographic cross section of the sample is shown as a dotted line, for positional reference.

Figure 6.1.5 and 6.1.6 are the overlay of simulations and experimental results in Figure 6.1.3 and 6.1.4, respectively, which matched their maximum and minimum points of the signals and used topography traces to calibrate the position of the signal. We choose two samples, sample1 and sample3, and several tip-lift heights, 0.5 μm, 1.0 μm, 1.5 μm and 2.5 μm, for comparison. Qualitatively, the model provides a good description of MFM forces. The main features from the simulations have a good agreement with the observed behavior in the experiments. However, there are some quantitative deviations which exceed expected experimental uncertainties.

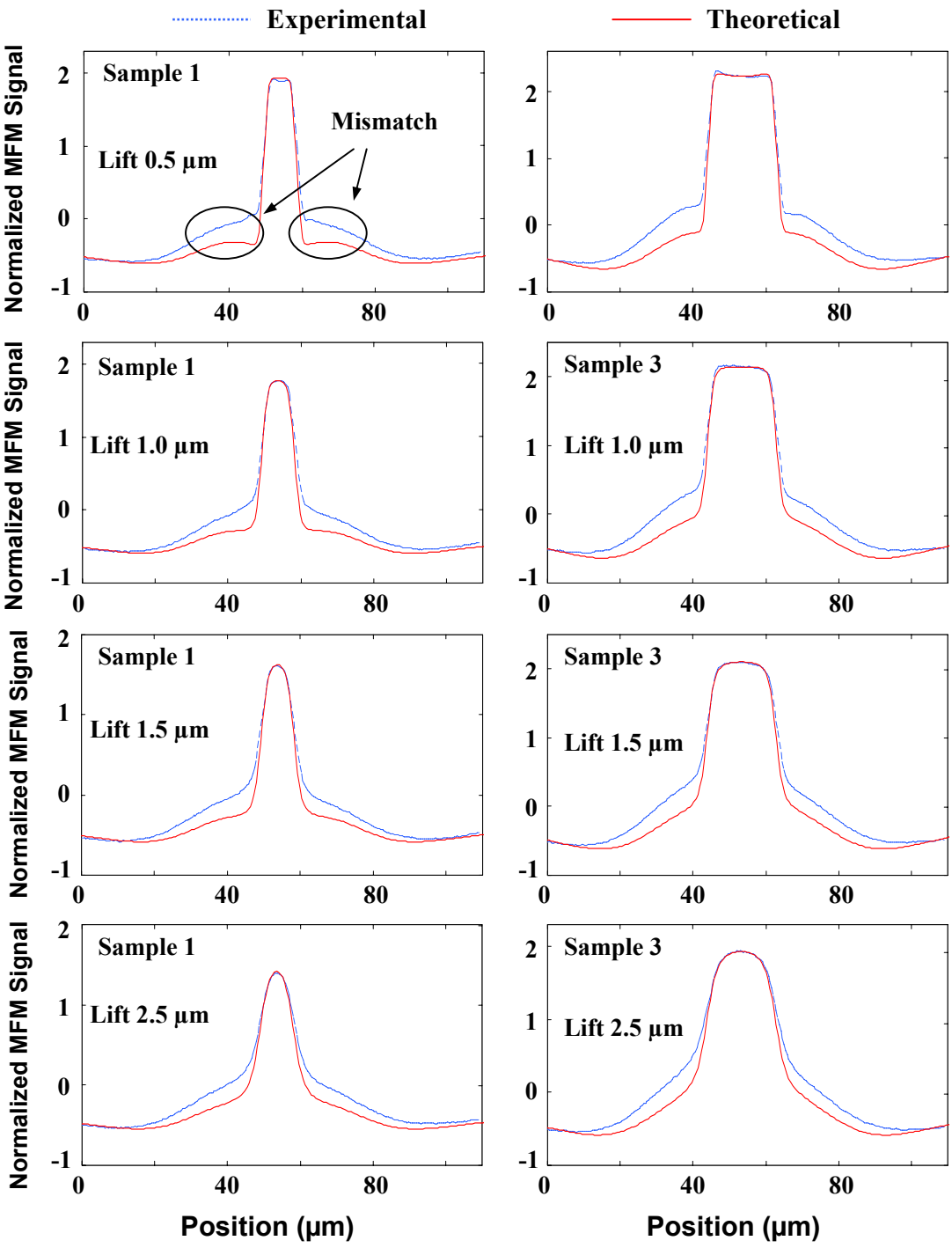

Figure 6.1.5. MFM line scan measurements and modeling calculations comparison taken along the dashed line (A-A') in Figure 6.1.1 (b) for sample1 and sample3 with a current of I_{rms}=1.0 mA at a tip lift height 0.5 µm, 1.0 µm, 1.5 µm, and 2.5 µm. Mismatch is indicated in first left plot.

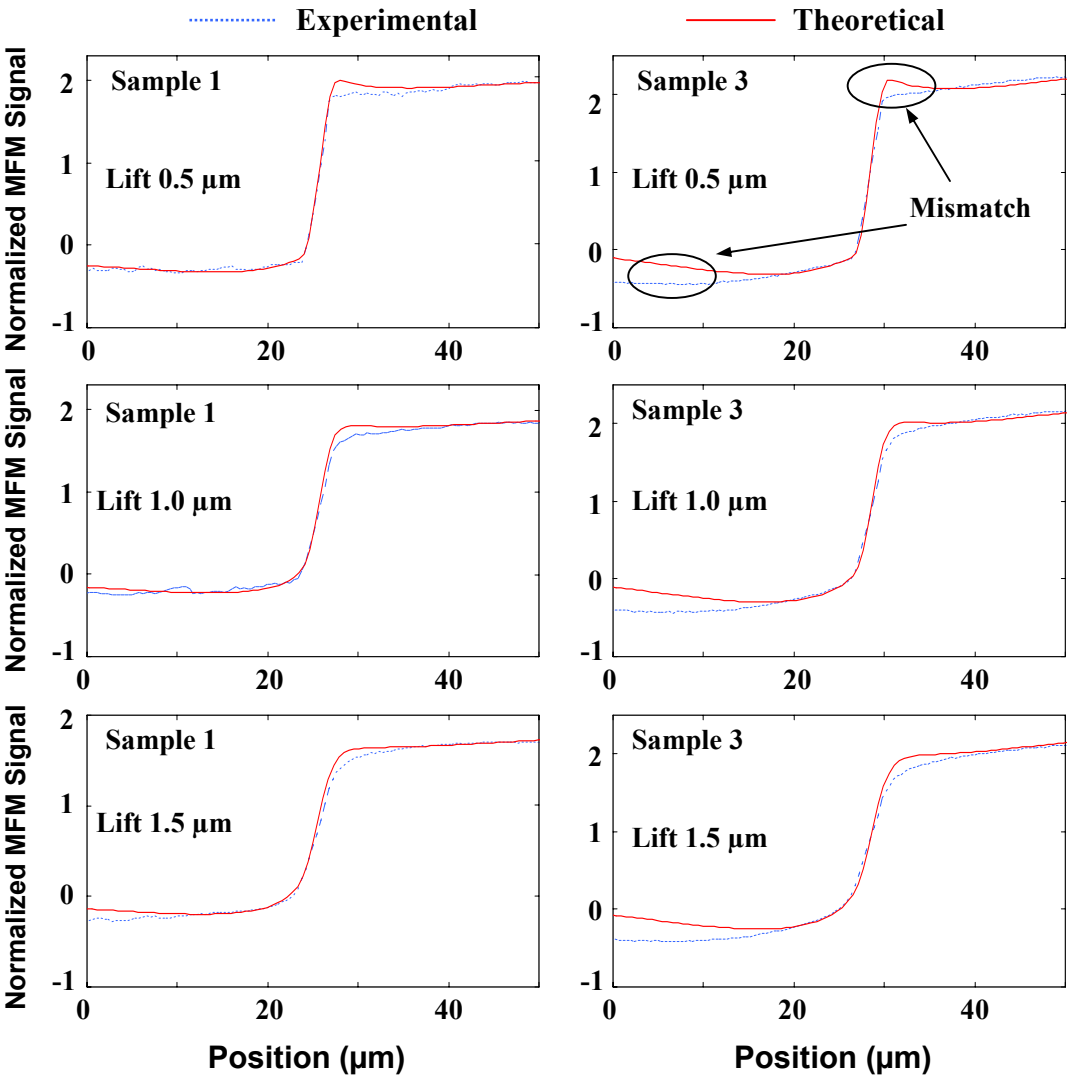

Figure 6.1.6. MFM line scan measurements and modeling calculations comparison taken along the dotted line (B-B') in Figure 6.1.1 (b) for sample1 and sample3 with a current of I_{rms}=1.0 mA at a tip lift height of 0.5 µm, 1.0 µm, and 1.5 µm. Mismatch is indicated in first right plot.

a.1) The effect of non-uniform magnetic film coating

There are obvious mismatches between the experiments and simulations in Figure 6.1.5 and 6.1.6. According to our modeling discussion in Chapter 4 (refer to Figure 4.4.11) this mismatch is mainly expected to be caused by an under estimation of the contribution from the cantilever. Thus, one possible explanation is that the magnetic coating is not uniform over the probe. This possibility has been explored using simulations that assume that the cantilever coating is thicker than the coating on the tip.

As an example, Figure 6.1.7 and 6.1.8 show the simulation results for sample 1 and 3 with different coating thickness on the cantilever and tip at the tip-lift height of 0.5μm and 1.0 μm. Others will have the same features but will not be presented here. We choose 1.0, 1.1, and 1.5 times thicker thickness of coating on the cantilever than that on the tip. In the comparisons, we normalize to the highest and lowest points of the plot at the right side of Figure 6.1.7 and 6.1.8 to better illustrate the change. When comparing these matched plots with Figure 6.1.5 and 6.1.6, the mismatch can be almost entirely eliminated by adjusting the thickness of the coating. A more detailed comparison shows in Figure 6.1.9 and 6.1.10, in which the simulated results with 1.5 times thicker coating on the cantilever ones are now very close to the observed ones. With this correction the maximum deviation is less than 10% of the normalized signal.

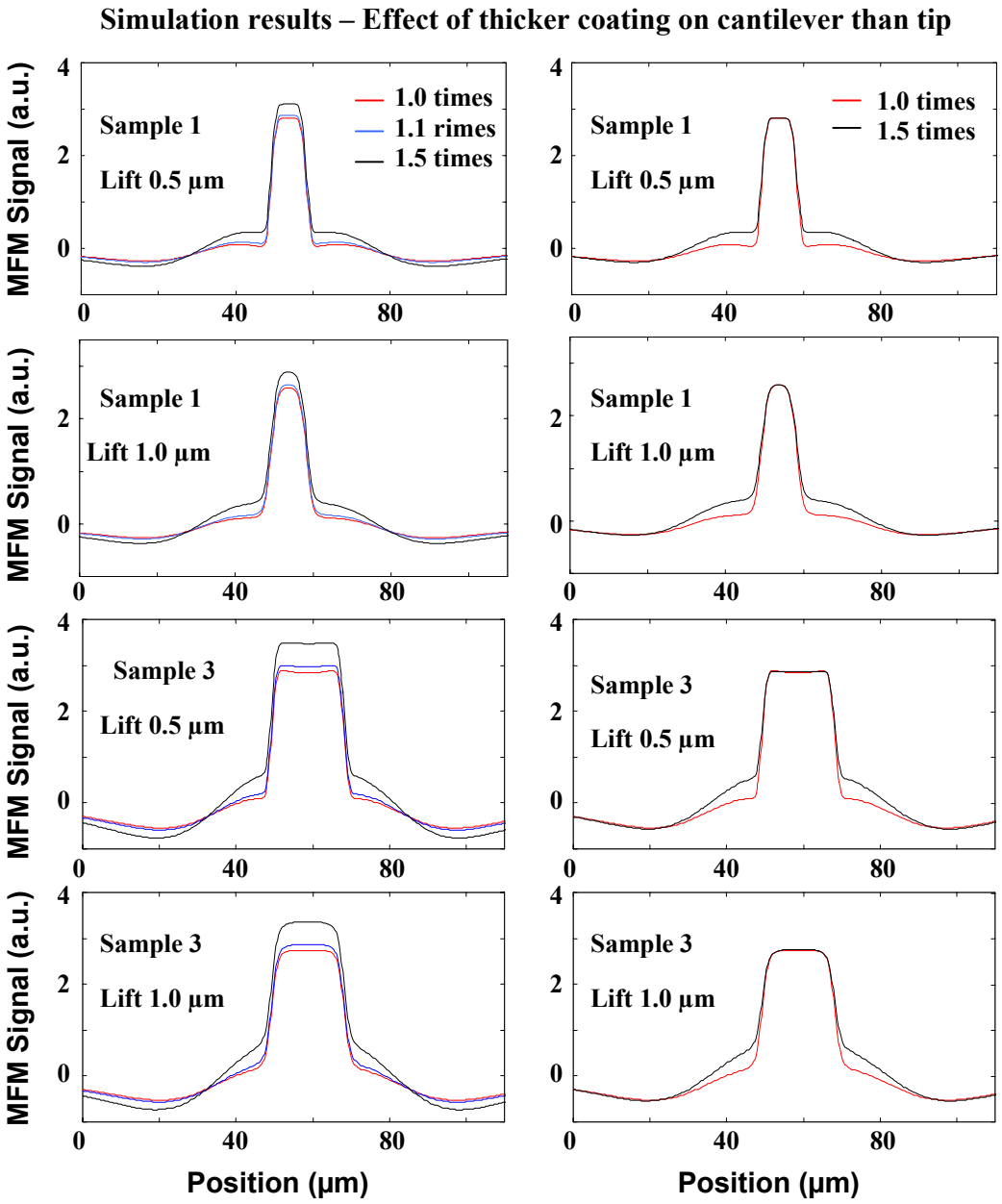

Figure 6.1.7. The simulation results taken along the dashed line (A-A') in Figure 6.1.1 (b) for the sample 1 and 3 with different coating thickness on the cantilever and tip at the lift height of 0.5µm and 1.0µm. The red, green, and black lines show MFM signal for 1.0, 1.1, and 1.5 times thicker coating on the cantilever than that on the tip, respectively. Left side plots show relative MFM signal change depending on the different coating, corresponding matching the highest and lowest points of the plots show in the right side for better illustration of the change.

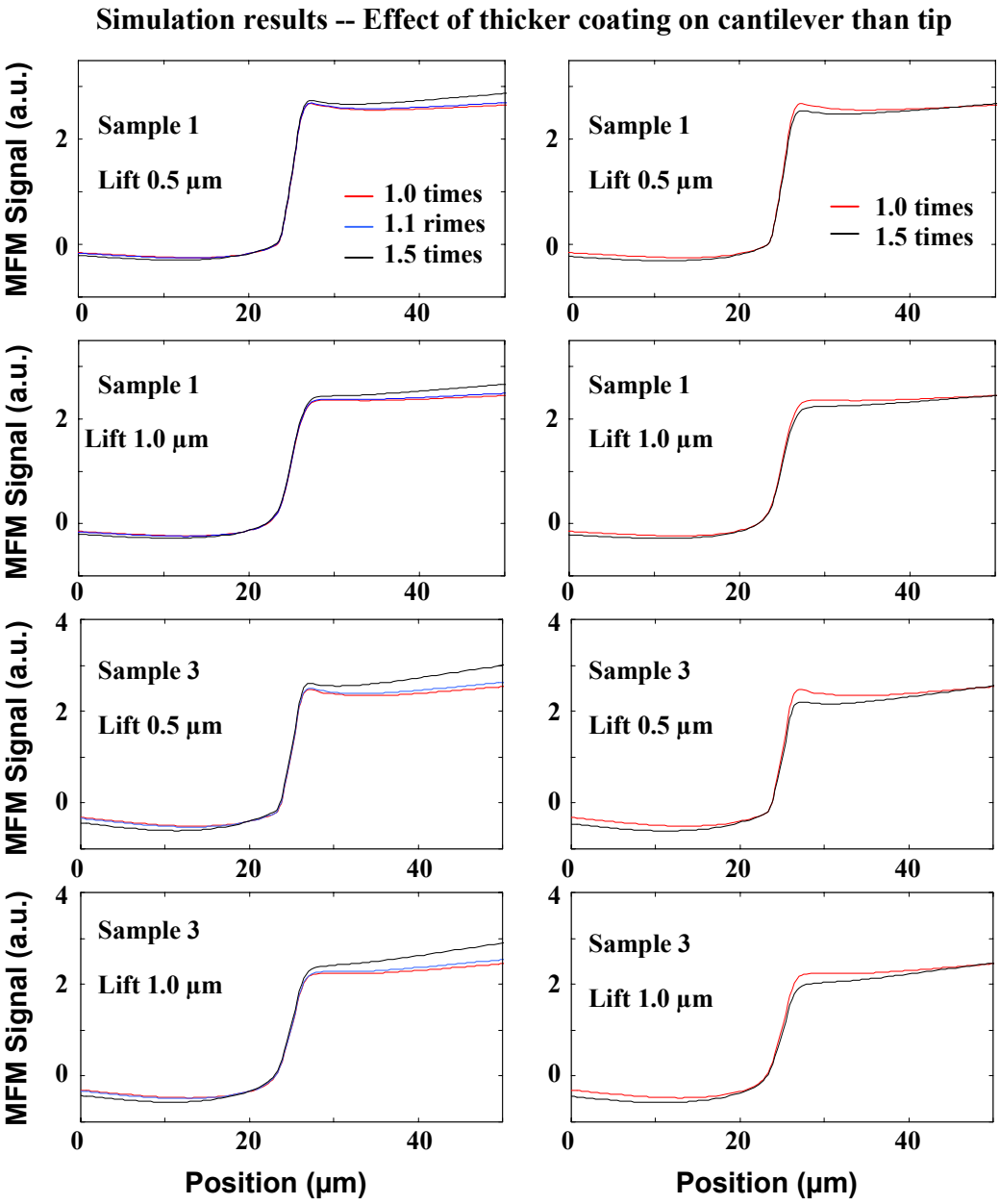

Figure 6.1.8. The simulation results taken along the dotted line (B-B') in Figure 6.1.1 (b) for the sample 1 and 3 with different coating thickness on the cantilever and tip at the lift height of 0.5µm and 1.0µm. The red, green, and black lines show MFM signal for 1.0, 1.1, and 1.5 times thicker coating on the cantilever than that on the tip, respectively. Left side plots show relative MFM signal change depending on the different coating, corresponding matching the highest and lowest points of the plots show in the right side for a better illustration of the change.

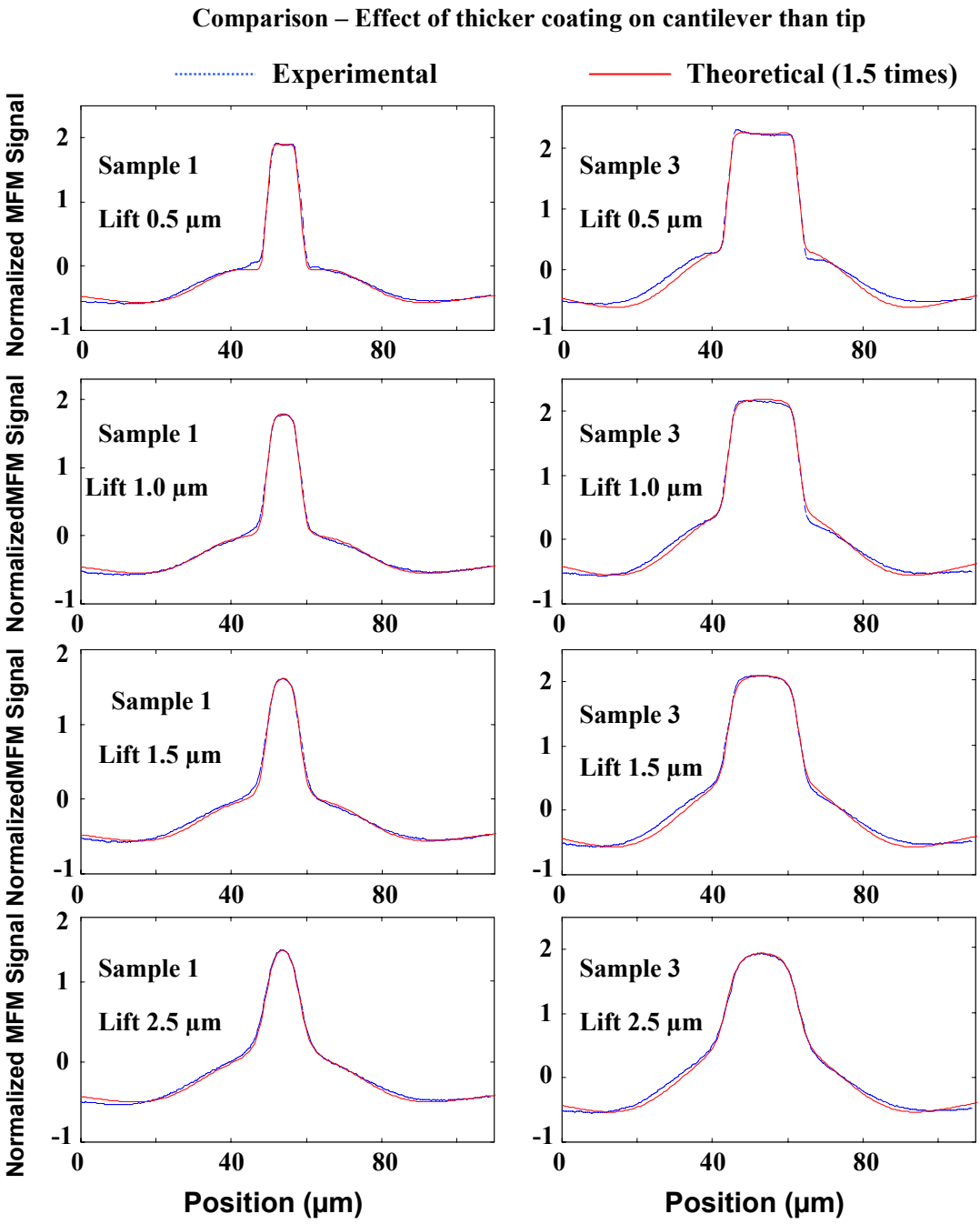

Figure 6.1.9. The simulation results with 1.5 times thicker coating on the cantilever than that on the tip overlay comparison with the experiment.

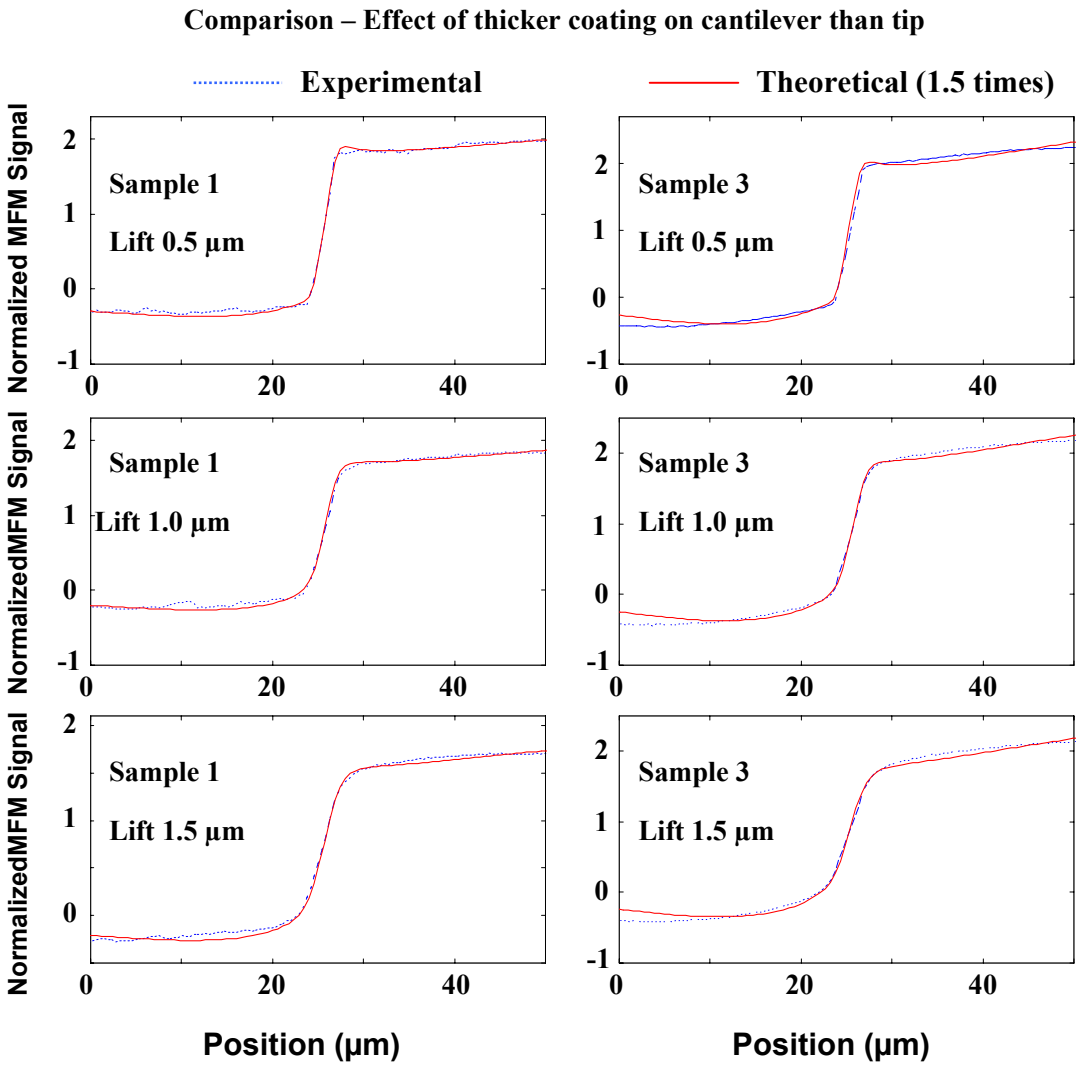

Figure 6.1.10. The simulation results with 1.5 times thicker coating on the cantilever than that on the tip overlay comparison with the experiment.

a.2) Cross section of MFM probes

Several techniques were explored to verify the variation of magnetic film thickness. In the end only the focused ion beam (FIB) proved to be adequate. A FIB was used to cross section the cantilever probe. Then SEM cross sectional images of the probe were used to measure the thickness of the Cobalt coating.

The Focused Ion Beam (FIB) system generates a finely focused beam of gallium ions in a high-vacuum environment, which can be used to ion mill to microscopic features on the samples. Material can be removed and cut from a sample by the ablative (sputtering) effect of the ion beam while the ion beam is being scanned. In this experiment, FIB was used to cut the cantilever probe in order to image its cross sections which would expect directly to show the different thickness of the materials made of the cantilever. Figure 6.1.11 (a) and (b) respectively show a probe before and after it was cut, (c) is for other cut. Since we expect to know the thickness of the Cobalt coating on the whole surface of the probe, the different areas of the cantilever probe are chosen to cut. A and B in Fig. 6.1.11 are used to represent the different cutting areas.

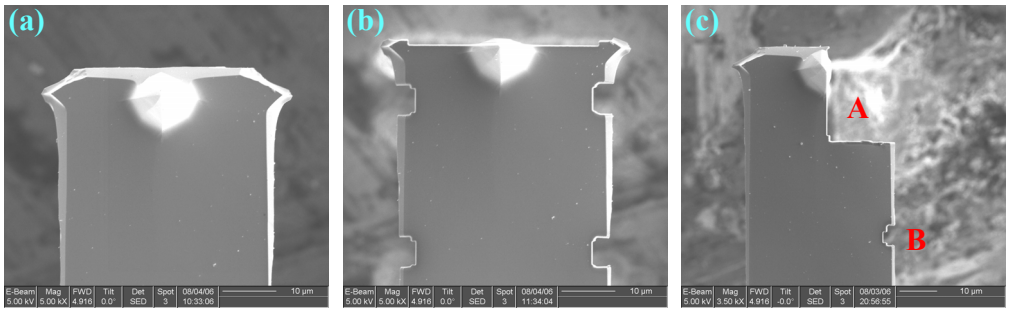

Figure 6.1.11. SEM image of a MFM tip cut by FIB. **(a)** before cut. **(b)** and **(c)** after cut. The different areas of the cantilever probe chosen to cut are for comparing the thickness of the Cobalt. A and B in (c) are used to represent the different cutting areas.

Figure 6.1.12 shows a cross section image of the cutting area B in Fig. 6.1.11. CoCr and Silicon with different contrast are easily identified in the image, but Chromium could not be separated from Cobalt in the SEM image, likely due to their similar atomic mass. Note that the bright contrast surrounding the cantilever surface is the surface effect from the electron reflection from the back of image plane. Obviously, CoCr coating in the two sides of the cantilever shows a different thickness in this cantilever. Fig. 6.1.13 shows images for the area A in Figure 6.1.11. CoCr coating has a thinner thickness on the surface of the tip than the cantilever. Especially, Fig. 6.1.13 (b) clearly shows a gradually changing thickness of the CoCr coating from the tip end near the cantilever (top of the image, ~100 nm thickness) to the middle of the tip (~30 nm thickness).

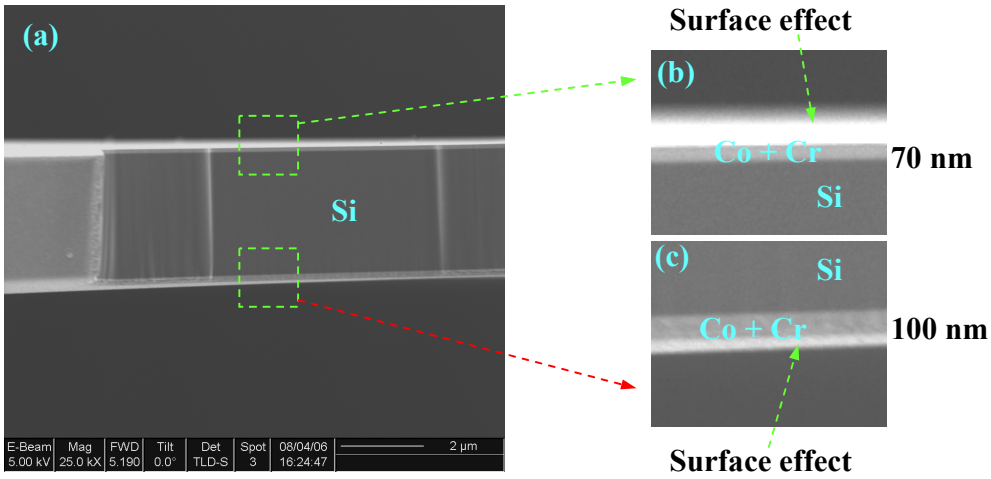

Figure 6.1.12. SEM cross section images of a MFM tip in cutting area B in Fig.6.1.11 (c). Cobalt and Chromium materials show different contrast with Silicon material in the image. Cobalt and Chromium have little contrast due to their similar atomic mass. (b) and (c) have a same magnification. Obviously, CoCr coating in the two sides of the cantilever shows a different thickness.

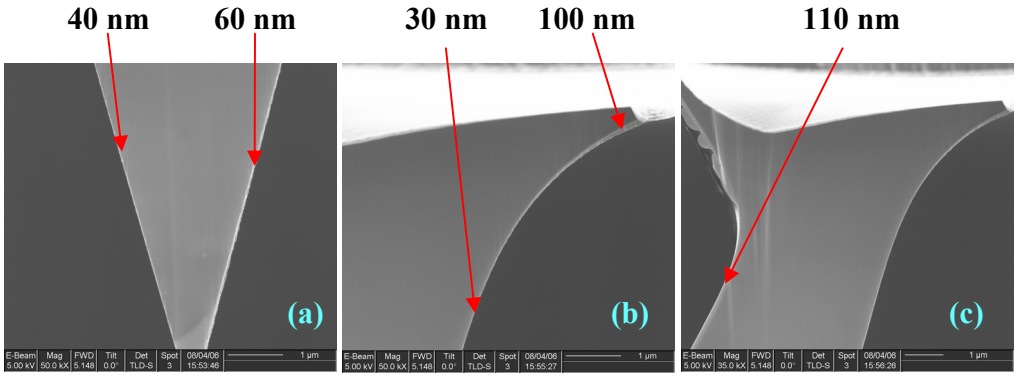

Figure 6.1.13. SEM cross section image of a MFM tip in cutting area A in Fig.6.1.11 (c). CoCr coating shows a thinner thickness on the surface of the tip than cantilever. Especially, image (b) clearly shows the thickness of CoCr coating gradually becoming thinner from the top (near the cantilever) to the bottom of the image (near middle of the tip).

Nine nominally identical tips were taken from two packs to be cut. Results show that the thicknesses of CoCr coating for all tips are not the same nor uniform. The thickness of the CoCr coating on the cantilever varies from 60 nm to 130nm, and the thickness on the tip is from 30 nm to 110 nm. It is apparent that there are thicker CoCr coating on the cantilever than that on the tip as predicted. However, we notice that there is no pattern to the thickness of CoCr coating on the probe, and its thickness differs on all regions of the probe. This result may also explain why Carl's results [60] for hystersis loop of the tips show a lack of reproducibility of the magnetic properties of MFM tips taken from different batches. Although the coating is not uniform as was assumed in the simulations, the excellent agreement between simulations and experiments are probably due to the averaging effects of the magnetic coupling.

b) Cantilever tilting off surface with $\theta = 15^0$ and $\alpha = 135^0$

For the most symmetrical case (section **a**), the model provides a satisfied simulation result of MFM forces. Whether or not the simulations are still suitable in any orientation of the cantilever with the sample will be examined in this section. Measurement apparatus setup and experimental arrangement are kept the same as in section a) except orientation of the cantilever. Figure 6.1.14 shows corresponding AFM (a) and MFM (b) images of sample 2 with the current of 1.0 mA and the scan height of 1.0 μm. The coordinate system and the cantilever orientation are indicated in Figure 6.1.14 (a). Similarly, we will choose two line-scan signals for our data analysis which are indicated as the dashed (A-A') and dotted (B-B') lines in Figure 6.1.14 (b). Since the main features for different sizes of the circuits are quite similar, here we will choose sample 2 as a representative.

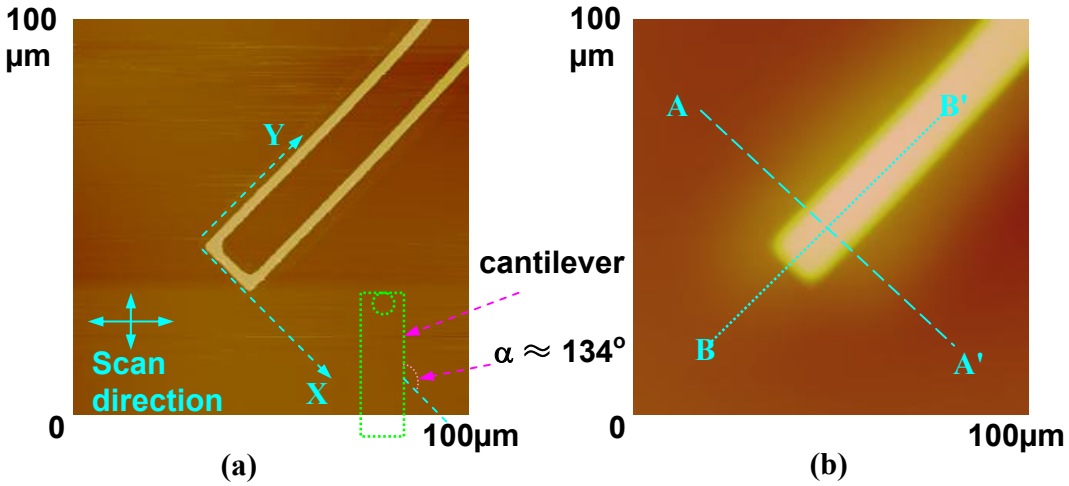

Figure 6.1.14. AFM **(a)** and MFM **(b)** images of the sample 2 used in our investigation with the current I_{rms}=1.0 mA and the scan height of 1.0 μm. Orientation of the cantilever and sample as well as the coordinate system is indicated in **(a)**. The dashed (A-A') and dotted (B-B') lines in **(b)** show MFM line-scan signals chosen for analysis.

Figure 6.1.15 and 6.1.16 show the dashed (A-A') and dotted (B-B') line-scans in Figure 6.1.14 (b), respectively, for two different scan height of 0.5 μm and 1.0 μm. The effect of the tip is almost the same as the case of α = 90, but the contribution of the cantilever results in the left side of MFM signal being higher than right side. It is like what was discussed in Chapter 4 (refer to see Figure 4.4.14).

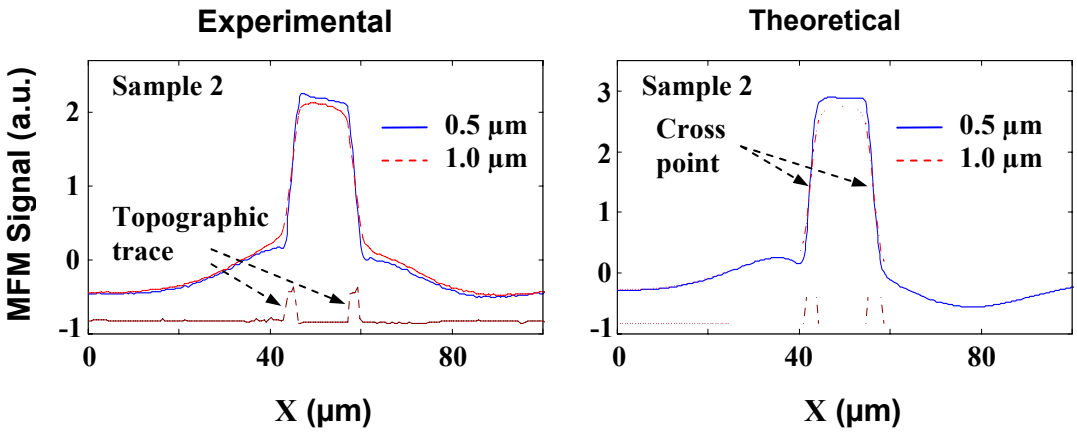

Figure 6.1.15. MFM line scan measurements and modeling calculations taken along the dashed line in Figure 6.1.14 (b) for sample 2 with a current of I_{rms}=1.0 mA at a tip lift height of 0.5 µm and 1.0 µm. Topographic cross section of the sample is shown as a dotted line, for positional reference.

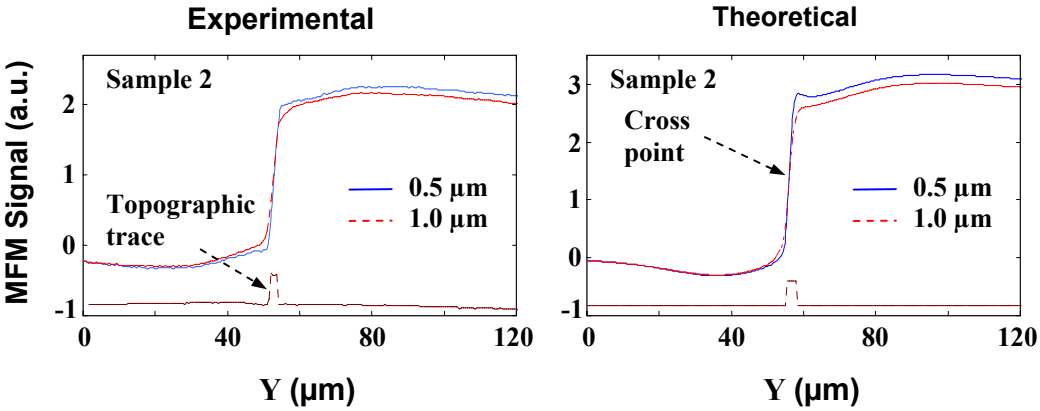

Figure 6.1.16. MFM line scan measurements and modeling calculations taken along the dotted line in Figure 6.1.14 (b) for sample 2 with a current of I_{rms}=1.0 mA at a tip lift height of 0.5 µm and 1.0 µm. Topographic cross section of the sample is shown as a dotted line, for positional reference.

The simulations and experimental results are overlaid in Figure 6.1.17. We still use a 1.5 times thicker coating on the cantilever for our simulation calculation although a different cantilever was used in this investigation. The simulations are very close to the observed results although there are some deviations greater than experimental uncertainty.

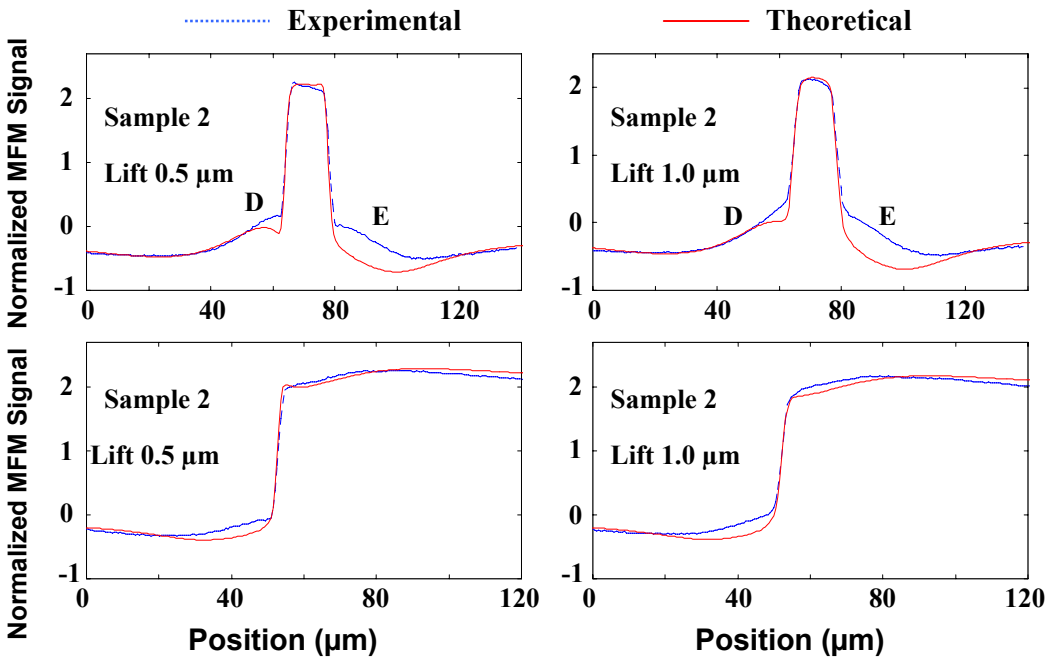

Figure 6.1.17. The simulation results with 1.5 times thicker coating on the cantilever than that on the tip overlay comparison with the experiment.

The small mismatch on the right side of the top two plots in Figure 6.1.17 may come from several sources: First, when the cantilever is scanning, it will be influenced by other parts of the sample due to the orientation ($\alpha = 134^0$), which is shown in Figure 6.1.18. When the tip is scanning the left side of the sample 2, for example at point D (also shown in Figure 6.1.17), the tip and the cantilever (area of the SEM image (a)) only interacts with sample 2. In this situation, the influence from the sample 3 can be neglected because its influence is not comparable with sample 2. When the scan is on the right side of the sample 2, which is at the point E as an example, very little of the cantilever is above the sample 2 except of a small corner area of the tip end. In other words, the cantilever, except for a small corner area, is in the weak magnetic field gradient induced by the sample 2. Obviously, the influence of the sample 3 at E exhibits a more important effect than that at D since it is much closer to the cantilever.

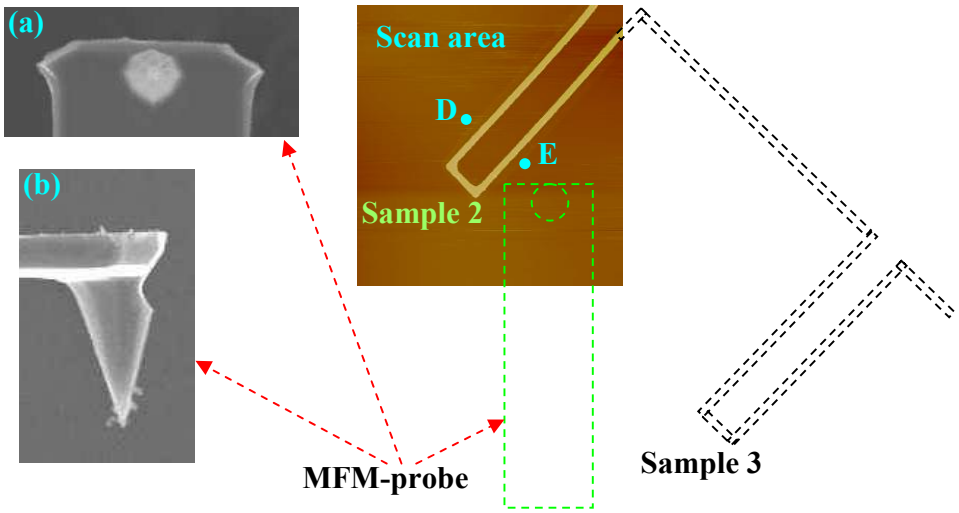

Figure 6.1.18. Schematic drawing of the cantilever and the sample circuits arrangement at $\alpha = 134^0$. Dashed line drawing of the circuits at outside of the scan area is for the analysis. When scanning sample 2, the cantilever will be influenced by sample 3 in this situation. The signal at right side of sample 2 has more influence than that at left side of it. Two SEM images of MFM-probe display a detailed corner of the cantilever which has an irregular shape and has a complex magnetic moment distribution.

A second reason for the discrepancy in Fig. 6.1.17 is that a small corner area is in the strong magnetic field gradient area of sample 2 at the scanning point E. SEM images in Figure 6.1.18 show the corner has an irregular shape and is very difficulty to model accurately. In our modeling calculations, only few point magnetic moments are used in this area. In addition, the thickness of the coating at the corner may not be uniform and the "edge effect" from the sample (about 350 nm thickness) may also produce errors in this area. Fortunately, from Figure 6.1.17, we found that the mismatch is not very large and is acceptable for our objective since it does not prevent us from locating conducting traces. In this configuration again, the model provides a good simulation of the MFM force.

6.1.1.2 The effect of the varying magnetic moments of the Probe

This is the most general case. Commercially available MFM thin film tips are supplied in this condition and most research work in MFM are taken in this condition. In order to obtain this configuration, the tip is simply magnetically saturated along the long tip axis prior to each measurement, but no magnet is used to maintain this orientation during the measurements. Note, the long tip axis is not the z-axis of the coordinate system. They will coincide when the cantilever is not tilted but oriented at $\theta = 0$. As discussed as section 4.4.2, so long as magnetization field is over 0.5T, the remanent magnetization of the cantilever in the bottom and top along this direction will be only $M_r = 0.086 \times 10^6$ Am^{-1}, according to the hysteresis loop perpendicular to the plane of the film in Figure 4.4.15, but the remanent magnetization of the tip and side of the cantilever along this direction will approximately be $M_r = 0.384 \times 10^6$ Am^{-1} according to the hysteresis loop parallel to the plane of the film in Figure 4.4.15. Although the easy axis of magnetization lies along the plane of the Co/Cr coating on the tip surface that is not along the long tip axis, the tip magnetization is predominantly oriented into the long tip axis [59]. Furthermore, considering the pyramidal tip has an asymmetrical shape leading to a small component of the magnetization which is vertical to the long tip axis. However, the absolute value of this component measures only 10% of the component along the long tip axis. A detailed discussion can be found in a recent work of Kebe and Carl [59]. Therefore, the tip magnetization is simply considered oriented into the long tip axis. In our modeling calculations and data analysis, we will neglect this small vertical component and only consider the tip-magnetization along the long tip axis.

In the following discussion, most of measurements are taken with $\alpha = 90^0$ and $\theta = 15^0$. Unless otherwise specified, we will assume using this arrangement.

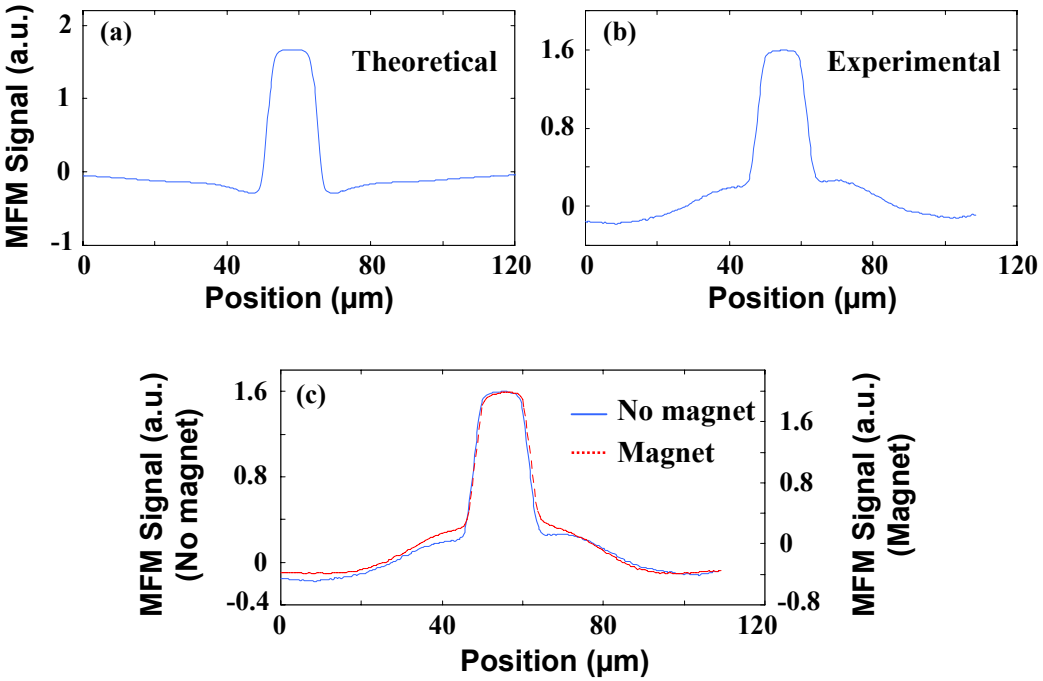

Figure 6.1.19. (a) The simulation result assumes that the different orientation substrate plane of the probe will hold different remanent magnetization according to the hysteresis loop in Figure 4.4.15. **(b)** The experimental result shows a different shape as expected in (a). **(c)** The experimental result comparison with the previous case in section 6.1.1.1 (where there is a permanent magnet under sample during scan). Related scales on the left and right side indicate that there is only 0.7 times difference of the signal between them and they almost keep the same shape of the signal. The ratio of the contributions between the tip and cantilever is the same with or without the magnet.

With the insight from the above discussion, the MFM line scan along the dashed line (A-A') in Figure 6.1.1 (b) is expected to be like the results shown in Figure 6.1.19 (a). The estimated contribution from the coating on the cantilever was quite small because of the perpendicular remanence. The experimental results shown as in Figure 6.1.19 (b) indicate a larger contribution from the cantilever. We have repeated the procedure of magnetizing the tip and doing (A-A') measurements many times in order to find whether or not the magnetization follows the hysteresis loop predicted by Carl *et al*. [60]. However, none of the measurement results are entirely repeatable, i.e. there is a different magnetization

configuration on the tip each time. This may result from the hand control used to position the magnetizing magnet. For the same tip, the measurement results are consistent. However for different tips, they can be quite different and are almost never consistent with the remanence expected from hysteresis loop in Figure 6.1.19 (a). Typically, we find that the signal strength is decreased 0.7 times as compared to the case (refer to Fig.6.1.19(c)), where the tip magnetization is fixed with an external magnet measurement, instead of about 0.5 times decrease from the Carl's work [60]. Clearly, the tips' magnetization does not follow the Carl's work [60], especially for the perpendicular case, where it appears that most magnetic moments stay oriented with the external magnetic field after the field is removed. In the previous section, we have shown our model provides a good description of the MFM force images. Comparing with the simulation can provide a technique that allows determining the magnetization reversal and coercivity of MFM tips and cantilevers. Given the variability in MFM tips observed in this work, techniques should be developed for more consistently behavior tips or more rapid techniques to characterize tips. .

If we adjust the strength of the external magnetic field used to magnetize the tip, such as using maximum fields of 0.04T, 0.1T, etc., some control of the remanence of the MFM tips can be obtained. Figure 6.1.20 shows several different results from this procedure. The stable images suggest that the MFM tip magnetization stays constant after the magnetization procedure, and also suggest that magnetic moments can have very different stable orientations. Some appear to have the cantilever and tip oriented 90^0 to each other. This result once again demonstrates the large potential variation in probe magnetization.

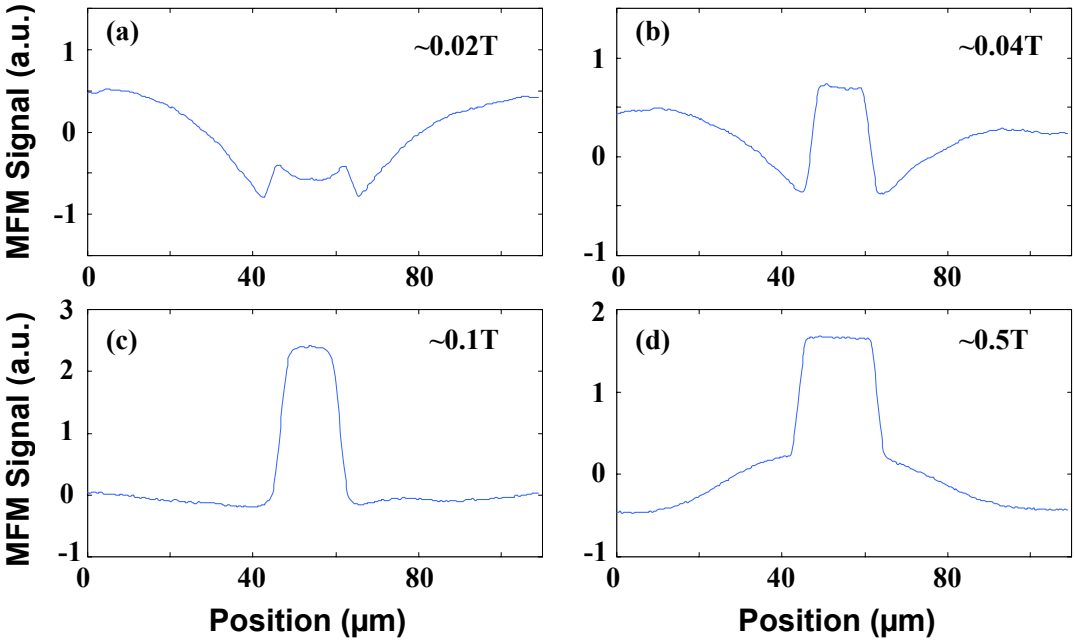

Figure 6.1.20. The experimental results with the different magnetization of the MFM tip can keep stable during scanning, even in the situation of the inverse magnetization between tip and cantilever. **(a)** Inverse magnetization on the small region of the tip with the rest regions of the probe. **(b)** More region on the tip has inverse magnetization comparing with (a). **(c)** Similar shape of signal as shown in Fig. 6.1.19(a). **(d)** Saturated magnetization before used. Magnetization fields are indicated in each plot.

6.1.2 Comparison of Simulation and Measured Results for Magnetic Force Gradient

As with the force detection analysis, we will choose two line scans for our discussion, one along the dotted line in Figure 5.4.2 (b), and the other along the dashed line in Figure 5.4.2 (b). Note that as mentioned in chapter 5, the tips are magnetically saturated into the long tip axis prior to each measurement, and the orientation of the cantilever is at $\alpha = 90^0$ and $\theta = 15^0$.

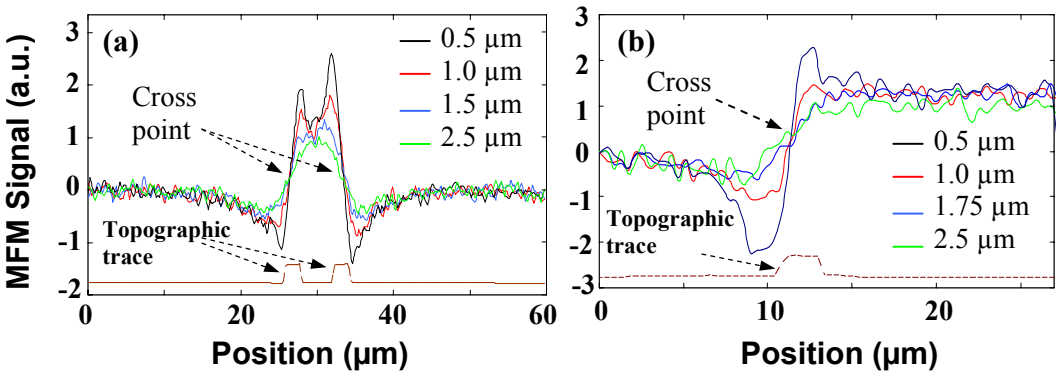

Figure 6.1.21. MFM force gradient line scan measurements **(a)** and **(b)** taken along the dashed and dotted line in Figure 5.4.2 (b), respectively, with a dc-current of I ≈18.1 mA at the different tip lift heights. Topographic cross section of the sample is shown as a dotted line, for positional reference.

Figure 6.1.21 (a) and (b) show MFM force gradient signals taken along these two lines at the different scan height of 0.5µm, 1.0µm, 1.5µm, 2.5µm, and 0.5µm, 1.0µm, 1.75µm, 2.5µm, respectively. During imaging a dc-current of I ≈ 18.1mA is driven through the sample circuits and the amplitude of the driven cantilever vibration is about 27 nm. Due to the large relative thermal noise, the MFM signal is not very clear, but some characteristics can still be identified. First, unlike the force signal, the cantilever contribution is not obvious, which as indicated in section 3.6 the force gradient minimizes it. Second, one notices that the MFM force gradient signal is mainly localized in the vicinity of the sample circuit due to the largest field gradients in this area; obviously, this will improve the spatial resolution of the measurement. Third, we found a rather large signal change from negative to positive, and vice versa, at the positions where the conducting lines are located, the topographic trace is illustrated in Figure 6.1.20 (a) and (b) as a dotted line. This is because the magnetic fields reverse directions on the two sides of the metal line. Although this should also occur in the force signal, the cantilever contribution neutralized it and made it invisible. This feature leads to a crossing point for the different lift height signals above the conducting line which can be used as a technique to locate the faulty device. This will be discussed in next chapter.

Since SNR is quite low, here we will not show many experimental results and will not show overlay comparisons. The simulation results are briefly shown in Figure 6.1.22. Qualitatively, all features of the MFM signal, such as the shape, high and low positions, and trend of the signal with different lift height, etc. show an excellent agreement with the experimental data.

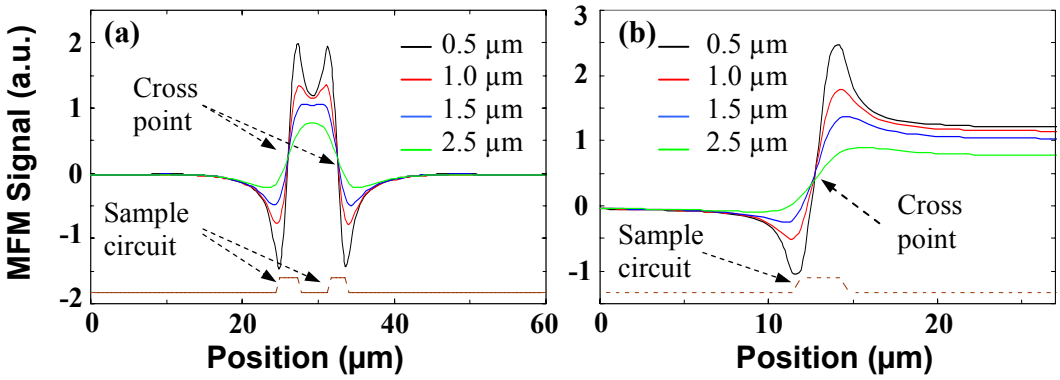

Figure 6.1.22. MFM force gradient line scan simulation results, **(a)** taken along the dashed line in Fig.5.4.2 (b). **(b)** taken along the dotted line in Fig.5.4.2(b), with a current of I at four different tip lift heights. The z-component of the tip magnetization was only considered in the simulation. Sample has the size of $w_1 = w_2 = w_3 = 2.0$ µm and $s = 4.5$ µm (see definition of the symbols in Fig.5.5.2 (b)). The cross section of the sample is shown as a dotted line, for positional reference.

6.2 Quantitative Comparison

In previous sections, normalized image comparisons, which only deals with the shape and size of the signal, show an excellent agreement between the simulation and the experiment. In this section we will focus on the quantitative comparison.

6.2.1 Magnetic Force

Figure 6.2.1 shows a quantitative comparison of the experimental results and the simulations as shown as in Fig.6.1.9 with the tip lift of 1.0 μm and a current of I_{rms}=1.0 mA.

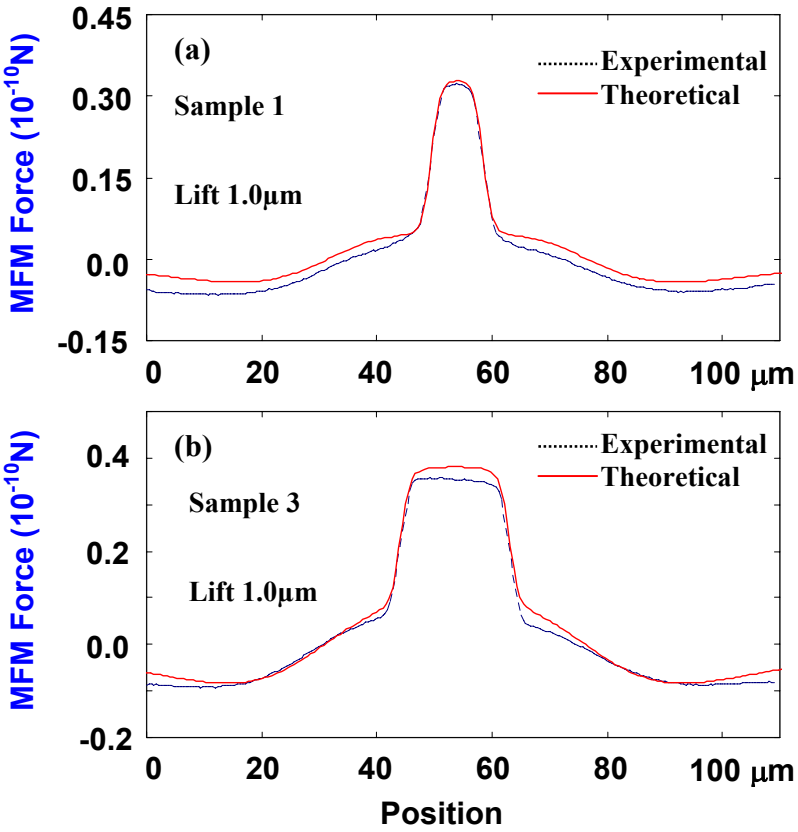

Figure 6.2.1. A quantitative comparison of the MFM line scan measurements and simulations as shown as qualitatively in Figure 6.1.9 with the tip lift of 1.0 μm and a current of I_{rms} =1.0 mA. 34 nm and 51 nm (51/34=1.5 times) thickness of Cobalt coating on the tip and cantilever surface, respectively, were used in the simulation. Saturation magnetization M_s= 0.87 ×10^6 Am^{-1}.

The previous results in this work showed that the contribution of the cantilever has to be considered and that the thickness of the Cobalt coating on the surface of the MFM probe is variable. From qualitative comparison we obtained a 1.5 times thicker Cobalt coating on the cantilever than that on the tip for this typical tip. Therefore, in Fig.6.2.1, we assumed 34 nm thickness of Cobalt coating on the tip surface and 51 nm on the cantilever

surface for the modeling calculations (these thicknesses are in the range of our experimental results from the cross section images of the tip). Other parameters used in this comparison are: for simulation, the saturation magnetization $M_s = 0.87 \times 10^6$ Am^{-1} is from Carl's results [60]. For the experiment, the deflection sensitivity of E-Scope is 70 nm/V (calibrated [139]), the spring constant is k = 4.0 N/m, and quality factor is Q = 340 (calculation refer to section 5.3.1).

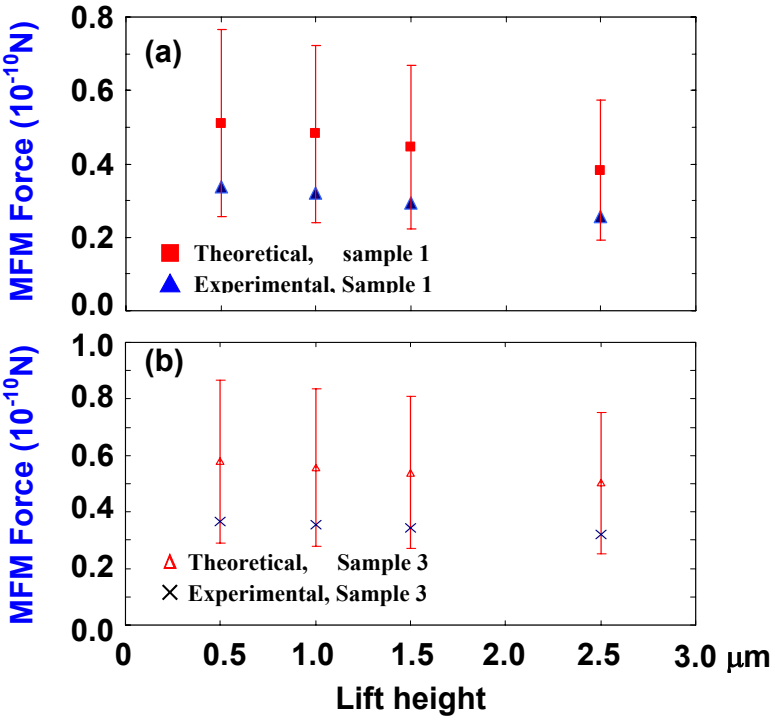

Figure 6.2.2. A quantitative comparison of the sample 1 (a) and sample 3 (b) with a current of I_{rms}=1.0 mA as a function of the tip lift height. The signals were chosen half way between the two parallel wires (w_1 and w_2) and ~ 50 μm away from the end wire (w_3). All results were obtained by using the same MFM-tip. The different thickness of Cobalt coating from 25nm to 75nm on the tip and from 37.5nm to 112.5nm (estimated from cross section images of the probe) produced a range of possible MFM forces in the modeling calculations.

In the quantitative comparison shown in Fig. 6.2.1, we can see that there is an excellent agreement between the simulation and the experiment. Similar results are found at tip lift heights from 0.5 to 2.5 μm for other sized sample circuits. Figure 6.2.2 shows the

quantitative comparison of the sample 1 and sample 3 (discussed in section 6.1) with a current of I_{rms} = 1.0 mA as a function of the tip lift height. The signals were chosen half way between the two parallel wires (w_1 and w_2) and ~ 50 μm away from the end wire (w_3). The results show that the experimental results are predicted within the known uncertainties.

As to the most general case of the magnetic moments of the tip along the long tip axis, in which there is no external field to hold the tip magnetization during measurements. The experimental values will decrease as we have discussed in previous section.

6.2.2 Magnetic Force Gradient

Since the cantilever holder includes ferromagnetic materials, a strong external field makes the piezoelectric vibration of the cantilever at resonance unreliable. So we have only performed measurements with tips which are magnetically saturated along the long tip axis prior to each measurement. As mentioned as section 5.5, the results of the ratio of the force SNR and force gradient SNR gave an excellent agreement between the simulation and the experimental data in both qualitatively and even quantitatively. Figure 6.2.3 quantitatively shows the force gradient values in Fig. 5.5.3 (experimental) and 5.5.4 (theoretical), respectively. In the calculation, we used the following parameters: spring constant k = 4.0N/m, quality factor Q = 327, dc current I = 18.0 mA, thickness of Cobalt coating in the whole probe from 25nm to 75nm, and magnetization from $0.5M_s$ to M_s (M_s = 0.87×10^{6} Am^{-1}). The first three parameters were obtained by the experimental measurements. The last two parameters, Cobalt thickness and magnetization, were estimated from experimental measurements. Cobalt thickness variation from 25nm~75nm can be estimated from cross section images. Since the magnetization does not precisely follow the hysteresis loop, there is a different magnetization configuration each time. We do not know accurately the magnetization M in this measurement and a range from $0.5M_s$ ~ M_s is a reasonable guess. Using the estimated uncertainty in Cobalt thickness and magnetization the uncertainty in the force gradient can be estimated. All the measurements are within this uncertainty as shown in Fig.6.2.3.

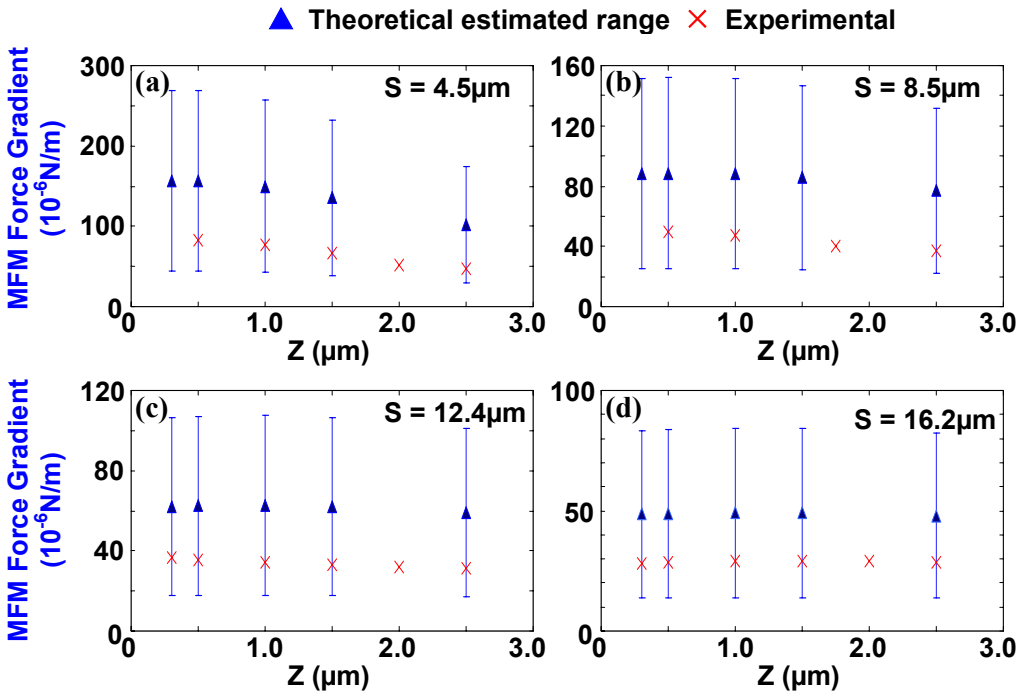

Figure 6.2.3. Quantitative results of the force gradient in Fig.5.5.3 (experimental) and Fig.5.5.4 (theoretical) as a function of the tip lift height with a current of 18.0 mA rms flowing through the circuits and sample size of $w_1 \approx w_2 \approx w_3 \approx 2.0$ μm with different separations of $s \approx 4.5$, 8.5, 12.4, and 16.2 μm for experimental and theoretical. The compared signals were chosen at the middle of the two parallel wires (w_1 and w_2) and ~25 μm away from the end wire (w_3). In simulation we simply assume that the thickness of Cobalt coating varies from 25nm to 75nm and the tip magnetization from $M_s = 0.87 \times 10^6$ Am^{-1} to $0.5 \times M_s$.

6.2.3 Summary

In this chapter, we have performed a normalized image and quantitative comparison of the simulation and experiment. The results show that the model provides an accurate means to simulate MFM images in both shape and absolute magnitude. In order to obtain a good fit to the shape it was necessary to assume that the cantilever magnetic coating was 1.5 times thicker than the tip magnetic coating. The greatest uncertainty in absolute magnitude is due to the thickness of the magnetic coating and the random magnetization of the probe.

Chapter 7
FAULT LOCATION IN FORCE AND FORCE GRADIENT

When current flows through a device buried under several passivation layers, no topographic features are available on the surface to provide clues about the position of the device. Locating this device from the MFM images can be problematic. In this chapter, a method will be presented for locating faulty devices from MFM images.

7.1 Magnetic Force

In Fig. 6.1.3 and 6.1.4, we found that there are cross over points between different lift separations above the conductor. These turn out to be a good indicator of conductor position. This is an important discovery as it leads to a simple method to locate accurately the position of the internal current carrying faults from MFM images without topographic mapping.

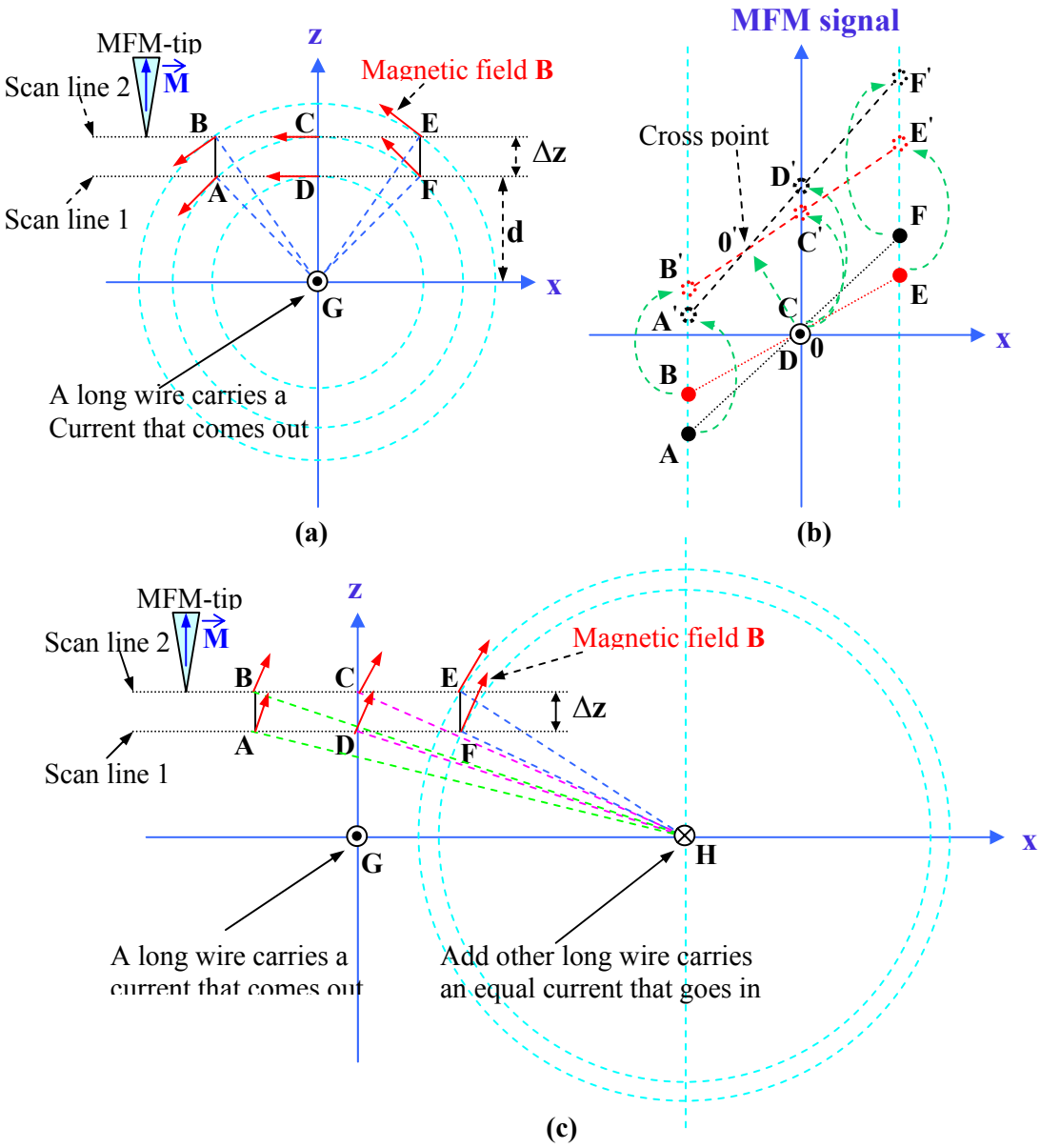

Figure 7.1.1. Illustrating the formation of the crossing point between two lift-heights. Red solid arrows indicate the magnetic field **B** at the different points. **(a)** A long wire carrying a current **I** will induce a magnetic field that interacts with the magnetic tip at two line-scans. **(b)** Relative locations of the MFM signal at the points of A, B, C, D, E, and F. Corresponding points of A', B', C', D', E', and F' is due to adding other long wire carrying equal and opposite current. The second long wire shifts the cross over point 0 to 0'. **(c)** The two long wires G and H carry equal and opposite currents.

To explain this method, let us consider a long wire carrying a current as shown in Figure 7.1.1 (a). For simplicity, we suppose that the wire is along the y-axis and carries a current **I** which flows out of the plane of the paper toward the observer, and also suppose that the MFM tip's moment is along the z-axis. Let us now consider the force F acting on the tip at several points of two line-scans taken at different separations. We choose C and D that are right above the wire and A, B and E, F are on the left and right side of this position. Since the magnetic field $\vec{\mathbf{B}}$ at the C and D is along the negative x-axis which is perpendicular to the tip moment, using equation 3.2.1 ($\mathbf{F} = \nabla \mathbf{M} \bullet \mathbf{B}$), we obtain F = 0 at these two points. For points E and F, if considering E and F are close to C and D, respectively, and Δz is small, we can approximate the angles between $\vec{\mathbf{B}}$ and $\vec{\mathbf{M}}$ at E and F are equal (also less than 90^o). So that, Forces at E and F are only depending on distance EG and FG, then from section 3.6 it is seen that F is inversely proportion to the square of the distance. Therefore, the force at F is larger than it is at E as shown in Figure 7.1.1 (b). Similarly, we can obtain force at B is larger than its force at A (note, force is negative since the angles between $\vec{\mathbf{B}}$ and $\vec{\mathbf{M}}$ at A and B are larger than 90^o). On the other hand, A, D, and F are on the one scan line, the MFM signal will continue from A via D to F, same for B via C to E. Obviously, there will be a cross over point located between A and F, or say between B and E (in this case C and D are at the cross over point) as shown in Figure 7.1.1 (b). It is clear, if there is only one wire and no other fields influence, the cross over point will be right above the wire, which is on the z-axis in Figure 7.1.1 (a). Second, let us consider two long wires carrying equal and opposite current as shown in Figure 7.1.1 (c). According to superposition theorem, we only need add the effect from the other wire to the previous results. Referring to the geometry of Figure 7.1.1 (c), we see that all chosen points are on the left side of the add wire H and all $\vec{\mathbf{B}}$ are acute angles with tip $\vec{\mathbf{M}}$, which will increase MFM signal at each point (A, B, C, D, E, and F). Considering distance FH < EH, we easily obtain Force at F will increase more than that at E, so it still keeps the same order as shown in Figure 7.1.1 (b) ($F^{'}$ and $E^{'}$ points). For C and D, they will not be the same. D will higher than C. As to A and B, it is not obvious. Since AH < BH, A will increase more than B, then whether or not A will go higher than B, let us compare force difference between A and B produced by wire G and it is produced by

wire H. Since distance AH > AG and BH > BG, using equation $\mathbf{F} = \nabla \mathbf{M} \bullet \mathbf{B}$ (F is inversely proportional to the square of the distance, and also note equal current flows in both wires), it is not difficult to conclude that the force difference between A and B produced by wire G is larger than that produced by wire H. Therefore, B will be higher than A as shown in Figure 7.1.1 (b). According to the previous analysis, there will still be a cross over point located between A and F, but it will be slightly shifted away from above the wire (not at C and D refer Figure 7.1.1 (b)). However, in a typical sample the separation between two wires is larger than 5.0 μm and width of the wire is larger than 2.0 μm, and noticing that the magnetic field gradient dramatically decreases after it is not above the sample (refer to Figure 4.4.7, width of magnetic field gradient at the half peak is less than 0.5 μm when tip lift height is below 1.0μm), we conclude that the cross over point will be somewhere over the top of the wire. However, if the assumptions, such as separation of the two wires, width of the wire, and tip lift height, are not satisfied, obviously, it may not be true. Generally, these conditions are expected to be met.

To the case of cross over points in Figure 6.1.4, which is on the top of the wire w_3 in Fig. 5.5.2 (b), instead of wire H, we need to consider the influence from two parallel wires which are perpendicular and connected to the wire G. They carry equal and opposite current. Using a similar argument, we can prove the cross over point is still within the width of the wire under the assumptions above. However, note that two parallel wires carrying two currents ($2\mathbf{I}$) either will increase or decrease the force signal around the wire G. The two parallel wires will produce more influence on the force signal around the wire G than the wire H will. In some situations, the force difference between A and B produced by wire G is less than that produced by the two parallel wires so that the cross point will shift out of the A and B, which makes the cross over point not above the wire. In general and under the assumptions above we can conclude there is a cross over point above the end wire of the rectangular shape sample which is the location of the faulty device in our model as shown in Figure 5.1.1. Later, modeling calculations and experimental results will be shown for some specific cases.

Though we only considered that the tip moment is along the z-axis, in fact, this will still be true for a slightly tilted tip. In other words, for small x- and y-components of the tip moment, the cross over will still be over the conductor.

Using these observations, we can devise a method to locate the fault devices as follow:

1. To obtain two MFM images at different tip lift heights.
2. Using the MFM image, we may roughly estimate where the faulty device lies. Choose a single scan line that crosses over the fault device, then to obtain two MFM line scan signals along this line from two MFM images, respectively.
3. Draw these two line scan signals as in Figure 6.1.3 and obtain a cross over point.
4. The estimated position of the fault is under the cross over point.

The accuracy of this method will be discussed later in this chapter and compared with the method of the force gradient measurement.

7.2 Magnetic Force Gradient

Similar to force signals, force gradient signals in Fig.6.1.21 and 6.1.22 with different lift heights will also have cross over points located above the conductor. Thus, the location method is the same as above. However, as mentioned in chapter 6, the force gradient minimizes the contribution from the cantilever and a change of the signal from negative to positive (and vice versa) is located over the conducting lines, there must be a zero signal point in between, which will become a cross point for the signals with the different currents due to the linear relationship of them as shown in Fig.5.4.5. Actually, this zero cross point is the force location point when the two tip lift heights are chosen very close (the difference $\Delta z \rightarrow 0$ from the definition of the force gradient). In later discussion the results show that the accurate location in the force measurements requires a certain amount Δz of the two tip lifts. Furthermore, the cross over points with different tip lifts are closer to the middle of the wire than the zero cross points. The following discussions have only chosen the cross points with different tip lifts as the location method.

Simulation results for these two kinds of cross points are briefly shown in Figure 7.2.1 and 7.2.2.

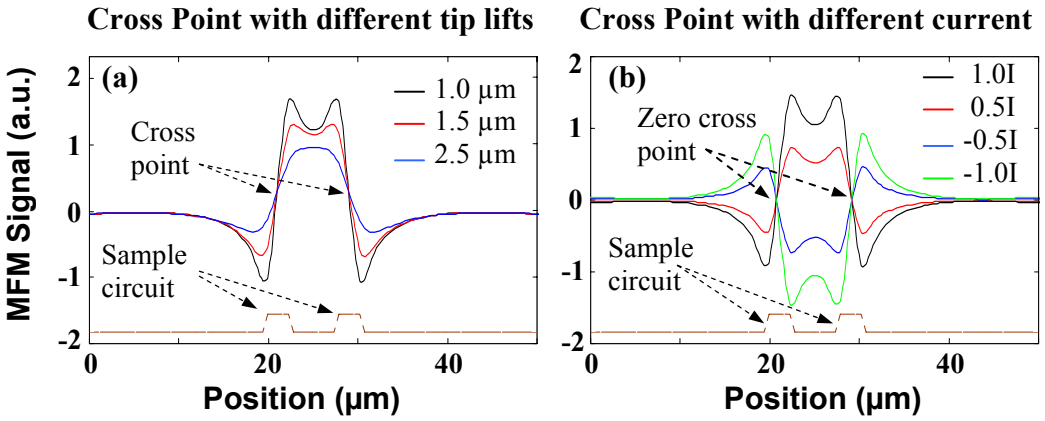

Figure 7.2.1. MFM force gradient line scan simulation results taken along the dashed line in Figure 5.4.2 (b), **(a)** with a current of I at three different tip lift heights. **(b)** with four different currents at a tip lift height of 1.0 µm. The z-component of the tip magnetization was only considered in the simulation. Sample has the size of $w_1 = w_2 = w_3 = 2.0$ µm and s = 6 µm (see definition of the symbols in Fig.5.5.2 (b)). Topographic cross section of the sample is shown as a dotted line, for positional reference.

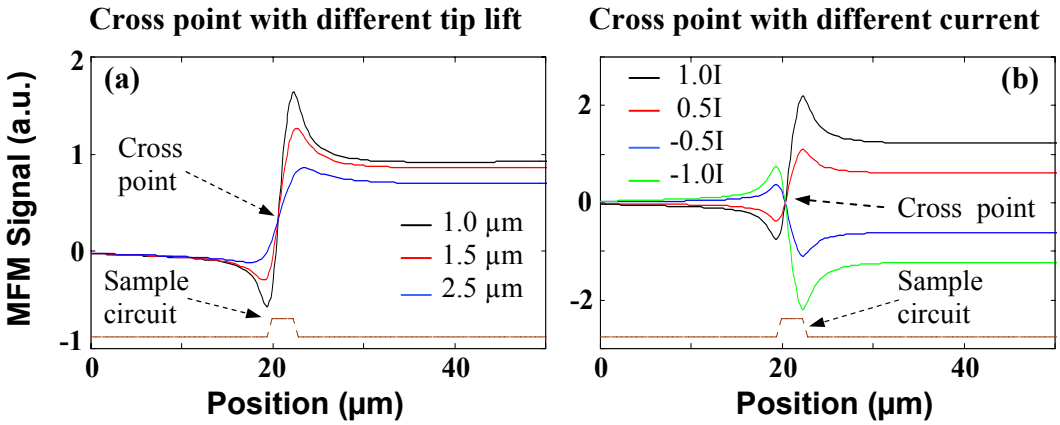

Figure 7.2.2. MFM force gradient line scan simulation results taken along the dotted line in Figure 5.4.2 (b), **(a)** with a current of I at three different tip lift heights. **(b)** with four different currents at a tip lift height of 1.0 µm. The z-component of the tip magnetization was only considered in the simulation. Sample has the size of $w_1 = w_2 = w_3 = 2.0$ µm and s = 6 µm (see definition of the symbols in Fig.5.5.2 (b)). Topographic cross section of the sample is shown as a dotted line, for positional reference.

7.3 Spatial Resolution

In this section, the spatial resolution of the MFM force and force gradient location techniques are investigated by experimental measurements and the model calculations. The results from previous sections lead to the conclusion that the force gradient is not practically used to map currents on ICs due its low sensitivity. The following results for force gradient with high currents are only as a point of reference for discussion of force imaging.

Spatial resolution is an important quantity that characterizes the MFM as well as other SFM. In general, the spatial resolution is an evaluation of the locality of the measurements done by the microscope and can be defined by the steepness of the gradient profile as a function of lateral movement. As mentioned in section 3.6, the force has an inverse relationship with respect to the tip-sample distance and the force gradient has a higher order inverse relationship. As a result, the force gradient has a steeper profile as a function of lateral movement than the force. In order to give an impression of how much better spatial resolution the force gradient has for mapping the current, let us consider a long straight conductor with a width of 2.0 μm and carrying a current I = 1.0 mA.

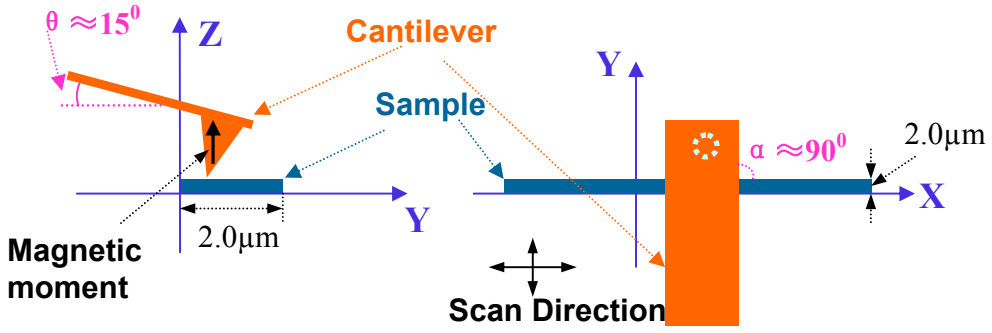

Figure 7.3.1. Schematic representation of orientation of the cantilever and sample in the simulation. The MFM probe assumed has the magnetic moments of the probe along the z-axis with respect to the sample plane.

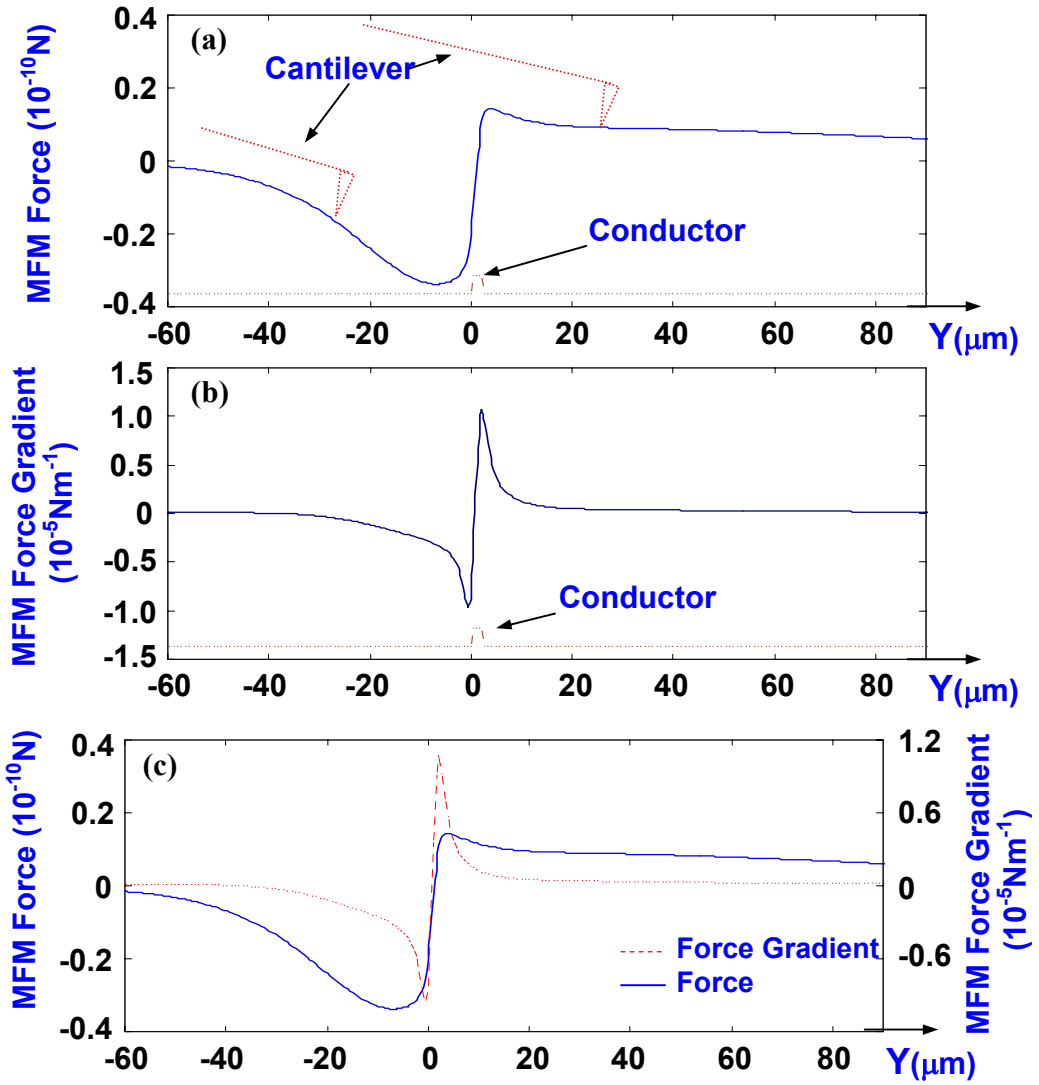

Figure 7.3.2. The numerical simulation of the force **(a)** and force gradient **(b)** profile of a tip located 1.0 μm above the conductor along the y-axis and cross over the middle of the conductor. z-component magnetic moments on the probe were only considered and assumed 1.0 mA current flowing through the conductor. Two cantilevers are shown as the dotted line in (a), for orientation reference of the cantilever at two sides of the conductor scan points. **(c)** the overlay of (a) and (b).

A brief schematic orientation of the conductor and cantilever probe is shown in Figure 7.3.1 and the numerical simulation of the force and force gradient profile of a probe tip located 1.0 μm above the conductor is shown in Figure 7.3.2.

In the simulation, we only consider the z-component of the magnetic moments on the probe. From the graph, the force gradient rolls off much steeper than the force does. If the spatial resolution may be estimated by measuring the width of the profile peak at the half maximum, the force gradient has about 5 μm for the negative peak and the force has 30 μm. For the positive polarity the force gradient is almost the same and the force can not be estimated as the profile is too flat.

Fig.7.3.2 (a) shows a schematic cantilever for illustrating its effect to the trace. When the tip started moving close to the conductor from the left side in the graph the force signal drops dramatically since there is only an attractive force acting on the probe, but when the probe was moved over the conductor on the right side of the graph the force signals drops slowly and the probe tip was far away from the conductor at the right end. A non zero force signal is still detected, due to the cantilever still being over the conductor.

Also, there are both attractive and repulsive forces acting upon the probe resulting in the absolute value of the signal peak on the right side which was less than it was on the left side. In addition, the cantilever-to-sample distance is > 20 times than the tip apex-to-sample distance. In this cases (tip height is about 22 μm) the cantilever is insensitive to the force gradient as seen in Fig.7.3.2 (b).

7.3.1 Spatial Resolution for Circuit Location

A) Force Detection

A.1) Contribution of Different Tip Lifts to Measurement Uncertainty

The location algorithm has been applied to calculations on the model circuits. For simplicity, we will only consider the z-component of the magnetic moments on the probe and the case of $\theta = 15^0$ and $\alpha = 90^0$ as shown as in Figure 7.3.3. As designed the model circuits in section 5.1, line segment w_3 is the model of faulty device. Thus, a single line-scan, indicated by the dashed line in Fig.7.3.3, over the middle of the w_3 will be used for the signal analysis to locate the faulty device (w_3).

Figure 7.3.4 shows the estimated fault position using model calculations and devised method as a function of the separation of the circuits. In order to systematically study these effects, five samples with five different separations of s = 2.0, 6.0, 10.0, 14.0, and 20.0 μm were used. The MFM images with different tip lift heights from 0.3μm to 2.5μm were used. Since there is a slight shift of the cross over point for the different tip lift height pairs, the error bar shows the range of cross over points. Figure 7.3.5 is an enlarged view of the cross over point for a typical configuration.

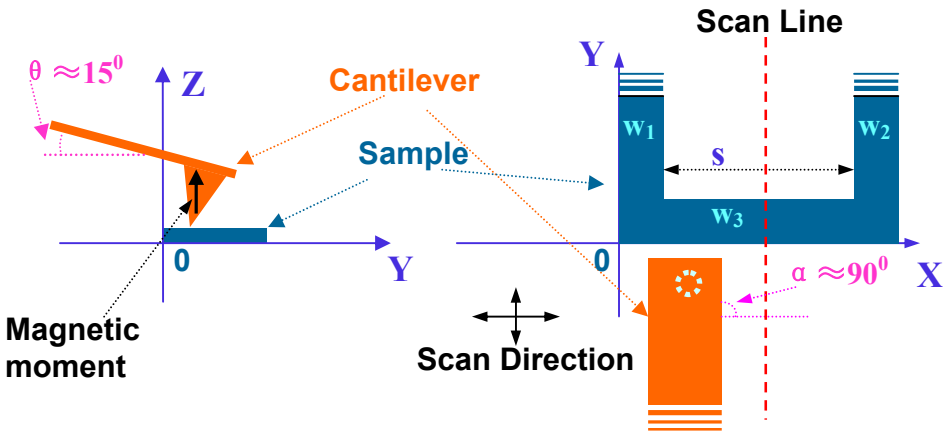

Figure 7.3.3. Schematic representation of orientation of the cantilever and sample in the modeling calculation. The MFM probe assumed has the magnetic moments of the probe along the z-axis with respect to the sample plane. The sample has a width $w_1 = w_2 = w_3 = 2.0$ µm. The separation s is varied stepwise from s = 2.0 µm to s = 20 µm. w_3 is the model of faulty device. The dashed line is selected along the y-axis and cross over the middle of the w_3 for the signal analysis to locate the fault. The coordinate system is for positioning the sample in the simulation.

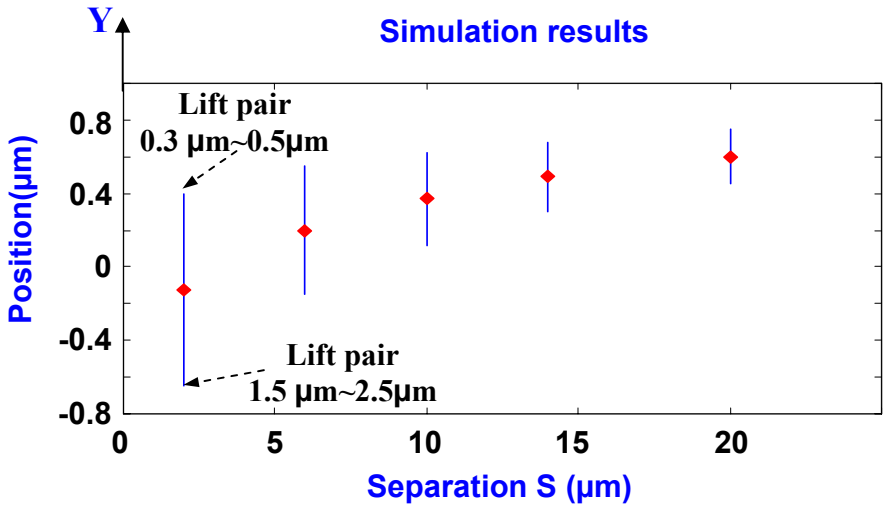

Figure 7.3.4. The estimated position of the faulty device was determined by the devised method as a function of the separation s of the sample. The cross over points from different tip lift height pairs in the range of 0.3µm to 2.5µm produces a distribution of estimated locations. Arrows indicate the positions from the different lift pairs. Obviously, the smaller lift height, the more accurate the location. Faulty device is in $0 < y < 2.0$ µm from our model. The locating position is out of the faulty device range for the small separation of s = 2.0 µm.

For most lift height pairs the algorithm locates the position of the device. The faulty device w_3 conductor starts at y = 0 and ends at y = 2.0μm. The results in Fig.7.3.4 show the located positions are in this range for all samples except for the small separation of s = 2.0 μm. This was expected as explained in arguments in previous section, in which the influence of w_1 and w_2 will shift the cross point over the w_3 range. In Fig.7.3.4, arrows indicate the located positions from the different lift pairs. The smaller lift height, the more accurate the location. The steeper the change of the signal corresponding to smaller lift heights gives a better spatial resolution (>0.4μm). From Fig.7.3.4, we see that the locating position shifts to the middle of the w_3 and error decreases with increasing the separation s. Theoretically, this is because the w_1 and w_2 is going to have less influence. When s becomes quite large, as is the case for a long w_3 conductor, the located position is very close to the middle of the w_3 and all scan lines with different lift heights cross at one point.

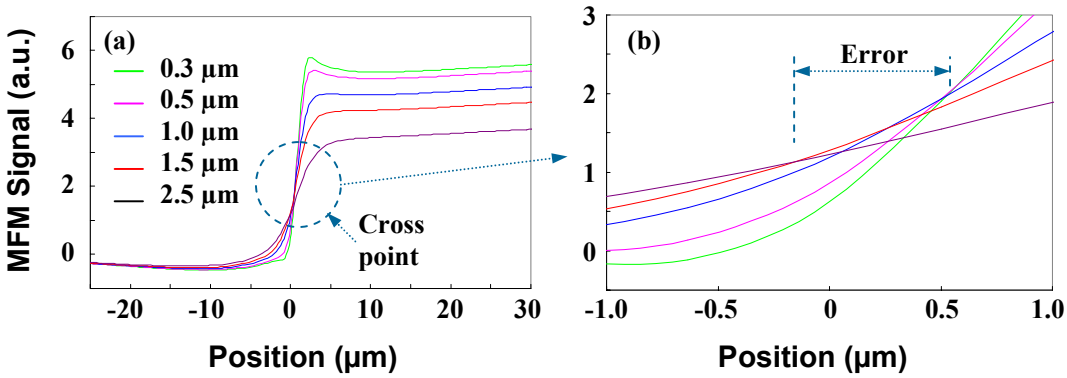

Figure 7.3.5. MFM line scan taken along the dashed line in Figure 7.3.3 for different tip lift heights. Cross point area enlarger view in (b) shows a slight shift of the cross over point for each lift pair.

From the analysis of the modeling calculations and results above, we conclude that the error in Fig.7.3.4 does not come from the cantilever contributions since there is only a slight difference of the signal from the cantilever contributions between the 0.3 μm and 2.5 μm of the tip lift height. It mainly comes from the fields produced by the current flowing in the w_1 and w_2 conductors and interactions with the magnetic moments of the

tip. Therefore, although the cantilever contributions have an effect on the spatial resolution of the MFM force images, it does not affect the location algorithm as these contributions remain largely unchanged at the two lift heights. In conclusion, this is a robust method for locating the current paths in devices. The closer the tip is to the faulty device, the stronger the signal is, and the more accurate the location.

A.2) Contribution of Noise to Measurement Uncertainty

In the above discussion, the error produced by noise in the MFM signal was not considered. Actually, it is a very important factor, especially for weak MFM signals. It makes the cross over position a probability distribution rather than a single point as shown in Fig.7.3.6. Obviously, this error depends on the value of the noise, SNR, and crossing slope (angle γ and ϕ). The larger the crossing slope, the less the error. Since the cantilever contribution flattens the curve of the signal which in turn decreases the crossing slope, the error will be increased. We may get a method to minimize the error due to noise by choosing two signals with a larger difference in the lift height which increases the crossing slope.

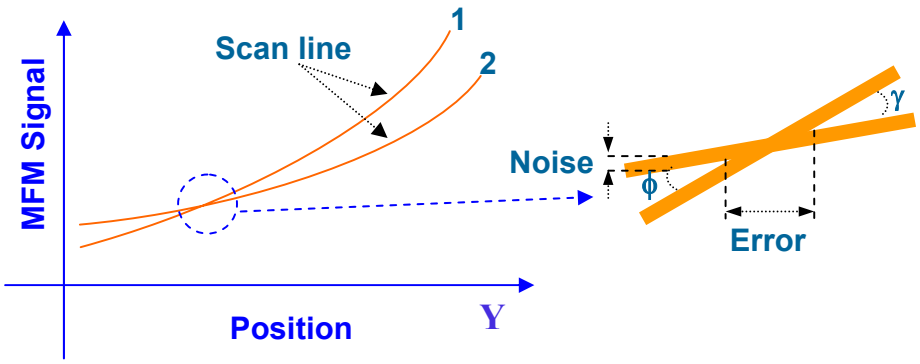

Figure 7.3.6. Schematic representation of the error produced by the noise. It depends on value of the noise, SNR and cross angle γ.

As an example, Table 7.1 gives the simulation results for the error produced by noise in the measurement for the sample s = 10 μm with different current and different lift height pairs.

Table 7.1. Simulation results about the error produced by the noise for the sample with a separation s = 10 μm. $N_f = 8.63 \times 10^{-14}$N.

Lift pair	0.3~2.5 μm			1.5~2.5 μm		
Current (μA)	1000	100	10	1000	100	10
Error (μm)	<±0.005	~ ± 0.025	±0.3	< ± 0.05	~ ± 0.25	N/A

Results show that we could ignore the noise effect when current I > 1 mA and lift is less than 2.5μm.

A.3) Comparison of Simulation and Experimental Results

The experimental and theoretical results for a group of four samples discussed in section 6.1 and shown in Fig.6.1.3 with the geometrical dimensions in Table 6.1 are summarized in Table 7.2.

Table 7.2. The experimental and theoretical results are for a group of the samples in Table 6.1. The signals were taken at three tip lift heights of 0.5, 1.0, and 1.5 μm with a current of I_{rms} = 1.0 mA. The experimental results come from the images in the scan range of 109 μm with 256 samples

Crossing position	Sample**1**(s=6.4) (0 < y < 2.5μm)		Sample**2**(s=11.3) (0 < y < 2.5 μm)		Sample **3**(s=16.2) (0 < y < 2.4 μm)		Sample**4**(s=21.3) (0 < y < 2.5 μm)	
	Theory	Exp.	Theory	Exp.	Theory	Exp.	Theory	Exp.
Y ±Error(μm)	0.575 ±0.1	1.4 ±0.125	0.735 ±0.06	0.598 ±0.1	0.775 ±0.05	0.778 ±0.625	0.87 ±0.05	0.853 ±0.3

The results show excellent agreement between the experimental data and the calculated predictions.

B) Force Gradient detection

The same setup as the force detection above were used for the force gradient calculations, Figure 7.3.7 shows the located position of the faulty device decided by the devised method for the force gradient detection as a function of the separation s of the circuits.

Unlike force detection, the devised method for the force gradient detection works quite well, even for a small separation s. The influence of the w_1 and w_2 is not enough to shift cross point out of the faulty device w_3 in this situation. The maximum error in the force gradient is around ± 0.225 rather than ± 0.525 in the force. Comparing Fig.7.3.7 with Fig.7.3.4, similar behavior is found as a function of the separation s and the locating position is more localized close to the middle of the w_3 for the force gradient. Therefore, the force gradient shows a higher spatial resolution than the force.

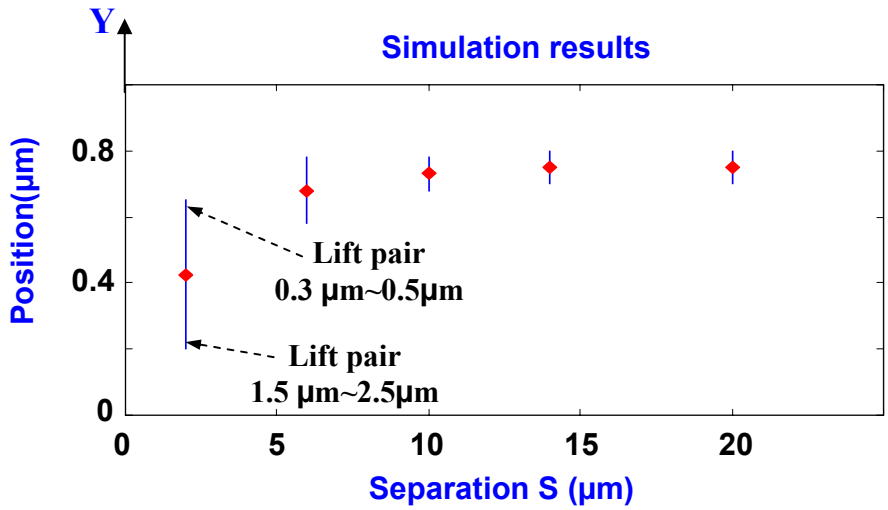

Figure 7.3.7. The estimated position of the faulty device was determined by the devised method for the force gradient detection as a function of the separation s of the sample. The cross over points from different tip lift height pairs in the range of 0.3μm to 2.5μm produces a distribution of estimated locations. Arrows indicate the positions from the different lift pairs. The smaller lift height, the more accurate the location. The faulty device is in the $0 < y < 2.0$ μm range from our model.

As to the other cross point, as mentioned above, at the zero signal point in the force gradient detection as shown in Fig.7.2.2 (b) has a similar behavior, but it has a larger error and shift to the negative y-axis. Thus, it is not a good method as the shifts push the estimate outside the actual device location. However, it could be used as a rough location. It is not shown here in the interests of brevity.

For noise, the above discussions can be repeated for force gradient. For force gradient, it is the most significant issue and limits its application. As a comparison (with Table 7.1) the simulation result about the error produced by the noise for the sample of s = 10 μm with different currents and different lift height pairs is given in Table 7.3.

Table 7.3. Simulation results about the error produced by the noise for the sample with a separation s = 10 μm in the force gradient. $N_{fg} = 3.45 \times 10^{-6}$ N/m.

Lift pair	0.3~2.5 μm			1.5~2.5 μm		
Current (mA)	20	10	2	20	10	2
Error (μm)	<±0.0001	~ ± 0.02	0.075	< ± 0.001	~ ± 0.1	~ ±0.4

When current is less than ~1.5mA, SNR < ≈ 1, The force gradient could not be used with good effect. For comparison, we used high current to minimize noise effect.

The experimental results for two samples with the different sizes and different conditions are summarized in Table 7.4.

Table 7.4. The experimental results are for sample 1 with $w_1 \approx w_2 \approx w_3 \approx 2.0\mu m$ and s =4.5μm, the signals were taken at four tip lift heights of 1.0, 1.2, 1.75, and 2.5 μm with a current of I ≈14 mA, sample 2 with $w_1 \approx w_2 \approx w_3 \approx 2.0\mu m$ and s =8.5μm, the signals were taken at three tip lift heights of 0.5, 1.0, 1.75, and 2.5 μm with a current of I ≈18.1 mA. The experimental results come from the images in the scan range of 60 μm with 256 samples for sample 1 and 109 μm with 256 samples for sample 2.

	Sample 1 (0<y<2.0μm)	Sample 2 (0<y<2.0μm)
Y ±Error (μm)	0.4 ±0.35	1.0 ±0.3

The results show excellent agreement between the experimental data and calculated predictions (shown in Fig. 7.3.7).

7.3.2 Effect of Current from Other Conductors

An important issue in relation to the spatial resolution is to determine how small changes of the current path near the faulty device will effect the measurement. In other words, if the current path is not a straight line between V_{DD} and V_{SS}, how will it effect the measurement? For this purpose, we designed a model circuit with offset interconnects as shown in Fig.5.1.3 (b) and 5.1.4 (b). More details are shown in Fig.7.3.8 with the experimental setup. Circuits with jogs in two different directions were investigated (Fig.7.3.8).

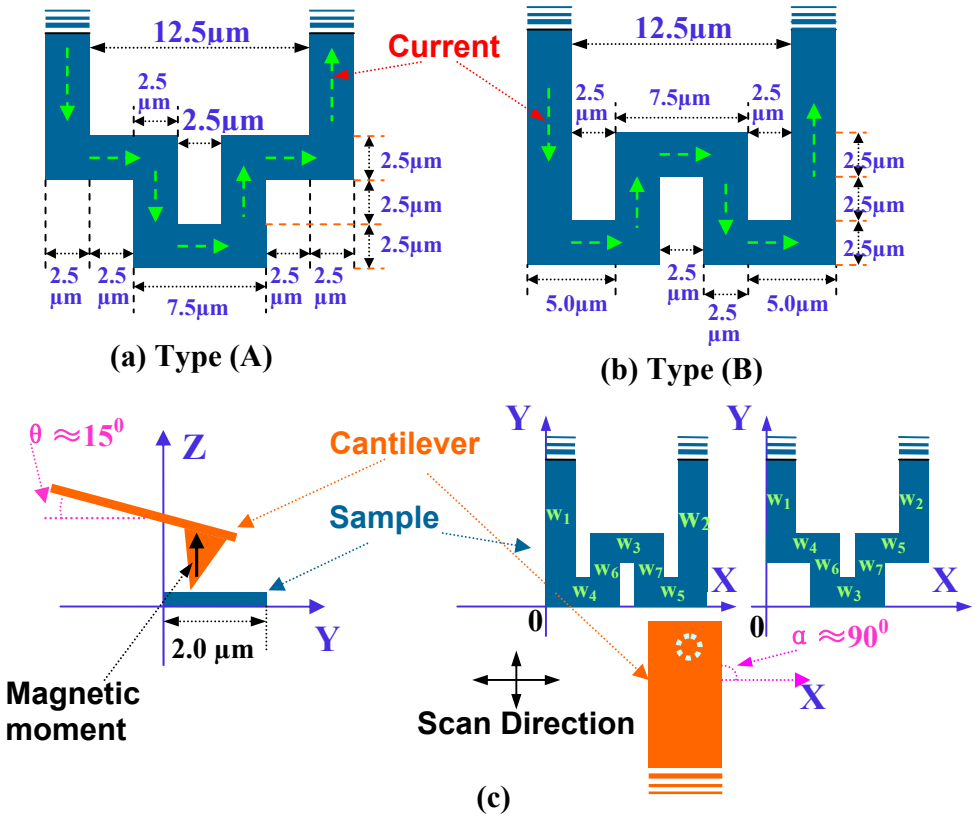

Figure 7.3.8. Schematic illustration of the two types of sample circuits, type (A) in **(a)** and type (B) in **(b)**. The current flows in form of the different pattern affecting the MFM image. **(c)** The orientation of the sample and the cantilever is for the experimental setup. The coordinate system is for positioning the sample in the modeling calculation. w_i (i = 1,2,3,4,5,6,7) denotes the different straight section of the conductor for our analysis.

Figure 7.3.9 shows MFM force (b), (c), and (d), and MFM force gradient (e), (f), and (g), images of a sample circuit of type (A) for three different tip lift heights of 1.0, 1.75, and 2.5μm, respectively. Figure 7.3.10 is for the type (B) sample circuit.

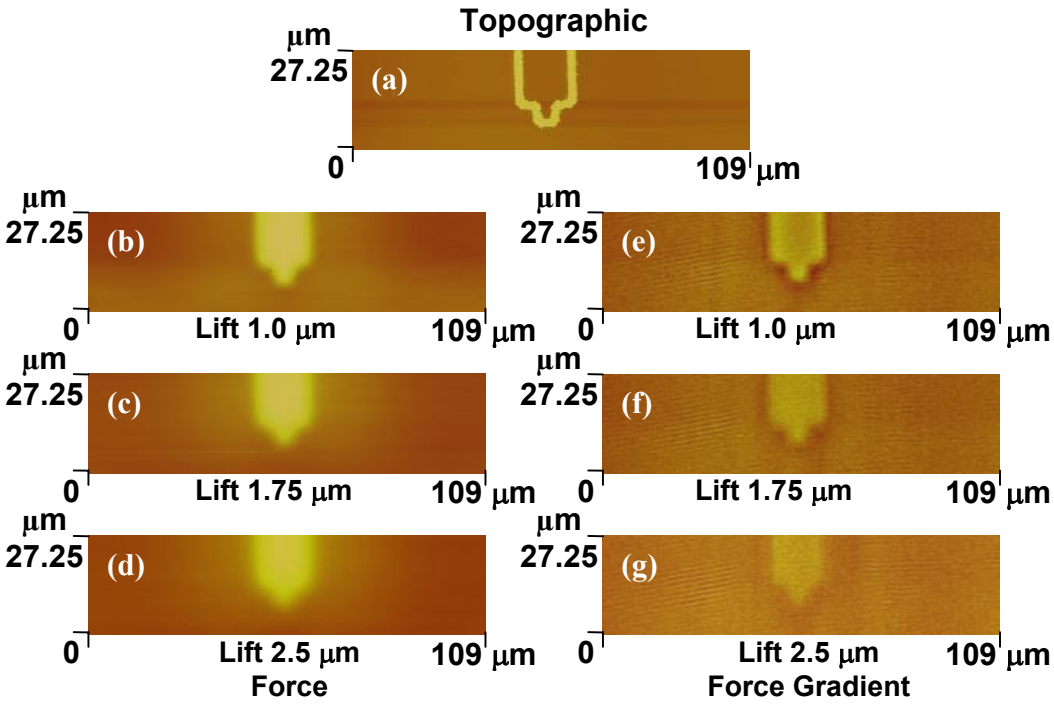

Figure 7.3.9. (a) AFM. Corresponding MFM force **(b)**, **(c)**, and **(d)**, and MFM force gradient **(e)**, **(f)**, and **(g)**, images of a type (A) sample circuit for three different tip lift heights of 1.0, 1.75, and 2.5 μm, respectively. MFM force with an ac-current $I_{rms} \approx 1.0$ mA and MFM force gradient with a dc-current $I \approx 9.1$ mA.

When comparing these images, obviously, the force gradient has a higher spatial resolution than the force has. For example, one can still see a small rectangular structure in the sample from Fig.7.3.10 (g) force gradient contrast image, but it shows as a rounded structure in Fig.7.3.10 (d) force contrast image.

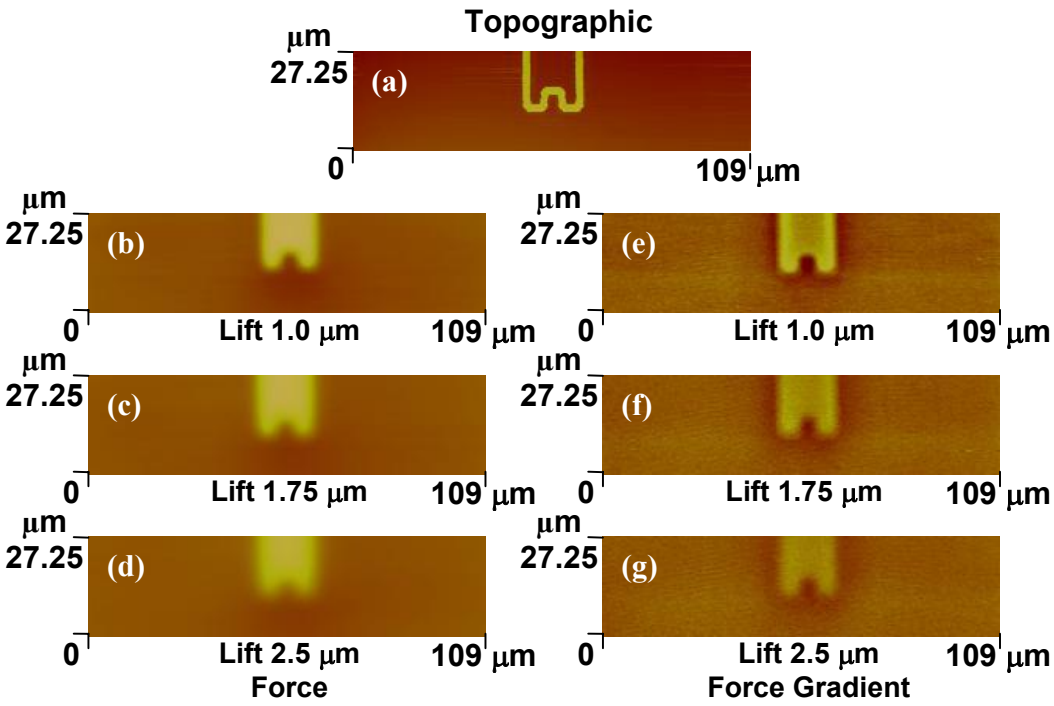

Figure 7.3.10. (a) AFM. Corresponding MFM force **(b)**, **(c)**, and **(d)**, and MFM force gradient **(e)**, **(f)**, and **(g)**, images of a type (B) sample circuit for three different tip lift heights of 1.0, 1.75, and 2.5 µm, respectively. MFM force with an ac-current $I_{rms} \approx 1.0$ mA and MFM force gradient with a dc-current $I \approx 23$ mA.

In contrast to the force gradient, the cantilever contribution in the force images shifts the minimum signal and blurs the contour of the sample circuits in the image, which decreases the spatial resolution. However, for force gradient this is only possible at much higher currents.

Before starting the data analysis, we will briefly discuss the resolution criteria. Unlike the sample containing one straight wire, we need to consider the inter-influence from the nearby wires for these two types of the circuits. We can see these two circuits as three rectangular turn structures superposed as shown in Fig.7.3.11.

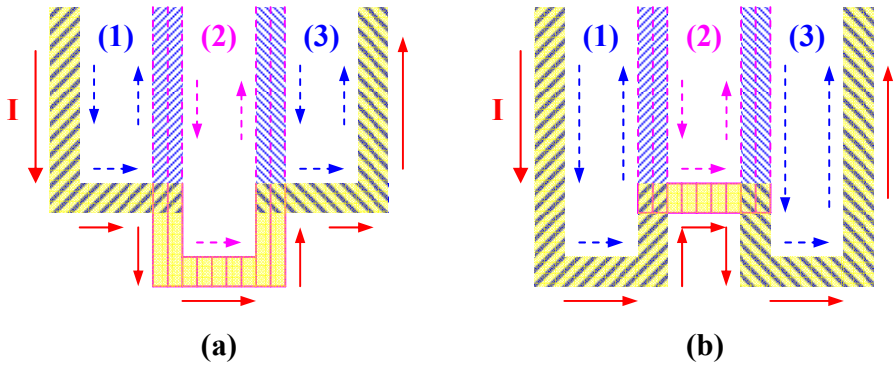

Figure 7.3.11. Schematic representation of the two types of samples consisted by three rectangular turn structures for each type. The dashed arrows represent the current for each rectangular turn and the full arrows are for final formed current path. The current in the intersection parts are cancelled out due to the inverse direction of the currents from different rectangular structures.

From the preceding results, the MFM signals for each rectangular turn show a localized image roughly in the area of the sample. This looks like we could use general criteria for microscopic resolution, such as the Rayleigh, Sparrow, and Houston resolution criteria [140-142], for our data analysis. But, after careful consideration, we found these criteria can not be used. The reasons are as follows:

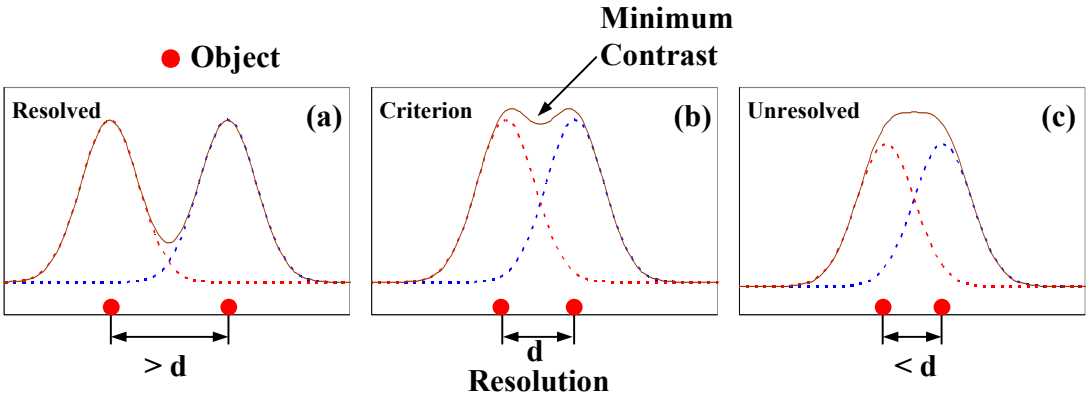

Figure 7.3.12. Schematic illustrating the general definition of the spatial resolution.

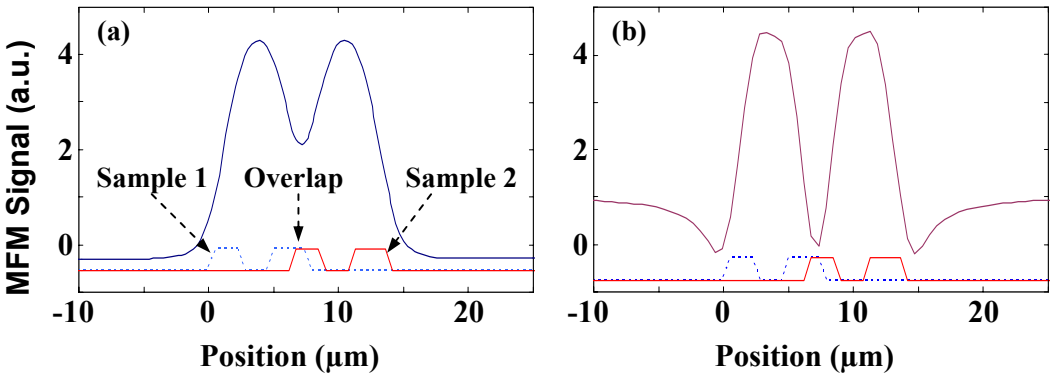

Figure 7.3.13. Simulation result of MFM signal for two rectangular turns overlapped with a lift height of 1.0 μm. **(a)** Force. **(b)** Force gradient. Obviously, force gradient has a higher spatial resolution than force has if comparing these two pictures.

Figure 7.3.12 shows an idea in general resolution criteria. The main point is two profile peaks from two sources move close together from resolved. When their overlapping profile comes to a minimum contrast that the human eye can detect as shown in Fig.7.3.12 (b), the separation between two sources is defined as the spatial resolution. The key point is two sources do not touch together at critical point even in the unresolved situation. But, if we consider two rectangular turns as two sources, since the FWHM of the signal peak for each one is narrower than the width of the rectangular turn, the overlap profile can still be resolved into two peaks when two rectangular turns touch together and even overlap. This is shown in Figure 7.3.13 from simulation result.

Therefore, we can not use these criteria to analyze MFM images. However, the objective is to locate a faulty device in this research. That is to try to obtain an accurate current path from MFM images. How accurate would it be to obtain the path from MFM images? This is the question about the spatial resolution we would like to answer in this work. In the previous case of the faulty current path formed a straight line between V_{DD} and V_{SS}, to obtain the current path we only need to locate a single point (Current path is perpendicular to V_{DD} and V_{SS} and passes through this point). In the zigzag shape of the current path, obviously, several points are needed to obtain an accurate path. For each straight line segment at least one point is needed. For example, in order to obtain the current path in Fig. 7.3.8 type (A) or (B) sample circuits, at least five points are needed to

locate w_3, w_4, w_5 w_6, and w_7, respectively. Note, here we ignored locating V_{DD} and V_{SS} (in general, they are easier to locate due to their larger sizes), we also assume there are only two possible directions of straight line segments in our discussions. One is along the x-axis, the other is along the y-axis. This assumption is generally true for most integrated circuit designs. After locating a point, the current path is assured to be in a line along the x-axis or y-axis and passing through the point. In addition, the MFM images show a round shape at each intersection since the current flowing through the intersection would not turn at a right angle. To minimize the error, the middle of each straight line segment will be chosen for the location. In the following we will use our devised method to locate w_3, w_4, w_5 w_6, and w_7 of sample circuits in Fig.7.3.8 from MFM images. MFM line scans are chosen along the y-axis for locating w_3, w_5, and w_7, and along the x-axis for w_4 and w_6. All line scans are crossed through the middle of each wire. We will use two lift pairs, 1.0 ~1.75 μm and 1.75 ~ 2.5 μm, to locate the wires, respectively. Table 7.5 shows the results for type (A) sample with the lift pair of 1.0 ~ 1.75 μm and 1.75 ~ 2.5 μm. The results for type (B) sample are shown in Table 7.6. The current path can be obtained from these results as shown in Figure 7.3.14 for type (A) and Figure 7.3.15 for type (B).

Table 7.5. The experimental and theoretical results are for type (A) sample. The signals were taken at tip lift pair of 1.0~1.75 μm and 1.75~2.5 μm with an ac-current I_{rms}≈1.0 mA for MFM force and a dc-current I ≈ 9.1 mA for MFM force gradient. The experimental results come from the images in the scan range of 109 μm with 256 samples and simulation uses 170μm/300points.

Detection method	w_3 (μm) (0 < y < 2.5)		w_4 (μm) (5.0 < y < 7.5)		w_5 (μm) (5.0 < y < 7.5)		w_6 (μm) (5.0 < x < 7.5)		w_7 (μm) (10 < x < 12.5)	
	Theory	Exp.	Theory	Exp.	Theory	Exp.	Theory	Exp.	Theory	Exp.
Force Lift pair:1.0~1.75μm (Position μm)	0.3	0.8	5.65	5.9	5.75	5.9	5.81	6.0	11.73	11.9
Force Lift pair:1.75~2.5μm (Position μm)	-0.05	0.5	5.39	5.6	5.44	5.6	5.52	5.8	12.20	12.4
Force gradient Lift pair:1.0~1.75μm (Position μm)	0.75	~1.5	5.91	~7.0	6.08	~6.5	6.14	~7.0	11.36	~11.4
Force gradient Lift pair:1.75~2.5μm (Position μm)	0.49	~1.5	5.85	~7.0	6.03	~6.5	6.06	~5.5	11.44	~12.3

Table 7.6. The experimental and theoretical results are for type (B) sample. The signals were taken at tip lift pair of 1.75 ~ 2.5 μm and 1.75 ~ 2.5 μm with an ac-current I_{rms}≈1.0 mA for MFM force and a dc-current I ≈ 23 mA for MFM force gradient. The experimental results come from the images in the scan range of 109 μm with 256 samples and simulation uses 170μm/300points.

Detection method	w_3 (μm) (5.0 < y < 7.5)		w_4 (μm) (0 < y < 2.5)		w_5 (μm) (0 < y < 2.5)		w_6 (μm) (5.0 < x < 7.5)		w_7 (μm) (10 < x < 12.5)	
	Theory	Exp.	Theory	Exp.	Theory	Exp.	Theory	Exp.	Theory	Exp.
Force Lift pair:1.0~1.75μm (Position μm)	6.12	6.9	0.28	1.2	0.28	1.2	6.58	6.2	10.96	11.3
Force Lift pair:1.75~2.5μm (Position μm)	5.87	5.5	-0.08	0.2	-0.06	0.3	6.78	5.7	10.76	12.4
Force gradient Lift pair:1.0~1.75μm (Position μm)	6.33	6.5	0.74	1.3	0.76	0.9	6.34	6.0	11.16	11.2
Force gradient Lift pair:1.75~2.5μm (Position μm)	6.48	~7.0	0.45	~0.7	0.46	~0.4	6.37	7.0	11.12	11.1

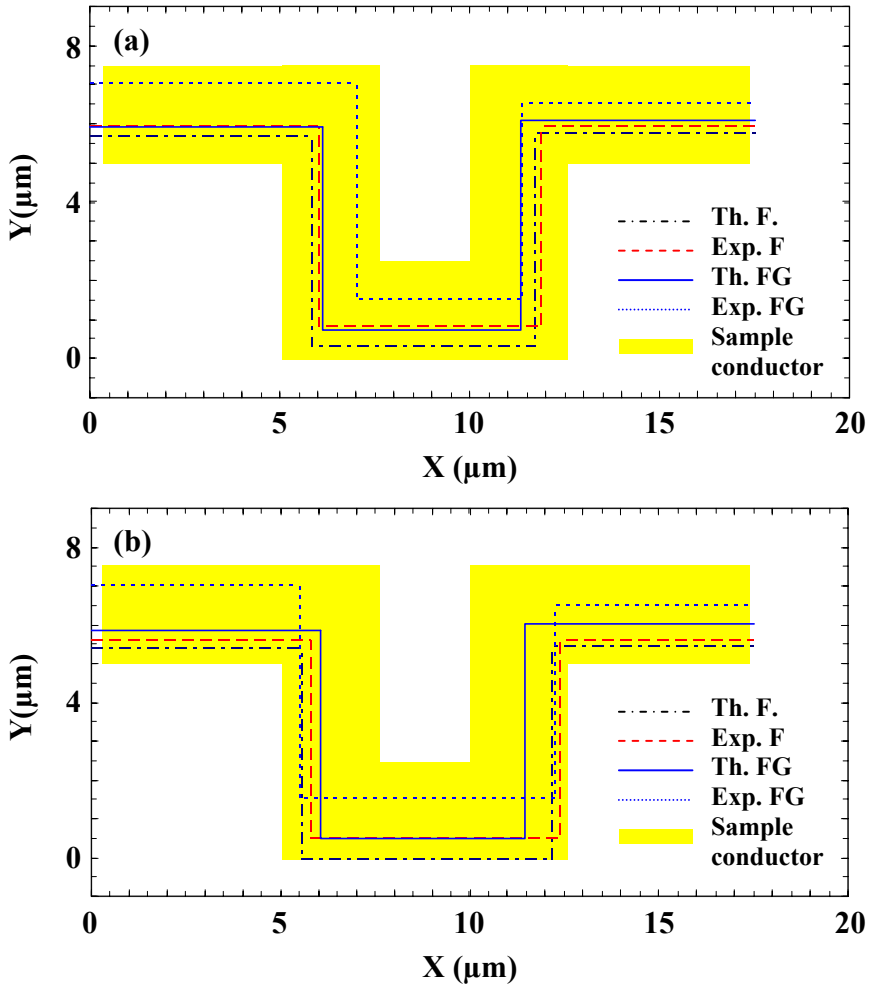

Figure 7.3.14. The current path for type (A) sample by using lift pair of 1.0 ~ 1.75 μm in **(a)** and 1.75 ~ 2.5 μm in **(b)**.

We did not consider the noise in these calculations. Experimental results were obtained by using Topographic images to calibrate the conductor positions. The results show excellent agreement between the experiment and the simulation. The slight difference between them mainly comes from the noise and digital sampling (~0.43 μm/sample). An accurate current path was obtained from MFM images by using the devised method even though the MFM images looks blurry at the lift height of 2.5 μm. Also, we can see that the location from the force gradient is much more accurate than the location from the force. The location from the force is at its limit with the lift pair of 1.75 ~ 2.5 μm since

the location is just at the edge of the sample for w_3 of type (A) and for w_4 and w_5 of type (B), which is the smallest structure that could be accurately located at the tip lift height over 1.75 μm by using the devised method.

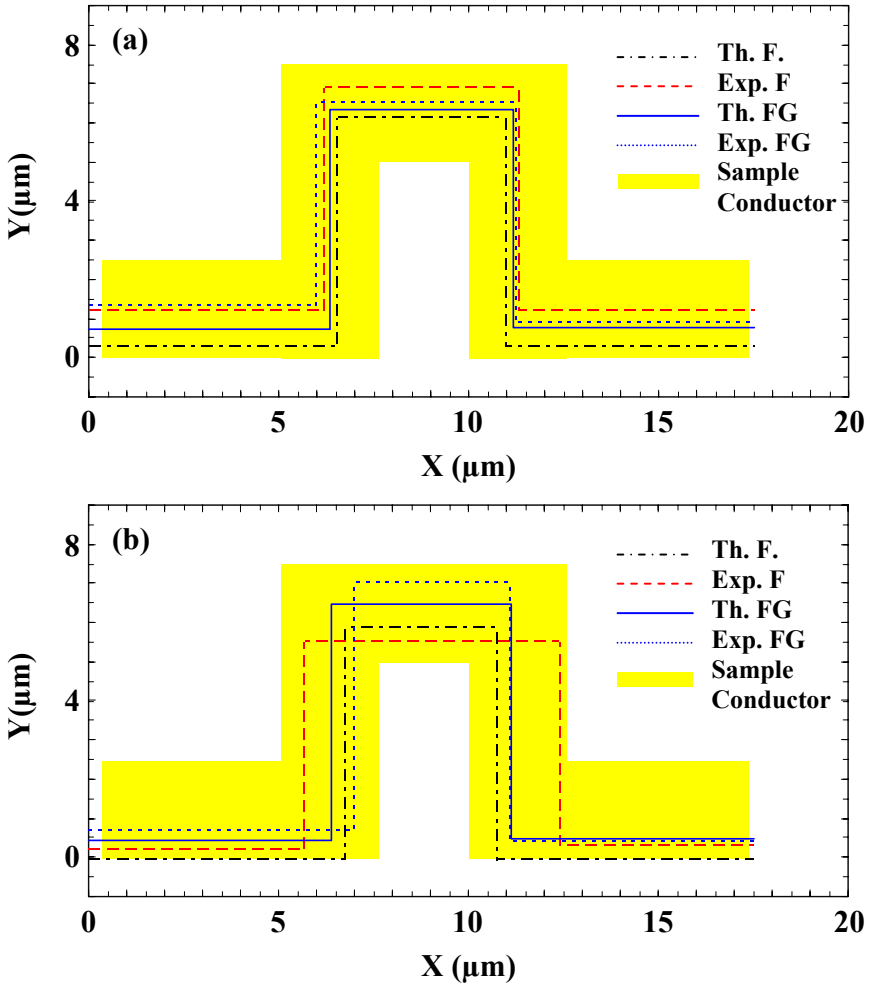

Figure 7.3.15. The current path for type (B) sample by using lift pair of 1.0 ~ 1.75 μm in **(a)** and 1.75 ~ 2.5 μm in **(b)**.

In addition, we can see the influence from the nearby wires on the location. For example, the influence on w_3 is different for these two types of samples. Type (B) has less error in locating w_3 from MFM images than type (A).

7.3.2.1 Simulations for Larger Sample to Probe Distances

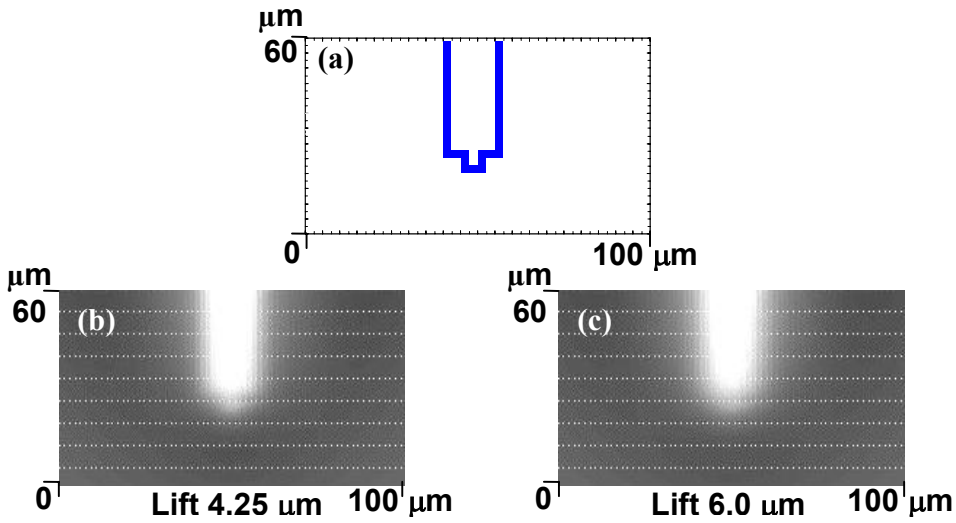

Figure 7.3.16. (a) Type (A) sample circuit. Corresponding simulation images of MFM force **(b)** and **(c)** with two different tip lift heights of 4.25 and 6.0 µm, respectively.

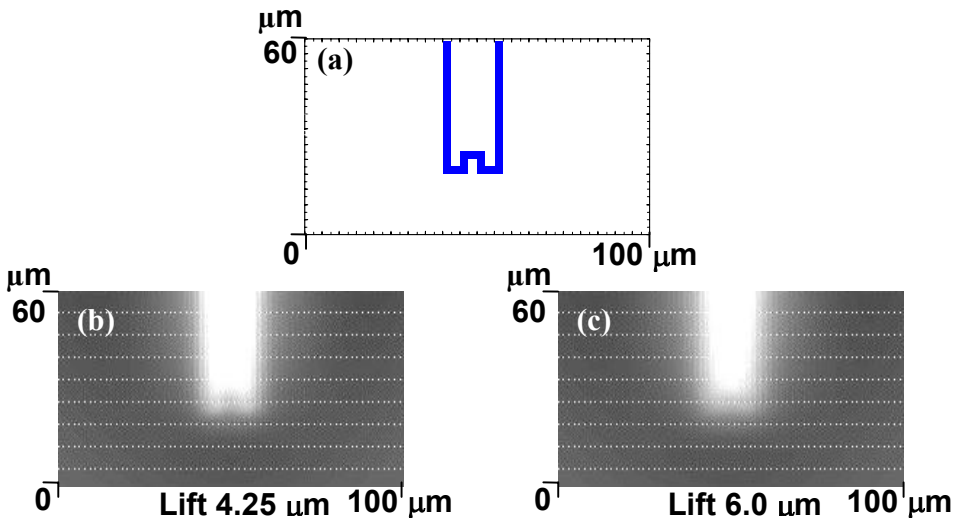

Figure 7.3.17. (a) Type (B) sample circuit. Corresponding simulation images of MFM force **(b)** and **(c)** with two different tip lift heights of 4.25 and 6.0 µm, respectively.

Before closing this section, we would like to see how high the tip lift is when we can not see the zigzag current path in MFM images for type (A) and (B) sample. In this case we

can use the general resolution criteria for our data analysis. From Fig. 7.3.9 and 7.3.10, we can still deduce a zigzag shape of the sample circuits from the MFM images at tip lift height of 2.5 μm. This is almost the highest lift height operated in contact/lift^{TM} mode of E-Scope. To perform a higher lift experiment, some changes are required, such as putting some layers above the sample circuits. An easier way is to use our modeling simulations. Figure 7.3.16 and 7.3.17 respectively show the MFM force images for type (A) and (B) at a tip lift height of 4.25 μm and 6.0μm (ignored current since the absolute values are not considered). From these images, it can be seen that the offset current path in the type A sample can not be observed at a tip lift of 6.0 μm in the MFM force image but it can still be easily seen at a lift of 4.25 μm. This means the MFM force image can not be easily distinguished at these small current paths over ~6.0 μm. Note that the noise was not considered in our simulation images. Obviously, the noise will blur the image and decrease the resolution of the experiment. A detailed analysis considering the SNR and thus the absolute value of the signal will be left for future work. Our modeling calculations will provide an easier way to perform this task.

7.4 Simple Imaging Technique Based on the Location Method

In the previous sections we have discussed the fault location. However, a way to make this technique more applicable and useful to find the location of the current paths is to use it in an imaging mode. Since the method uses the crossing point of two tip lift images, we can simply subtract two images and then set a threshold at zero point which should trace the current paths. As an example, let us consider images shown in Fig. 7.3.10. Figure 7.4.1 (a) shows a subtracted and threshold image from force images at tip lift heights of 1.0 μm and 2.5 μm (Fig.7.3.10 (b) and (d), respectively). The zero threshold outline indicated by the dashed line is clearly seen in the image. Fig.7.4.1 (b) is the overlay of the zero point outline and the corresponding topographic image. The zero points located inside the conducting line demonstrate the the method works very effectively.

Experimental force gradient results are shown in Fig. 7.4.2. The simulation results of force and force gradient are respectively shown in Fig.7.4.3 and Fig.7.4.4. The

simulations verify the experimental results. This technique is simple as we only need two images with different tip lift heights, then subtract them from each other, and simply process the result image to show the zero crossing contour which directly indicates the current paths.

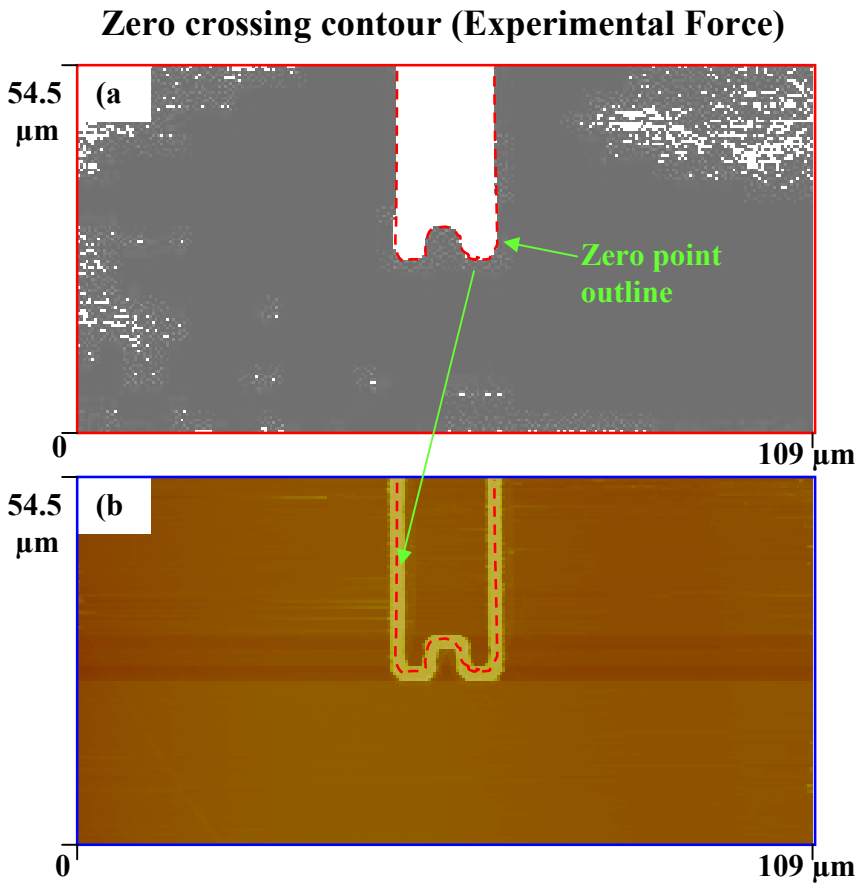

Figure 7.4.1. (a) A subtracted and processed image of the two experimental force images with different tip lift height (1.0µm and 2.5µm) clearly shows the outline of the zero points which is indicated by the dashed line. **(b)** Dashed line (zero points) overlaid on the corresponding topographic image illustrates that zero points are located inside the conducting line. The image uses 109 µm per 256 data points.

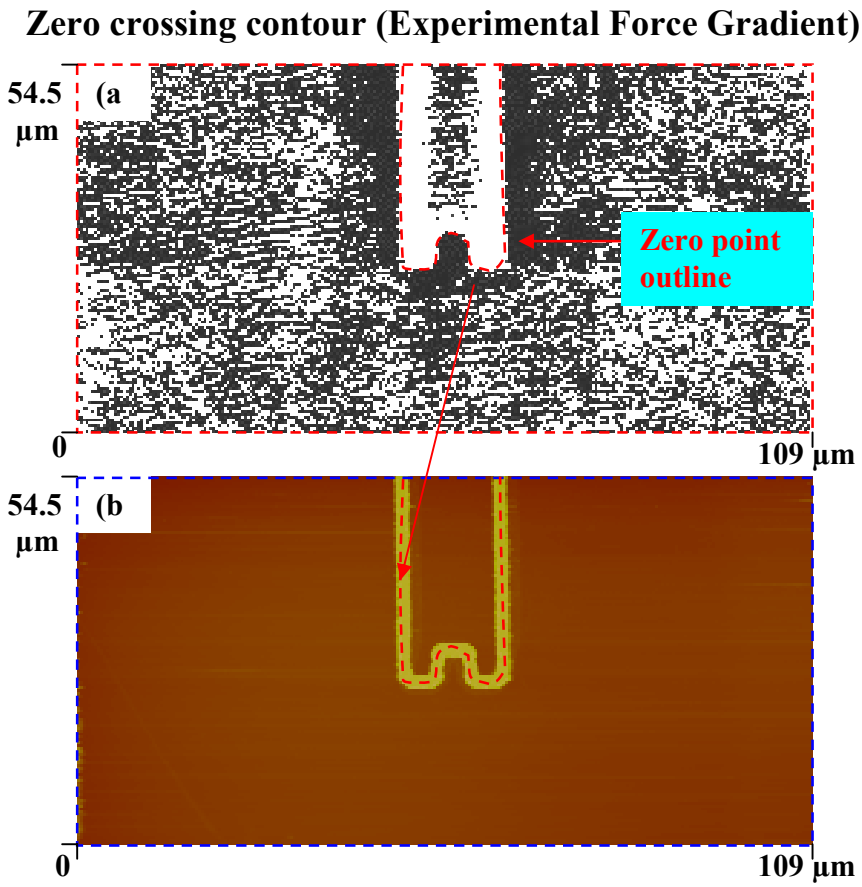

Figure 7.4.2. (a) A subtracted and processed image of the two experimental force gradient images with different tip lift height (1.0µm and 2.5µm) clearly shows the outline of the zero points which is indicated by the dashed line. **(b)** Dashed line (zero points) overlaid on the corresponding topographic image illustrates that zero points are located inside the conducting line. The image uses 109µm per 256 data points.

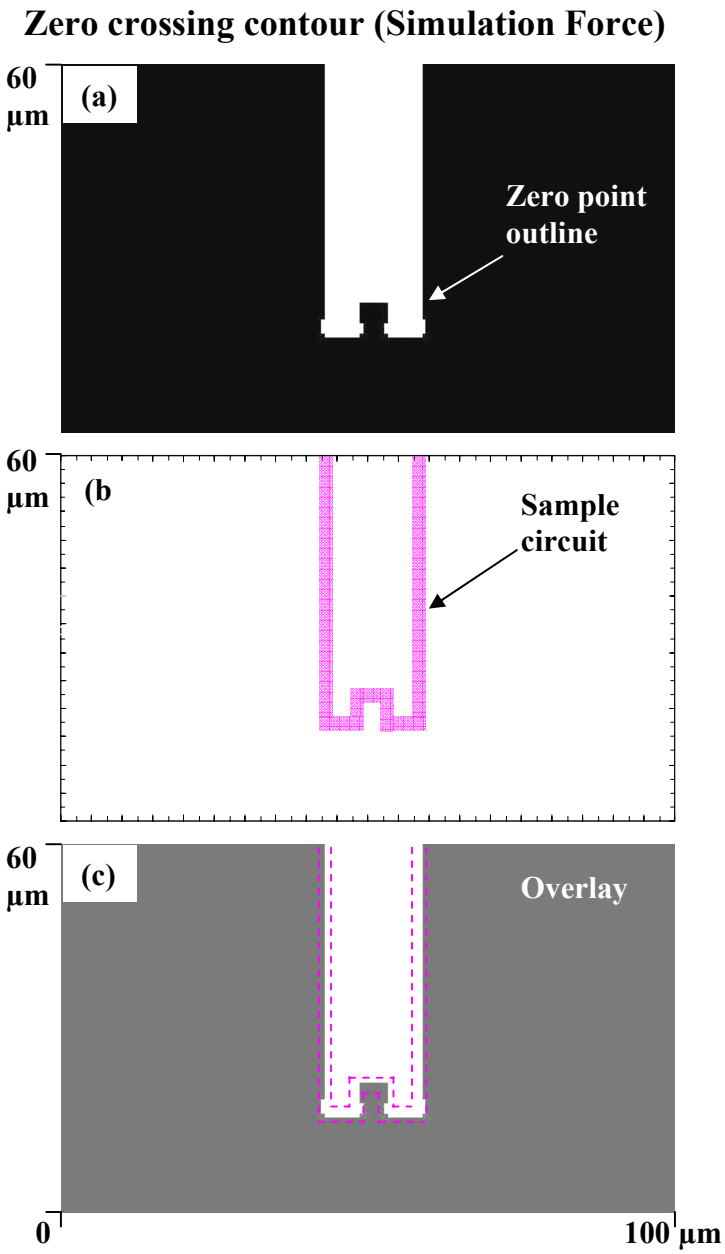

Figure 7.4.3. (a) A subtracted and processed image of the two simulation force images with different tip lift height (1.0µm and 2.5µm) clearly shows the outline of the zero points. **(b)** Corresponding model circuit. **(c)** Overlay of the (a) and (b) illustrates that zero points are located inside the conducting lines indicated by the dashed lines. The irregular shapes of the outline come from the limitation of the data points chosen in the simulation. The image uses 170 µm per 300 samples.

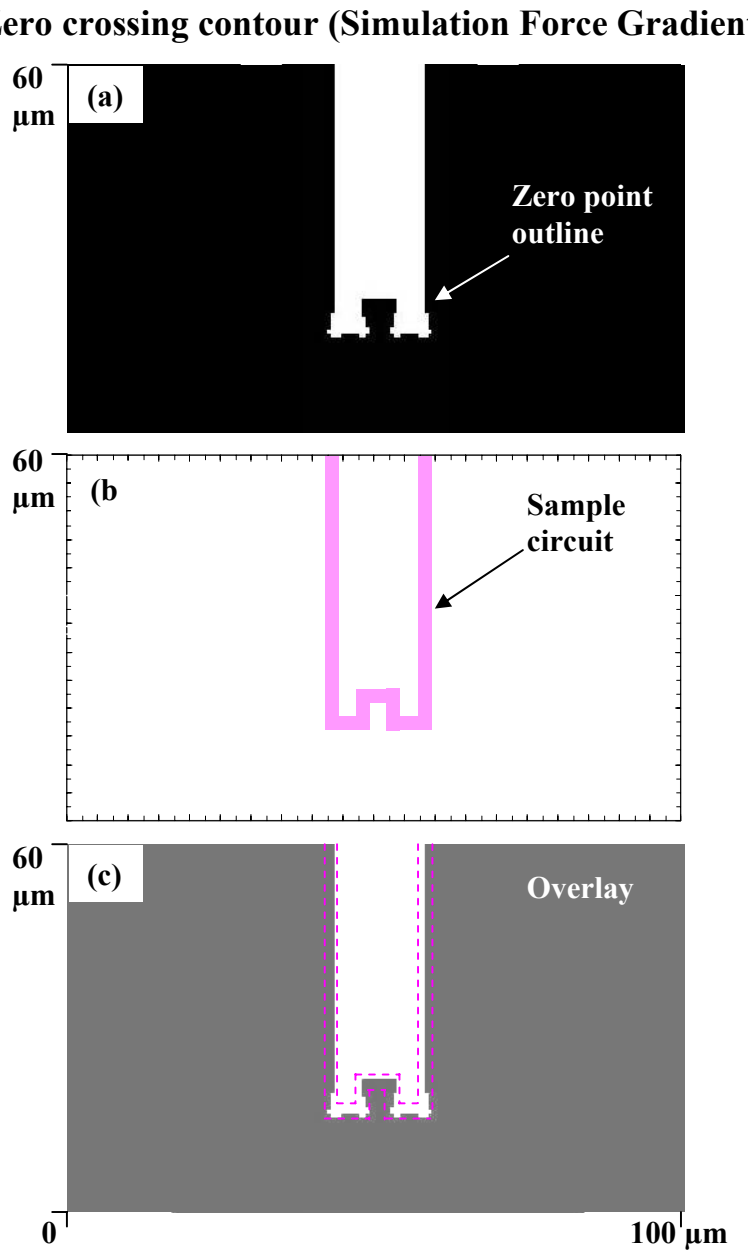

Figure 7.4.4. (a) A subtracted and processed image of the two simulation force gradient images with different tip lift height (1.0µm and 2.5µm) clearly shows the outline of the zero points. **(b)** Corresponding model circuit. **(c)** Overlay of the (a) and (b) illustrates that zero points are located inside the conducting line indicated by the dashed lines. Irregular shapes of the outline come from the limitation of the data points chosen in the simulation. The image uses 170 µm per 300 data points.

7.5 Locating Faults with Current Flowing in the Power Lines

The model circuit for an IC fault shown in Fig.5.1.1 is quite simple. In reality, there are many circuits between V_{DD} and ground V_{SS} in ICs. If there is more than one fault in the circuit or the circuit has considerable steady state current flow, the current will flow through V_{DD} and V_{SS} in addition to the faulty device. In this situation, the current will go through the V_{DD} and V_{SS} forming the current path as shown as in Fig.7.4.5. The following will present the simulation results for imaging this type of current.

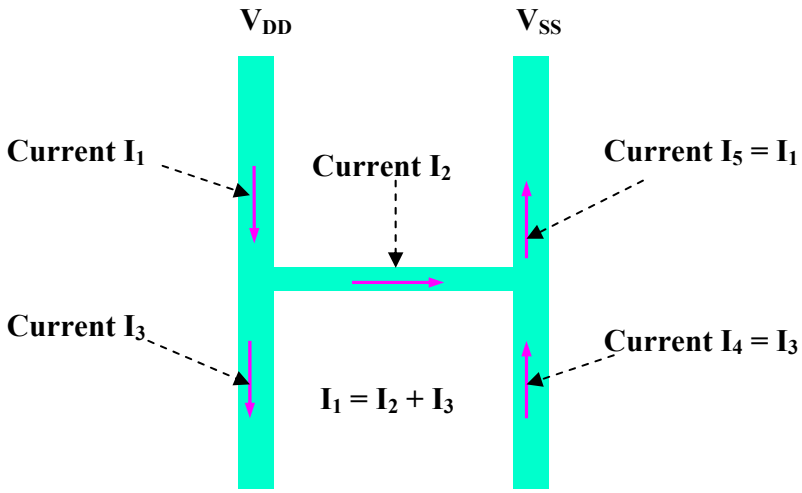

Figure7.4.5. A model circuit illustrates the current goes through the V_{DD} and V_{SS}. Assumption of the current relation is for simple case.

In this section, a simple case is considered. We assume that current $I_1 = 2I_2 = 2I_3$ and the conducting lines, V_{DD} and V_{SS}, are long. Simulations of MFM images of force and force gradient with a tip lift height of 1.0 μm are shown in Figure 7.4.6 (a) and (b), respectively. MFM signals along the dashed line in Fig.7.4.6 (c) and cross the middle of the w_3 with three tip lift heights are shown in Figure 7.4.7 (a) for force and (b) for force gradient. In Fig.7.4.7, we see that there is no cross over point with different lift heights in the force signal. This is due to the force generated by I_3 and I_4 as shown in Fig.7.4.5, which can be understood using a similar analysis as in section 7.1. Therefore, the devised method can not be used directly in the force detection for this situation. However, a further analysis

of the subtracted signal shown in Figure 7.4.8 (a) suggests a modification to the method. By increasing threshold from zero crossover to cut the subtracted signal as indicated by the dashed-dotted line in Fig.7.4.8 (a), a circuit path can be estimated. A processed image in Fig. 7.4.8 (b) shows the outline of the threshold crossing points located inside the conducting lines, which demonstrates the modified method works reasonably well.

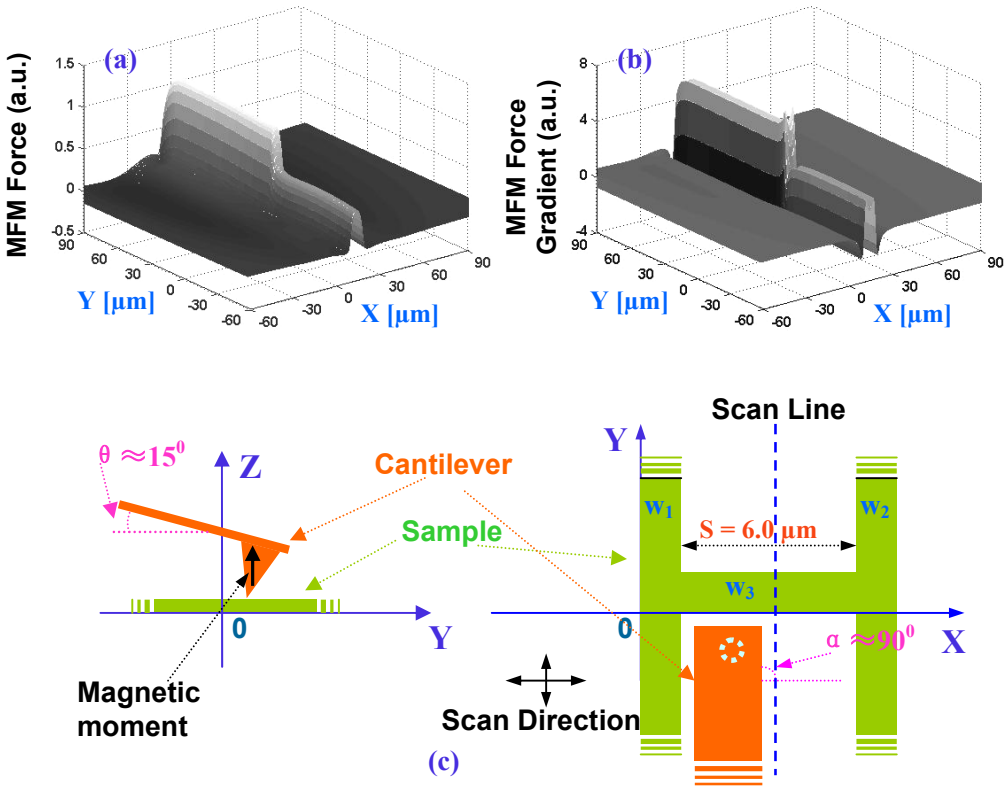

Figure 7.4.6. Simulation magnetic force **(a)** and force gradient **(b)** with the scan height of d = 1.0 μm, magnetization along the z-axis, and $\alpha = 90^0$, $\theta = 75^0$ for the cantilever. Schematic drawing of orientation of the sample, cantilever, and magnetic moment in **(c)**. Sample size $w_1 = w_2 = w_3 = 2.0$ μm, and s = 6.0 μm.

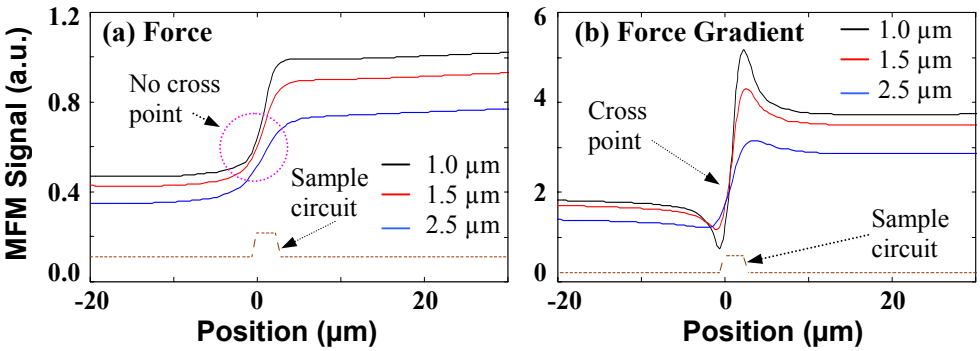

Figure 7.4.7. MFM signals, force (a) and force gradient (b), taken along the dashed line in Fig.7.4.6 (c), which crosses the middle of the w_3, with three tip lift heights, magnetization along the z-axis, and $\alpha = 90^0$, $\theta = 75^0$ for the cantilever. The cross section of the sample is indicated by the dashed lines.

Many other cases could be imagined. However, these will not be explored in this thesis. This simple example shows that faults can be located in the presence of a steady state current in the power and ground lines. It is left for future work to explore the effects of noise and the dynamic range of this modified technique.

In this thesis force using an applied sinusoidal current was investigated for imaging current with over layers. Application of the method to integrated circuits will be discussed in Appendix 3.

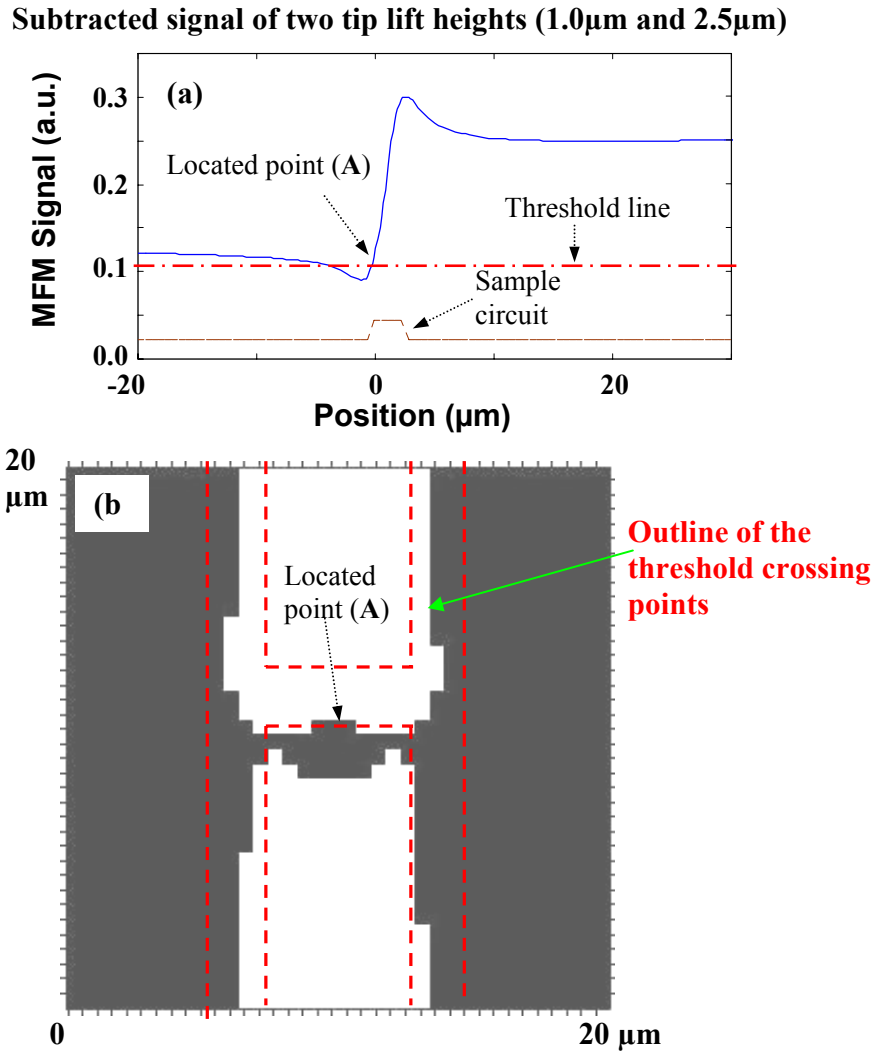

Figure 7.4.8. (a) Subtracted line signal of two tip-lift heights (1.0µm and 2.5µm) along the dashed line in Fig.7.4.6 (c). Located point (A) is from the threshold line crossing the signal. **(b)** The processed image of the two force images with different tip lift height (1.0µm and 2.5µm) clearly shows the outline of the threshold crossing points. Corresponding located point (A) is indicated in the image. The dashed lines indicate the location of the conducting lines of the sample circuits. Outline of the threshold crossing points located inside the conducting lines demonstrate that the method works well. Irregular shapes of the outline come from the few data points chosen in the simulation. The image uses 170 µm per 300 data points.

Chapter 8
CONCLUSIONS AND FUTURE CHALLENGES

8.1 Conclusion

In this research, we have presented a systematic study on current imaging of model circuits by MFM force and force gradient techniques. By comparing the signal to noise ratio and spatial resolution of these two techniques, we concluded that the force has much greater SNR, which results in better sensitivity, and enables the detection of much smaller currents than that of the force gradient. However, this comes at the price of reduced spatial resolution for force detection. We have experimentally achieved a measurement sensitivity of approximately 1.02 $\mu A/\sqrt{Hz}$ for force and 0.29 $mA/\sqrt{Hz}$ for force gradient in air without magnet to maintain the orientation of the magnetic moments of the probe during the measurement (~0.64 $\mu A/\sqrt{Hz}$ in air and ~0.095 $\mu A/\sqrt{Hz}$ in a vacuum for force with a magnet), which is consistent with the theoretical calculations.

We have also carried out a numerical modeling calculation of the magnetic fields and the MFM images. It has been concluded that the simple point-probe model that considers magnetic coating on the probe as a single moment, usually used to model MFM images, was not adequate to simulate MFM images of current flow in ICs. An extended model based on realistic MFM probe geometries that includes the magnetic coating on the cantilever of the probe has been introduced. Qualitative and quantitative comparison of the experimental results and simulation results were excellent. This has contributed to an understanding of the image formation in MFM. From the simulations we predicted that the thickness of the magnetic coating is not same on the different regions of the probe, which was verified by the cross section SEM images of the FIB milled probes. Therefore, this model provides an accurate means to simulate MFM images of currents flowing in Integrated Circuits.

From the simulation and experimental results, a method was devised to accurately locate the internal current path from MFM images with micrometer uncertainty for the model circuits. Since this technique can be easily implemental in commercial SPM systems this should be a useful technique for fault location in IC failure analysis when current flows through the device buried under several layers and no topographic features are on the surface to provide clues about the position of the device.

8.2 Future Challenges

In this research, we have performed a study on MFM current imaging in a vacuum, which improved the measurement sensitivity (~0.095 $\mu A/\sqrt{\mathbf{Hz}}$ in force). However, the SNR in a vacuum does not exhibit a square root of Q_{vacuum}/Q_{air} dependence, which is expected from theory. This requires further investigation.

The model provides some information about the tip magnetization. Using simulation comparing with the experimental to deduce the tip magnetization will be a good research topic.

Our research is based on the simple model circuits, more complicated and practical circuits are required to conduct further research.

Explore the effects of large currents flowing in V_{DD} and V_{SS} and demonstrate the technique on real devices.

APPENDIX 1
MAGNETIC FILED AND MAGNETIC FIELD GRADIENT

A1.1 Magnetic Field

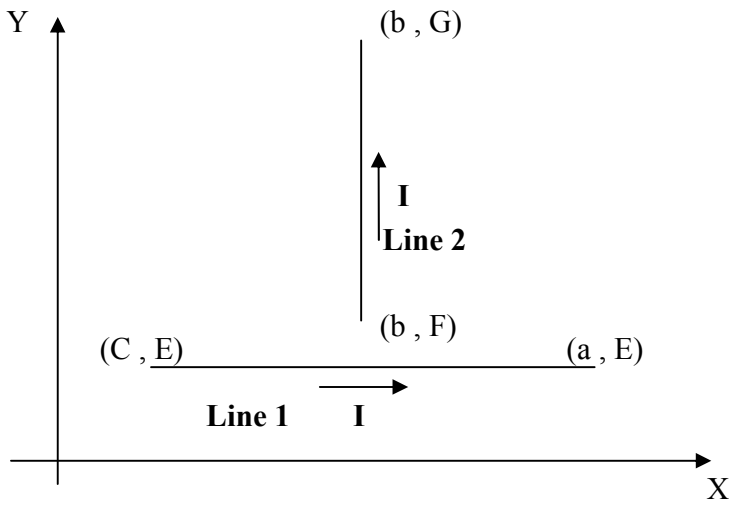

Figure A1.1. Two straight-line segments carry a current I.

Line 1

$B_x = 0$

$$B_y = \frac{I\mu_0}{4\pi}\left\{\frac{z}{\left((x-C)^2+(y-E)^2+z^2\right)^{1/2}\left((x-C)+\sqrt{(x-C)^2+(y-E)^2+z^2}\right)}-\frac{z}{\left((x-a)^2+(y-E)^2+z^2\right)^{1/2}\left((x-a)+\sqrt{(x-a)^2+(y-E)^2+z^2}\right)}\right\}$$

$$B_z = -\frac{I\mu_0}{4\pi}\left\{\frac{y-E}{\left((x-C)^2+(y-E)^2+z^2\right)^{1/2}\left((x-C)+\sqrt{(x-C)^2+(y-E)^2+z^2}\right)}-\frac{y-E}{\left((x-a)^2+(y-E)^2+z^2\right)^{1/2}\left((x-a)+\sqrt{(x-a)^2+(y-E)^2+z^2}\right)}\right\}$$

Line 2

$B_y = 0$

$$B_x = -\frac{I\mu_0}{4\pi}\left\{\frac{z}{\left((x-b)^2+(y-F)^2+z^2\right)^{1/2}\left((y-F)+\sqrt{(x-b)^2+(y-F)^2+z^2}\right)}-\frac{z}{\left((x-b)^2+(y-G)^2+z^2\right)^{1/2}\left((y-G)+\sqrt{(x-b)^2+(y-G)^2+z^2}\right)}\right\}$$

$$B_z = \frac{I\mu_0}{4\pi}\left\{\frac{x-b}{\left((x-b)^2+(y-F)^2+z^2\right)^{1/2}\left((y-F)+\sqrt{(x-b)^2+(y-F)^2+z^2}\right)}-\frac{x-b}{\left((x-b)^2+(y-G)^2+z^2\right)^{1/2}\left((y-G)+\sqrt{(x-b)^2+(y-G)^2+z^2}\right)}\right\}$$

A1.2 Magnetic Field Gradient

Line 1

$$\frac{\partial B_x}{\partial x} = 0$$

$$\frac{\partial B_y}{\partial x} = \frac{I\mu_0}{4\pi}\left\{\begin{array}{l}\dfrac{-z(x-C)}{\left((x-C)^2+(y-E)^2+z^2\right)^{3/2}\left((x-C)+\sqrt{(x-C)^2+(y-E)^2+z^2}\right)}+\dfrac{-z\left(1+\dfrac{x-C}{\sqrt{(x-C)^2+(y-E)^2+z^2}}\right)}{\sqrt{(x-C)^2+(y-E)^2+z^2}\left((x-C)+\sqrt{(x-C)^2+(y-E)^2+z^2}\right)^2} \\ +\dfrac{z(x-a)}{\left((x-a)^2+(y-E)^2+z^2\right)^{3/2}\left((x-a)+\sqrt{(x-a)^2+(y-E)^2+z^2}\right)}+\dfrac{z\left(1+\dfrac{x-a}{\sqrt{(x-a)^2+(y-E)^2+z^2}}\right)}{\sqrt{(x-a)^2+(y-E)^2+z^2}\left((x-a)+\sqrt{(x-a)^2+(y-E)^2+z^2}\right)^2}\end{array}\right\}$$

$$\frac{\partial B_z}{\partial x} = -\frac{I\mu_0}{4\pi}\left\{\begin{array}{l}\dfrac{-(y-E)(x-C)}{\left((x-C)^2+(y-E)^2+z^2\right)^{3/2}\left((x-C)+\sqrt{(x-C)^2+(y-E)^2+z^2}\right)}+\dfrac{-(y-E)\left(1+\dfrac{x-C}{\sqrt{(x-C)^2+(y-E)^2+z^2}}\right)}{\sqrt{(x-C)^2+(y-E)^2+z^2}\left((x-C)+\sqrt{(x-C)^2+(y-E)^2+z^2}\right)^2} \\ +\dfrac{(y-E)(x-a)}{\left((x-a)^2+(y-E)^2+z^2\right)^{3/2}\left((x-a)+\sqrt{(x-a)^2+(y-E)^2+z^2}\right)}+\dfrac{(y-E)\left(1+\dfrac{x-a}{\sqrt{(x-a)^2+(y-E)^2+z^2}}\right)}{\sqrt{(x-a)^2+(y-E)^2+z^2}\left((x-a)+\sqrt{(x-a)^2+(y-E)^2+z^2}\right)^2}\end{array}\right\}$$

$$\frac{\partial B_x}{\partial y} = 0$$

$$\frac{\partial B_y}{\partial y} = \frac{I\mu_0}{4\pi}\left\{\begin{array}{l}\dfrac{-z(y-E)}{\left((x-C)^2+(y-E)^2+z^2\right)^{3/2}\left((x-C)+\sqrt{(x-C)^2+(y-E)^2+z^2}\right)}+\dfrac{-z(y-E)}{\left((x-C)^2+(y-E)^2+z^2\right)\left((x-C)+\sqrt{(x-C)^2+(y-E)^2+z^2}\right)^2} \\ +\dfrac{z(y-E)}{\left((x-a)^2+(y-E)^2+z^2\right)^{3/2}\left((x-a)+\sqrt{(x-a)^2+(y-E)^2+z^2}\right)}+\dfrac{z(y-E)}{\left((x-a)^2+(y-E)^2+z^2\right)\left((x-a)+\sqrt{(x-a)^2+(y-E)^2+z^2}\right)^2}\end{array}\right\}$$

$$\frac{\partial B_z}{\partial y} = -\frac{I\mu_0}{4\pi}\left\{\begin{array}{l}\dfrac{(x-C)^2+z^2}{\left((x-C)^2+(y-E)^2+z^2\right)^{3/2}\left((x-C)+\sqrt{(x-C)^2+(y-E)^2+z^2}\right)}+\dfrac{-(y-E)^2}{\left((x-C)^2+(y-E)^2+z^2\right)\left((x-C)+\sqrt{(x-C)^2+(y-E)^2+z^2}\right)^2}\\ -\dfrac{(x-a)^2+z^2}{\left((x-a)^2+(y-E)^2+z^2\right)^{3/2}\left((x-a)+\sqrt{(x-a)^2+(y-E)^2+z^2}\right)}+\dfrac{(y-E)^2}{\left((x-a)^2+(y-E)^2+z^2\right)\left((x-a)+\sqrt{(x-a)^2+(y-E)^2+z^2}\right)^2}\end{array}\right\}$$

$$\frac{\partial B_x}{\partial z} = 0$$

$$\frac{\partial B_y}{\partial z} = \frac{I\mu_0}{4\pi}\left\{\begin{array}{l}\dfrac{(x-C)^2+(y-E)^2}{\left((x-C)^2+(y-E)^2+z^2\right)^{3/2}\left((x-C)+\sqrt{(x-C)^2+(y-E)^2+z^2}\right)}-\dfrac{z^2}{\left((x-C)^2+(y-E)^2+z^2\right)\left((x-C)+\sqrt{(x-C)^2+(y-E)^2+z^2}\right)^2}\\ -\dfrac{(x-a)^2+(y-E)^2}{\left((x-a)^2+(y-E)^2+z^2\right)^{3/2}\left((x-a)+\sqrt{(x-a)^2+(y-E)^2+z^2}\right)}+\dfrac{z^2}{\left((x-a)^2+(y-E)^2+z^2\right)\left((x-a)+\sqrt{(x-a)^2+(y-E)^2+z^2}\right)^2}\end{array}\right\}$$

$$\frac{\partial B_z}{\partial z} = -\frac{I\mu_0}{4\pi}\left\{\begin{array}{l}\dfrac{-(y-E)z}{\left((x-C)^2+(y-E)^2+z^2\right)^{3/2}\left((x-C)+\sqrt{(x-C)^2+(y-E)^2+z^2}\right)}+\dfrac{-(y-E)z}{\left((x-C)^2+(y-E)^2+z^2\right)\left((x-C)+\sqrt{(x-C)^2+(y-E)^2+z^2}\right)^2}\\ +\dfrac{(y-E)z}{\left((x-a)^2+(y-E)^2+z^2\right)^{3/2}\left((x-a)+\sqrt{(x-a)^2+(y-E)^2+z^2}\right)}+\dfrac{(y-E)z}{\left((x-a)^2+(y-E)^2+z^2\right)\left((x-a)+\sqrt{(x-a)^2+(y-E)^2+z^2}\right)^2}\end{array}\right\}$$

Line 2

$$\frac{\partial B_x}{\partial x} = -\frac{I\mu_0}{4\pi}\left\{\begin{array}{l}\dfrac{-z(x-b)}{\left((x-b)^2+(y-F)^2+z^2\right)^{3/2}\left((y-F)+\sqrt{(x-b)^2+(y-F)^2+z^2}\right)}+\dfrac{-z(x-b)}{\left((x-b)^2+(y-F)^2+z^2\right)\left((y-F)+\sqrt{(x-b)^2+(y-F)^2+z^2}\right)^2}\\ +\dfrac{z(x-b)}{\left((x-b)^2+(y-G)^2+z^2\right)^{3/2}\left((y-G)+\sqrt{(x-b)^2+(y-G)^2+z^2}\right)}+\dfrac{z(x-b)}{\left((x-b)^2+(y-G)^2+z^2\right)\left((y-G)+\sqrt{(x-b)^2+(y-G)^2+z^2}\right)^2}\end{array}\right\}$$

$$\frac{\partial B_y}{\partial x} = 0$$

$$\frac{\partial B_z}{\partial x} = \frac{I\mu_0}{4\pi}\left\{\begin{array}{l}\dfrac{(y-F)^2+z^2}{\left((x-b)^2+(y-F)^2+z^2\right)^{3/2}\left((y-F)+\sqrt{(x-b)^2+(y-F)^2+z^2}\right)}+\dfrac{-(x-b)^2}{\left((x-b)^2+(y-F)^2+z^2\right)\left((y-F)+\sqrt{(x-b)^2+(y-F)^2+z^2}\right)^2}\\ -\dfrac{(y-G)^2+z^2}{\left((x-b)^2+(y-G)^2+z^2\right)^{3/2}\left((y-G)+\sqrt{(x-b)^2+(y-G)^2+z^2}\right)}+\dfrac{(x-b)^2}{\left((x-b)^2+(y-G)^2+z^2\right)\left((y-G)+\sqrt{(x-b)^2+(y-G)^2+z^2}\right)^2}\end{array}\right\}$$

$$\frac{\partial B_x}{\partial y} = -\frac{I\mu_0}{4\pi}\left\{\begin{array}{l}\dfrac{-z(y-F)}{\left((x-b)^2+(y-F)^2+z^2\right)^{3/2}\left((y-F)+\sqrt{(x-b)^2+(y-F)^2+z^2}\right)}+\dfrac{-z\left(1+\dfrac{y-F}{\sqrt{(x-b)^2+(y-F)^2+z^2}}\right)}{\sqrt{(x-b)^2+(y-F)^2+z^2}\left((y-F)+\sqrt{(x-b)^2+(y-F)^2+z^2}\right)^2}\\ +\dfrac{z(y-G)}{\left((x-b)^2+(y-G)^2+z^2\right)^{3/2}\left((y-G)+\sqrt{(x-b)^2+(y-G)^2+z^2}\right)}+\dfrac{z\left(1+\dfrac{y-G}{\sqrt{(x-b)^2+(y-G)^2+z^2}}\right)}{\sqrt{(x-b)^2+(y-G)^2+z^2}\left((y-G)+\sqrt{(x-b)^2+(y-G)^2+z^2}\right)^2}\end{array}\right\}$$

$$\frac{\partial B_y}{\partial y} = 0$$

$$\frac{\partial B_z}{\partial y} = \frac{I\mu_0}{4\pi}\left\{\begin{array}{l} \dfrac{-(x-b)(y-F)}{\left((x-b)^2+(y-F)^2+z^2\right)^{3/2}\left((y-F)+\sqrt{(x-b)^2+(y-F)^2+z^2}\right)}+\dfrac{-(x-b)\left(1+\dfrac{y-F}{\sqrt{(x-b)^2+(y-F)^2+z^2}}\right)}{\sqrt{(x-b)^2+(y-F)^2+z^2}\left((y-F)+\sqrt{(x-b)^2+(y-F)^2+z^2}\right)^2} \\ +\dfrac{(x-b)(y-G)}{\left((x-b)^2+(y-G)^2+z^2\right)^{3/2}\left((y-G)+\sqrt{(x-b)^2+(y-G)^2+z^2}\right)}+\dfrac{(x-b)\left(1+\dfrac{y-G}{\sqrt{(x-b)^2+(y-G)^2+z^2}}\right)}{\sqrt{(x-b)^2+(y-G)^2+z^2}\left((y-G)+\sqrt{(x-b)^2+(y-G)^2+z^2}\right)^2} \end{array}\right\}$$

$$\frac{\partial B_x}{\partial z} = -\frac{I\mu_0}{4\pi}\left\{\begin{array}{l} \dfrac{(x-b)^2+(y-F)^2}{\left((x-b)^2+(y-F)^2+z^2\right)^{3/2}\left((y-F)+\sqrt{(x-b)^2+(y-F)^2+z^2}\right)}-\dfrac{z^2}{\left((x-b)^2+(y-F)^2+z^2\right)\left((y-F)+\sqrt{(x-b)^2+(y-F)^2+z^2}\right)^2} \\ -\dfrac{(x-b)^2+(y-G)^2}{\left((x-b)^2+(y-G)^2+z^2\right)^{3/2}\left((y-G)+\sqrt{(x-b)^2+(y-G)^2+z^2}\right)}+\dfrac{z^2}{\left((x-b)^2+(y-G)^2+z^2\right)\left((y-G)+\sqrt{(x-b)^2+(y-G)^2+z^2}\right)^2} \end{array}\right\}$$

$$\frac{\partial B_y}{\partial z} = 0$$

$$\frac{\partial B_z}{\partial z} = \frac{I\mu_0}{4\pi}\left\{\begin{array}{l} \dfrac{-(x-b)z}{\left((x-b)^2+(y-F)^2+z^2\right)^{3/2}\left((y-F)+\sqrt{(x-b)^2+(y-F)^2+z^2}\right)}+\dfrac{-(x-b)z}{\left((x-b)^2+(y-F)^2+z^2\right)\left((y-F)+\sqrt{(x-b)^2+(y-F)^2+z^2}\right)^2} \\ +\dfrac{(x-b)z}{\left((x-b)^2+(y-G)^2+z^2\right)^{3/2}\left((y-G)+\sqrt{(x-b)^2+(y-G)^2+z^2}\right)}+\dfrac{(x-b)z}{\left((x-b)^2+(y-G)^2+z^2\right)\left((y-G)+\sqrt{(x-b)^2+(y-G)^2+z^2}\right)^2} \end{array}\right\}$$

APPENDIX 2
MODELING MAGNETIC FIELD GRADIENT

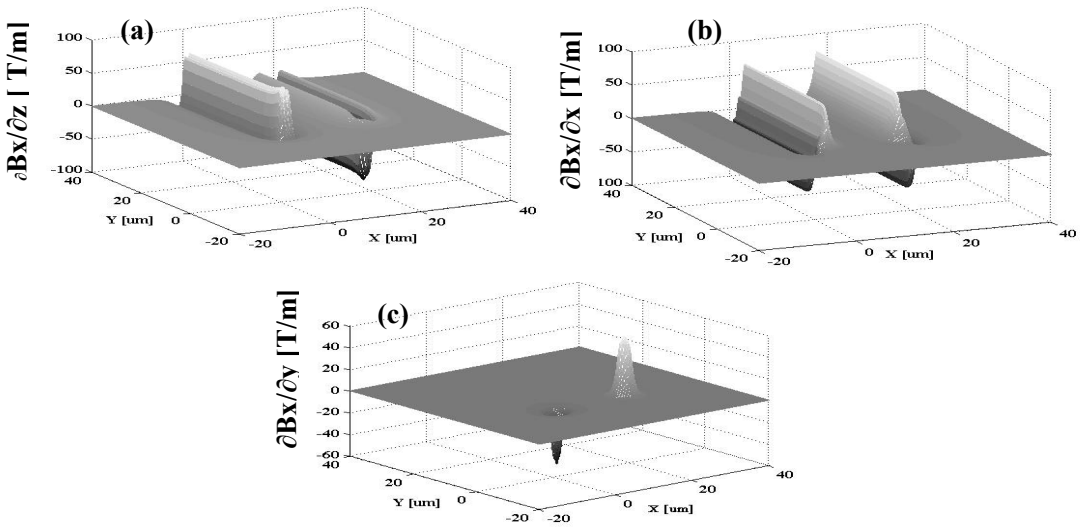

Figure A2.1. x-component of the magnetic field derivatives with respect to the x, y, z-coordinate at z =1.0 μm above the sample surface (z =0 plane) with a current of I = 1 mA in a direction as indicated in Figure 4.4.1(d).

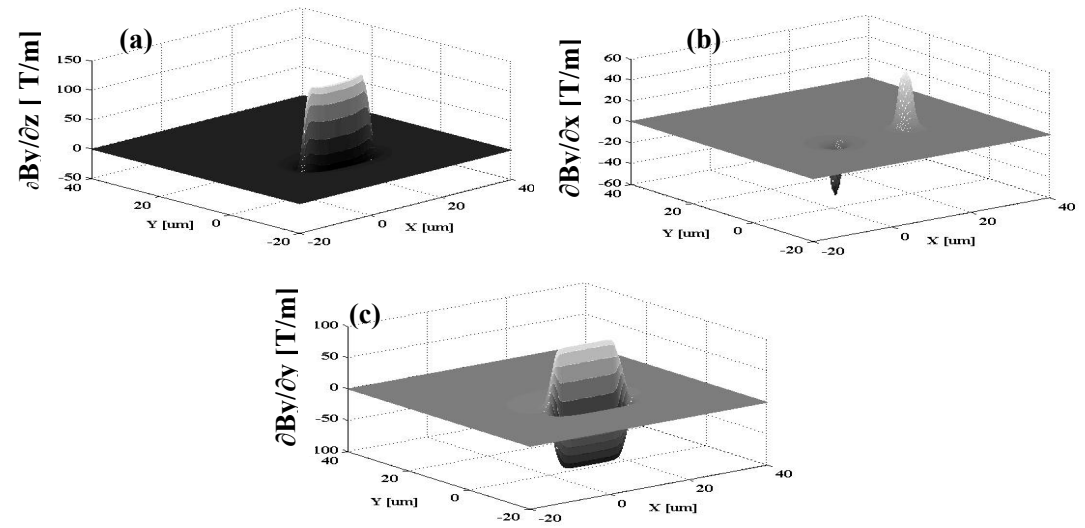

Figure A2.2. y-component of the magnetic field derivatives with respect to the x, y, z-coordinate at z =1.0 μm above the sample surface (z =0 plane) with a current of I = 1 mA in a direction as indicated in Figure 4.4.1(d).

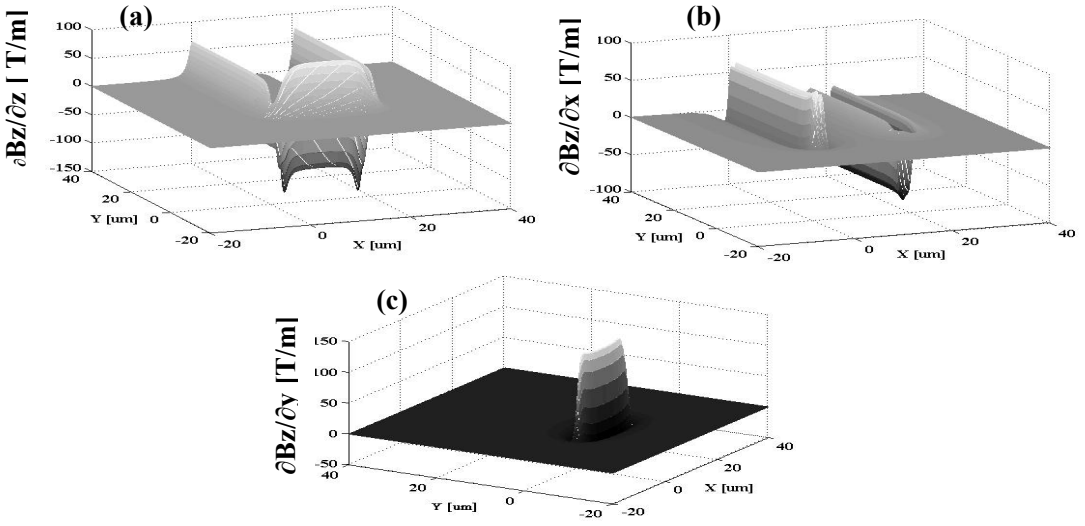

Figure A2.3. z-component of the magnetic field derivatives with respect to the x, y, z-coordinate at z =1.0 μm above the sample surface (z =0 plane) with a current of I = 1 mA in a direction as indicated in Figure 4.4.1(d).

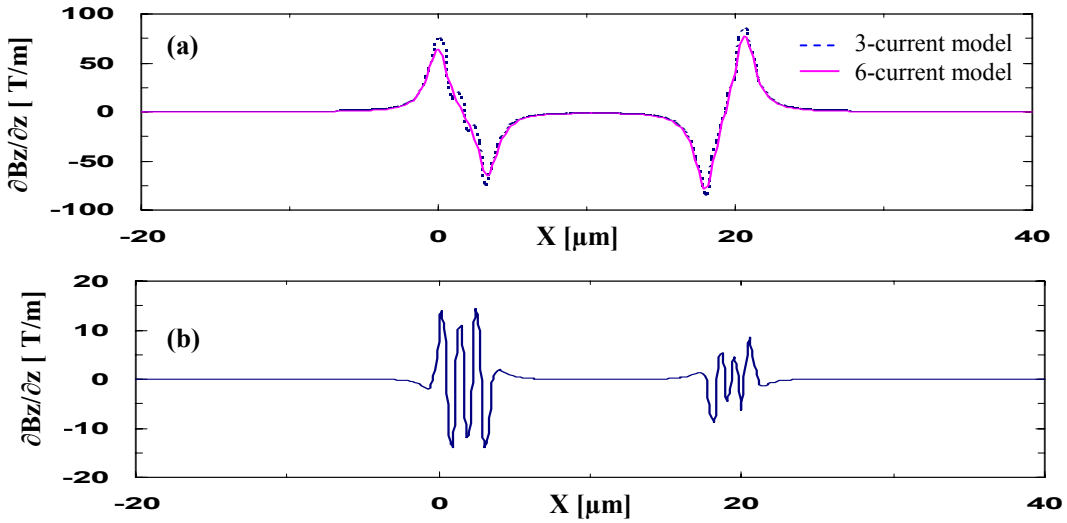

Figure A2.4. (a) 3- and 6-linear current model line-scan of z-component of the magnetic field derivatives with respect to the z- coordinate at z =0.8 µm above the sample surface (z =0 plane) with a current of I = 1 mA taken along the dashed line in Figure 4.4.1(d). **(b)** Difference between 3-current and 6-current model. Maximum deviation is less than 15%.

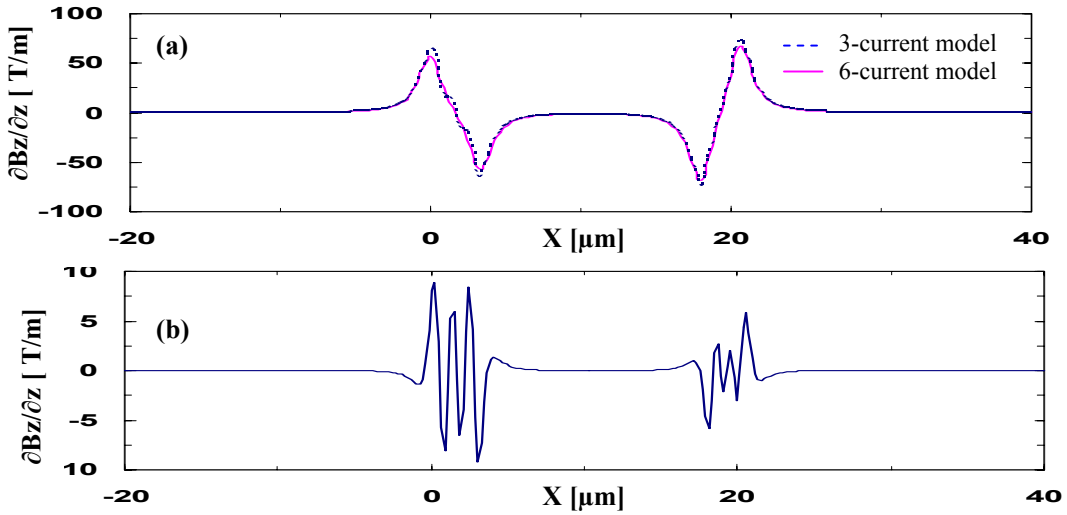

Figure A2.5. (a) 3- and 6-linear current model line-scan of z-component of the magnetic field derivatives with respect to the z- coordinate at z =1.0 µm above the sample surface (z =0 plane) with a current of I = 1 mA taken along the dashed line in Figure 4.4.1(d). **(b)** Difference between 3-current and 6-current model. Maximum deviation is less than 10%.

Appendix 3
APPLICATION OF THE METHOD TO INTEGRATED CIRCUITS

In this thesis force using an applied sinusoidal current was investigated for imaging current with over layers. However, the method of energizing a real circuit with an ac current signal has been considered in the different failure modes [12,23,39,147].

A3.1. Power to ground short.

This is a common failure mode in ICs. In this case the defect could be activated by applying a sinusoidal ac voltage from V_{DD} to ground.

A3.2. Logic shorts

In this case a set of vectors is needed to activate the defect from input. To perform force measurement could use several different ways:

a) A set of vectors activates the defect from input and a sinusoidal ac voltage is applied from V_{DD} to ground with a dc offset of more than one-half of the peak voltage (V_{pp}) to maintain a positive bias as shown in Fig.A3.1.

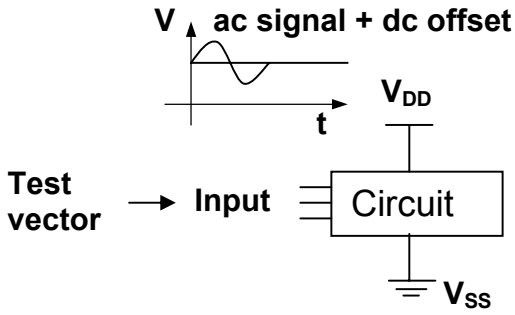

Figure A3.1. Test vector activates the defect from input and ac signal with a dc offset is applied from V_{DD}.

b) A dc voltage is applied from V_{DD} to ground. The test vector is generated by pulse with a frequency.

c) A dc voltage is applied from V_{DD} to ground. Test vector activates the defective local bitline, and then ac current is applied through the defect I/O.

d) A dc voltage is applied from V_{DD} to ground and test vector activates the defect from input. An ac flipping field is used to flip the magnetization direction of MFM tip as shown in Fig.A3.2 [148].

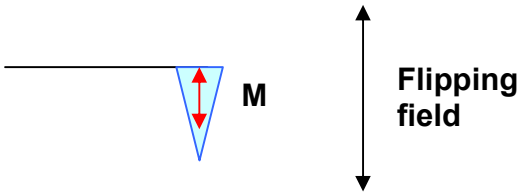

Figure A3.2. An ac flipping field flips the magnetization direction of MFM tip.

In these methods, it is expected that sample surface will have an appreciable potential and electrostatic force effects will play a role. In order to distinguish electrostatic and

magnetic interactions, Bonnell *et al.* proposed a technique [68] that allows the simultaneous collection of surface potential and magnetic force images, and then adjusts the tip bias by the values of surface potential, therefore eliminates the electrostatic force.

References

[1] "Semiconductor Industry Association; National Technology Roadmap for Semiconductors (NTRS), 2000", http://public.itrs.net/

[2] Sematech, Inc., "The National Technology Roadmap for Semiconductor, 1997 Edition, Technological Section.

[3] L.Wagner, "Failure Analysis Challenges", Proceedings of 8th IPFA, Singapore, 2001.

[4] D.Sarid, "Scanning Force Microscopy with Applications to Electric, Magnetic and Atomic Forces", edited by M.Lapp and H.Stark, Oxford University Press, New York, 1991.

[5] R.Wiesendanger, "Scanning Probe Microscopy and Spectroscopy Methods and Application", Cambridge University Press, Cambridge, 1994.

[6] R.Wiesendanger and H.-J.Guntherodt (Eds.), "Scanning Tunneling Microscopy II: Further Applications and Related Scanning Techniques", Springer-Verlag Berlin Heidelberg, Germany, 1992.

[7] D.A.Bonnell (Eds.), "Scanning Probe Microscopy and Spectroscopy: Theory, Techniques, and Applications", Wiley-VCH, Inc. USA, 2001.

[8] N.H.E.Weste and K.Eshraghian, "Principles of CMOS VLSI Design", Addison Wesley, pp. 498, 1993.

[9] S.Sabade, "Leakage Current-based Testing of CMOS ICs", IEEE Potentials, March/April, 2004.

[10] W.Mertin, R.Weber, F.Seifert, E.Kubalek, G.Zimmermann and C.Boit, "Contactless Failure Analysis of Integrated Circuits Via Current Contrast Imaging with Magnetic Force Microscopy", Proc. 27th Intern.Symp.Testing and Failure Analysis, Santa Clara, CA, 199-208 (2001).

[11] K.Nose and T.Sakurai, "Integrated Current Sensing Device for Micro IDDQ Test", Seventh Asian Test Symposium (ATS'98), 1998.

[12] D.P.Vallett, "Scanning SQUID Microscopy for Die Level Fault Isolation", Proceedings from the 28th International Symposium for Testing and Failure Analysis, Phoenix, Arizona, 391 (2002).

[13] R.Yongsunthon, A.Stanishevsky, J.McCoy, and E.D.Williams, "Observation of current crowding near fabricated voids in gold lines", Appl. Phys. Lett. **78**, 2661 (2001).

[14] R.Yongsunthon, P.J.Rous, A.Stanishevsky, K.Siegrist, and E.D.Williams, "Phase imaging of buries structures", Appl. Surface Sci. **210**, 6 (2003).

[15] T.Takahashi and D.Saida, "Magnetic field detection for current evaluation by magnetic force microscopy", Ultramicroscopy, **100**, 293 (2004).

[16] F.Kral, D.Perednis, B.Huey, D.A.Bonnell, G.Kostorz, and L.J.Gauckler, "Imaging current flow distributions in polycrystalline $Bi_2Sr_2CaCu_2O_x$ superconductors by magnetic force microscopy", Adv. Mater. (Weinheim, Ger.) **10**(17), 1442 (1998).

[17] B.D.Schrag and Gang Xiao, "Submicron electrical current density imaging of embedded microstructures", Appl. Phys. Lett. 82, 3272 (2003).

[18] E.Kinsbron, "A model for the width dependence of electromigration lifetimes in aluminum thin-film stripes", Appl. Phys. Lett. **36**, 968 (1980).

[19] Y.-C.Joo, C.V.Thompson, S.P.Baker, and E.Arzt, "Electromigration proximity effects of two neighboring fast-diffusion segments in single-crystal aluminum lines", J. Appl. Phys. **85**, 2108 (1999).
[20] R.J.Gleixner and W.D.Nix, "A physically based model of electromigration and stress-induced void formation in microelectronic interconnects", J. Appl. Phys. **86**, 1932 (1999).
[21] R.Rajsuman, "Iddq Testing for CMOS VLSI", Proceedings of the IEEE, **88**, 544 (2000).
[22] S.Sabade and D.M.H.Walker, "Evaluation of Outlier Rejection Methods for IDDQ Limit Setting", VLSI Design/Asia South Pacific Design Automation Conference, 2002.
[23] Keithley Instruments, Inc. "I_{DDQ} Testing and Standby Current Testing with Series 2600 System SourceMeter Instruments", www.keithley.com
[24] J.M.Soden and C.F.Hawkins, "I_{DDQ} Testing: Issues Present and Future", IEEE Design & Test of Computers, 61 (1996).
[25] M.Sachdev, "Deep sub-micron I_{DDQ} testing: Issues and solutions", European Design and Test Conference, 271 (1997).
[26] M.W.Levi, "CMOS is most testable", Int. Test Conf., 217-220, 1981.
[27] J.Acken and S.Millman, IEEE International Workshop on Iddq Testing, pp. 69-72, October 1995.
[28] J.M.Soden and R.E.Anderson, "IC Failure Analysis: Techniques and Tools for Quality and Reliability Improvement", Proceedings of the IEEE, **81**, 703 (1993).
[29] J.Ouellette, "Failure Analysis in a Nanometer World", The Industrial Physicist, 11 (1998).
[30] G.Deboy and J.Kolzer, "Fundamentals of Light Emission from Silicon Devices", Semicond. Sci. Technol. **9**, 1017-1032 (1993).
[31] W.Roesch, "Light Emission as an Analysis Tool for GaAs ICs", GaAs REL Workshop, Orlando, FL, 1996.
[32] J.A.Kash, J.C.Tsang, R.F.Rizzolo, A.K.Patel, and A.D.Shore, "Backside Optical Emission Diagnostics for Excess I_{DDQ}", IEEE J. of Solid-state Circuits, **33**, 508-511 (1998).
[33] A.Geol and A.Gray, "Liquid crystal technique as a failure analysis tool", Proc. Int. Rel. Phys. Symp., 115-120 (1980).
[34] D.Burgess, "Liquid Crystal: The Best Ideas From 15 Years", Electronic Device Failure Analysis News, 7-10 (1999).
[35] D.Pote, G.Thome, and T.Guthrie, "An overview of infrared thermal imaging techniques in the reliability and failure analysis of power transistors", Proc. Int. Symp. Testing and Failure Anal., 63-75 (1988).
[36] P.Kolodner and J.A.Tyson, "Microscopic fluorescent imaging of surface temperature profiles with 0.01^{o}C resolution", Appl. Phys. Lett. **40**, 782-784 (1982).
[37] P.Kolodner and J.A.Tyson, "Remote thermal imaging with 0.7 μm spatial resolution using temperature dependent fluorescent thin films", Appl. Phys. Lett. **42**, 117-119 (1983).
[38] O.C.Khiam, W.Z.Min, S.Redkar, C.Cheong, and T.Yang, "A new fluorescent and photoemission microscope for submicron VLSI IC failure analysis", IEEE, ICSE, Proc. Penang, Malaysia, 2002.

[39] L.A.Knauss, A.B.Cawthorne, N.Lettsome, S.Kelly, S.Chatraphorn, E.F.Fleet, F.C.Wellstood, and W.E.Vanderlinde, "Scanning SQUID microscopy for current imaging", Microelectronics Reliability, **41**, 1211-1229 (2001).

[40] D.A.Bonnell (Eds.), "Scanning Probe Microscopy and Spectroscopy: Theory, Techniques, and Applications", Wiley-VCH, Inc. USA, pp.243-244, 2001.

[41] A.N.Campbell, E.I.Cole, B.A.Dodd, and R.E.Anderson, "Magnetic force microscopy/Current contrast imaging: A new technique for internal current probing of ICs', Microelectronic Engineering, **24**, 11-22 (1994).

[42] A.N.Campbell, E.I.Cole, B.A.Dodd, and R.E.Anderson, "Internal current probing of integrated circuits using magnetic force microscopy", IEEE International Reliability Phyics Symposium, 31st Annual Proceedings, International, pp. 168-177(1993).

[43] A.V.Goryachev and A.F.Popkov, "Calibration parameters for the probing tip of a magnetic force microscopy in the field of a test current loop", Tech. Phys. **51**, 1223 (2006).

[44] G.Dumpich, B.Leven, and M.Brands, "Electron transport in magnetic nanostructures", Phys. Stat. Solidi A **201**, 3237 (2004).

[45] P.J.Rous, R.Yongsunthon, A.Stanishevsky, and E.D.Williams, "Real-space imaging of current distributions at the submicron scale using magnetic force microscopy: Inversion methodology", J. Appl. Phys. **95**, 2477 (2004).

[46] F.Seifert, R.Weber, W.Mertin, and E.Kubalek, "A new technique for contactless current contrast imaging of high frequency signals", Microelectronics Reliability, **43**, 1633 (2003).

[47] R.Yongsunthon, A.Atanishevsky, E.D.Williams, and P.J.Rous, "Mapping electron flow using magnetic force microscopy", Appl. Phys. Lett. **82**, 3287 (2003).

[48] R.Yongsunthon, E.D.Williams, J.McCoy, R.Pego, A.Atanishevsky, and P.J.Rous, "Test of response linearity for magnetic force microscopy data", J. Appl. Phys. **92**, 1256 (2002).

[49] F.Z.Wang, H.L.Na, W.W.Clegg, J.F.C.Windmill, and D.Jenkins, "Current-modulating magnetic force microscope probe", J. Appl. Phys. **89**, 6778 (2001).

[50] J.Lohau, A.Carl, S.Kirsch, and E.F.Wassermann, "Magnetization reversal and coercivity of a single-domain Co/Pt dot measured with a calibrated magnetic force microscope tip", Appl. Phys. Lett. **78**, 2020 (2001).

[51] L.Gan, S.H.Chung, K.H.Aschenbach, M.Dreyer, and R.D.Gomez, "Pulsed-current-induced domain wall propagation in permalloy patterns observed using magnetic force microscope", IEEE Trans. Magn. **36**, 3047 (2000).

[52] R.Weber, W.Mertin, and E.Kubalek, "Voltage-influence of biased interconnection line on integrated circuit-internal current contrast measurements via magnetic force microscopy", Microelctron. Reliab. 40, 1389 (2000).

[53] F.Kral, G.Kostorz, N.Ari, L.J.Gauckler, D.Perednis, and K.H.Han, "Spatial and force resolution of magnetic force microscopy in current imaging", Czechoslovak J. Phys. **49**, 1567 (1999).

[54] K.L.Babcock, V.B.Elings, J.Shi, D.D.Awschalom, and M.Dugas, "Field-dependence of microscopic probes in magnetic force microscopy", Appl. Phys. Lett. **69**, 705 (1996)

[55] W.Mertin, S.-W.Bae, U.Behnke, R.Weber, and E.Kubalek, "Contactless voltage and current contrast imaging with scanning force microscope based test systems", Proceeding from the 26th International Symposium for Testing and Failure Analysis, 12-16 Nov. 2000, Bellevue, Washington.

[56] C.Hartmann, R.Weber, W.Mertin, E.Kubalek, A.-D.Muler, and M.Hietschold, "Simultaneous IC-internal voltage and current measurements via a multi lever Scanning Force Microscope", Microelectron. Reliab. **42**, 1759 (2002).

[57] T.Goddenhenrich, H.Lemke, M.Muck, U.Hartmann, and C.Heiden, "Probe calibration in magnetic force microscopy", Appl. Phys. Lett. 57, 2612 (1990).

[58] R.Yongsunthon, J.McCoy, and E.D.Williams, "Calibrated magnetic force microscopy measurement of current-carrying lines", J. Vac. Sci. Technol. A 19, 1763 (2001).

[59] Th.Kebe and A.Carl, "Applied physics reviews – focused review: Calibration of magnetic force microscopy tips by using nanoscale current-carrying parallel wires", J. Appl. Phys. 95, 775 (2004).

[60] A.Carl, J.Lohau, S.Kirsch, and E.F.Wassermann, "Magnetization reversal and coercivity of magnetic-force microscopy tips", J. Appl. Phys. **89**, 6098 (2001).

[61] L.Kong and S.Y.Chou, "Quantification of magnetic force microscopy using a micronscale current ring", Appl. Phys. Lett. **70**, 2043-2045 (1997).

[62] L.Kong and S.Y.Chou, "Study of magnetic properties of magnetic force microscopy probes using micronscale current rings", J. Appl. Phys. **81**, 5026(1997).

[63] J.Lohau, S.Kirsch, A.Carl, G.Dumpich, and E.F.Wassermann, "Quantitative determination of effective dipole and monopole moments of magnetic force microscopy tips", J. Appl. Phys. **86**, 3410(1999).

[64] C.Liu, K.Lin, R.Holmes, G.J.Mankey, H.Fujiwara, H.Jiang, and H.S.Cho, "Calibration of magnetic force microscopy using micron size straight current wires", J. Appl. Phys. **91**, 8849 (2002).

[65] M.Neinhus, R.Weber, U.Behnke, W.Mertin, E.Kubalek, R.A.Breil, M.Detje, and A.Feltz, "Contactless current and voltage measurements in integrated circuits by using a needle sensor", Microelectron. Reliab. **42**, 1695 (2002).

[66] C.Hartmann, W.Mertin, and G.Bacher, "Circuit-internal signal measurements with a needle sensor", Microelectron. Reliab. **45**, 1505 (2005).

[67] C.Hartmann, W.Mertin, and G.Bacher, "Contactless current measurements using a needle sensor", Ultramicroscopy, **105**, 228 (2005).

[68] T.Alvarez, S.V.Kalinin, and D.A.Bonnell, "Magnetic-field measurements of current-carrying devices by force-sensitive magnetic-force microscopy with potential correction", Appl. Phys. Lett. **78**, 1005 (2001).

[69] U.Hartmann, "The point dipole approximation in magnetic force microscopy", Phys. Lett. A **137**, 475 (1989).

[70] G.Binnig, H.Rohrer, Ch.Gerber, and E.Weibel, "Surface studies by scanning tunneling microscopy", Phys. Rev. Lett. **49**, 57 (1982).

[71] G. Binnig, C.F. Quate, and Ch. Gerber, "Atomic force microscope", Phys. Rev. Lett. **56**, 930(1986).

[72] D.Sarid, "Scanning Force Microscopy with Applications to Electric, Magnetic and Atomic Forces", edited by M.Lapp and H.Stark, Oxford University Press, New York, pp.55-64, 1991.

[73] C.Schonenberger and S.F.Alvarado, "A differential interferometer for force microscopy", Rev. Sci. Instrum. **60**, 3131 (1989).
[74] D.Rugar, H.J.Mamin, R.Erlandsson, J.E.Stern, and B.D.Terris, "Force microscope using a fiber-optic displacement sensor", Rev. Sci. Instrum. **59**, 2337 (1988).
[75] Y.Martin and H.K.Wickramasinghe, "Magnetic imaging by force microscopy with 1000 Å resolution", Appl. Phys. Lett. **50**, 1455 (1987).
[76] D.Rugar, H.J.Mamin, and P.Guethner, "Improved fiber-optic interferometer for atomic force microscopy", Appl. Phys. Lett. **55**, 2588 (1989).
[77] M.J.Cunningham, S.T.Cheng, and W.W.Clegg, "A differential interferometer for scanning force microscopy", Meas. Sci. Technol. **5**, 1350 (1994).
[78] G.Meyer and N.M.Amer, Appl. Phys. Lett. **53**, 2400 (1988); " Erratum: novel optical approach to atomic force microscopy", Appl. Phys. Lett. **53**, 1045 (1988).
[79] S.Alexander, L.Hellemans, O.Marti, J.Schneir, V.Elings, P.K.Hansma, M.Longmire, and J.Gurley, " An atomic-resolution atomic-force microscope implemented using an optical lever", J. Appl. Phys. **65**, 164 (1989).
[80] D.Sarid, "Scanning Force Microscopy with Applications to Electric, Magnetic and Atomic Forces", edited by M.Lapp and H.Stark, Oxford University Press, New York, pp.119-128, 1991.
[81] G.Neubauer, S.R.Cohen, G.M.McClelland, and D.Horne, "Force microscopy with a bidirection capacitance sensor", Rev. Sci. Instrum. **61**, 2296 (1990).
[82] T.Goddenhenrich, H.Lemke, U.Hartman, and C.Heiden, "Force microscope with capacitive displacement detection", J. Vac. Sci. Technol. **A 8**, 383 (1990).
[83] D.Sarid, "Scanning Force Microscopy with Applications to Electric, Magnetic and Atomic Forces", edited by M.Lapp and H.Stark, Oxford University Press, New York, pp.65-73, 1991.
[84] D.J.Thomson, "Experimental Methods for Electronics Materials", Lecture Notes, University of Manitoba, 1996.
[85] R.Wiesendanger, "Scanning Probe Microscopy and Spectroscopy Methods and Application", Cambridge University Press, Cambridge, pp. 226-264, 1994.
[86] National University of Singapore, "Scanning Probe Microscopy", http://courses.nus.edu.sg/course/phyweets/PC4250/Projects2002/Scanning%20Probe%20Microscopy.htm
[87] R.Howland and L.Benatar, "Guide to Scanning Probe Microscopy", Park Scientific Instruments, 1996.
[88] S. Porthun, L. Abelmann, and C. Lodder, "Review article: Magnetic force microscopy of thin film media for high density magnetic recording", J. Magn. Magn. Mater. **182**, 238 (1998).
[89] D.Sarid, "Scanning Force Microscopy with Applications to Electric, Magnetic and Atomic Forces", edited by M.Lapp and H.Stark, Oxford University Press, New York, pp.5-17, 1991.
[90] O.Wolter, Th.Bayer, and J.Greschner, J. Vac. Sci. Technol. B **9**, 1353 (1991).
[91] T.D.Stowe, "Extending the lower limits of force detection using micromachined silicon cantilevers", Ph.D. Thesis, Department of Applied Physics, Stanford University, 2000.

[92] D.Sarid, "Scanning Force Microscopy with Applications to Electric, Magnetic and Atomic Forces", edited by M.Lapp and H.Stark, Oxford University Press, New York, pp.21, 1991.
[93] T.D.Stowe, K.Yasumura, T.W.Kenny, D.Botkin, K.Wago, and Rugar, "Attonewton force detection using ultrathin silicon cantilevers", Appl. Phys. Lett. 71 (2), 288 (1997).
[94] J.A.Sidles, J.L.Garbini, K.J.Bruland, D.Rugar, O.Zuger, S.Hoen, and C.S.Yannoni, "Magnetic resonance force microscopy", Rev. Modern Phys. **67**, 249 (1995).
[95] Y.Akama, E.Nishimura, A.Sakai, and H.Murakami, J. Vac. Sci. Technol. A8, 429 (1990).
[96] M.J.Vasile, D.Grigg, J.E.Griffith, E.Fitzgerald, and P.E.Russell, J. Vac. Sci. Technol. B9, 3569 (1991).
[97] H.Dai, J.H.Hafner, A.G.Rinzler, D.T.Colbert, and R.E.Smalley, Nature (London) **384**, 147 (1996).
[98] http://www.spmtips.com
[99] D.Sarid, D.Iams, V.Weissenberger, and L.S.Bell, Opt. Lett. **13**, 1057 (1988).
[100] D.Sarid, D.Iams, J.Ingle,V.Weissenberger, and J.Ploetz, J. Vac. Sci. Technol. A **8**, 378 (1990).
[101] Digital Instruments. Santa Barbara, California, USA.
[102] Park Scientific Instruments. Mountain Viev, California, USA.
[103] C.A.J.Putman, B.G.deGrooth, Niek F.van Hulst, and J.Greve, "A detailed analysis of the optical beam deflection technique for use in atomic force microscopy", J. Appl. Phys. **72**, 6 (1992).
[104] D.Sarid, "Scanning Force Microscopy with Applications to Electric, Magnetic and Atomic Forces", edited by M.Lapp and H.Stark, Oxford University Press, New York, pp.153-181, 1991.
[105] R.Wiesendanger and H.-J.Guntherodt (Eds.), "Scanning Tunneling Microscopy II: Further Applications and Related Scanning Techniques", Springer-Verlag Berlin Heidelberg, Germany, pp.151-207, 1992.
[106] J.J.Saenz, N.Garcia, P.Grutter, E.Meyer, H.Heinzelmann, R.Wiesendanger, L.Rosenthaler, H.R.Hidber, and H.-J.Guntherodt, J. Appl. Phys. **62**, 4293 (1987).
[107] Y.Martin, D.Rugar, and H.K.Wickramasinghe, Appl. Phys. Lett. **52**, 244 (1988).
[108] A.DiCarlo, M.R.Scheinfein, and R.V.Chamberlin, Appl. Phys. Lett. **61**, 2106 (1992).
[109] P.Grutter, A.Wadas, E.Meyer, H.Heinzelmann, H.-R. Hidber, and H.-J.Guntherodt, J. Vac. Sci. Technol. **A8**, 406(1990).
[110] H.J.Mamin, D.Rugar, J.E.Stern, R.E.Fontant, Jr., and P.Kasiraj, Appl. Phys. Lett. 55, 318(1989); Y.Luo and J.-G.Zhu, IEEE trans. Magn. **30**, 4080(1994).
[111] D.Rugar, H.J.Mamin, P.Guethner, S.E.Lambert, J.E.Stern, I.McFadyen, and T.Yogi, J. Appl. Phys. **68**, 1169(1990).
[112] T.Ohkubo, Y.Maeda, and Y.Koshimoto, IEICE Trans.Electron. **E78-C**, 1523(1995).
[113] H.J.Hug, B.Stiefel, P.J.A.van Schendel, A.Moser, R.Hofer, S.Martin, H.-J.Guntherodt, S.Porthun, L.Abelmann, J.C.Lodder, G.Bochi, and R.C.O'Handley, "Quantitative magnetic force microscopy on perpendicularly magnetized samples", J. Appl. Phys. **83**, 5609(1998).

[114] S.L.Tomlinson and A.N.Farley, "Micromagnetic model for magnetic force microscopy tips", J. Appl. Phys. **81**, 5029(1997).
[115] M.Mansuripur, "Computation of fields and forces in magnetic force microscopy", IEEE trans. Magn. **25**, 3467(1989).
[116] J.M.Garcia, A.Thiaville, J.Miltat, K.J.Kirk, J.N.Chapman, and F.Alouges, Appl. Phys. Lett. **79**, 656 (2001).
[117] Magnetic silicon cantilevers MSC12/15 data sheet. www.spmtips.com.
[118] Magnetic silicon cantilevers MSC12/15 data sheet. www.spmtips.com.
[119] D.T.Paris and F.K.Hurd, "Basic Electromagnetic theory", McGraw-Hill, Inc. U.S.A. pp. 201-204 (1969).
[120] U. Hartmann, "Theory of magnetic force microscopy", J. Vac. Sci. Technol. **A8**, 411(1990).
[121] D.Rugar, H.J.Mamin, P.Guethner, S.E.Lambert, J.E.Stern, I.McFadyen, and T.Yogi, "Magnetic force microscopy: General principles and application to longitudinal recording media", J. Appl. Phys. **68**, 1169 (1990).
[122] T.Goddenhenrich, U.Hartmann, M.Anders, and C.Heiden, "Investigation of bloch wall fine structures by magnetic force microscopy", Proc. STM88 Conference, Oxford, U.K., 1988; J. Microsc. **152**, 527 (1988).
[123] H.J.Mamin, D.Rugar, J.E.Stern, R.E.Fontana, Jr., and P.Kasiraj, Appl. Phys. Lett. **55**, 318 (1989).
[124] J.J.Saenz, N.Garcia, and J.C.Slonczewski, Appl. Phys. Lett. **53**, 1449 (1988).
[125] D.W.Abraham and F.A.McDonald, Appl. Phys. Lett. **56**, 1181 (1990).
[126] S.Rast, C.Wattinger, U.Gysin, and E.Meyer, "The noise of cantilevers", Nanotechnology, **11**, 169 (2000).
[127] T.R.Albrecht, P.Grutter, D.Horne, and D.Rugar, "Frequency modulation detection using high-Q cantilevers for enhanced force microscope sensitivity", J. Appl. Phys. **69**, 668 (1991).
[128] Y.Martin, C.C.Williams, and H.K.Wickramasinghe, J. Appl. Phys. **61**, 4723 (1987).
[129] S.Watanabe, K.Hane, M.Ito, and T.Goto, Appl. Phys. Lett. **63**, 2573 (1993).
[130] U.Hartmann, "Magnetic force microscopy", Annu. Rev. Mater. Sci. **29**, 53 (1999).
[131] A.Hubert, W.Rave, and S.L.Tomlinson, "Imaging magnetic charges with magnetic force microscopy", Phys. Status Solidi B **204**, 817 (1997).
[132] C.D.Wright and E.W.Hill, "Reciprocity based transfer function analysis in magnetic force microscopy", Appl. Phys. Lett. **68**, 1726 (1996).
[133] U.Hartmann, Adv. Electron. Electron Phys. **47**, 49 (1994).
[134] S.L.Tomlinson and E.W.Hill, J.Magn.Magn.Mater. **161**, 385 (1996).
[135] D.Sarid, "Scanning Force Microscopy with Applications to Electric, Magnetic and Atomic Forces", edited by M.Lapp and H.Stark, Oxford University Press, New York, pp.4-7, 1991.
[136] R.A.Said, "Scanning force potentiometry techniques for semiconductor circuit characterization", Ph.D. Thesis, Department of Electrical and Computer Engineering, University of Manitoba, 1996.
[137] V.Wittpahl, U.Behnke, B.Wand, and W.Mertin, "Cantilever influence suppression of contactless IC-testing by electric force microscopy", Microelectron. Reliab. **38**, 981 (1998).
[138] J.O.Oti, IEEE Transactions on Magnnetics, **29**, 2359 (1993).

[139] Digital Instruments, "NanoScope IV Controller Manual", Software Version 5.12r3, part No. 004-115-000, Rev. A, 2002; "NanoScope Software 6.12 User Guid", part No. 004-132-000, Rev. C, 2004; "EnviroScope Manual", Version 5.30, part No. 004-102-000, Veeco Instruments Inc. 2004.
[140] J.W.Strutt, (III Lord RAYLEIGH), "Investigations in Optics, with special reference to the spectroscope", Philosophical Magazine, **VIII**, 261, 4303; 477 (1879) and **IX**, 40 (1880).
[141] P.F.Meilan and M.Garavaglia, "Rayleigh Resolution Criterion for light sources of different spectral composition", Braz. J. Phys. Vol.27 n.4 Sao Paulo Dec. 1997.
[142] A.W.Jones, and J.Bland-Hawthorn, "Towards a general definition for spectroscopic resolution", ASP Conference Series, Vol. 77, 1995.
[143] D.M. Pozar, Microwave Engineering, 2nd ed., Wiley, 1998.
[144] H.-J. Krause and M.V. Kreutzbruck, "Recent developments in SQUID NDE", Physica C 368, 70-79 (2002).
[145] S. Hirsekorn, U. Rabe, A. Boub, and W. Arnold, "On the contrast in eddy current microscpy using atomic force microscopes", Surf. Interface Anal. 27, 474-481 (1999).
[146] B. Hoffmann, R. Houbertz, and U. Hartmann, "Eddy current microscopy", Appl. Phys. A 66, S409-413 (1998).
[147] Y.Yamada and H.Komoda, "An example of fault site localization on a 0.18 μm CMOS device with combination of front and backside techniques", Microelectronics Reliability, 44, 771(2004).
[148] R.P.Cowburn, A.M.Moulin, and M.E.Welland, "High sensitivity measurement of magnetic fields using microcantilevers". Appl. Phys. Lett. 71, 2202-4 (1997).